

Explorations of post-synthetic acid treatment and operando site-titration for hydrogenation catalysis on transition metal sulfides

Ferdinand Vogelgsang

Vollständiger Abdruck der von der TUM School of Natural Sciences der Technischen Universität München zur Erlangung eines
Doktors der Ingenieurwissenschaften (Dr.-Ing.)
genehmigten Dissertation.

Vorsitz: Prof. Dr. Klaus Köhler

Prüfer*innen der Dissertation:

1. Prof. Dr. Johannes A. Lercher.
2. Prof. Dr.-Ing. Kai-Olaf M. Hinrichsen

Die Dissertation wurde am 14.02.2023 bei der Technischen Universität München eingereicht und durch die TUM School of Natural Sciences am 23.06.2023 angenommen.

To my parents, who made it possible!

Omnia autem probate quod bonum est tenete.

Biblia sacra vulgata, 1 Thess. 5, 21

Acknowledgements

Without any doubt, a PhD time has many facets and includes the scientific work itself as well as a personal arrangement and development in a highly dynamic social research environment. Now, at the end of this journey it is time to recapitulate and show some gratitude to the people who supervised and accompanied me along this way.

First and foremost I would like to express my sincere thanks to Prof. Dr. Johannes A. Lercher for giving me the opportunity and chance to work in his group. Dear Johannes, I highly appreciate the scientific education I was allowed to receive, constant questions for hypotheses you drive on your students and the request for dedicated thinking about catalytic research and experimental results you insisted on. Consequently, the ‘Lercher School’ trained for being capable with many different catalytic systems, I will benefit from for my future career. I will always remember moments we shared, from first interactions when ‘great minds traveled on same tracks’ over wild discussions during a Christmas party to the point you taught me the taste of iron chloride and many others. Finally, I want to thank for the overall trust and support you granted over the years!

Of utmost importance for a decent scientific education is a thoughtful guidance. I highly appreciated when Dr. Hui Shi took over this part. Dear Hui, thank you for your lessons in the art of catalysis and always being patient while explaining energy landscapes of reactions and lecturing physical chemistry. Your profound knowledge about kinetics and intellectual way to combine data to a comprehensive and knowledge-orientated study helped to finally publish the work of this thesis. Thank you Hui for the time in Munich and the productive and constructive cooperation!

In order to deliver fine scientific work, excellent sponsors and partners are of invaluable importance. I would like to thank Dr. Alexander Kuperman and Dr. Axel Brait for their trust in this research and support over the years. Dear Alex and Axel, I highly appreciated your thoughtful and always open minds for ideas coming from the lab in Munich and the discussions we had on the data the S-group presented in the evening times. I could learn from the comments, explanations and experiences you shared which also helped to proceed into the right direction. I enjoyed to work in a project where without any doubt two experts in the field of sulfur catalysis participated. Thank you!

In a big research group, a strong constant helps to maintain quality and stores knowledge and experience over time. Prof. Dr. Andreas Jentys is the strong basis at TC II who always was able to help out when questions about catalysis research popped up. Dear Andy, I appreciate the scientific talks and informative and funny stories I was able to listen during your visits in lab, placing your ‘Haferl’ at any free spot or during ‘EXAFS’ trips. Thank you for the amusement you carried with your educational conversations.

Before I joined the group as a PhD student, my studies led me to research work about catalysis in the form of Bachelor / Master Theses and internships. During that time I found trust and support by several people who I thank in chronological order; Eva Schachtl, Maximilian Hahn, Christian Gärtner and Sebastian Foraita. Special thanks go to Yuran Wang and Prof. Yuriy Román-Leshkov who hosted me during my internship work in the USA where I found passion for scientific research and finally decided to apply for a PhD position.

Directly at the beginning of my PhD work I was heartily welcomed in the so-called 'Männerbüro' hidden in the side floor of the chair of Technical Chemistry II. Peter Hintermeier, Matthias 'Hias' Steib, Sebastian Müller and Felix Kirchberger, thank you for a wonderful time in our temple of extra-ordinariness and greatness. You, together with Andreas 'Ehrmi' Ehrmaier, Daniel Melzer, Martin Baumgärtl, Wanqiu Luo, Manuel Weber and particularly Manuel Wagenhofer, who in the beginning played the role of a senior in sulfide research and acted as my mentor, accompanied me over the years and were help and support at the same time. Thank you!

Sometimes during a PhD time when one is totally over his or her head and the motivation is critical, there is need for mental medical care. In these moments it helps to sit down with a cold drink and talk the frustration away. Roland Weindl, Verena Höpfl, Niklas Pfriem, Insu Lee and Alexander Wellmann, thank you for all the sit-ins, political and scientific discussions, a lot of restaurant visits and for turning the work place into a little bit of home.

Next to the life at the institute, there was the 'Garching Crew' who met regularly and enjoyed my life in 'Novogarchinsk'. In addition to above mentioned colleagues, I want to thank Lingli Ni, Teresa Schachtl and Martina Aigner for wonderful evenings and late night discussions. At this point I would also like to emphasize the value of cross-over relations and comradeship with colleagues from other groups. Especially, the friends from TC I united in the TC soccer team, Philipp Donaubaue, Thomas Burger, Thomas Kleiner, Sebastian Standl and Sebastian Eckstein, always grouped to illustrious company, for example during a legendary evening at Europacat conference in Florence or when the Chemistry soccer tournament ended in a bacchanalian celebration.

While acting at a university's chair and preparing your own scientific work, there is help of technical and administrative nature required. First of all, I want to thank Xaver Hecht, who taught me all relevant skills needed while working in Technical Chemistry laboratories. Next, I want to thank Bettina Federmann, who helped to fill out all official documents which lie as hurdles on the way to the PhD defense. Special thanks also go to Ulrike Sanwald, who was a real enrichment to the group's cultural education. Finally, I want to thank Andreas Marx, Martin Neukamm and Ulrike Ammari for their ad hoc support whenever needed.

Last but not least, I am full of invaluable gratefulness to my family and friends, whom I have been receiving endless support over the years. At this point, I want to say a big “Thank You!” to my closest friends Ferdi, Heni, Domi and Katha. For more than 25 years we have been sharing awesome moments and I am sure we will continue having exciting adventures. It is a pleasure for me to have some wonderful people around me I can always rely on!

Finally, all this was only possible because of the secure background I was allowed to grow up in. Gratitude goes to my siblings Alex and Caro, who accompanied me during my way. Thank you for giving me the feeling that we are united in our individual diversity. Now it is time to express my infinite gratitude to my parents Joachim and Martina! I thank for a strong and reliable environment you created and always guaranteed over the years, for your assistance, love and overall trust you spend on me. I was able to receive full back up by both of you and I am thankful that I could flee the warm nest without any reservations and always have the chance to return back and be welcomed. Thank you for your invaluable and endless support!

Ferdinand Vogelgsang, June, 2022

Abstract

The rate of phenanthrene hydrogenation linearly correlates with the amount of accessible Ni-promoted sites located at the edges of Mo/WS₂ slabs. For low Ni-decoration degrees (<20%) the influence of less active unpromoted sites dominates the overall hydrogenation activity. At high Ni contents, Ni_xS_y particles form in large quantities and block active sites but contribute to the overall hydrogenation activity to small extent. However, the site-specific activity of Ni-associated edge sites, revealed by *operando* and volumetric pulsing techniques, is independent of surrounding Mo or W atoms provided by the sulfide slab, while being more active than unpromoted sites. For the first time, an *operando* titration technique allowed to quantify and discriminate between CUS and S-H groups, Lewis and Brønsted acid sites, and uncovered a third unknown type of sites. Further, these experiments prove that Ni increases the total active site density as well, compared to unpromoted slabs.

Kurzzusammenfassung

Die Phenanthrene Hydrierrate korreliert linear mit den verfügbaren Ni promotierten aktiven Zentren, welche sich an den Kanten der Mo/WS₂ Platten befinden. Bei zu niedriger Konzentration von Ni Zentren (<20%) an den Kanten dieser Platten wird die Gesamthydrieraktivität des Sulfides durch weniger aktive unpromotierte Zentren dominiert. Bei hohem Nickelgehalt blockieren Ni_xS_y die aktiven Zentren, tragen jedoch zu einem kleinen Teil zur Gesamthydrieraktivität bei. Dabei ist die spezifische Aktivität von Ni-Zentren, welche über *operando* und volumetrische Pulsmethoden bestimmt wurde, unabhängig von den umgebenden Metallen, Mo oder W. Allerdings sind Ni Zentren aktiver als reine Mo oder W-Zentren. Zum ersten Mal konnte mit Hilfe der *operando*-Titration zwischen CUS und SH-Gruppen, Lewis und Brønsted Säurezentren, unterschieden werden und ein drittes unbekanntes Zentrum gemessen werden. In weiteren Experimenten wurde gezeigt, dass Ni die Gesamtzentrenzahl der Sulfide erhöht.

Abbreviations and Symbols

Chemicals

Asym-OHPhe	1,2,3,4,4a,9,10,10a-octahydrophenanthrene	NO	Nitric oxide
ATM / ATT	Ammonium tetrathio molybdate / tungstate	O ₂	Oxygen
CH ₄	Methane	PerHPhe	Perhydrophenanthrene
Co	Cobalt	M	Metal
D ₂	Deuterium	Mo	Molybdenum
DBT	Dibenzothiophene	NH ₃	Ammonia
DiHPhe	9,10-dihydrophenanthrene	NH ₄ OH	Ammonium hydroxide
DMDS	Dimethyl disulfide	(NH ₄) ₆ Mo ₇ O ₂₄	Ammonium heptamolybdate
DMS	Dimethyl sulfide	(NH ₄) ₂ WS ₄	Ammonium tetrathiotungstate
Fe	iron	(NH ₄) ₆ W ₁₂ O ₄₀ H ₂	Ammonium metatungstate
HCl	Hydrochloric acid	Ni	Nickel
HD	Hydrogen deuterate	Ni(C ₁₁ H ₇ O ₂) ₂	Nickel naphthenate
H ₂	Hydrogen	S	Sulfur
H ₂ S	Dihydrogen sulfide	Sym-OHPhe	1,2,3,4,5,6,7,8-octahydrophenanthrene
H ₂ WO ₄	Tungstic acid	TetHPhe	1,2,3,4-tetrahydrophenanthrene
Ni(NO ₃) ₂	Nickel nitrate	W	Tungsten

Formulas / Measures

c	concentration	v	Stoichiometric coefficient
C_{SH-HD}	Correlation factor SH-HD	R	Universal gas constant
E_A	Energy of activation	r	Reaction rate
e^-	Electron	r	radius
F_{NO}	Reference factor based on NO	ρ	Density
f_{Mo}	Edge fraction of Metal atoms at the slab	S	Entropy
G	Gibbs free energy	S	Selectivity
H	Enthalpy	ST	Space Time
K	Thermodynamic equilibrium constant	T	Temperature
k	Rate constant	t	Time
k_0	Pre-exponential factor	TOF	Turn-over-frequency
k_B	Boltzmann constant	V, \dot{V}	Volume, volumetric flow
M	Molar Mass	w	Weight fraction
m	Mass	wt. %	Weight percentage
n	Amount	X	Conversion
n	Reaction order	Y	Yield
p	Pressure		

General Abbreviations

A(H)	(hydrogenated) aromatic	(L)	Leached formulation
BET	Brunauer Emmet Teller (Isotherm)	LUMO	Lowest unoccupied molecular orbital
B.J.H.	Barrett, Joyner, Halenda (Pore volume)	(P)	Parent (formulation)
CUS	Coordinative unsaturated sites	r.d.s.	Rate determining step
HDA	Hydrodearomatization	SH	Sulfhydryl groups
HDN	Hydrodenitrogenation	STM	Scanning tunneling microscope
HDS	Hydrodesulfuization	TEM	Transmission electron microscopy
HOMO	Highest occupied molecular orbital	TMS	Transition metal sulfide
HREM	High-resolution transmission electron microscopy	TPR	Temperature programmed reduction
HYD	Hydrogenation	TS	Transition state
ICP-OES	Inductively coupled plasma atomic emission spectroscopy	XPS	X-ray photo-electron spectroscopy
Ind.S	Industrial catalyst sulfided		

Indices

*	Free active site	i	Component i
≠	Transition state	Intr.	intrinsic
n,m, x,y,z	Partial order of reactant	Inhib.	inhibitor

Table of contents

Acknowledgements	V
Abstract.....	VIII
Kurzzusammenfassung.....	VIII
Abbreviations and Symbols.....	IX
Table of contents	XIII
Chapter 1	1
General Introduction	1
1 Crude oil – a never ending story	2
2 Refining and Hydrotreating – a way to clean fuels.....	7
3 Catalysts for Hydrotreatment – the optimal system.....	11
4 Scope of the Thesis	16
Chapter 2	19
Transition Metal Sulfides and Hydrotreatment	19
1 Transition metal sulfides for hydrotreatment.....	20
1.1 Choice of catalysts based on Sabatier’s principle	20
1.2 Crystal structure of MoS ₂ and WS ₂	22
1.3 Bulk structure of Mo/WS ₂ – the slab model.....	23
1.4 Promotion of Mo/WS ₂ phases with Ni and Co.....	25
2 Active sites in hydrotreatment	32
2.1 Active sites of Ni promoted Mo/WS ₂	32
2.2 Hydrogen activation and SH formation.....	34
2.3 Hydrogenation of aromatic structures	37
Chapter 3	41
Procedures and Methods for Research on Transition Metal Sulfides.....	41
1 Synthetic routes towards bulk NiMo(W)S ₂	42
1.1 Preparation of TMS catalysts by co-precipitation	42
1.2 Preparation of bulk TMS by thermal decomposition method	45

1.3	'Leaching' of TMS catalysts	48
2	Most commonly used characterization techniques	51
2.1	Morphology and Surface Structure	51
2.2	Measuring active sites	56
3	Reaction Kinetics	61
3.1	Primary measures – reaction rate, selectivity and yield	61
3.2	Secondary measures – reaction order and activation energy	63
3.3	Reaction kinetics experimental	66
3.4	H ₂ -D ₂ scrambling	69
Chapter 4	75
Comparison of Ni promoted Mo and W sulfides in HDA	75
1	Preface	76
2	Experimental.....	77
2.1	Characterization of bulk NiMo(W) sulfides.....	77
2.2	Synthesis and characterization of bulk NiMoW sulfides	77
2.3	H ₂ -D ₂ scrambling	78
2.4	Reaction kinetics	79
2.5	Alternative protocols	80
3	Results.....	82
3.1	Effect of leaching	82
3.2	Estimation of surface SH-groups	87
3.3	Phenanthrene hydrogenation on bulk NiMoWS ₂	90
3.4	Hydrogen activation on TMS.....	96
3.5	Precursor synthesis and S-protocol	97
4	Conclusion	102
Chapter 5	105
On the multifaceted roles of NiS _x in hydrodearomatization reactions catalyzed by unsupported Ni-promoted MoS ₂	105
1	Abstract.....	106

2	Introduction.....	106
3	Experimental.....	108
3.1	Synthesis of catalysts.....	108
3.2	Characterization.....	110
3.3	Catalytic evaluation.....	110
3.4	Experiments with physical mixtures and stacked beds of Ni _m S _n and MoS ₂	111
4	Results and Discussion.....	112
4.1	Elemental and phase compositions of Ni _a MoS ₂ catalysts before and after leaching	112
4.2	Textural and slab properties of Ni _a MoS ₂ catalysts before and after leaching	116
4.3	Phenanthrene hydrogenation on Ni _a MoS ₂ catalysts.....	118
4.4	Phenanthrene hydrogenation on physical mixtures and stacked beds of Ni _m S _n and MoS ₂	124
4.5	Structure-activity correlations for promoted and unpromoted sites in bulk Ni _a MoS ₂	126
4.6	On the complexity of the HCl treatment.....	128
5	Conclusion.....	129
6	Acknowledgement.....	130
7	Addendum to ‘multifaceted roles of NiS _x ’.....	131
7.1	Preface.....	131
7.2	Experimental and characterization.....	131
7.3	Over leaching of Ni _{a>0.5} MoS ₂	132
7.4	Leaching of Ni _a WS ₂	137
Chapter 6	143
	Toward quantification of active sites and site-specific activity for polyaromatics hydrogenation on transition metal sulfides.....	143
1	Abstract.....	144
2	Introduction.....	145

3	Experimental.....	148
3.1	Catalyst preparation.....	148
3.2	Feed preparation for phenanthrene hydrogenation and titration experiments	149
3.3	Reaction and titration in the trickle bed reactor system.....	149
4	Results and Discussion	151
4.1	Phenanthrene hydrogenation.....	151
4.2	Breakthrough of titrant and tracer in a blank reactor and during a titration experiment	152
4.3	Validation of the titration method for site quantification.....	154
4.4	Comparison of site counts and average site-based activities across different catalysts.....	157
4.5	Insights into the heterogeneity of active sites	159
4.6	Effects of temperature and H ₂ pressure on the titrant uptake and residual activity	162
4.7	On the potential and limitations of the in situ titration methods for studying sulfide catalysts.....	164
5	Conclusions.....	165
6	Acknowledgement	166
	Summary and Final Conclusions	169
	References	174
	Appendices	188
A1.	Supporting information chapter 4.....	189
A2.	Supporting information chapter 5.....	202
A3.	Supporting information chapter 6.....	214
A4.	Copyright	222
	Publications and conference contributions.....	225

Chapter 1

General Introduction

“The stone age did not end because the world ran out of stones, and the oil age will not end because we run out of oil. It ended because bronze tools became cheaper.”^[1]

Ahmed Zaki Yamani

1 Crude oil – a never ending story

It all began “on a hot Saturday afternoon”, August 27th, 1859 when Edwin Laurentine Drake (1819-1880) executed the first successful oil drilling near Titusville, Pennsylvania.^[2] Petroleum (Lat. *petra*, rock, and *oleum*, oil), also crude oil, was known since the ancient times in Babylon (Herodotus), in Sicily for illumination (Plutarch), in China and Japan for lighting and heating, from the 13th century on in Europe and used for medical purposes in the first half of the 19th century. Then the Chemist James Young distilled the first light thin oil and the Canadian Chemist Abraham Gesner introduced kerosene obtained from petroleum as a better combustion fuel in lamps compared to whale oil used at that time.^[3,4] Based on Gesner’s invention, the Seneca Oil Company (former Pennsylvania Rock Oil Company) sent Drake in 1858 to Pennsylvania with the aim to drill for crude oil and produce carbon oil fuel for lamps, which illuminated the streets and houses in America. Drake’s successful discovery “in a valley along a creek” launched the modern oil industry and reveals as a historical important date as it was the first planned and organized drill for commercial reasons.^[2]

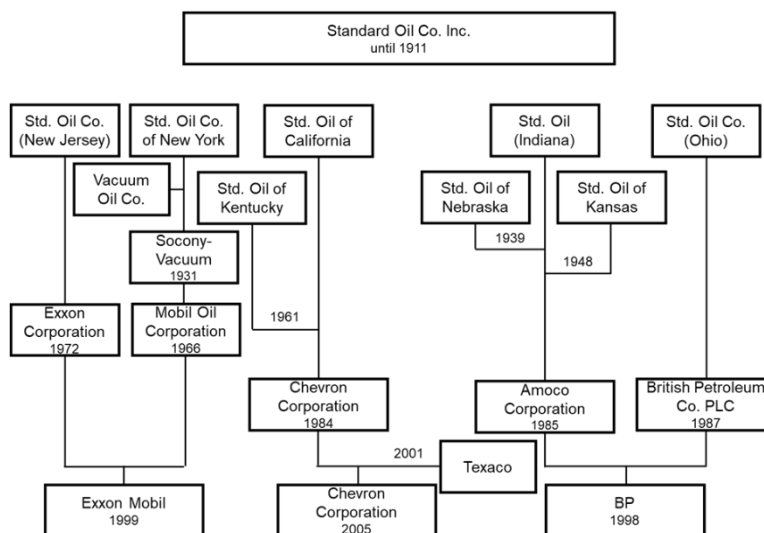
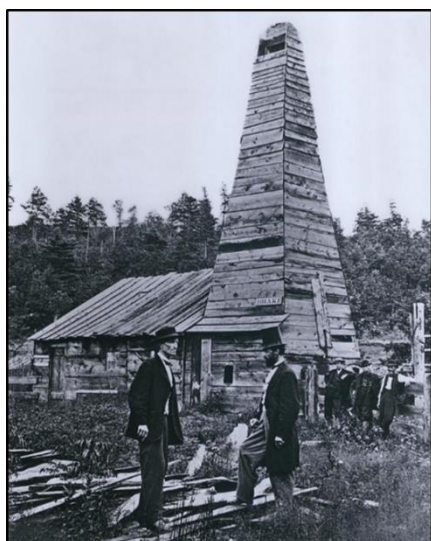


Figure 1-1. Picture on the left: Edwin Drake standing on the right in front of his oil derrick with Peter Wilson. Photo was taken by John Mather, July, 1866 in Titusville. Reprint gratefully permitted by the Pennsylvania Historical & Museum Commission. Scheme on the right: Development of oil companies still operating today after Standard Oil break up in 1911 under the Sherman Antitrust Act.

The following years were an era of expansion for the oil industry, at the end of which one of the biggest oil producing, manufacturing and marketing, multinational companies of the world evolved. Inspired by the news from Titusville, oil fields in Canada (1860ties) and later all over the globe (1870 Baku/Russia, 1878/1880 Rumania/Galicia, 1880ties South East Asia) were developed.^[3] In Pennsylvania, the first oil rush started in 1859 when oil wells and refineries sprout from the ground. The production of crudes increased from 2000 barrels in 1859 to 10000000

barrels in 1873 when the rush slowly decayed. During this turbulent decade, John Davison Rockefeller and Henry Flagler founded the Standard Oil Co. Inc. By focusing on efficiency and responsibility, the company had a monopoly on the oil industry and by 1904 they controlled 91% of the oil refining and 85% of the final sales in the US, making Rockefeller one of the wealthiest persons ever. Due to abusive and anticompetitive actions, the Supreme Court of the United States divided the monopoly of Standard Oil into smaller competitive firms (e.g., Exxon, Mobil, Chevron, Amoco), which in part still operate today.^[5-9]

However, after the triumphant boom in the second half of the 19th century, the conquest for oil continued in the first half of the 20th century. After the Russian empire had passed the USA in oil production capacity, the access to oil became an important factor during the military conflicts in the first half of the 20th century.^[10] Additionally, new oil fields in Saudi Arabia were developed in 1938^[7,11] After the 1960ties Saudi Arabia and the Soviet Union^[10] had overtaken the USA by the production of oil. The importance of oil in an internationalized and globalized world economy was demonstrated in 1973, when Arab nations imposed an oil embargo against western nations which caused the oil crisis and other international conflicts were caused by oil (-reserves) in the second half of the 20th century, too. Accordingly, this century can be described as the age of oil^[7] which has not found an end until today. To that date, oil is still one of the biggest resources for energy and industrial manufacturing worldwide and expected to grow the next decade.

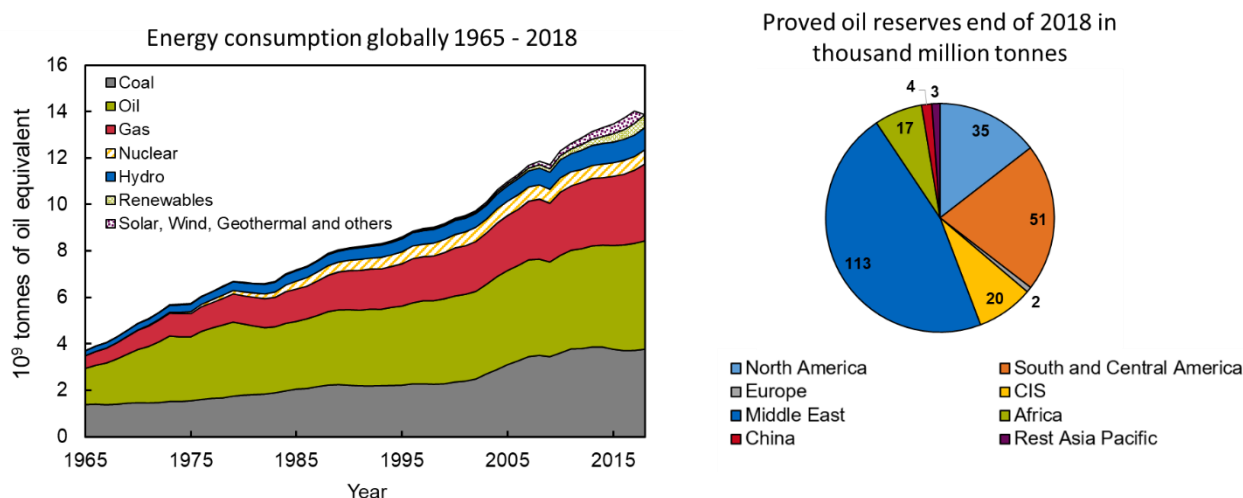


Figure 1-2. (Left): Global Energy consumption from 1965-2018. Usage of all primary energy resources increased with oil as one of the main energy carriers. (Right): Proved oil reserves by world regions. Data obtained from *BP Statistical Review of World Energy*, 68th edition, 2019.^[12]

Today, the primary energy consumption by fuel (commercially traded fuels, including modern renewables used to generate electricity) lies at 13865 million tonnes of oil equivalent worldwide. It grew in a rate of 2.9% in 2018 and is the fastest in a ten-year average of 1.5%. Main contributors were China, which had the fastest growth in the last 30 years, followed by the USA

and India. The main energy carriers oil, coal and natural gas contributed to over 85% of energy consumption and 4474 million tonnes of crude oil (83161 thousand barrels a day) were produced which is more than 2.2% compared to 2017. Although production and consumption of oil increased the last decade, the proved oil reserves rose as well to about 244 thousand million tonnes where the majority is located in the Middle East and the American continent.^[12]

The physical properties of crude oils strongly vary by its geographical origin and composition. Its appearance “ranges from pale yellow through red and brown to black or greenish” in color. The specific gravity ranges from 0.771 to 1.06 and the flash point from -18 to 180°C.^[3] Important characteristics of crude oils are the density, sulfur content and distillation curve. A commonly used number for the density is the so-called API degree (American Petroleum Institute gravity), a measure to compare the density of a crude to the specific gravity of water.

$$^{\circ}API = \frac{141.5}{\text{specific gravity (60}^{\circ}F)} - 131.5 = 10^{\circ} API \text{ for density} = 1$$

If the °API is larger than 10, the crude floats on water, otherwise it sinks. Based on this number, crudes are further classified into extra-light (condensates, >45°API), light (33 to 45°API), medium (20 to 33°API), heavy (10 to 20°API) and extra-heavy and bitumens (<10°API).^[13–15]

Table 1-1. Boiling fractions of chosen crudes including sulfur content, crude density and API (calculated). Noteworthy, the Venezuelan crude is very heavy and contains a lot of sulfur.^[16]

Crude / property	Gas [wt.%]	Gasoline [wt.%]	Middle Distillates [wt.%]	Heavy Products [wt.%]	Sulfur [wt.%]	Density [kg m ⁻³]	API [°]
Brent (North Sea)	2	29	33	36	0.38	834	38.2
Arabian light	2	27	21	40	1.7	855	34
Safaniyah (Saudi Arabia)	3	17	28	52	2.8	893	27
Ural	2.6	16.6	33.9	46.9	1.35	866	31.9
Boscan (Venezuela)	-	-	22	78	5.27	990	11.4

All crudes are complex liquid hydrocarbon and organic compound mixtures which exhibit elemental compositions of C (79.5-87.1%), H (10 – 14.8%), S (0.05 – 6%), N (0.1 – 2%) and O (0.05 – 1.5%).^[14,17] Additionally, metals (mainly Ni and V) are present in small quantities. In a first step of crude processing, the complex mixture of alkanes, paraffins, cyclo-alkanes and (poly-) aromatics is separated into fractions with different boiling ranges. Conventionally, a distillation process differentiates according to the molecular sizes (the boiling point increases with carbon number) into light fractions up to gasoline, C₁-C₁₀, (fuel gas, propane, butane, light naphtha, gasoline, heavy naphtha), bp: -1 to 205°C; kerosene, C₁₀-C₁₃, (aviation fuel, solvents, light heating

oils), bp: 205 to 260°C; atmospheric gas oil, C₁₃-C₂₅, (heavy and light gas oil, diesel oil, heating oil), bp: 260 to 425°C) and atmospheric residue, C₂₅₊, (distillates and vacuum residue), bp: > 400°C.^[14,18]

Light crude oils typically yield in 3, 39, 23 and 35% of light gas, gasoline, middle distillates and heavy products while heavy crudes yield in 1, 19, 9 and 71%, respectively.^[14] Based on this product distribution, crudes from different geographical origins can be classified and ranked by quality, whereas light distillates, which have a low sulfur content, are preferred.^[16,18]

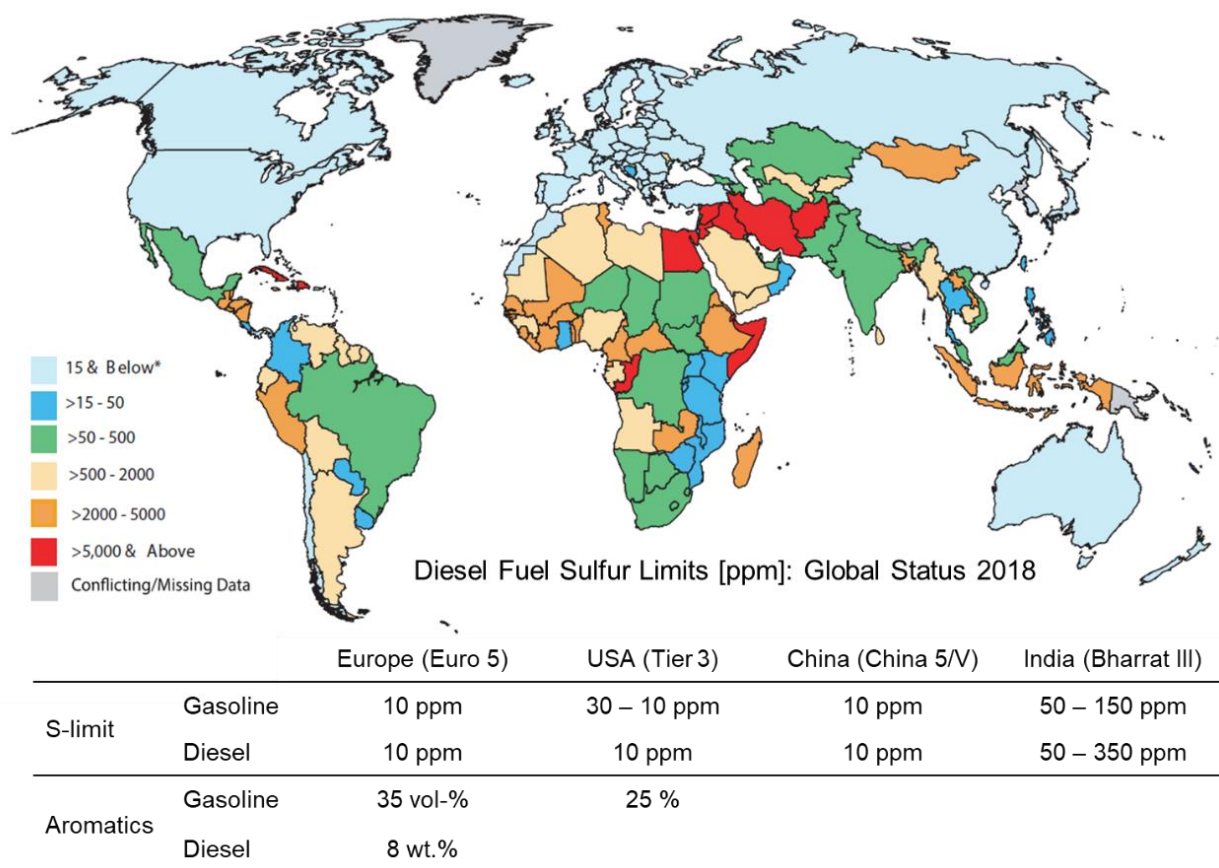


Figure 1-3. World map of Diesel sulfur limits in 2018.^[23] The table below shows regulations for sulfur and aromatic limits in Europe, the USA, China and India. Note, that other countries e.g. Japan, Brazil, Australia, South Korea and others in part share the presented standards.^[22]

Crude oil is a product of biogenic origin, which results from sedimentation, compression, low-temperature heating and bacteriological action of ancient organic matter. During the transformation of the ancient vegetation into petroleum, elements like S and N were enriched.^[13] The invention of the combustion engine for heating and transportation (Otto, Benz, Daimler, Diesel) and its mass production in 1908 (Model T, Ford) led to the massive production of transportation fuels,^[7] so that today the most used products are gasoline for vehicles, aviation fuel, diesel and heavy fuel oil.^[18] After combustion of these products, SO_x, CO₂ and NO_x (e.g. being responsible for acid rain), and particulate matter escape as environmental poisons. Further,

aromatics in the end-use products are cancerogenous and their content in fuels should be limited.^[19,20] Therefore, the maximum content of sulfur and nitrogen in transportation fuels (including marine fuels)^[21] as well as too high carbon content is strictly regulated.^[18,22,23] In order to meet regulations such as Euro 5,^[24] Clean Air Act (Tier 3),^[25] China 5/V^[26] and Bharat III^[22] and to avoid poisoning of catalytic materials during the processing of (heavy) crudes, S and N containing compounds as well as metals have to be removed from the primary resource by hydrotreatment processes in the refinery.^[15,17,19]

2 Refining and Hydrotreating – a way to clean fuels

Over time, many different products based on crude oil have been developed. They include fuels, heating fuels, petrochemical raw materials, hydrocarbon solvents, specialty products (bitumens, lubricant oils, food-grade or medical grade paraffins, etc.) and petrochemical base products.^[18] Since petroleum is a complex mixture of chemical compounds, it has to be purified and processed to obtain high quality and demanding end-use products.^[16] All the processes involved in the upgrading of crudes are summarized to ‘refining operations’, in a refinery.

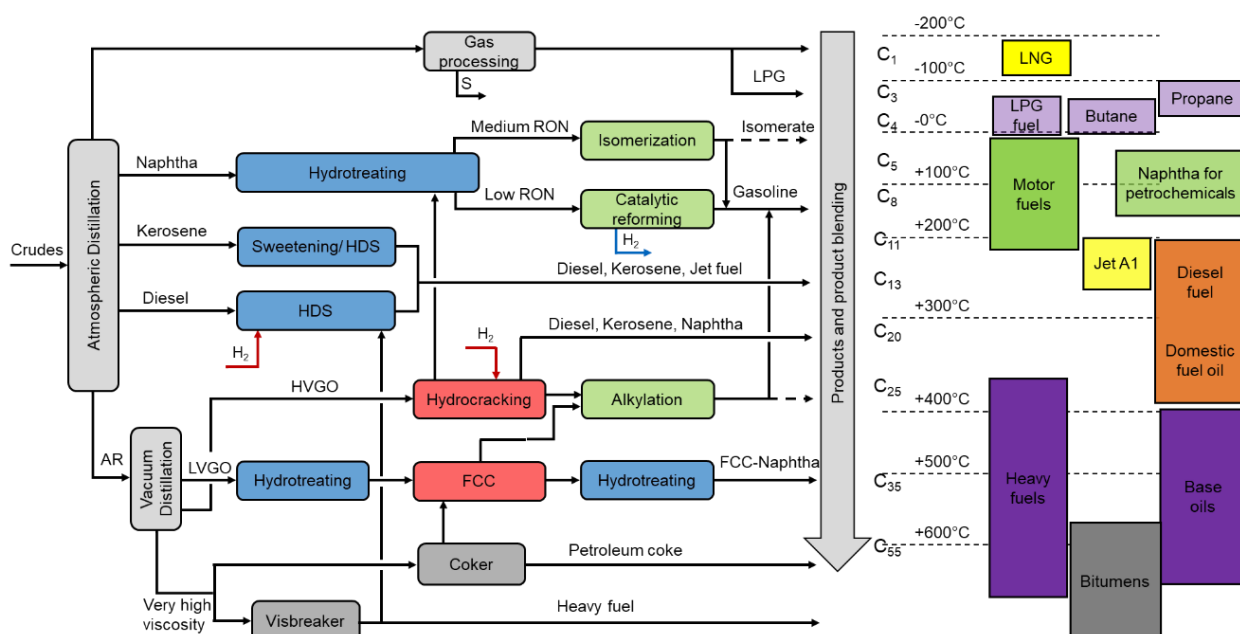


Figure 1-4. Flow chart of a modern refinery. Classical hydrotreating operations are indicated in blue, carbon removal and chain shortening processes are labeled red and reactions adjusting the octane number (research octane number, RON) are indicated in green. Additional information of boiling point and carbon number for desired energy carriers is given on the right.

In 2018, world's total refining capacity was at 100049 thousand barrels a day^[12] with the biggest refinery located in Jamnagar, Gujarat, India.^[27] A refinery is a large complex of different manufacturing plants and individual processes are chosen based on feedstock quality and supply, operation costs, environmental regulations and a changing or developing market demand to operate economically. However, depending on the process units installed, refineries can be categorized into four major types with increasing complexity to fulfill the three main refinery process categories of separation (distillation), conversion (coking and catalytic cracking) and finishing (hydrotreatment). These types range from *simple / hydroskimming* refineries (no conversion of residual fraction after distillation) over a *typical conversion* refinery (including catalytic cracking, olefin conversion, alkylation) to *deep conversion* refineries (conversion of vacuum distillate fraction into vacuum and atmospheric distillates and solid coke) and *ultra deep*

conversion refineries (to treat extra heavy crudes).^[13,18] Figure 1-4^[15,16,28] gives a complex scheme of a modern refinery.

Most targeted and valuable products of a refinery are transportation fuels such as gasoline, kerosene, diesel and domestic fuel oils and heavy fuels. All of these products show a similar chemical composition and characteristic. For example, a high octane number, which represents the quality of gasoline, is achieved with molecules containing 5 to 10 C atoms of mixtures of branched alkanes and aromatics. Diesel fuels are characterized by their density and polyaromatic content as well as the cetane number which is high for non-branched 12 to 20 C atoms containing molecules.^[20] In order to meet specifications of these products, the refining units intervene by adjusting the H/C ratio and the carbon content of the boiling fractions obtained after distillation.^[16,18]

Some important processes are *Fluid Catalytic Cracking, FCC*, (reduction of molecular weight, conversion of HVGO into gasoline), *Hydrocracking, HCR*, (dual function of cracking and hydrogenation to produce diesel and kerosene), *Alkylation* (obtaining higher octane numbers by using light alkenes, propene, butene), *Isomerization* (skeletal isomerization of light alkanes for higher octane numbers) and *Catalytic Reforming* (increase of octane number by aromatization, hydroisomerization, cyclization and hydrogenolysis), which also is a net hydrogen producer in a refinery.^[16]

As seen in Figure 1-4 the process of *Hydrotreatment* is present in nearly every conversion step of crude oil fractions, which makes it one of the largest applications in a refinery.^[19] The necessity for gas-oil hydrotreatment are the environmental legislations for refining and combustion products as described above (see Figure 1-3). Therefore, its main purpose is saturation of aromatic and olefinic feed molecules and elimination of heteroatoms such as S, N, O and metals (mainly Ni and V), which are present in refining feeds (see 1). These (hetero-, poly-) aromatic hydrocarbons accumulate in higher boiling fractions.^[20]

Overall, hydrotreatment reactions are exothermic and heteroatom removal is not limited by its thermodynamics while aromatic hydrogenation reactions are reversible. Typical process conditions are high hydrogen pressures of 15 – 110 bar and moderate temperatures of 320 – 400°C. The reactions are carried out in fixed bed reactors equipped with stacked catalytic beds with quench gas injection in-between to regulate and moderate the temperature (exothermicity, equilibria of hydrodearomatization, sintering and deactivation of the catalyst by coking) and reaction type (selectivity). The hydrotreating processes are described and named after their main purpose.^[19,20,29]

Hydrodesulfurization (HDS) converts compounds such as thiols, (di-) sulfides, thiophenes (low boiling naphtha) and (di-, benzo-) thiophenes (kerosene, gas-oil middle distillate) into S-free molecules. The term *deep desulfurization* describes the processes for treating least reactive S-molecules in heavy boiling feeds or the post-treatment of gas oils to on-road diesel.

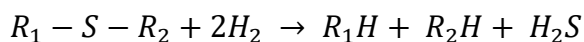
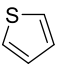
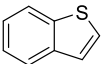
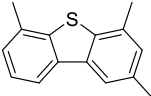
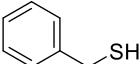


Table 1-2. Structures of S-containing molecules in crude oils.

			
Thiophene	Benzothiophene	2,4,6-trimethyldibenzo [b,d]thiophene	Benzothiol

Hydrodenitrogenation (HDN) converts basic N-containing molecules with a pyridine nucleus like pyridines, quinolines, indoles, pyrroles and acridines. These compounds are present in heavier and cracked fractions. Due to its increased aromaticity compared to S-compounds the HDN, reaction requires a higher H₂ pressure than HDS.

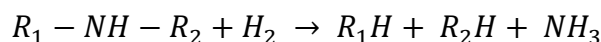
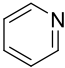
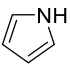
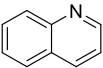
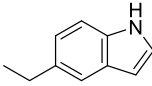
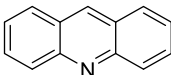


Table 1-3. Structural formula of typical N-containing molecules in crude oils.

				
Pyridine	Pyrrol	Quinoline	5-Ethyl-1H-Indole	Acridine

Hydrodearomatization, (also aromatic hydrogenation, HDA) is the conversion of (naphtheno-) aromatics such as benzene, tetralin, naphthalenes, phenanthrenes, anthracenes and pyrenes into naphthenic compounds. The multi-step process is reversible and thermodynamically favored at high pressures and low temperatures but kinetically preferred at high temperatures. The compromise temperatures are between 380 – 400°C.

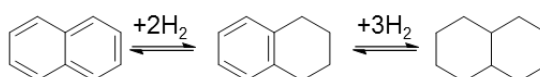
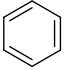
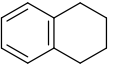
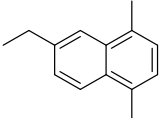
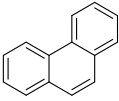
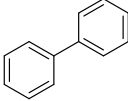
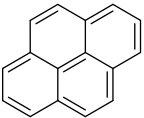
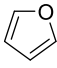
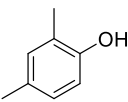
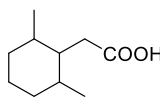


Table 1-4. Aromatics and polyaromatic compounds in crude oils.

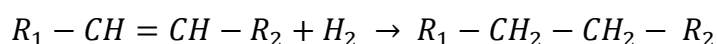
					
Benzene	Tetralin	6-Ethyl-1,4-dimethylnaphthalene	Phenanthrene	Biphenyl	Pyrene

Hydrodeoxygenation (HDO) is mainly applied for coal and biomass derived feeds, since the O content in conventional crudes is low. Molecules present are usually phenols, carboxylic acids and aryl ethers.

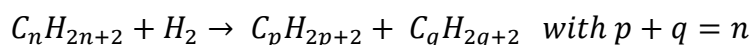
Table 1-5. Structures of molecules containing O typically found in biomass derived feedstocks.

		
Furan	2,4-dimethylphenol	2-(2,6-Dimethylcyclohexyl) Acetic acid

Olefin saturation is irreversible, kinetically fast and favored at high temperatures. Its main purpose is preventing the formation of higher alkylates.



Cracking and *Coking* are unwanted processes occurring during hydrotreatment. The first reduces the gas-oil yield by fractioning of the long chain products and the second poisons the catalysts by converting polyaromatics into C and H₂ in an equilibrium depending endothermic process.



In recent years the demand for high value products like gasoline, kerosene, lube oil and gas oil (Diesel) increased. At the same time, the crudes used became heavier causing refineries to increase their efforts in heavy oil and residua treatment. These residues can make up to 85 vol-% of a barrel crude and boil over 343°C (*atmospheric residue, AR*) or over 565°C at 33-133 mbar vacuum (*vacuum residue, VR*). Additionally, these fractions contain a high portion of S, N and metal (as porphyrin) containing molecules as well as polycyclic aromatics (low H/C ration of 1.2 to 1.4) and asphaltenes. Hence, the spotlight of a refinery shifted to demanding reactions like thermal methods^[30] and the catalytic reactions of *deep desulfurization*, *hydrodemetallation (HDM)* and *hydrodearomatization (including ring opening)*, which require a lot of hydrogen to break down asphaltenes and increase the H/C ratio of the polyaromatic feeds. Especially, N and metal containing molecules as well as the process of coking cause deactivation of the hydrotreating catalysts. With these challenges and high requirements, a highly stably and selective catalyst is needed to meet demanding specifications of the end-use products and to operate the hydrotreatment process economically.^[20,30,31]

3 Catalysts for Hydrotreatment – the optimal system

In fact, the hunt for active materials in hydrotreating started early on in the beginning of the 20th century. For the development of modern processes, the introduction of catalytic hydrogenation and realization of high pressure catalysis to liquefaction of coal as well as implementation of an effective research apparatus were of upmost significance.^[32] In Germany, Friedrich Bergius (Nobel Prize 1931)^[33] developed between 1910 and 1913 non-catalytic high-pressure processes for hydrotreatment of heavy petrol distillates to produce gasoline fractions formed by cleavage reactions. Additionally, he succeeded in hydroliquefaction of coal at 400-450°C and 150 atm H₂ pressure and yielded 80% of fuels. Nevertheless, these fuels were of too low quality for motor fuels due to their relative high molecular weight and large contents of O, S and N.^[34]

After WW I, Germany was cut off the supply of guano to produce nitrates (as explosives) so that the need for a N source (fertilizers) led to the invention of the Haber-Bosch process. Further, Germany had no natural sources of oil to produce fuels needed in warfare engines, so that the production of synthetic gasoline based on coal was of prior interest. Inspired by the work of Bergius and earlier of Sabatier (Nobel Prize 1912)^[33] and the success of large scale catalytic processes (ammonia and methanol production), researchers of I.G. Farbenindustrie (IGF) and later Badische Anilin und Sodafabrik (BASF) started to look for metals catalyzing the hydrogenation of coal. Between 1920 and 1930 over 6000 materials were tested and two important observations were made: i) that metals turned into their sulfides after coal hydrogenation and ii) that some (e.g., iron sulfide) were more active and stable in their sulfide form. Particularly, Matthias Pier and Carl Krauch observed that during thermal treatment of coal, hydrogen accumulated in super light boiling fraction while an H-poor residua remained. They concluded that high pressure H₂ addition was needed, but the products still had too high O, N and S contents and the boiling fraction was too low for motor fuels. In thermal treatment the hydrogenation speed was too low (mainly gaseous products or polymerized olefins were produced), therefore they suggested using a catalyst to accelerate the hydrogenation. Highest reaction velocities and stability in treating complex mixtures of gas, liquid and partially solids in combination with sulfur being present as a poison were obtained by molybdenum and tungsten based sulfides and H₂O, H₂S and NH₃ were produced.^[32,35] In the following many patents came out which peaked in a controversy between German and US researchers about the origin of the invention of using sulfides (or even heterogeneous catalysts) in industrial applications. Anyhow, the knowledge about catalysts had been there even before the time of Bergius.^[34]

After 1930, other researchers outside Germany joined the field of fundamental research on hydrotreatment catalysis, e.g., in the Soviet Union, Japan, Great Britain and Italy and before WW II sulfides were established in petroleum processing (HDS, aromatization of cycloalkanes). Early on, attempts in using HDS processes were made by Standard Oil New Jersey who wanted to increase the yield of fuels and the Union Oil Company of California who faced high S-content crudes with the need to decrease the sulfur level in gasoline and CoMo-based catalysts were used. In 1943, A.C. Byrns described Co as a promotor atom in MoS₂ catalysts for HDS reactions.^[32,36] With the end of the war, coal processing was declining in Europe and research efforts were shifted to petroleum processing, mainly in the USA, where many companies achieved developments in the application of sulfides.^[34] The state of the art catalysts were combinations of Co, Ni, Mo and W sulfides^[37,38] and a first systematic study with varying atomic ratios of Co/Mo and Ni/Mo on γ -Al₂O₃ supported catalysts for HDS was conducted by Harold Beuther (1959) who worked for the Gulf Research and Development Co.^[39] Anyhow, in the following years the established catalytic system was considered to be the most stable and active among all and no improvement was expected.^[32]

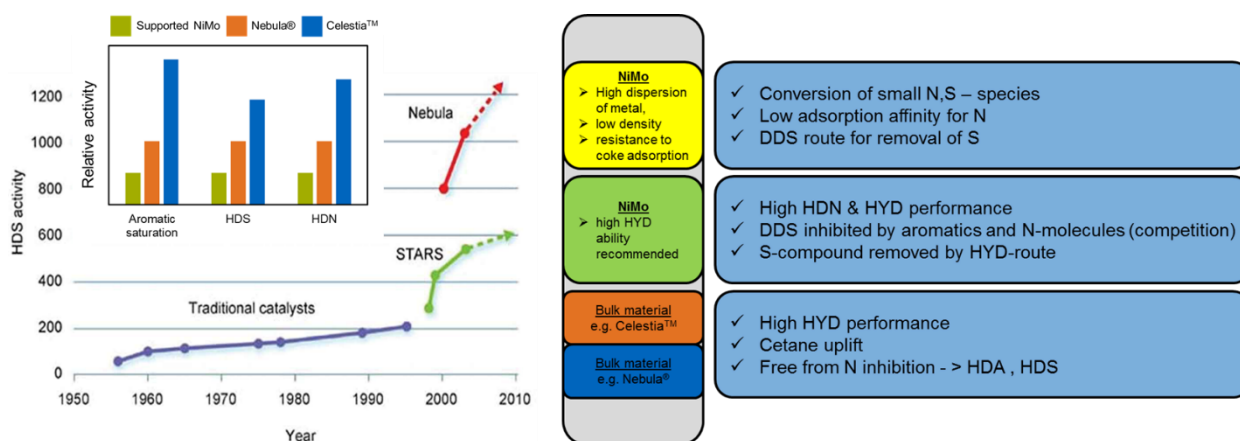


Figure 1-5. (left) Activity development of TMS catalysts at the example of Albemarle STARS ('super type II active reaction sites'), Nebula ('new bulk activity') and Celestia technology. (right) Example for stacked bed technology with different tasks for each bed and the optimal choice of a catalyst.^[59,63,64]

First fundamental studies on sulfide based catalysts started to arise in the 1980's with a large contribution from Europe.^[40] T. A. Pecoraro and Russel R. Chianelli studied unsupported transition metals of 3d, 4d and 5d rows in the HDS of dibenzothiophene as a model compound. They found the first row transition metal sulfides (TMS) to be mainly inactive while the second and third row TMS peaked in activity at Ru and Os sulfide.^[38] Later, they also investigated binary mixtures of Ni-, Co-, Mo- and W-sulfides, which were better HDS catalysts than RuS₂.^[41] In the second half of the 1980ties, other groups investigated TMS catalysts for different reactions such as other HDS, HDN and HYD on supported or unsupported catalysts (see a list in *Catalysis by Transition Metal Sulphides*^[42]). Depending on the system studied, a maximum in activity was found for RuS₂, Rh₂S₃ and IrS₂ giving a volcano type curve among the periodic position of transition metals similar to what Pecoraro *et al.* had found before.^[42]

Simultaneously, models explaining the morphology, chemical structure and nature of the active sites of the catalysts were developed.^[20,33] Suggestions were given by J.M.J.G. Lipsch and G.C.A. Schuit (1969),^[43–45] R.J.H. Voorhoeve and J.C.M. Stuiver (1971),^[46,47] Bernard Delmon (1979),^[48,49] Henrik Topsøe (1981)^[50–53] and others.^[42]

However, detailed attempts to understand periodic trends in TMS catalysts had to be waited for until the late 1990ties when Pascal Raybaud and Hervé Toulhoat used DFT calculations in their investigations. The studies showed clearly, that optimal catalysts for hydrotreatment reactions are obtained by Ni(Co) promotion of Mo(W) sulfides.^[54–57] Following up, Pavel Afanasiev (2007) extended the study to tertiary mixtures of those metals.^[58] In 2013, Toulhoat and Raybaud described the modern catalyst as binary and tertiary mixed sulfides supported on γ -Al₂O₃ or carbon with a very high activity for both, HDS and HYD.^[42]

A modern catalyst faces many challenges. Not only environmental requirements for ultra clean refinery end-products (mainly diesel, gasoline, kerosene and non-transportation fuels) and the rising usage of extra heavy crudes but also process aspects like catalyst life time, activity towards side reactions, pressure drop build-ups, ease of activation, regenerability and price are hurdles for the catalytic system.^[20,59] Depending on the nature of the feedstocks and the processes applied, different catalysts are loaded as separated beds into the reactor. CoMo structures are good HDS catalysts (low H₂ consumption) while NiMo formulations are better for HDN and HDA (high H₂ consumption) and NiW catalysts are used for aromatic hydrogenation.^[20,33,59] The promoter content typically varies between 0.2 and 0.4. Usually, Mo and W are supported on a carrier with a concentration of 8-16 wt.% and 12 – 25 wt.%, respectively. The most common support is γ -Al₂O₃, but silica-alumina, silica, zeolites, etc., are used as well. Although the main task of the support is dispersing the active phase (limiting costs) and not to take a major role in the catalysis, for example, adding P to the support favors hydrogenolysis before hydrogenation. It is common to load a shaped (reduction of pressure drop) oxidic precursor of the catalysts into the reactor before it is activated by sulfidation either using a real feed or additives like DMDS, DMS and H₂S.^[20]

Although TMS catalysts are widely studied and reasonable structure – activity models exist, there is still room for improvement driven by the pursuit of ultra-low sulfur diesel. In 2001, ExxonMobil, Akzo Nobel and Nippon Ketjen introduced a new catalyst technology called ‘NEBULA[®]’, which exceeded the HDS activity of commercialized CoMo/Al₂O₃ by far. These catalysts are trimetallic NiMoW sulfides obtained by decomposition of nickel (ammonium) molybdotungstes without any support.^[60–64] The problem in using highly active trimetallic unsupported NiMoWS₂ catalysts was, that the hydrogen consumption and heat release as well as the price for the metals was too high for conventional processes. Sonja Eijsbouts (Albemarle) dedicated an article in 2007 to that topic arguing for the beneficial role of NEBULA[®] technology.^[65] This outstanding invention might have motivated other companies to search for similar highly active bulk trimetallic NiMoWS formulations, which are able to hydro-treat heavy boiling residua in the following years. In this field, ExxonMobil and Albemarle once again

achieved latest success. In 2019, they introduced Celestia™, which alone or in combination with NEBULA® offers an ‘ultra-high’ HDS, HDN and especially aromatic hydrogenation activity.

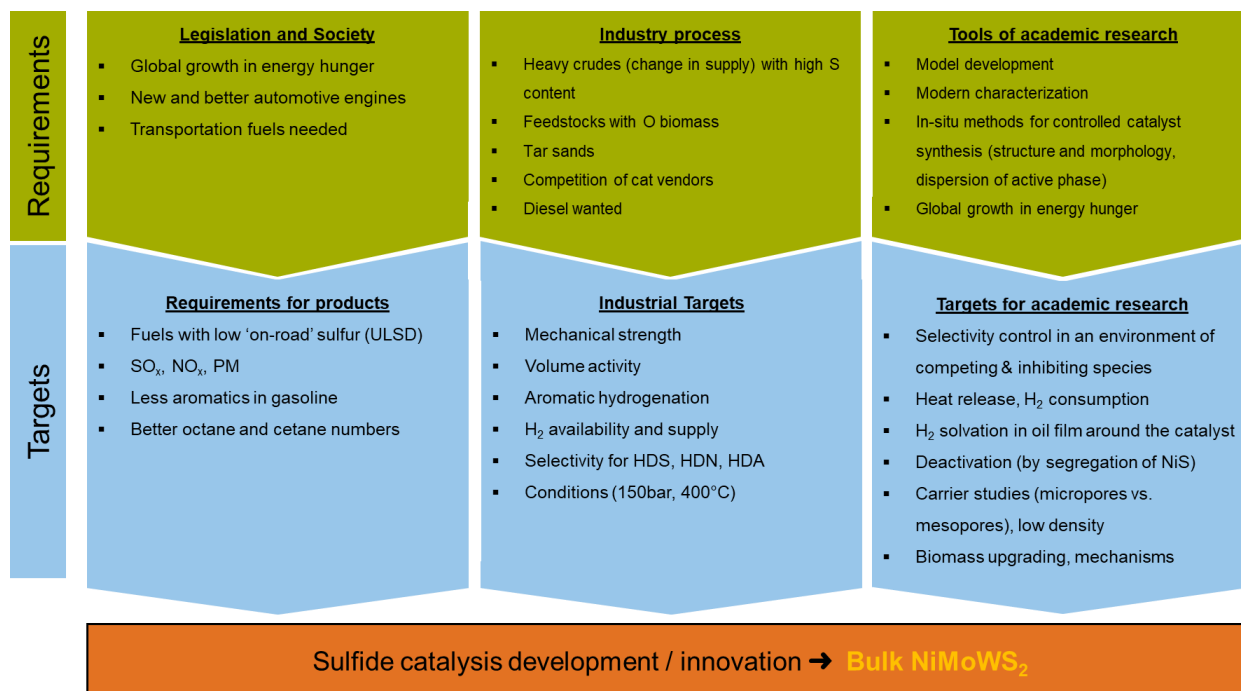


Figure 1-6. Driving forces for modern hydrotreatment catalysts development. On the top row the requirements and challenges for the three chosen fields of ‘legislation and society’, ‘industry’ and ‘academia’ are listed. Below, the targets, aims and duties are presented which have to be dealt with in order to achieve a suitable catalyst. Nowadays, bulk NiMoWS₂ materials emerged.^[32,66]

By looking at the history of TMS catalysts for hydrotreatment of crude oils in refining, reaching back over 100 years, it shows that this system is not fully understood and described yet; so its story continues. Many contributors (e.g., Chevron, ExxonMobil, Albemarle, IFP, RIPP, Haldor Topsøe, Criterion, UOP, BP, BASF, etc.) have generated a tremendous amount of data and knowledge about hydrotreatment processes and catalytic systems over the years.^[32,59] Born out of coal liquefaction in the beginning of the 20th century at BASF and IGF and its industrial implementation for oil upgrading to more useful products in the 1930ties, followed by a research boost in the 1980ties (probably initiated by Topsøe’s model and better characterization as well the oil crisis in 1973), the field of Ni(Co)Mo(W) sulfides is still a topic of big interest and research efforts are ongoing.

In general, ultra-stable low-priced catalysts, which tolerate more and more demanding crudes with a lot of poisonous compounds and severe hydrotreating conditions, are wanted. Open tasks for academic research and catalyst development are the quantification and description of the nature of the active sites in these structures, the exact role of the promoter (Ni) and its interaction with the structure giving elements of W and Mo. Furthermore, mechanism studies for biomass upgrading, the design of guard beds, control of selectivities towards HDN, HDA and HDS, which compete about the same active sites and cause inhibition effects, and the understanding of

deactivation processes during the reaction e.g., by phase separation of Ni and Co sulfides, are targeted by scientific questions. Traditionally, the focus of research studies was on supported catalysts due to their ability to disperse the active phase and suitability for many in-situ characterization techniques. However, the main problems are that the supports offer micropore structures while hydrotreatment reactions require mesopores and that due to the low density of these catalysts the volume activity, which is a key parameter for industrial applications, is very low. Therefore, the trend goes to unsupported trimetallic NiMoWS formulations with excellent volumetric activity and the ability to hydrogenate polyaromatics and favor their ring opening. Special problems to be solved are the control of the high heat release caused by the high activity and the control of stacking degree and sulfide layers per particle. Last but not least, most studies are examined in gas phase reactions and characterization techniques, but the real system involves an oily film around the catalyst particle and the interaction and activation of hydrogen on these surfaces depend on transportation processes in an unideal environment. Hence, there are a lot of open questions to be answered and room for improvement given for academic research in the future.^[32,59,66]

4 Scope of the Thesis

After this comprehensive but by far not complete introduction into the field of oil as an energy resource, its upgrading to valuable products in refineries and finally the history of catalyst development and modern challenges in hydrotreatment, the scope and outline of the present thesis has to be given.

As described above, the modern catalyst system of interest is a bulk Ni promoted Mo/W based sulfide used to overcome the current challenge of hydrodearomatization of polyaromatic structures remaining after atmospheric distillation of crudes. Although many different challenges and tasks for academic research are listed above, the main focus of this work is to understand and establish structure–function relationships between hydrogen activation and polyaromatic hydrogenation and the type of the active site(s) involved. More specifically, the differences and similarities of bulk molybdenum and tungsten catalysts, unpromoted and Ni promoted, are investigated, especially the quantification and differentiation of Lewis (CUS) and Brønsted (SH-groups) acid sites are the *sine qua non* for comparing specific activities of the materials studied.

Since the whole thesis is focused on hydrotreatment, boundary conditions for catalytic testing were chosen as close to industrial parameters as possible. To simplify the research object, a model system for heavy crudes of phenanthrene in decalin was selected for reaction studies on self-synthesized bulk NiMo(W)S₂ as well as on a bulk trimetallic NiMoWS₂ provided by the industrial partner. Throughout this study the catalytic testing was carried out in an in-house made micro kinetic reactor system and relevant conditions of 250–400°C and 60 bar gas pressure.

This thesis is structured into six chapters that starts with a short introduction (chapter 1) into the field of crude oil, refining and TMS catalysts and a detailed scientific literature review about transition metal sulfides and their structure and reactivity in hydrotreatment reactions (chapter 2). After that, methods for synthesis and characterization and those procedures and techniques applied in this study will be presented (chapter 3). The following chapters (chapter 4-6) deal with the key scientific aspects addressed in this work. Highlights are:

i) Synthesis of TMS catalysts

For the first, precursors were synthesized by co-precipitation of oxide salts prior to sulfidation in liquid phase using dimethyl disulfide as sulfiding agent. Three types of catalysts, NiMoS, NiWS and NiMoWS, were prepared. Second, the thiosalt impregnation method was used to prepare Mo/WS catalysts with varying Ni loading.

ii) Reducing structural complexity of TMS by leaching

Finally, an in-house developed method for preparing a well-defined sulfide catalysts was applied. This so-called ‘leaching’ method selectively removes NiS_x from the catalysts surface which makes the sulfide slabs more suitable for characterization techniques. In this work the

method was extended to the full concentration range of Ni loaded on the Mo/WS₂ and allowed to quantify Ni-promoted active centers and discuss the role of NiS_x in these systems.

iii) Characterization of TMS catalysts

In order to investigate TMS catalyst systems, standard characterization techniques established in this field were used. Properties such as chemical composition, surface area and pore volume (N₂-physisorption), phase composition (XRD) and particle length and stacking (TEM) are presented. Additionally, measurements of active sites by NO-pulsing (volumetric uptake) and an estimation of the activity by H₂-D₂ scrambling are examined.

iv) Measurement of active sites under working conditions

Last but not least a method for quantifying and separating different active sites on the catalysts, namely Lewis acidic CUS and Brønsted acidic SH-groups, was developed and presented. This new method allows to investigate TMS catalysts under working conditions in the reactor at relevant reaction temperatures and pressures for hydrogenation taking into proper account the high sensitivity of TMS catalysts to their reaction environment.

Chapter 2

Transition Metal Sulfides and Hydrotreatment

“[...] [Eine] Erhöhung der Hydrierungsgeschwindigkeit kann lediglich durch Verwendung von geeigneten Katalysatoren erreicht werden, [...] Außerdem muß er [der Katalysator] die Reaktionen nicht nur gasförmiger Ausgangsprodukte beschleunigen, sondern auch flüssige, sogar feste Produkte von verschiedener Zusammensetzung mit Wasserstoff in Reaktion bringen. Besondere Schwierigkeiten waren zudem [...] von den stets in den Ausgangsprodukten vorhandenen Metalloiden, wie insbesondere dem Schwefel, zu erwarten. [...]”

Es ist der I.G. Farbenindustrie A.G. gelungen, Katalysatoren herzustellen, die allen diesen Anforderungen genügen. [...] Die größte Aktivität haben jedoch Katalysatoren, die Elemente der 6. Gruppe, besonders Molybdän und Wolfram, enthalten, deren Wirksamkeit durch bestimmte Kombinationen mit Metalloiden weiter gesteigert werden kann. [...]

Eine weitere für viele Anwendungsgebiete wichtige Eigenschaft der Druckhydrierungskatalysatoren ist, daß sie die Verunreinigungen der Ausgangsstoffe, insbesondere Sauerstoff, Schwefel und Stickstoff unter Bildung von Wasser, Schwefelwasserstoff und Ammoniak aus dem Molekülverband lösen. [...]“

Carl Krauch und Matthias Pier, Über katalytische Druckhydrierung, 1931.^[35]

“[...] An increase of the hydrogenation rate is only achievable with usage of suitable catalysts. [...] Further, its [the catalysts] duty is not only to accelerate the reaction of gaseous compounds, but also liquid, even solid products of different composition have to be reacted with hydrogen. It was expected, that nonmetals, especially sulfur, which are always present in the feedstocks, would cause extra troubles. [...]”

I.G. Farbenindustrie succeeded in synthesizing catalysts which fulfill all the requirements. [...] However, the highest activity is exhibited on catalysts of elements of the 6th group, particularly molybdenum and tungsten, whose effectivity can be further boosted in combination with nonmetals. [...]

Another important property of this high pressure hydrogenation catalysts for many applications is, that they eliminate impurities, such as oxygen, sulfur and nitrogen, from the feedstocks under the production of water, hydrogen sulfide and ammonia. [...]”

Translated by Ferdinand Vogelgsang

1 Transition metal sulfides for hydrotreatment

“A catalyst is a substance that increases the rate of a reaction without modifying the overall standard Gibbs energy change in the reaction; the process is called catalysis. The catalyst is both a reactant and product of the reaction”^[67] By this definition (IUPAC), the above described catalysts of choice for industrial hydrotreatment reactions are transition metal sulfides (TMS), namely Ni or Co promoted Mo or W sulfides either supported on e.g. Al₂O₃ or SiO₂ or as self-supported (bulk) formulations. However, the structure of these TMS is very different to their corresponding oxides and exhibits unique properties which are needed for catalytic activity.

The research for hydrotreating catalysts shows a long history and over the years many authors tried to sum up the state of understanding the catalysts’ structure and describing catalytic hydrotreating processes at their times.^[18,20,74,34,48,68–73] In this chapter most important aspects of TMS catalysts focusing on bulk Ni promoted Mo/WS₂ are discussed.

1.1 Choice of catalysts based on Sabatier’s principle

During the race for better processes producing liquid fuels from coal the companies in the 1920’s and 1930’s tested several different metal (oxides) and found that their catalysts had changed their nature completely after the reaction.^[33] The most stable phases seemed to be sulfided versions of the oxides loaded. In the following many different transition metal sulfides were studied – mainly in the process of hydrodesulfurization – in order to obtain and understand the formulation of the most stable and active catalysts for this purpose. Within the group of transition metals a systematic research of activity will typically lead to a so-called ‘volcano (-type)’ plot. This behavior is described by the ‘Sabatier’s principle’ which relates the activity of a reaction on a catalyst to an energetic descriptor (e.g., the strength of adsorption of the reactant measured by its heat of formation). According to the principle named after Paul Sabatier^[75,76] the adsorption strength of the reactant at the maximum of that volcano curve has to be ‘just right’. On the increasing left side of the plot the overall reaction rate increases with the adsorption rate of the reactant while on the right hand side of the curve the overall rate decreases with the desorption rate of the product. Based on this, researchers have tried to describe periodic trends in catalytic activity for HDS using several (energetic) descriptors.

For transition metal sulfides the activity (HDS of dibenzothiophene) follows in a volcano shaped curve the position of the transition metal in the periodic table and therefore the number of d-electrons in the valence shell. A similar behavior is found for hydrogenation reactions such as hydrogenation of biphenyl.^[77] This behavior is further related to the d-character of the elements (‘electronic’ descriptor) with the highest activity for bulk sulfides of second row Ru and Rh and third row Os and Ir^[38] and carbon supported counterparts,^[78,79] where the maximum occurs at half-

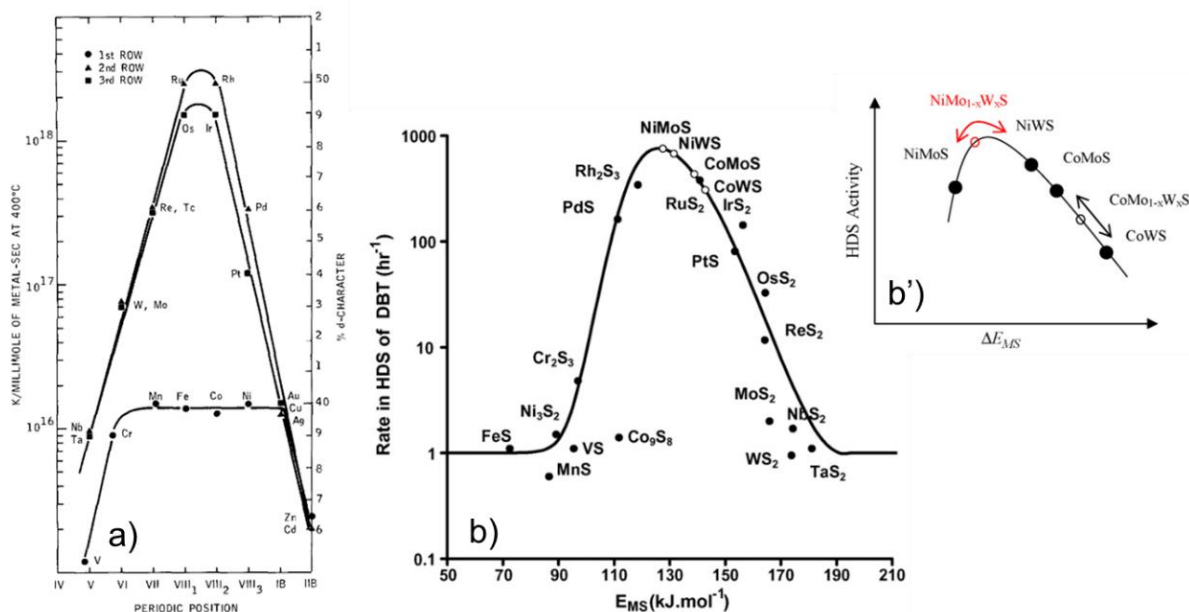


Figure 2-1. Volcano plots for transition metal sulfides. a) HDS activity vs. periodic position vs. Pauling % d character. The periodic trend is an ‘electronic’ effect and the maximum is found for sulfides with the highest d-character. These systems have the optimal ability to create and disable S vacancies.^[38] b) DBT rates vs. sulfur-metal bond energy, E_{MS} . The DFT calculation suggests the chemical descriptor as the ‘optimal’ bond strength and explains the high activity of Ni and Co promoted Mo and W sulfides. b’) The calculations also predict an optimum trimetallic system for Ni-Mo-W sulfides while Co-Mo-W sulfides show lower synergetic effects.^[84]

filled d bands and empty anti-bonding bands.^[80] Compared to these sulfides the first row transition metal sulfides are relatively inactive. The electronic character is described by the state of the d electrons and therefore covalency of the metal sulfur bond and covalent bond strength^[81] or the S addition energy to the TMS surface^[82] which leads to a Sabatier system for transition metal sulfides. The high covalency of the most active catalysts reflects a high metal character as measured by XPS analysis.^[78] According to the hydrodesulfurization mechanism the S-aromatic molecule undergoes a coordination of its S-atom with the metal atom of the TMS catalyst via a π back donation of d electrons to the π^* orbitals of the C-S bond of the organic molecule to form a moderate interaction at the plots maximum.^[57] The validity of the metal–S bond strength being a reasonable good descriptor for meeting Sabatier’s principle for hydrodesulfurization and hydrogenation^[83,84] lies in its linear relationship with the adsorption enthalpies of the organo-sulfuric compounds.^[54] On formulations with too weak bond strength the barriers for activation of the molecule (assuming Langmuir-Hinshelwood rate expressions with energetic values for adsorption enthalpies etc.) are too high and the reaction is impeded. If the metal–S bond strength is too high the catalyst surface is poisoned by either the reactant itself or other poisons in the feed such as H₂S.^[85,86]

Another descriptor reflecting the metal–S bond strength is the heat of formation of the sulfides (correlated to the heat of adsorption of sulfur)^[87] and the same trend in activity for HDS

is observed.^[38] While the 4 and 5 d transition metal sulfides RuS₂, IrS₂, OsS₂ and Rh₂S₃ are at the top of this plot, MoS₂ and WS₂ exhibit a high metal-S bond strength and the 3d transition metal sulfides of Ni and Co show a low bond strength.

In hydrotreating research, a strong promotion effect by Ni and Co for Mo/WS₂ based structures has been found.^[88] By combining Mo/W and Ni/Co into one promoted sulfide catalyst, the structure exhibits a very high activity by an increase of d electrons in the Mo with 3d metal (Ni or Co) electrons (formal reduction of Mo, ‘filling of electronic states above the Fermi-level’) whereby the metal – S bond strength is weakened and the heat of sulfide formation is shifted to an intermediate one.^[41,57,83,89] For HDS, the intermediate bond strength results in an activity order of CoMoS₂, RuS₂, NiMoS₂, NiWS₂, CoWS₂, FeMoS₂.^[90] Based on the experimental findings and theoretical support of the volcano shaped curve of the activity vs. metal–sulfur bond strength plot, the catalysts of choice for hydrotreatment reactions are Ni(Co) promoted Mo/WS₂ as bulk or supported structures.

1.2 Crystal structure of MoS₂ and WS₂

Among all the materials studied, molybdenum and tungsten based sulfides developed into compounds of interest whose structure will be presented here. Note that the sulfides of Mo and W are considered to be isomorph,^[91] due to the similarity of their metals ionic radii what is reflected in their relative position in the periodic table of elements.

The electronic state of the transition metals Mo and W are [Kr] 4d⁵ 5s¹ and [Xe] 4f¹⁴ 5d⁴ 6s², respectively. This electron configuration leads to the two most stable oxidation states of +IV and +VI. Hence, a formal stoichiometry of MS₂ and MS₃ are conceivable for the catalytic structure. Note that several other stoichiometries are known, such as M₂S₅, Mo₂S₃ and MS₄. Anyhow, the sulfur rich formulation is hard to stabilize^[92] and after heating to about 250°C MS₃ loses sulfur, further transforms into an amorphous metal poor M_{0.8}S₂ until it finally stabilizes at 400°C as MS₂.^[91,93] Therefore the M(IV)S₂ phase is present in hydrotreatment processes. The stoichiometry window of sulfur to metal is in between 2.0-1.9.^[92]

These minerals are called molybdenite or tungstenite, respectively. Their crystal structure is known for many years and goes back to the time of Linus Pauling (molybdenite).^[94] X-ray diffraction and Laue photograph analysis identified a unit cell in a hexagonal prism (dihexagonal dipyramidal), where the Mo atom is coordinated to six S atoms (equidistant to Mo) sitting at corners of the prism. The lattice parameters are a ≈ 3.160 (3.155 WS₂) and c ≈ 12.294 (12.350 WS₂).

Due to this ‘holohedral hexagonal’ structure, the crystallites orientate randomly into planes of S-M-S, a ‘sandwich-graphene’ like layered structure with diamagnetic and semi-conducting^[95] properties (band gaps E_{g,Mo} = 0.89 eV and E_{g,W} = 0.91 eV).^[56] At low temperatures the material structures in an amorphous manner while by heating higher ordered crystallization sets in^[91] and

the hexagonal arrangement transforms into rhombohedral arrangement. Controlled heating (rearrangement) forces the system into a controlled stacking of the S-M-S slabs and a characteristic diffraction plane of (002) is observed. The orientation around the c-axis is randomly and only temperatures above 500°C create parallel or antiparallel stacking.^[91]

Under hydrotreatment conditions the S-M-S layers are present in an amorphous and antiparallel stacked form. The distance between the S atoms of two layers is about 3.49 Å which is smaller than the combined atomic radii of the S ($r = 1.05 \text{ \AA}$). This can explain the lubricant character of MS_2 by the possibility of shifting the layers relatively to each other.^[94]

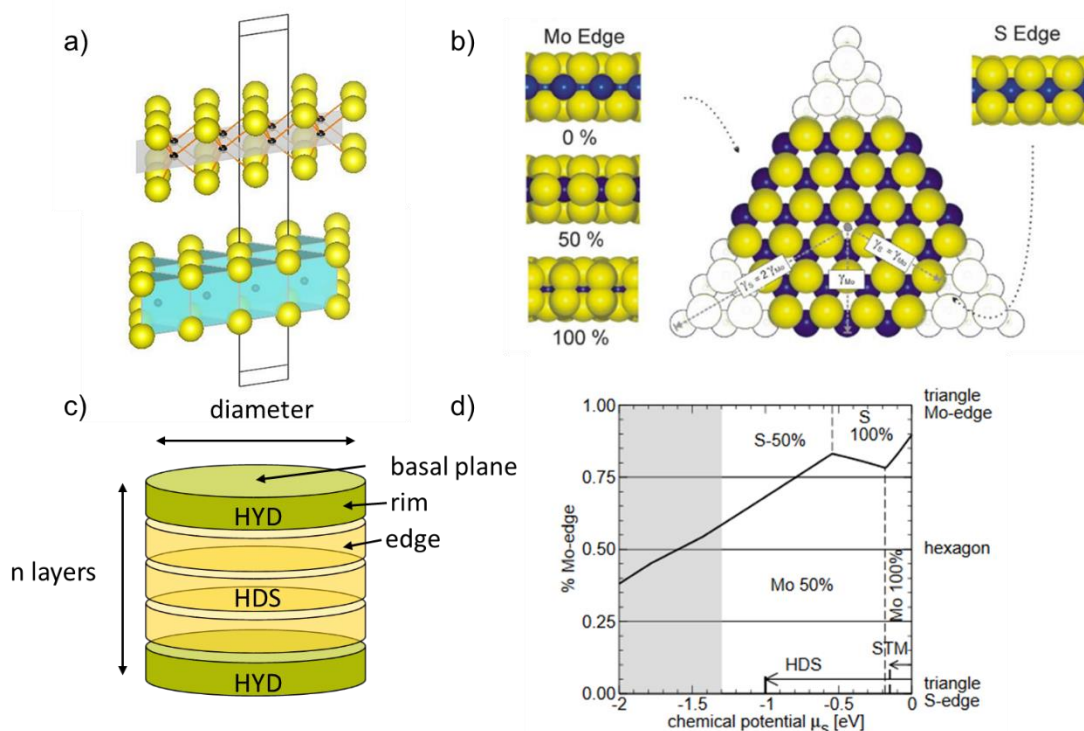


Figure 2-2. a) Demonstration of the unit cell of MoS_2 . b) Ball model of a MoS_2 slab and visualization of edge decoration degrees by S. A hexagonal slab is shown from the top view by ‘cutting’ a triangular shape along the c-axis.^[96] c) Catalyst model suggested by Chianelli. According to this model hydrogenation mainly takes place at the rim of the basal plane of a stacks of slabs while HDS reactions are located the edges of this particle.^[97] d) Morphology of MoS_2 particles depending on the chemical potential of sulfur.^[98] Shape of the particle and sulfidation degree of the Mo and S edges are presented. The two arrows indicate typical working conditions applied in STM and HDS.

1.3 Bulk structure of Mo/WS_2 – the slab model

In the following the structure and active sites for a ‘working’ catalyst under realistic hydrotreatment conditions is presented. It has to be clarified that MoS_2 and WS_2 are isostructural.^[99] Whenever in the following it is referred to one of each, the other compound is included into the explanations, exceptions are indicated. Generally, the model bases on the 2H-MoS_2 system, a structure of S-Mo-S stacked layers with a prismatic hexagonal coordination of 6

S to Mo. First, the unpromoted bulk structure and active sites will be discussed followed by the presentation of different models dedicated to Ni(Co)-promoted Mo/WS₂ catalysts.

During synthesis the Mo/WS₂ mainly grow into a and b direction^[100] forming a slab where [MoS₆] prismatic units share their S-edges with the Mo atom located in the trigonal prismatic holes.^[99] The slabs top and bottom (c-direction) are called basal planes (0001) which expose a homogeneous layer of S atoms and are mainly inactive for hydrotreatment reactions.^[101–104] By cutting the slab along the c axis different geometries are obtained such as linear chains, (truncated) triangles rhombs and hexagons,^[99] while the last is the most likely under HDS conditions.^[105] Independent of the slabs shape two edge planes are created, i) a metal edge (10 $\bar{1}0$) and ii) a sulfur edge ($\bar{1}010$). A full saturated (all Mo six-fold coordinated) slab has an excess of S and the edge atoms can further be specified into corner and edge ions. More specifically, each plane shows one type of Mo ion and only three differently coordinated S ions are present.^[106,107]

Table 2-1. Coordination of Mo and S atoms at the edges of a MoS₂ slab.

Plane	Mo coordination	S coordination
(10 $\bar{1}0$), metal edge	two terminal S-ions (S dimers); four basal S-ions	terminal S-ion bonded to one Mo
($\bar{1}010$), sulfur edge	four bridged S-ions, two basal S-ions	bridging between two Mo atoms
(0001), basal plane	six basal S-ions	tri-bonded in basal plane

Under hydrotreatment conditions, the exact S decoration of the edges and even the morphology (non-equilateral hexagon, capped or corner truncated triangles, orientation on a support) of the slab strongly depend on the environment of the catalyst.^[96,98,105,108–110] The notation is ‘plane edge XX%’, e.g., ‘Mo edge 50%’ describes the metal edge with 50% sulfur decoration, meaning that every second sulfur is removed from the edge site. The atmosphere determining the slabs shape and decoration is described by the ratio of H₂S (strong sulfiding agent) and H₂ (strong reducing agent). Schweiger *et al.* modeled surface energies as a function of the chemical potential of H₂S of a MoS₂ slab.^[98] According to this study the hexagonal slab is truncated (60% Mo-edge) and both edges are 50%^[111] covered under HDS conditions (10% H₂S in H₂, 650 K). The Mo-edge is more stable and abundant than the S-edge and a reconstruction of the MoS₂ particle is not favorable.

Between the S atoms of the slabs van-der-Waals forces hold the layers in contact allowing a vertical movement. These layers, which may be bended or truncated, align in c-direction to multiple stacks exposing steps and kinks. The morphology of the system is characterized by the slab length (max. diameter of the hexagon, typically 2-5 nm)^[112] and stacking degree. Usually, the size distribution of the slabs is narrow.^[99] Depending on the conditions during synthesis and whether the sulfide is supported or present in its bulk structure the number of slabs typically varies

from 1 to 5.^[112,113] The ‘stacking degree’ gives the characteristic for the average number of slabs aligned in c-direction. Another measure is the decoration degree which describes the number of edge atoms exposed at the edges of the slab. It can be given as the fraction ($f_{\text{Mo/W}}$) of all metal (Mo/W) atoms present.

It is generally believed that the active sites for hydrotreatment are located at the edge sites of the MoS₂ slab.^[99,114] A more detailed model for the location of active sites based on the morphology of the bulk MoS₂ crystallite was proposed by Chianelli.^[97] Next to the basal planes (inactive for hydrotreatment) a particle consisting of several slabs exhibits two different edge sites, the (basal-) rim edges of the top and bottom layer and the edges of the layers in between. Due to steric hindrance during the adsorption of large HDS molecules (e.g., DBT) the hydrogenation takes place at the rim edges while the desulfurization occurs on the edges. However, this ‘rim-edge’ model does not consider electronic effects and is only based on morphologic arguments neither promotor atoms such as Ni or Co are discussed.

1.4 Promotion of Mo/WS₂ phases with Ni and Co

Pure Mo/WS₂ catalysts are stable and active under HDS conditions, but to be competitive to more noble metal-based sulfides in activity a promotion with Ni or Co is needed (see volcano plot Figure 2-1). Over the years different models for the location of the promoter atom^[33,115] as well as the influence on activity by, e.g., prevention of coking, degree of reduction or increase of dispersion of the active Mo phase (see also a list provided by Topsøe^[116]), have been developed.

Voorhoeve and Stuver (1970’s) studied a Ni-WS₂ system for hydrogenation of benzene. They found by electron resonance spin analysis that the hydrogenation of aromatics involves a π -complex between the hydrocarbon and surface W³⁺ ions, which are considered to be sulfur deficient or anion vacancies. Additionally, no phase beside Ni₃S₂ and WS₂ was identified.^[47] In this model (‘intercalation model’) Ni promotion takes place at the octahedral holes between two WS₂ layers which increases the W³⁺ ion concentration by charge transfer (reduction of W⁴⁺ to W³⁺) and therefore its activity.^[117] Further, the intrinsic activity of Al₂O₃-supported and bulk Ni-WS₂ catalysts was the same.^[46] This model had to be extended to the ‘pseudo-intercalation model’ which locates the promoter atom at the edges of the crystallites only in order to comprise for the fact that no evidence for intercalated Ni²⁺ could be found under realistic HDS conditions. However, the active site for hydrogenation in this model is the reduced W³⁺ and Ni promotion only increases the number and not the nature of those sites by a charge transfer.^[33,71]

Concurrently, Delmon and his group identified sulfur rich species (Co₉S₈, Ni_xS_y, Fe_xS_y) to have an important role in promoting activity of the MoS₂ phase.^[49,118,119] They investigated a catalyst system of physically mixed MoS₂ and Co₉S₈ (‘contact synergy model’) at which the phases are in close contact and the HDS reaction takes place by a ‘remote control mechanism’.^[118] The hydrocarbon is activated at the MoS₂ slab and H₂ is added by a spill-over from the Co₉S₈ phase.

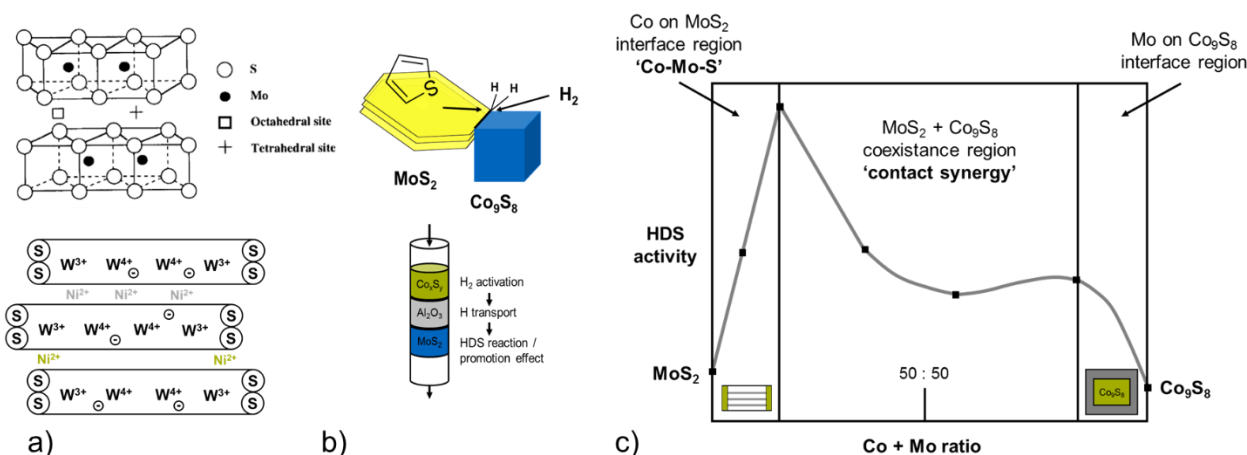


Figure 2-3. a) Intercalation model by Voorhoeve and Stuver. Top: Stacking of WS₂ layers with octahedral holes indicated.^[71] Bottom: Insertion of nickel into the holes and increase of W³⁺ sites. Ni²⁺ position at the edges is corrected by the pseudo-intercalation model.^[117] b) Top: Contact synergy according to Delmon.^[71] The hydrocarbon is activated at the MoS₂ phase and migrates to the interphase of the MoS₂ and Co₉S₈ particle. There, H₂ is activated and the HDS reaction takes place. Bottom: Experimental setting for testing the 'spill-over' effect of H₂ in TMS catalysis. H migration was proved by separated catalyst beds experiments.^[120] c) Representation of 'symmetrical synergy' and 'immiscible phases'. In this hypothetical phase diagram three regions are depicted, i) linear increase of the promotion effect of Co at MoS₂ edges until full coverage is reached, ii) segregation of CoS phases and iii) promotion of Co sulfide with Mo, symmetrical to i).^[71]

Strongest prove for such a mechanism was given by experiments of separated beds.^[120] Here, a promotional effect was observed by placing a Co_xS_y or Ni_xS_y layer above an unpromoted MoS₂ separated layer with different (inactive) compounds (Al₂O₃, SiO₂, SiC). This observation led to the conclusion that hydrogen migration from a Co(Ni)S phase onto a MoS₂ phase over a distance of 5 mm (γ-Al₂O₃ and SiO₂) is possible. However, the model is based on the assumption that at higher promoter loading phase separation of Co₉S₈ and MoS₂ takes place. Therefore, it only gives information about macroscopic, "helping" ("simplified")^[71] effects and misses any explanation of the promoter atom environment. Chianelli and Berhault specified the model by applying the idea of 'symmetrical synergism' (idea based on Phillips and Fote)^[71,121] to the system of immiscible Co₉S₈ and MoS₂ phases. They viewed the system as a phase diagram of i) Co-Mo-S phase with low content of Co up to 0.3 metal ratio with increasing activity by promotion ii) further addition of Co and phase segregation of the sulfides and iii) a Mo-Co-S phase, where the Co_xS_y is promoted by Mo (symmetrical to i).^[122] According to them, most of the industrial used catalysts fall into the region ii) as well as Delmon's model where close contact causes promotional effects by, e.g., formation of Co-Mo bonds between the bulk particle interfaces.^[123]

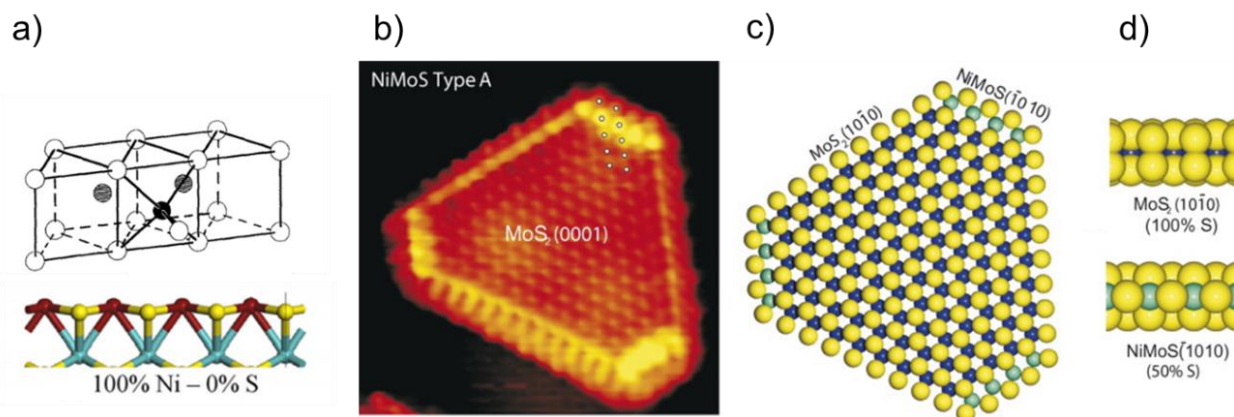


Figure 2-4. Location, visualization and representation of a Ni promoted MoS₂ single slab.^[124,133,149,186] a) Square pyramidal and square planar site for Ni promotion at the edge. b) Atom-resolved STM image of the truncated triangular slab. The bright spots correspond to Ni atoms which are mainly located at the edge positions. The bright brim is interpreted as strongly localized e^- perpendicular to the edge creating a one-dimensional metallic electron state. c) Ball model of the slab presented in STM. d) Side views of the MoS₂ 10 $\bar{1}0$ edge and Ni-Mo-S edge $\bar{1}010$, respectively. Color code: S: yellow, Ni: cyan and Mo: blue.

Anyhow, the left-hand side of the phase diagram cannot be explained by each of these models. First experimental evidence of this Co-Mo-S phase and its relevance for catalytic HDS was given by Topsøe in 1981^[50] and led to the formulation of the ‘edge decoration model’. By in-situ Mössbauer emission spectroscopy studies on Co promoted MoS₂, bulk and alumina supported, it was concluded that Co most likely sits below the surface indicating a substitution of edge or corner Mo atoms. The study excluded the intercalation model due to the fact that all features of the Co-Mo-S phase were present at a single slab structure. In more detail they could identify three different types of Co present, a) Co in Co₉S₈, b) Co as aluminate in the Al₂O₃ support and c) Co in small amounts associated with the MoS₂ phase. Further studies (HREM, AEM and STM) ensured that Co and Ni substitute the edge position without phase separation in the case of highly dispersed MoS₂ phase and prevent the MoS₂ slab to grow or order.^[52,124,125] It was also stated that the model applied for high surface bulk materials as well as for supported Co-Mo-S. Additionally a linear correlation between activity and Co substitution into the edge structure was found.^[126]

Later, this ‘edge-decoration’ model was specified by theoretical studies.^[102,124,127–130] It was shown that Co promotion mainly takes place at the ($\bar{1}010$)-edge of the slab and excluded bulk Co substitution. Further, the promoter causes the formation of truncated hexagonal shaped slabs. On the contrary Ni was found to promote both, the metal and the S edge. It sits in a 5-fold coordination (tetragonal pyramidal) at the (10 $\bar{1}0$) edge and can easily form a four-fold square arrangement after S removal^[131–133] (CUS formation, see below) up to a Ni loading of 0.48. More specifically the difference between Co and Ni promotion was seen by STM analysis. In the case of Ni two types of slab structures were found, one similar to a truncated triangular unpromoted MoS₂ slab (type A Ni-Mo-S, for large particles) where full Ni promotion occurs on the S-edge only and a second

matching a dodecagonal shape with a third ($11\bar{2}0$) edge. Here, all edges incorporate Ni into the Mo slab.^[124] However, the preferred location of the promoter atoms depends on their population as well the potential of $\text{H}_2\text{S} / \text{H}_2$ during sulfidation.

In the discussion of the models presented above, the role of support was left aside mainly because this study focuses on bulk materials only. However, many studies referenced in this chapter were investigating supported TMS so that it is appropriate to mention some aspects shortly. Generally, the active material, mainly (noble) metals, is very dense (e.g., W in TMS catalysis), price intensive and exhibits low surface area. To overcome this problem it is dispersed on low density, high surface carriers which might also show catalytic activity itself.^[134] An argument for bulk NiMoWS and a problem occurring for supported TMS is, that the pores of the supports usually are in a microporous range while the molecules to convert (polyaromatic structures) require at least mesoporous pockets to adsorb and react. For academic research several carriers like silica-alumina, zeolites, bauxite, silicon carbides, ceria, titania-alumina, magnesia and other binary oxides have been investigated mainly with the aim to understand MoS_2 -support interactions (reducibility, dispersion, sulfidability). More extensive studies were done on silica, carbon and alumina supports, while the latter one is by far the most commonly used in research and industrial application.^[20] Regardless, all supports share that the Ni-Mo-S phase is formed and stabilized as given with the example of Maugè *et al.* on aluminates and zirconia.^[135]

Although the type of support is not essential for the formation of the active species (the sulfided Mo or W phase) itself, the interaction (oxysulfides) of alumina with the MoS_2 influences the preparation and stabilization of small single slab structures. Those small slabs in turn have a high edge area to disperse Co or Ni according to the Co-Mo-S model resulting in very active catalysts.^[20] The MoS_2 sheets are linked via edge Mo-S-Al (or Mo-O-Al) bridges^[136] to the support. Those interactions exhibit greater forces between the slab and the support compared to the van der Waals forces in between MoS_2 layers. This formation was described by Candia and Topsøe and called ‘type I’ Co-Mo-S structure.^[137,138] On carbon supported Co-Mo catalysts no oxygen linkages are present and the slabs are weakly bonded to the support. Consequently, this so called ‘type II’ structures allow slabs to grow larger and stack to several layers. Although larger slabs expose less atoms and therefore active sites at the edges, the type II structures are intrinsically more active than type I Co-Mo-S. The oxygen bridges in the type I structure decrease the covalent character of Mo-S bond and increase its strength. Hence, the creation of S-vacancies is favored on type II structures, which are directly correlated to the intrinsic activity.^[139,140] By increasing the sulfidation temperature the oxygen linkages are broken and type I structures transform into type II structures. The temperature range under which the transformation occurs lies between 400 and 600°C. The Mo-O-Al linkages break when the Co content is close to saturation^[136] which proves that these linkages mainly are located at the edges of the slab and compete with Co. Additional to

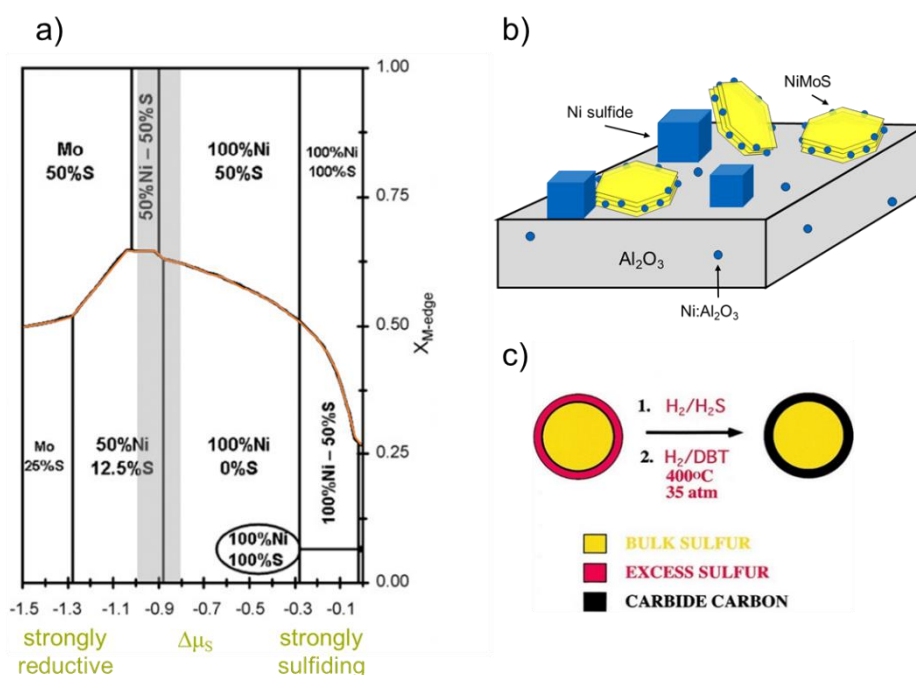


Figure 2-5. a) Morphology diagram for NiMoS crystallites. $X_{\text{M-edge}}$ is the proportion of M (metal) edge sites, hence for $X_{\text{M-edge}} = 0.5$ a perfect hexagon shape is obtained. The marked line gives the proportion of the M-edge with the S-edge composition demonstrated above and the M-edge composition below the line. Under strong reductive gas-phase conditions (chemical potential of sulfur, $\Delta\mu_s$, very low) promotor segregation takes place. It can be seen that under typical HDS conditions (grey bar) a labile phase composition is present.^[149] b) Schematic view of γ - Al_2O_3 supported NiMoS. Three Ni-containing phases are indicated, the Ni promoted MoS₂ slab, segregated NiS_x and Ni incorporated into the Al_2O_3 framework.^[124] c) Schematic representation of the formation of the carbosulfide phase.^[122] Sulfidation / decomposition of precursor in $\text{H}_2/\text{H}_2\text{S}$ without any organo-sulfide compounds leads to MoS₂ particles with excess sulfur at the edges (1.). At HDS conditions this excess sulfur is exchanged with carbon to form the carbosulfide phase supported on the underlying S phase (2.).

the higher amount of active sites in type II Co-Mo-S the accessibility of hydrocarbons to the MoS₂ is increased when the slab support interaction is weak.^[138]

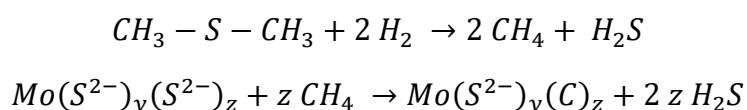
Both models discussed above, Topsøe's edge decoration and Delmon's contact synergy, not only described the (promoted) MoS₂ slab, but also included their observations on nickel and cobalt sulfide phases. The promotion effect for hydrotreatment activity of Ni or Co undergoes a maximum with promoter metal atom content. However, the maximum varies depending on preparation method (supported, bulk, co-precipitated, impregnated, industrial etc.) and experimental study (HDS, HDA, HDN, crude oil feeds, etc.) but typical values of 'optimal' atomic ratios of Ni(Co) to Ni(Co) + Mo(W) range from 0.16 to 0.5 mol mol⁻¹.^[132,133,141-146]

During HDS reaction and sulfidation of the binary TMS catalysts' precursor mixed oxides obtained by co-precipitation or impregnation, not only promoted 'Ni-Mo-S' slabs but also several Ni (Co) sulfide phases form and separate from the Mo/WS₂.^[50,51,53,147-150] This process is thermodynamically favored^[149] at reaction conditions and dominant species are Ni₉S₈ (Co₉S₈),

Ni_3S_2 and Ni_3S_4 with a size range from 5 to 100 nm.^[151] These segregated crystals attached to the promoting Ni at the edge of the Mo/WS₂ may block active sites^[51,152–154] and do not contribute significantly to,^[151] or even decrease, the catalytic activity with increasing the Ni content above 0.5 mol mol⁻¹. Admittedly, the phases are not static under reaction conditions whereas Ni sulfides ($T_{\text{Tammann}} \approx 532$ K, $T_{\text{melt}} \approx 1063$ K) are more mobile than Co sulfides ($T_{\text{Tammann}} \approx 686$ K, $T_{\text{melt}} \approx 1373$ K) and aggregate more rapidly during sulfidation.^[155,156] The segregated most stable Ni_3S_2 phase can show a support character at Ni loadings higher than 0.25 mol_{Ni} mol_{totalmetal}⁻¹ and explains a possible flattening of the reactivity–Ni loading curve at higher loadings.^[151,157]

Finally, yet importantly, another aspect of the catalyst system is the formation of carbide phases under HDS conditions. Specifically, based on observations on RuS₂ and MoS₂ catalysts, Chianelli suggested an active phase of (Co)MoS_yC_z ('carbosulfide') supported on the underlying MoS₂ phase where carbon replaces excess sulfur atoms (MoS_{2+x}) located at the edge of the slab.^[122,158,159]

According to different investigations on the 'structural' carbon, three methods of obtaining the carbosulfide phase are possible. Once the catalyst underwent a reaction under HDS conditions (such as DBT hydrodesulfurization)^[122] the phase is formed. Secondly, during the decomposition of alkyl ammonium tetrathiometalates as precursors for MeS₂ catalysts structural carbon forms.^[160] These first two methods are described as an 'in-situ' sulfidation method. Last, a post-synthetic treatment with dimethyl (di-)sulfide (DM(D)S) after the decomposition of (NH₄)₂MoS₄ catalyst precursors ('ex-situ' sulfidation with H₂S/H₂ only, no carbon present during process) leads to a C containing MoS₂ phase.^[161,162] Note that all methods involve an S-heteroaromatic reactant or organo-sulfide compounds. However, since hydrotreatment occurs in a trickle bed reactor with a condensed phase hydrocarbon pool and high pressure hydrogen the carbosulfide is always formed under catalytic reactions, presumably. Therefore, the following mechanism is suggested:^[161]



'Structural' carbon influences the morphology of the MoS₂ catalyst by reducing the particle size and stacking which leads to a better dispersion, higher surface area, and a narrow pore size distribution and textural stability.^[162] Additional, the interaction of carbon and the MoS₂ phase was observed by HRTEM and structural changes such as bending were monitored.^[163] Promotion with Co increases the ability to incorporate structural carbon most likely due to its electronic promotion and induced reducibility of the MoS₂ phase.

Although there is limited information about the site specific activity of the carbosulfide phase itself (despite a higher activity in HDS induced by morphological changes such as dispersion, surface area) the molybdenum carbide phase was investigated mainly by Oyama *et al.* in hydrotreatment. They showed that $\alpha\text{-MoC}_{1-x}$ ($x < 0.5$) catalyzes the HDS of thiophene with the same

product selectivities as MoS_2 . Additionally, after reaction (HDN, HDS, HDO, HYD) the catalyst showed incorporation of sulfur / a sulfided surface. At low sulfur levels in the feed the Mo_2C had a higher rate for HDN compared to a commercial Ni-Mo catalyst.^[164–167]

2 Active sites in hydrotreatment

Transition metal sulfides accelerate the reaction rates of hydrotreating reactions or allow them to occur at the solid material's surfaces under specific conditions. In this process of catalysis not every atom exposed to the surface acts as a moderator for the catalytic reaction. Only those spots at which reactants adsorb, are activated and react with each other are 'active sites (active centers)'.^[168] One challenge for hydrotreating catalysts is to activate hydrogen and overcome its high dissociation energy of ca. 432 kJ mol^{-1} .^[169,170] Additionally, the catalyst has to bring the adsorbed hydrocarbon and the activated H_2 molecule in contact and allow them to react. In order to understand the nature of active sites, researchers have developed models for TMS catalysts which explain promotion effects and reactant–catalyst interaction (see chapter 1.4).

Promotion effects can be explained by the models of 'contact synergy' and 'edge decoration'. While the first model mainly describes macroscopic interaction of the Co(Ni)S phases with the Mo/WS₂ phase, the second model is better qualified^[126] to explain the activity – promotion degree correlation of Ni(Co)-MoS₂ catalysts by describing the electronic state and environment of the promoter atoms and the edge structure of the catalysts. Based on the 'edge decoration' model the active sites for hydrotreatment reactions are 'coordinative unsaturated sites (CUS)' located at the edge positions of the slabs and Brønsted acidic sulfhydryl groups (SH) are created thereof (see chapter 2.2). In the following, first, the formation of such sites in unpromoted systems is presented, followed by the discussion of the influence of Ni(Co) promotion on the site creation.

2.1 Active sites of Ni promoted Mo/WS₂

As mentioned above (see 1.3) the active sites for hydrotreatment are located at the edge positions of the Mo/WS₂ slabs while the basal plane is inactive. Under realistic hydrotreatment conditions the edges of a MoS₂ slab are not fully covered by S atoms which leads to the formation of under-coordinated, so-called 'coordinative unsaturated sites (CUS)' with Lewis acidic character. By measuring the uptake of O₂^[171], NH₃^[172] and NO^[116,173] obtained by chemisorption experiments the HDS activity correlates with the concentration of S-anion vacancies proving that S-anion vacancies / CUS are the responsible active sites for HDS.^[53] They expose the underlying Mo atoms which may interact with an electron donor^[174] and serve as an adsorption sites for the sulfo-organic molecule.^[175] Therefore, it is believed that fully coordinated metal atoms at the edges do not activate S-containing molecules.^[126] This concept is also in line with the finding that HDS activity correlates with the sulfur-metal bond strength of sulfide catalysts (see 1.1).

Technically, S-vacancies are created by the removal of one S atom out of its edge position which is an endothermic process until 50% of coverage^[111,176] is reached. This process is assisted / influenced by the presence of H₂ / H₂S under HDS conditions which causes additional CUS formation or blocking, whereat corner S atoms are easier to remove than edge S atoms.^[98]

However, it has been shown by radioisotope pulse tracer methods^[177] that the S exchange with gas phase S-molecules is rapid under HDS conditions and there is competition between H₂S and S-molecule about the same sites.^[178]

The distribution of S-vacancies is not uniform along the edges of the MoS₂ slab and its formation depends on the plane of the crystal as well as structural re-arrangement after S-removal. For the ($\bar{1}010$) sulfur edge the equilibrium structure is a fully S-covered surface.^[106,179] Hence, CUS are created by S removal (13 kJ mol⁻¹) under HDS conditions. In doing so, the edge of a single slab reconstructs by flipping an S atom into the Mo plane and the accessibility to the Mo atom at the CUS is better compared to the Mo edge. At the fully covered (S dimers) Mo ($10\bar{1}0$) edge S removal (one per Mo atom, 14 kJ mol⁻¹) leads to a reconstruction by moving the S atoms half a lattice constant to be two-fold coordinated (Mo coordination to S is six)^[180,181] and the equilibrium coverage is 50%. However, the reconstruction was shown for a single slab while for layered structures it is unlikely to happen.^[174] Further S removal at the same site is energetically unlikely and double vacancies hardly occur.^[102,182]

The Lewis-acid character of the CUS sites on the one hand serves as adsorption site for Lewis bases such as S,N-heteroaromatics, H₂S or π -systems but also have a second function of activating the H₂ molecule for hydrogenation. They facilitate the formation of sulfhydryl (SH) groups by dissociative splitting of H₂S or H₂ molecules (see below) whereby the H-atoms are stabilized by low valence state sulfur atoms^[188,174,183,184], e.g. single S⁻ or (S-S)²⁻ dimers, adjacent to the vacancy. These resulting SH-groups can be seen as active centers involved in the catalytic cycle for hydrodearomatization. However, since the formation of SH-groups is related to CUS the hydrogenation activity is in correlation to both, SH and / or CUS concentration.

Next to the CUS sites as active centers for hydrotreatment reactions Lauritsen *et al.*^[96,174,179,185,186] introduced brim sites as catalytic relevant locations (see Figure 2-4). In STM images a bright yellow brim along the Mo edges of a triangular MoS₂ slab was observed. It is characterized by localized metallic states 0.8 Å away from the edge originated from the p-d bonding between the S and Mo atoms and the d-d bonding of the Mo atoms. These brim sites have electron accepting and donating properties similar to metallic surfaces and catalyze hydrogenation of aromatic ring systems even at fully S-covered edges by serving as an adsorption site for the organic molecule. The H₂ for hydrogenation is provided by the SH-groups next to the brim and S vacancies are not involved in the catalytic cycle. This explains why hydrogenation of aromatic rings is not inhibited by H₂S and competition about CUS sites. Additionally, this model is in line with Chianelli's picture of the catalysis on MoS₂ particles at which desulfurization and hydrogenation happen at different locations.

By looking at the volcano-type plot for the TMS system it is obvious that promotion of Mo/WS₂ slabs with Ni or Co has a large effect on the activity in HDS (see 1.1). Promotion with Co or Ni creates more active and a higher density of CUS sites located at the edge or corner

positions of the slab as shown by NO chemisorption.^[173] However, the exact concentration of CUS depends on the promoter and a general order is $\text{CoMo} > \text{NiMo} \approx \text{NiW} > \text{Mo}$.^[187–193] The promoted CUS sites do not manipulate the unpromoted sites but create sites which are different in nature and intrinsically more active than unpromoted CUS. Therefore two different CUS might be present at the Mo/WS₂ slab while the promoted one is dominating the catalysts activity. The promoter increases the electron density (and therefore basicity)^[146,194] at the S and Mo atoms^[195] which enhances H₂ activation (followed by SH formation) and S vacancy formation by an intramolecular red(Mo)–ox(S) process.^[116]

More specifically, as suggested by theory and electron microscopy, Co promoted S edge intrinsically shows anion vacancies (first S removal -70 kJ mol^{-1} , compare to unpromoted S–edge: vacancy formation endothermic)^[127,196] and if the metal edge is promoted the energy required for vacancy creation (first S removal -62 kJ mol^{-1}) is more favorable compared to the unpromoted edge and pure Co₉S₈.^[197] Additionally, the morphology and shape of the slab is changed from a triangular one to hexagonal truncated as observed in STM images and the brim sites defined at the metal edge of an unpromoted MoS₂ slab are formed by Co incorporation at the S–edge.^[128] In the case of Ni the sulfur binding energy (first S removal -79 kJ mol^{-1}) is even lower than in the case of Co.^[102] In other words, both promoters (Ni stronger than Co) reduce the binding energy of the metal–S bond (the higher the promoter content the stronger the effect) and create more CUS sites at the edges. Consequently, the S coverage decreases in the order $\text{MoS}_2 > \text{CoMoS}_2 > \text{NiMoS}_2$ where at the latter one the Ni–S bonding is very unstable. Additionally, deactivation by S adsorption is diminished.^[127,198–200] A possible explanation based on electronic arguments for the promotional effect of Ni and Co is that the Fermi level of these CUS lies above the anti-bonding states of S (Ni d to S 3p states) which causes a weak coupling by filling of the anti-bonding orbitals.^[102]

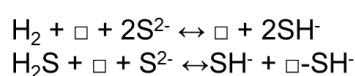
2.2 Hydrogen activation and SH formation

Hydrotreatment includes several different chemical reactions such as HDS, HDN, HDO, HDM and HYD. They all have in common that they require a huge supply of activated, adsorbed hydrogen on the catalysts surface which subsequently reacts with the adsorbed hydrocarbons. Therefore, the activation of H₂^[69] becomes a crucial point in the whole catalytic process.

In the early stages of HDS research, it was suggested that Brønsted acidic sulfhydryl groups are present as catalytic functional groups located at the edges of the MoS₂ slab (blank Co₉S₈ does not activate hydrogen^[201]) in the HDS of thiophene.^[45,188] Following up, their existence was proven by infra-red studies of thiophene HDS on bulk MoS₂,^[202] in-situ Raman spectroscopy^[93] and H₂S adsorption on Al₂O₃ supported MoS₂.^[203] Additional prove was given by inelastic neutron and neutron Compton scattering for both supported and bulk MoS₂.^[201,204–207] However, the location

and detailed mechanistic understanding of formation and the role of a promotor atom such as Co were not discussed and remained unclear.^[208]

In the current model for SH-group formation as active species for hydrotreatment, the above discussed S-vacancies with Lewis-acidic character play an initiative role. Molecular H₂ and H₂S are split at these CUS located at the edges of the hexagonal Mo/WS₂ slabs which are meant to be the active sites for HDS, HDN or the like (see 2.1), while their activation and stabilization on top of the slabs basal plane is energetically not favored as shown by theory (~0.97eV)^[209] and proven by experiment.^[101,199,210,211] Formally, the following reversible reactions have to take place under hydrotreatment conditions. Note that the mechanistic interplay of H₂, H₂S and surface vacancies leads to the strong dependence and dynamic rearrangements of the surface states of the MoS₂ edges on the partial pressures of H₂S and H₂ in the atmosphere.^[209,212]



It is generally believed that the uptake of H₂ is activated and reversible^[213] and two mechanisms for its associative dissociation (chemisorption) have to be considered.^[214] In the homolytic pathway molecular H₂ dissociates on two weakly coupled disulfide groups, (S–S)²⁻, mainly present at over-sulfided edges and reduces the surface by the opening of the S–S bridges to form 2 SH⁻ groups even at low temperatures. Under hydrotreatment conditions only the S-edge of the MoS₂ shows a high S coverage (see above) and therefore this mechanism mainly occurs at that edge. With increasing temperature the S-edge will lose sulfur atoms as H₂S due to recombination of SH⁻ groups leaving vacancies behind.^[187,191,202,212,215–220]

On the CUS sites at sulfur under-coordinated edges of the MoS₂ slab a second, energetically favored^[182] mechanism for H₂ and H₂S chemisorption is dominating. First, H₂ or H₂S are cleaved heterolytically at these Lewis acid-base pairs (vacancies and S²⁻ anions) and finally stabilize as 2 SH⁻ similar to the homolytic pathway. The hydrogen molecule physisorbs on an edge S-vacancy and dissociates into an acidic SH-group and a Mo-H bridge followed by surface migration of the hydride to a neighboring S to form the second SH-group (cis and trans configuration) and a reduction of the metal at the edge. The detailed mechanism at the different edges is mainly discussed by theoretical calculations since the presence of Mo-H is hard to detect in spectroscopic experiments given that the population of Mo-H is small compared to SH (1:200).^[54,69,221–224,108,187,192,202,205,212,216,217] On unpromoted edges the overall process is endothermic (+26 kJ mol⁻¹) and the highest activation barrier is found in the heterolytic cleavage of molecular H₂ (ΔE = 88-94 kJ mol⁻¹), therefore showing first order relationships in H₂-D₂ scrambling experiments on MoS₂ catalysts. The barriers for surface migration (ΔE = 38-52 kJ mol⁻¹) and desorption (ΔE ~ 58 kJ mol⁻¹) of H₂ are comparatively low.

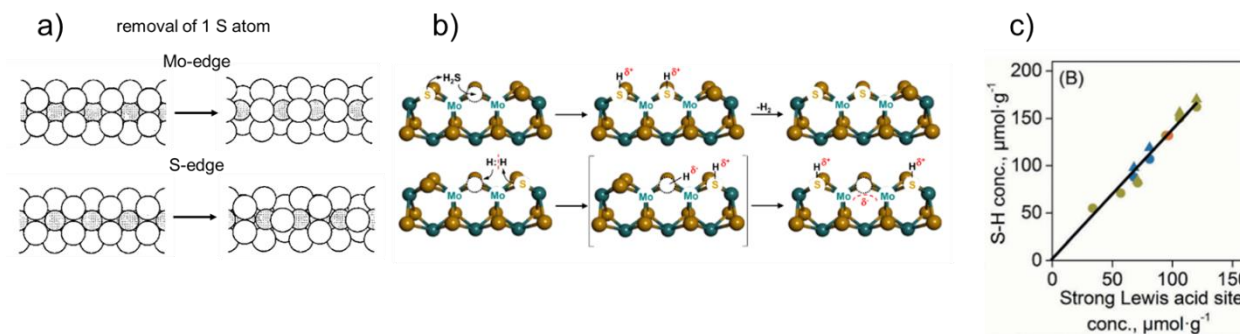


Figure 2-6. Depiction of CUS sites, SH formation and experimental prove of correlation thereof. a) Rearrangement of S atoms at the Mo and S edge by removal of one S atom. ^[102] b) Mechanistic picture of SH formation at CUS sites by H₂S or H₂.^[192] c) Experimental prove of correlation between SH concentration and Lewis acid site concentration for Ni promoted Mo (blue), W (green) and MoW (orange) sulfides.^[193]

Overall, H₂ activation is not sensitive to the promoter^[198] and the mechanism is not changed drastically by promotion as shown by H₂-D₂ and D₂-H₂S exchange and TPD experiments. Thus, the promoter Ni does not change the strength of the acid site but increases Brønsted acid site concentration (SH) at the edges. Promotion with Ni or Co not only increases the CUS concentration by weakening of the metal-S bond but also increases the e⁻ density at the bridging S atoms adjacent to the sites. This results in an increase of basicity and concentration of labile S²⁻ anions and the ability to bind H at the edge. As a result hydrogen dissociation at a promoted edge site is slightly exothermic or athermic and on the Co promoted edge desorption exhibits the highest barrier while the barriers for activation of H₂ and surface migration of H⁻ are modest so that an order of 0.5 for H₂ is found in H₂-D₂ scrambling experiments. The bonding in a Ni-S pair is very weak and during the heterolytic cleavage of H₂ a Ni-H (spectroscopically observable)^[69] might be present.^[82,192,198,199,204,216,217,221]

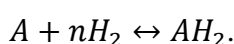
Additionally, the instability of the Ni-S bond causes the release of H₂S (observed in TPR and TPD experiments) from the promoted surface by recombination of Ni-H with adjacent SH even at low temperatures. Ni accelerates the elimination of H₂S compared to the unpromoted MoS₂ formulation and H₂S desorption is more likely than H₂ recombination. This is basically the reverse reaction of the second surface process producing SH-groups, the heterolytic dissociation of molecular H₂S. Here, one H atom of the H₂S molecule adsorbed at CUS reacts with an S atom attached to a neighboring Mo atom to form a Brønsted acidic SH-group in a slightly exothermic process.^[46,99,226-228,179,188,190,191,198,207,221,225] By this process the number of S-vacancies is strongly manipulated and the Lewis-acidic CUS will diminish in the favor of SH creation. Given that H₂ and H₂S are activated at identical sites and S vacancies and SH-groups interconvert, a linear correlation between CUS and SH-groups can be established.

Although H₂ activation is energetically demanding, it seems not to be rate limiting during the hydrotreatment process.^[198] In the overall catalytic mechanism, the weakly adsorbed

hydrogen^[110] reacts with the adsorbed hydrocarbon. In the following, the mechanistic view on aromatic hydrogenation and the interplay of the SH-groups and the adsorbed hydrocarbon is discussed.

2.3 Hydrogenation of aromatic structures

Heavy boiling residua contain a lot of polyaromatic structures whose hydrogenation proceeds under more demanding conditions compared to desulfurization or denitrogenation. In the HDS literature, most of the studies deal with HDS and HDN processes and the reaction mechanisms and networks are discussed extensively while there is limited information about HDA present. Formally, the hydrogenation is described by the general chemical equation:



In more detail, polyaromatic hydrogenation proceeds via successive steps of hydrogenation of ring by ring whereas each step is reversible. Thus hydrogenation is limited by thermodynamic equilibria of the systems. The reactions are highly exothermic,^[229] strongly dependent on H₂ pressure and the equilibrium constants decrease with temperature causing an increase in aromatic concentration. Usually, hydrogenation of the first ring is thermodynamically favored over hydrogenation of the last rings.^[70]

For a microkinetic description of the hydrogenation mechanism the Langmuir-Hinshelwood formalism is applied, which requires an equilibrated adsorption of all reactants and reaction intermediates at the active centers of the catalyst. The formulation also allows to account for inhibiting effects of other compounds present during reaction. For polyaromatic hydrogenation those could be heterocyclic aromatics, H₂S and other basic gases and hydrogenated products of the substrate. The generalized rate equation for hydrogenation is

$$r = \frac{k_{intr.} \cdot (p_{H_2} K_{H_2})^n \cdot (p_A K_A)^m}{(1 + \sum_i^n (K_{AH,i} p_{AH,i})^x + \sum_j^n (K_{Inhib,j} p_{Inhib,j})^y + (p_A K_A)^z)^a}$$

For low concentrations a first order dependency of the rate on the hydrocarbon partial pressure is assumed and the higher the ring number the higher the rate constants. On a NiMo/Al₂O₃ catalyst an order of benzene < phenanthrene < naphthalene < anthracene was found.^[20]

A more detailed description of the surface mechanism starts with the differentiation between the HDS and HDA mechanism and the active sites involved. As discussed above the H₂-molecule is adsorbed and activated at the CUS sites of the slabs edges and stabilized as SH-groups. These CUS are also the adsorption sites for S-heterocyclic aromatics undergoing a desulfurization and a competition about the S-vacancies occurs between the substrates and inhibitors such as H₂S. Contrary to that, hydrogenation of polyaromatics is hardly affected by those inhibitors and CUS sites are not required as adsorption sites.^[179,230,231] An increase of the MoS₂ particle stacking

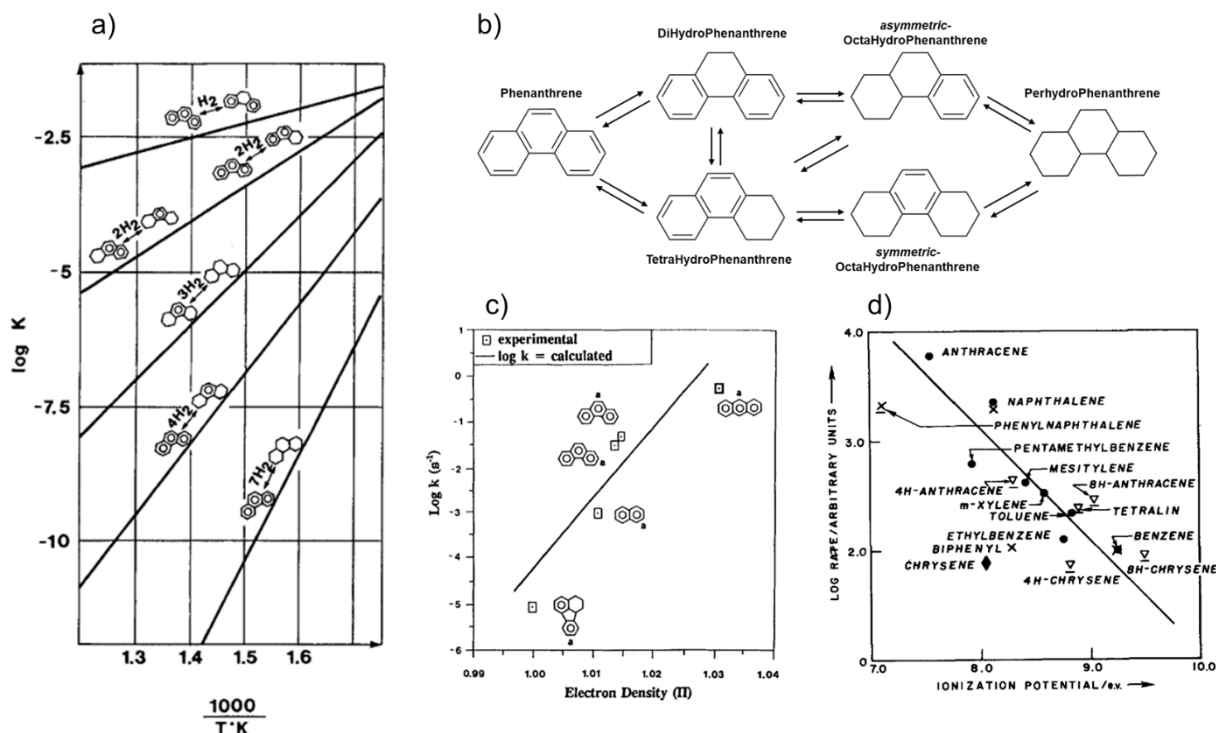


Figure 2-7. a) Equilibrium constants for the hydrogenation of phenanthrene.^[70] b) reaction network of phenanthrene hydrogenation including possible reaction pathways. Note, that all steps can be considered as reversible reactions. c) Relation between hydrogenation activity and electron density. The marked positions are the most reactive rings and the ring with the lowest aromaticity might be hydrogenated first (DiHPhe vs. TetHPhe). A lower e^- density might lead to a lower adsorption strength (Phe vs Anthracene).^[70] d) Correlation between the ionization potential and hydrogenation rates of aromatic compounds.^[235]

enhances the hydrogenation rate of aromatics.^[113] Hence, aromatic molecules adsorb planar via π -interaction (van der Waals interactions $\sim 3.5 \text{ \AA}$ above the MoS_2 plane)^[117,232-234] at the basal plane near the edges of the MoS_2 slabs. These sites correspond to the so-called ‘Brim’ sites in the catalyst model suggested by Lauritsen *et al.*

During the hydrogenation of aromatic compounds it is essential to break the aromatic double bonds stabilized by resonance. By the formation of a strong π -complex (transfer of e^- from bonding HOMO to antibonding LUMO of the aromatic via the metallic surface of the catalyst) the aromatic bonds are weakened and susceptible for a hydrogen attack. The higher the HOMO state (and inversely the ionization potential) of the aromatic π -donor the stronger π -complex is formed. In other words, an increase in e^- donating ability, which is reflected in a weaker resonance energy and hence aromaticity, will lead to an increase in hydrogenation activity. Therefore, alkyl substituents at the aromatic ring are beneficial for hydrogenation of the core ring but can be compensated by steric constraints for flat adsorption.^[70,235]

Investigations on polyaromatic hydrogenation and the understanding of the surface mechanism are executed using model compounds for heavy boiling crudes. The model compounds

used for catalytic research are benzene, toluene, naphthalene, biphenyl, anthracene, fluorene, etc., and the 3-ring angled phenanthrene (phenylanthracene, Phe), which was used throughout the present thesis. Reaction kinetic test parameters for its hydrogenation range from 280-350°C under total pressures of 40-100 bar at low concentrations of Phe in organic solvents such as decalin or linear alkanes and fixed H₂/hydrocarbon ratios. The process is described as a solid-liquid catalytic reaction^[236] and usually studied in continuous flow reactors by varying space times.

Phenanthrene, C₁₄H₁₀, is a planar full aromatic 3 ring 6 ring system (178.23 g mol⁻¹; MP: 101°C; BP: 340°C; density: 1.18 g cm⁻³; soluble in organics; insoluble in water) with a resonance energy of 366-386 kJ mol⁻¹.^[70] Its hydrogenation occurs typically in multiple successive and inherently reversible steps, though several (even contradicting) reaction networks and reactivity studies are presented and discussed in literature.^[236,237,246-249,238-245] Here, the reaction network including all products and pathways is presented.

The networks routes can be divided and named after their primary products. Symmetric hydrogenation will lead to 9,10-dihydrophenanthrene, DiHPhe, while asymmetric hydrogenation results in 1,2,3,4-tetrahydrophenanthrene, TetHPhe. Further hydrogenation to the secondary products gives the symmetric 1,2,3,4,5,6,7,8-octahydrophenanthrene, *sym*-OHPhe, and the asymmetric 1,2,3,4,4a,9,10,10a-octahydrophenanthrene, *asym*-OHPhe, and finally the fully hydrogenated perhydrophenanthrene, PerHPhe. In general, the reaction network may allow interconversion between the pathways from DiHPhe to TetHPhe and TetHPhe to *asym*-OHPhe and the direct formation of *asym*-OHPhe from DiHPhe might not occur or is very slow. But these observations are controversially discussed in literature and may depend on the catalytic system and reaction conditions investigated. Note, that in the present network only hydrogenation is considered, while ring-opening and isomerization are not discussed. Those processes require more demanding conditions to occur and are excluded in this work.

Mechanistically, we found that the hydrogenation follows a subsequent addition of surface H as pairs to the flat adsorbed Phe with the rate determining step (r.d.s.) being the first addition for forming DiHPhe and the third addition for forming TetHPhe. DFT calculations suggest that Phe preferentially adsorbs on the basal plane and hydrogen is activated on the edge of the slabs. SH, which carries a protic H species, is typically thought to mediate the H-addition events, but in general, there is no consensus on the rate-limiting step, the nature of the H species (hydride, protic, or neutral), or the adsorption sites for Phe and H (i.e., whether these two reactants adsorb competitively or not).^[236]

On unpromoted Mo(W)S₂ catalysts the main product is DiHPhe (olefin-like hydrogenation) with a carbon selectivity > 80% and almost no deep hydrogenation occurs. Promotion with Ni will shift the selectivities towards TetHPhe and to higher hydrogenated products and accelerate the overall rate while not changing the reaction network. The shift towards TetHPhe can be explained

by a stabilization of the transition state ('H₂Phe') through more basic Ni promoted sites compared to unpromoted thus decreasing the hydrogenation barrier towards lateral rings.^[236]

Chapter 3

Procedures and Methods for Research on Transition Metal Sulfides

“[...] indeed, one catalysis PhD entering Shell around 1980 announced that he was ready to work on any subject, except sulphides. [...]”

From: “What’s new? On the development of sulphidic HT catalysts before the molecular aspects” – Rob van Veen^[32]

1 Synthetic routes towards bulk NiMo(W)S₂

For catalytic research it is essential to understand and optimize protocols for synthesizing the catalytic active material in order to obtain targeted features for investigation and application. Industrial relevant protocols focus on easy and harmless handling while academic research may use more complex preparation techniques. Typical synthetic routes start with preparing metal oxide precursors by impregnation of a support (Al₂O₃, SiO₂, TiO₂, ZrO₂, carbon, zeolites, etc.) or precipitation as bulk metal oxides. Most often a posttreatment is applied to finalize the active phase by calcination (drying and oxidizing in synthetic air or inert gases) and shaping depending on the application. Then, the oxides are sulfided in-situ, either in gas phase with H₂S or in liquid phase using a real S-containing feedstock and / or adding a sulfiding agent to the liquid solvent. Although many different protocols for TMS catalyst synthesis are out in the literature (for an overview see Chianelli^[71]), here the two methods applied for this study are presented.

1.1 Preparation of TMS catalysts by co-precipitation

In the synthesis of self-supported (bulk) nickel promoted Mo(W)S₂ catalysts the aim lies in preparing under reaction conditions stable and highly active materials by controlling the Ni incorporation into the slabs structure and providing a high surface area. In this work the two methods of co-precipitation of metal oxides followed by sulfidation and impregnation/thermal decomposition of thiometallates are applied.

Conventional oxidic precursors of CoMo catalyst are prepared by sequential or simultaneous impregnation of Co and Mo salts onto an alumina support. Additives might be added to influence the morphology and dispersion of the active phase. After that, the catalyst is dried, calcined and sulfided. However, it has been shown that bulk and supported structures exhibit similar catalytic behavior and that the active phase is the same.^[20]

A bulk oxide precursor is obtained by co-precipitation of Ni and Mo/W salts. Ni²⁺ and MoO₄²⁻ (WO₄²⁻) ions form a bimetallic oxide and precipitate as green solids (exact appearance depends on the Ni content) in solution depending on the pH. All metals in the mixed oxide show distorted coordination geometry with Ni²⁺ in oxygen octahedral, [MoO₄] tetrahedra and [WO₆] octahedral.^[250] Usually, two solutions are mixed in a stirred vessel at moderate temperatures of 80 – 90°C. One contains the highly water soluble Ni(NO₃)₂ exhibiting a pH slightly below 7. The second solution contains (NH₄)₆Mo₇O₂₄ whereas the ammonia formed causes the formation of MoO₄²⁻ ions at a pH of 8-9. The composition of the precursors is manipulated by the concentration and flow rate of the solution.^[251] Additionally, complexing agents such as short chain organic acids (maleic, succinic, citric, etc.) are used to re-disperse Ni and/or increasing the surface area. Upon aging of the NiMoO precursor it is dried and calcined at 120-150°C to remove remaining NO₃⁻ and other additives.^[252–255]

In chapter 4 of this thesis, NiMo(W) sulfides obtained by co-precipitation are studied. In the following the exact synthetic protocol is given. In a three-neck 250 mL bottle flask equipped with a condenser the ammonium heptamolybdate and/or metatungstate were provided in 120 mL deionized water and stirred at room temperature until complete dissolution (pH 5.5-6). Then, 4.5 mL NH_4OH (28-30%) were added and stirred for about 10 min. The solution was heated to 90°C and the pH was adjusted to 9 to 9.5 by adding small amount of NH_4OH solution.

A second solution was prepared in a 100 mL beaker. $\text{Ni}(\text{NO}_3)_2 \cdot 6\text{H}_2\text{O}$ was dissolved in 7.5 mL deionized water (pH ~6) and stirred on a heating plate at 60°C . Then, the warm, green Ni-solution was added dropwise into the hot, colorless Mo/W containing solution over a time of 45 min. In the moment of contact of the two solutions small, pale green particles were formed but dissolved immediately. By progress of the experiment the particles did not dissolve anymore and a precipitate was formed due to a drop in pH. After combining the two solutions, stirring was kept for 30 min at 90°C . Then, the mint green precipitate was filtrated and dispersed with a maleic acid solution (0.5282 g in 90 mL H_2O) in the three-neck flask and stirred at $75\text{--}80^\circ\text{C}$ for 30 minutes. After that, the precipitate was filtrated and dried over night at room temperature, grinded and finally dried in synthetic air for 12 hours (200 mL min^{-1} ; 1 K min^{-1} heating rate to 120°C).

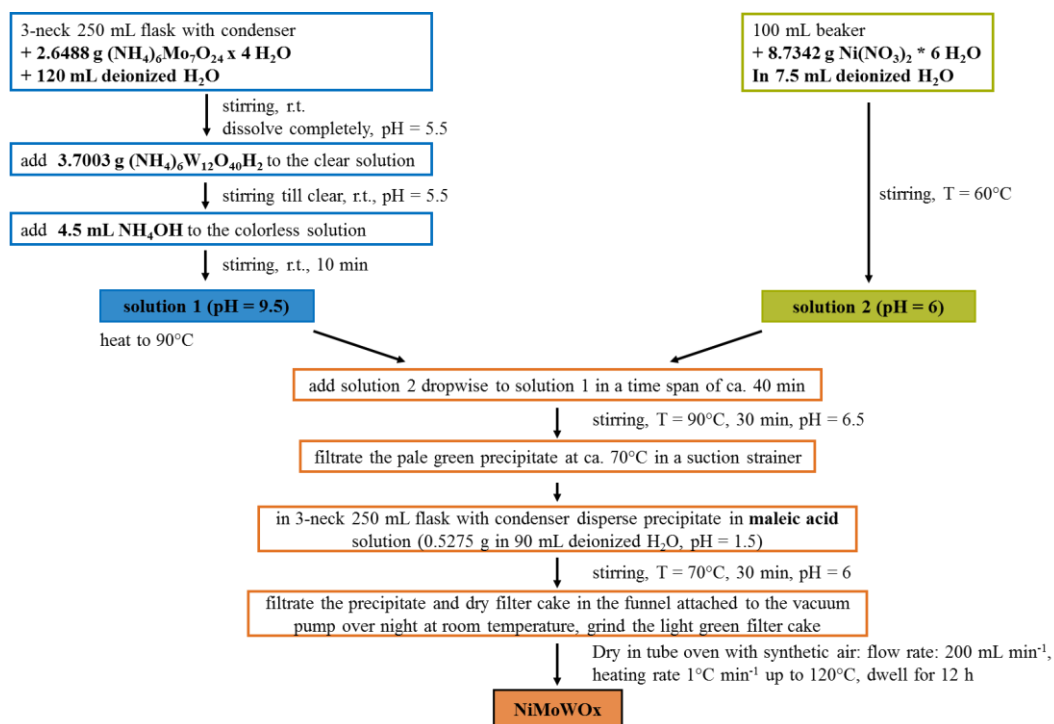
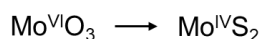
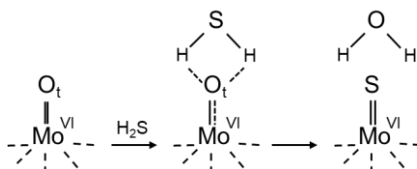


Figure 3-1. Experimental protocol for synthesizing a bi- or trimetallic oxide precursor for NiMoWS catalysts.

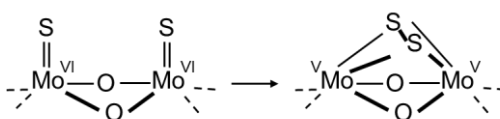
After synthesizing by co-precipitation or impregnation the oxidic precursors are usually pre-treated via gas-phase sulfidation before introducing a reaction feed. Typically, the precursor is reacted with 5-10 vol-% H_2S in H_2 at 400°C for some hours to be transformed into the active sulfide catalyst. Formally, the oxide precursor is reduced and the sulfidation happens in successive steps depending on the temperature.^[256-260]



Sulfidation already sets in at room temperature but is not completely achieved. Below 100°C bridging Mo-O-Mo structures break and form reactive terminal Mo=O_t groups where the oxygen is protonated by H_2S with at the same time weakening the Mo-O and the S-H bonds. After rotating the resulting Mo-O-H-H-S complex, water is released which is the thermodynamic driving force of the process.



The reduction of Mo^{VI} to Mo^{V} occurs simultaneously with the oxidation of two terminal adjacent S^{2-} ligands to bridging S_2^{2-} groups.



This formation causes a distorted arrangement and as a consequence additional Mo-O bonds break into terminal Mo=O_t groups again. Below 200°C no deeper sulfidation occurs so that precursor is stabilized as a Mo oxysulfides with a MoO_2 core. In the temperature range between 200 and 260°C more Mo-O bonds transform in Mo-S, but higher temperature is required for full transformation into the MoS_2 . By an increase in temperature up to 400°C the oxysulfide formed by O-S exchange is further reduced by rupture of Mo-S bonds and reduction of elemental sulfur to H_2S .^[261,262] Additionally, high temperature is required to form the sulfides of the promoter, NiS or Co_9S_8 .^[263] The influence of system pressure on the sulfidation is depicted by sulfidation of NiW-based precursors which usually require harsher sulfiding conditions than NiMo based catalysts.^[264] At 400°C and atmospheric pressure large amounts of WO_xS_y phases are present while full sulfidation to NiWS_2 requires increased pressure of 15 bar which also reduces the dispersion of WS_2 and NiS.^[264,265]

Modern sulfidation takes place in liquid phase using organosulfide agents (e.g., dimethyl disulfide, DMDS) instead of H_2S . Main benefits are easier handling and above all the exothermic character of the sulfidation is reduced by the capability of the solvent to dissipate heat and prevent sintering of the sulfide. Consequently, higher activities for liquid-phase sulfided TMS are reported

compared to H₂S sulfidation.^[266–268] While sulfidation already takes place at low temperatures when using H₂S, the situation changes when using DMDS due to its thermal decomposition behavior. Below 230°C DMDS is decomposed into methane thiol not being able to sulfide molybdenum oxides. Between 230 and 330°C the methane thiol is condensed to dimethyl sulfide and H₂S. Above 330°C hydrogenolysis to CH₄ and H₂S sets in. Either way dihydrogen sulfide is present for sulfidation and acts as the sulfiding agent.

In this study, sulfidation was carried out in liquid phase according to US patent from Maesen *et al.*^[269] About 400 mg of catalysts precursor powder was mixed 1 / 5 with SiC (355–500 μm) and placed into the tubular reactor system. Then, the catalysts was dried at 120 °C overnight, after which a liquid sulfidation feed containing dimethyl disulfide (DMDS) in decalin was introduced together with gas phase hydrogen. For sulfidation the system was pressurized to 20 bar and a heating ramp to a first temperature stage was set followed by a second ramp and T-stage. In between, depending on the exact protocol, the concentration of DMDS was changed. The influence of different sulfidation protocols is discussed in chapter 4.

1.2 Preparation of bulk TMS by thermal decomposition method

Impregnation or thermal decomposition of thiometallates^[270,271,280,272–279] basically is a bottom up method at which sulfides are first synthesized as either alkylammonium Mo/WS₄²⁻ or bimetal [Ni(Mo/WS₄)₂]²⁻ salts. Usually the MS₄²⁻ is obtained by bubbling H₂S through an aqueous solution of the ammonium metal oxide in which the salt precipitates during cooling in ice. Another method is to transform a Mo-oxide in (NH₄)₂S solution into (NH₄)₂MoS₄. Then, the (ammonium)MS₄ salt is either impregnated with a Ni salt or not treated before reduction in H₂S/H₂ atmosphere (>300°C) to the final (promoted) Mo(W)S₂. The alkyl chain decomposes during the thermal treatment and depending on its nature, the catalyst will expose surface areas up to 400 m² g_{cat}⁻¹ reported.

Catalysts obtained by the method of thermal decomposition are used for investigating the influence of the promoter Ni content in bulk Mo(W)S₂ on the hydrogenation and their behavior after leaching (chapter 5). Additionally, these catalysts are used for titration experiments to study function and distribution of active sites in TMS catalysts (chapter 6). The protocol follows a multi-step synthetic route, inspired by literature.

Synthesis of (NH₄)₂MoS₄ (ATM) and (NH₄)₂WS₄ (ATT)

In order to obtain a phase pure precursor thiometallate the sulfidation of an oxidic precursor was performed. Most of the literature choose a protocol from “Annalen der Chemie, 1884”,^[281,282] where H₂S was bubbled through a solution of ammonium molybdate/tungstate. In contrast to that, in the present work, for the sake of easiness, (NH₄)₂S was used as sulfiding agent as suggested by

Brimont *et al.*^[280] and the protocol was slightly different for Mo-based sulfides compared to W-based sulfides.

To synthesize $(\text{NH}_4)_2\text{MoS}_4$ typically 8 g of ammonium heptamolybdate tetrahydrate, $(\text{NH}_4)_6\text{Mo}_7\text{O}_{24}\cdot 4\text{H}_2\text{O}$, were dissolved in 20 g of ammonium hydroxide solution and once no crystals were observed in the colorless solution 72 g of a $(\text{NH}_4)_2\text{S}$ solution were added in excess ($\text{S}/\text{Mo} = 10$) and the color changed to dark red. This mixture was stirred for 1 h at 60°C and cooled in ice to allow precipitation of dark red crystals. These dark red to purple ATM crystals had to be filtered off and washed with cold isopropanol several times.

To synthesize $(\text{NH}_4)_2\text{WS}_4$ the best result was obtained by using tungstic acid, H_2WO_4 , as precursor as suggested by Stiefel *et al.*^[277] First, 5.0 g of the acid were dissolved in 40 mL of ammonium hydroxide solution in a three-neck round bottle flask (250 mL) connected to a washing cylinder containing sodium hydroxide solution to wash acidic gases. Then, 20 mL min^{-1} dihydrogen sulfide, 10 vol% H_2S in H_2 , were bubbled through the stirred solution.^[277,283] The blue suspension was heated to 60°C in an oil bath for 30 minutes, after which a dark blue solid was filtered off. This solid might be a polyoxoanion, which is known to form when trioxide hydrates of Mo and W (H_2WO_4) are exposed to reducing agents ($\text{H}_2\text{S}/\text{H}_2$). This effect is more severe for W-based solutions, since they are hard to sulfide and oxosulfyl species such as $\text{W}_3\text{OS}_8^{2-}$ are unavoidable in acidic solutions.^[277,283] The remaining yellow and clear filtrate was heated to 60°C and kept overnight under H_2S passing through. Then, the solution was allowed to cool down and no precipitation of any solid was observed.

Synthesis of hexamethoniumtetrathiometallate

The ammonium tetrathiometallate salt could be decomposed in $\text{H}_2\text{S}/\text{H}_2$ at 400°C to form the layered dichalcogenide^[122,284] but usually exposes a very low surface area. It was shown that by changing the cation from NH_4^+ to a tetraalkylammonium, the pore volume and surface area was increased after reduction.^[160,283] By using bromide salts of the tetraalkyl ammonium ion for re-crystallization the whole process is carried out in water what makes the protocol clean and easy. For the present study the bidentate hexamethonium bromide was chosen to exchange the NH_4^+ ion and to act as a chelating spacer during the later reduction step. The re-crystallization offers purification of the material due to a very clean, water insoluble product. The cleaned up $(\text{NH}_4)_2\text{MS}_4$ was dissolved in 100 mL water again and in another beaker stoichiometric amount of hexamethonium bromide, $(\text{CH}_3)_3\text{N}(\text{Br})(\text{CH}_2)_6\text{N}(\text{Br})(\text{CH}_3)_3$, was dissolved in 30 mL water. This solution was added to the ammonium thiometallate and orange (Mo) or yellow (W) precipitate was formed immediately which was filtered off and washed with a lot of water to remove potential Br^- residues. The paste was dried in dynamic vacuum and ground to powder.

Formulation of Ni_aMo/WS_2

The final step is the thermal decomposition of the thiosalts. Here, the promoter Ni content was adjusted and values of $0 < a < 0.7$ were obtained in this work. Usually, 3 g of hexamethonium tetrathiomethylate were put into a batch autoclave (300 mL Parr reactor) and a solution of Ni naphthenate, $Ni(C_{11}H_7O_2)_2$ (8.09 wt% Ni according to the certificate of this specific batch of chemical), in decalin was added stoichiometrically. The volume in the reactor was filled up to 100 mL with decalin after which the reactor was closed, first purged with N_2 then with H_2 up to 5 bar three times each and finally pressurized to 45 bar with H_2 . The reactor was heated to $350^\circ C$ and stirred for 3 h while the pressure increased to 84 bar. After that, the reactor heating was stopped, the heating jacket removed and the reactor was left closed for cooling over-night. The next day the reactor was opened and a strong odor of NH_3 , H_2S and CH_4 was detected. After degassing the organic phase was decanted and the catalyst washed into a falcon tube with hexane, centrifuged and washed again for at least 5 times. After that the catalyst was dried in dynamic vacuum overnight.

This dried Ni_aMo/WS_2 had to be sulfided again because of some carbon residues and partial oxidation of the formulation as seen by a non-closed mass balance according to elemental analysis. This was conducted in the TPR set-up with ca. 100 mg of catalyst loading. The volumetric flow of 10 H_2S/H_2 , (Westfalen, certified mixture of 98% purity H_2S and 99.999% purity H_2), was 8 mL min^{-1} and the temperature was ramped to $400^\circ C$ with $5^\circ C\text{ min}^{-1}$.

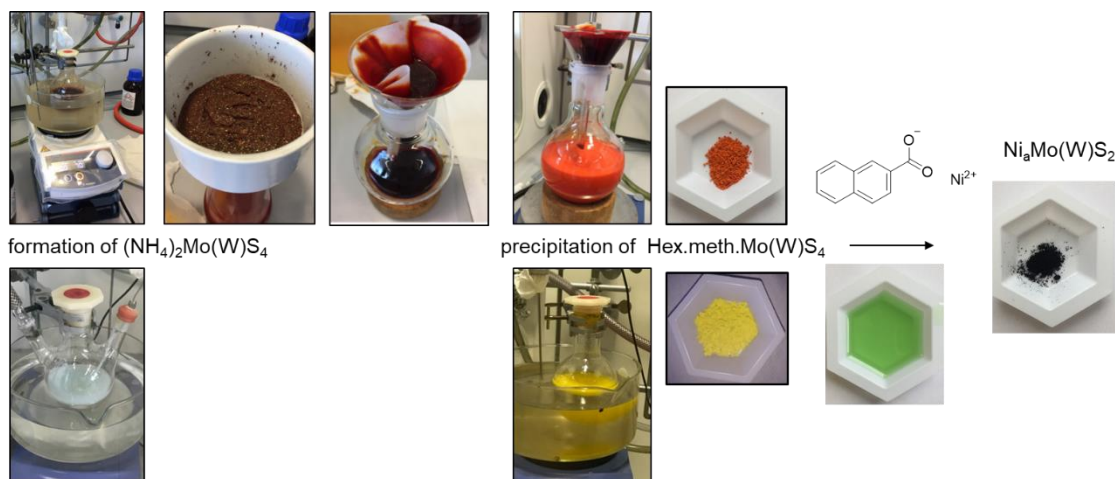


Figure 3-2. Pictures of synthesis sequence for TMS catalysts obtained via the thiosalts impregnation route. First, the ammonium tetrathiomethylate is obtained by either stirring the ammonium oxide in $(NH_4)_2S$ or via H_2S bubbling. Then, the precipitate or solution is reprecipitated with hexamethonium bromide to obtain a clean precursor. This is decomposed in decalin and hydrogen together with a green solution of Ni naphthenate dissolved in decalin at $350^\circ C$ and 45 bar.

Table 3-1. Elemental composition for catalysts and corresponding precursors. 'P' stands for the parent catalyst as synthesized and resulfided; 'L' stands for the leached formulation. Especially the precursors were of high purity and the targeted metal to sulfide or carbon ratio was achieved. Also, Ni incorporation was successful using the naphthenate as Ni source and leaching successfully the promotor once incorporated for both formulations presented here.

	Elemental composition [mmol g _{cat} ⁻¹]						Atomic ratio [mol mol ⁻¹]	
	Ni	Mo/W	S	N	H	C	Ni/M	S/M
(NH ₄) ₂ MoS ₄	0	3.8	15.6	7.6	29.9	0	0	4.07
(Hexmeth.)MoS ₄	0	2.4	9.4	4.8	72.2	28.0	0	4.02
MoS ₂	0	5.3	12.4	1.6	14.6	4.7	0	2.34
Ni _{0.5} MoS ₂ (P)	3.5	3.9	11.6	1.1	9.0	2.3	0.47	1.57
Ni _{0.5} MoS ₂ (L)	2.3	4.8	12.5	<0.1	2.4	0.3	0.32	1.76
(NH ₄) ₂ WS ₄	n.a.	n.a.	n.a.	n.a.	n.a.	n.a.	n.a.	n.a.
(Hexmeth.)WS ₄	0	2.0	7.8	4.0	58.9	23.5	0	4.00
WS ₂	0	3.1	7.1	0.8	25.6	13.0	0	2.27
Ni _{0.5} WS ₂ (P)	3.1	2.6	8.0	0.8	11.4	4.5	0.54	1.40
Ni _{0.5} WS ₂ (L)	2.3	2.8	8.9	0.2	9.3	4.3	0.45	1.75

1.3 'Leaching' of TMS catalysts

A post-synthetic treatment, developed in house, was applied to the catalysts in order to remove nickel sulfides selectively and study the enhancement of activity. Inspired by metallurgic studies on phase compositions of Ni and Mo sulfides,^[285] M. Wagenhofer^[286] studied the effect of HCl treatment ('leaching') on Ni_aMoS₂ obtained by hydrothermal synthesis methods.

For leaching of catalysts obtained by thermal decomposition (see chapter 5) ca. 400 mg of the material was exposed to 3 mL conc. HCl in a 5 mL glass tube. Depending on the pore volume and surface area of the material the hydrophobic particles floated and had to be forced to be soaked with HCl solution by centrifugation. Once the HCl was in contact with the sulfide H₂S was evolved (indicated by odor) and the solution was colored green (Ni²⁺ in solution). After 1 h the water phase was replenished with 3 mL HCl solution and the protocol was repeated 2 times. Then, the sulfide was washed with water (slurred up and waited to be settled, gas evolving because of reaction of adsorbed HCl) several time to remove remaining Cl⁻ and Ni²⁺. In order to finalize the formulation, a gas phase sulfidation was indispensable to remove water and re-sulfide the surface of the catalysts which might have been partially oxidized. Different to this protocol, formulations

obtained by co-precipitation followed by liquid-phase sulfidation were leached at 80°C in an oil bath. The acid solution was replenished up to 10 times before washing.

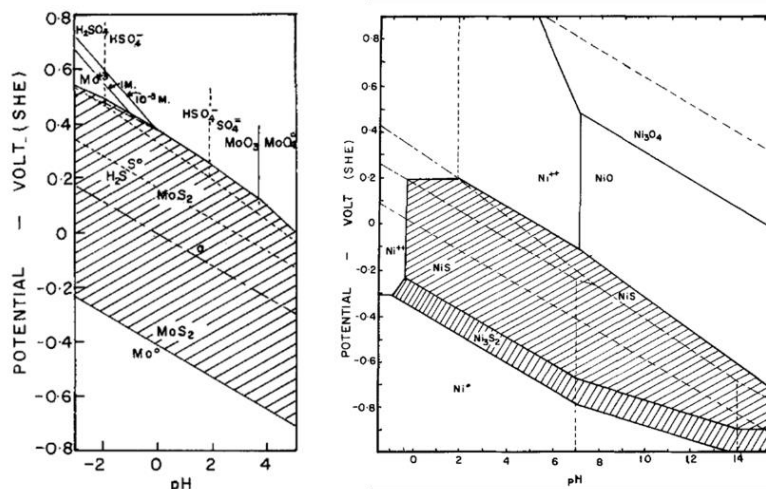


Figure 3-3. Eh-pH diagrams of Mo-S-H₂O and Ni-Fe-S systems at standard conditions.^[285] At zero potential the MoS₂ slab is intact over the pH range of -2 to 4 while NiS_x are dissolved below pH = 0 in the form of Ni²⁺. Used with permission of The Minerals, Metals & Materials Society and ASM International.

Although MoS₂ slabs stay intact under strong acidic treatment (according to Figure 3-3) the surface of the particles can be partially oxidized due to handling under air atmosphere and in HCl-water solution. These surface MoO_xS_y are soluble in water, which leads to solvation of Mo atoms. Three samples Ni_{0.0}MoS₂, Ni_{0.5}MoS₂ and Ni_{0.1}MoS₂ were leached (3 × 1 h) and the decanted water phase was analyzed by ICP-OES. Prior to the measurement, the samples were diluted 1:600 with DI- water and calibration samples using Mo-standard were prepared.

Table 3-2 summarizes the concentration of Mo found in decanted solutions during leaching. Most of Mo was leached on the low content Ni_{0.1}MoS₂ (4.51 mol-%) followed by Ni_{0.5}MoS₂ (3.21 mol-%) and the sample with the very little loss of molybdenum Ni_{0.0}MoS₂ (0.49 mol-%). This data shows that a sulfided MoS₂ slab is stable in strong acidic water solutions and only small amounts of Mo are partially oxidized and leached out. In the case of Ni promoted samples the situation changes. The loss of Mo during leaching is measurable higher and goes up to 4.5 mol-% what corresponds to 25% of Mo atoms exposed on the edges of the slabs (assuming 20 % edge distribution). Ni introduces more surface vacancies and therefore adsorption sites for O₂ from air or H₂O. This might lead to a higher degree of surface oxidation and therefore loss of Mo. Especially the low Ni content sample seems to be mostly affected by this treatment. Consequences of this are discussed in chapter 5 ‘On the multifaceted roles of NiS_x in hydrodearomatization reactions catalyzed by unsupported Ni-promoted MoS₂’.

Procedures and Methods for Research on Transition Metal Sulfides

Table 3-2. Analysis of decanted solutions obtained from leaching. The HCl–water phase was removed and replenished three times (approximately 4.5–5.5 mg) and the concentration of Mo was determined by ICP-OES. The last column gives the percent of Mo atoms leached based on the total Mo atoms present according to elemental analysis of the whole sample. Mass of sample leached: 212 mg ($\text{Ni}_{0.0}\text{MoS}_2$ and $\text{Ni}_{0.5}\text{MoS}_2$) and 292 mg ($\text{Ni}_{0.1}\text{MoS}_2$).

	Concentration and mass of Mo in leached solution						Sum of leached Mo		Percent of Mo leached
	Step 1		Step 2		Step 3				
	[mg g ⁻¹]	[g]	[mg g ⁻¹]	[g]	[mg g ⁻¹]	[g]	[mg]	[μmol]	[mol-%]
$\text{Ni}_{0.0}\text{MoS}_2$,	0.345	4.68	0.104	5.26	0.071	4.52	2.48	26	0.49
$\text{Ni}_{0.1}\text{MoS}_2$	3.176	5.62	0.606	6.09	0.205	6.49	22.87	238	4.51
$\text{Ni}_{0.5}\text{MoS}_2$	1.203	4.32	0.389	5.44	0.071	5.49	7.71	80	3.21

2 Most commonly used characterization techniques

After synthesizing a catalytic material it is indispensable to characterize the obtained substance in order to measure the features which were targeted by the synthetic protocol chosen. Characterization techniques are used to get physico-chemical information about the morphology and crystal structure of the catalysts and to determine and quantify the active centers by several different methods. In the following the most commonly applied methods which are used in TMS catalysis research are presented based on literature and examples of experiments and their evaluation for this work are examined.

2.1 Morphology and Surface Structure

Transition metal sulfides show a unique structure among catalytic active materials and their bulk and surface properties have to be measured to ensure reasonable comparison between different formulations. Therefore, some 'standard' measures are established in TMS research which have to be presented for each catalyst.

Elemental analysis

The synthesis of bulk TMS contains many individual steps involving several different chemicals and therefore elements. In order to check for impurities or if the targeted elemental composition was achieved the catalysts can be analyzed via ICP-OES, combustion analysis and photometry.

N₂-Physisorption

In general the surface area of a catalyst is a quantitative correlation to its activity. The more area available the higher the total accessible number of active sites is possible. The fact that the basal plane of layered Mo/WS₂ exhibits a large proportion of the surface area and being inactive causes a non-linear relation of activity and area in many cases.^[71] Anyhow, a large surface area can provide more adsorption sites for the organic molecule and might be beneficial. The isotherms of N₂-physisorption experiments allow conclusions about the surface area by applying the BET (Brunauer-Emmet-Teller) method and pore volume by applying the method of B.J.H. or Gurvich.^[287] Common values for the surface area are between 5-100 m² g_{cat}⁻¹ and the measured pore volume should be considered as cavities or inter-particle voids rather than the volume of a primary pore structure. The data presented in the at hand thesis was obtained from an automated nitrogen adsorption analyzer Sorptomatic 1990 Series (Thermo Finnigan). Prior to adsorption the sample (100 – 250 mg) was outgassed at 250°C for 2 h. Analysis of the measurement was done by the software provided by the machine supplier.

Powder X-ray diffraction

A non-destructive characterization method is the crystal structure analysis via X-rays.^[288,289] Here, the property of materials of diffracting an incoming X-ray beam (photons) at the lattice planes of its crystal is used. A periodic crystalline structure will scatter the radiation constructively or destructively which leads to a characteristic pattern of diffraction peaks when changing the angle of the impinging beam. Even multiple phases present in the sample are detected and their relative proportion is reflected in the intensity of their peaks. The geometrical condition of the sample is described by the Bragg equation:

$$n\lambda = 2d_{hkl}\sin\theta$$

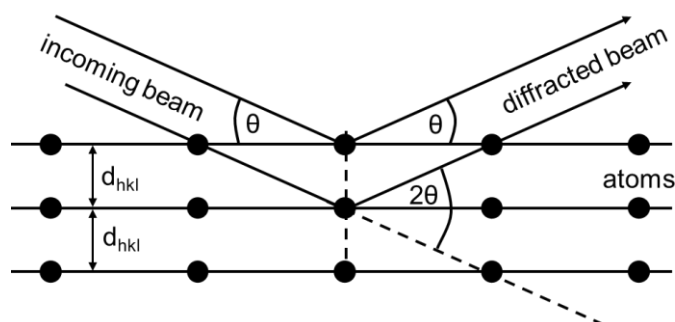


Figure 3-4. Geometrical conditions representing Bragg's law.

All constructive interferences of the beam and the lattice planes in the sample follow this law, where the product of the order of diffraction, n (set to 1 in this thesis), and the wavelength of the incident beam, λ (equals 154 Å for Cu radiation used here) equals two times the lattice spacing, d_{hkl} , times the sinus of the angle of diffracted beam, θ (in degree). By comparing an X-ray diffraction pattern of an unknown sample with patterns from crystalline, pure phases of model compounds a qualitative comparison and phase indication can be made.

In this work XRD patterns were recorded on an Empyrean system from PANalytical equipped with a Cu X-ray tube (Cu-K α radiation, 0.154 nm), a nickel K β -filter, and solid-state detector (PIXcel1D) operated at 45 kV and 40 mA with step size of 0.017 ° and scan time of 115 s per step. The peaks were assigned according to matches with the Highscore software database. In the following, one characteristic example of a parent (not leached) NiMoWS₂ catalyst which exhibits several phases is given.

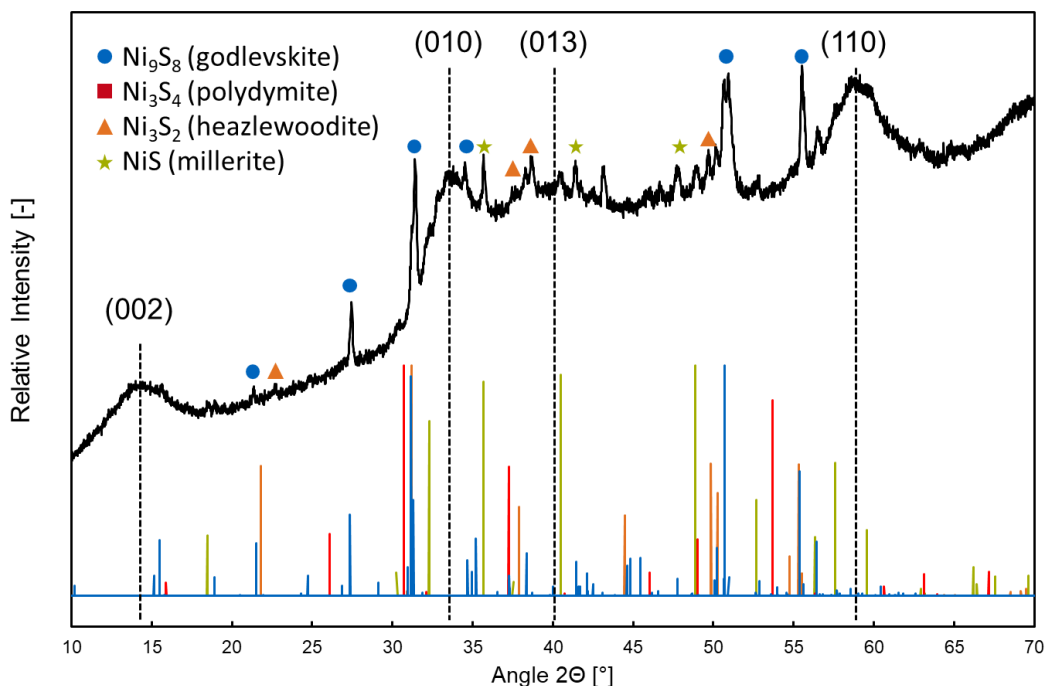


Figure 3-5. XRD pattern of a NiMoWS₂ catalyst. Baseline upshift is caused by fluorescence of nickel in a Cu_{Kα} x-ray. In parenthesis four lattice indices of Mo/WS₂ phase are given. The stick patterns of four reference substances (obtained from Highscore database) are shown at the bottom: blue, godlevskite (Ni₉S₈); green, millerite (NiS); orange, heazlewoodite (Ni₃S₂); red, polydymite (Ni₃S₄).

In Figure 3-5 several phases of nickel and molybdenum / tungsten sulfides can be identified. Clean and sharp peaks usually correspond to crystalline NiS_x phases while the underlying Mo/WS₂ pattern is X-ray amorphous. However, due to an upshift in signal caused by Ni fluorescence only the small angle region of the pattern is used for quantitative analysis. Molybdenum and tungsten sulfides align in c-direction by stacking their slabs. This alignment is seen in the XRD pattern of the crystals in the signal of the (002) plane. Its reflection maximum is shifted compared to a crystalline Mo/WS₂ and hints to a disorder (bending, curvature) of the slabs.^[65] Observed line broadening occurs due to the turbostratic disorders of the slabs in the sample.^[290–292] Therefore, applying the Debye-Scherrer equation to calculate the crystal size and stacking may lead to another measure than observed in TEM.^[150] Anyhow, the stacking number based on XRD is calculated by dividing the crystal size by the inter slab distance obtained by the reflection position of the (002) plane (Bragg-equation) plus 1.

Transition electron microscopy (TEM)

Another way to measure the stacking is counting slabs based on microscopic imaging.^[112,125,293,294] Transition electron microscopy (TEM) on Mo(W)S₂ gives a picture where layers of slabs are observable as lines (slabs parallel to the e⁻ beam). Figure 3-6 gives an example for an unpromoted MoS₂ and a Ni_{0.6}MoS₂ catalyst.

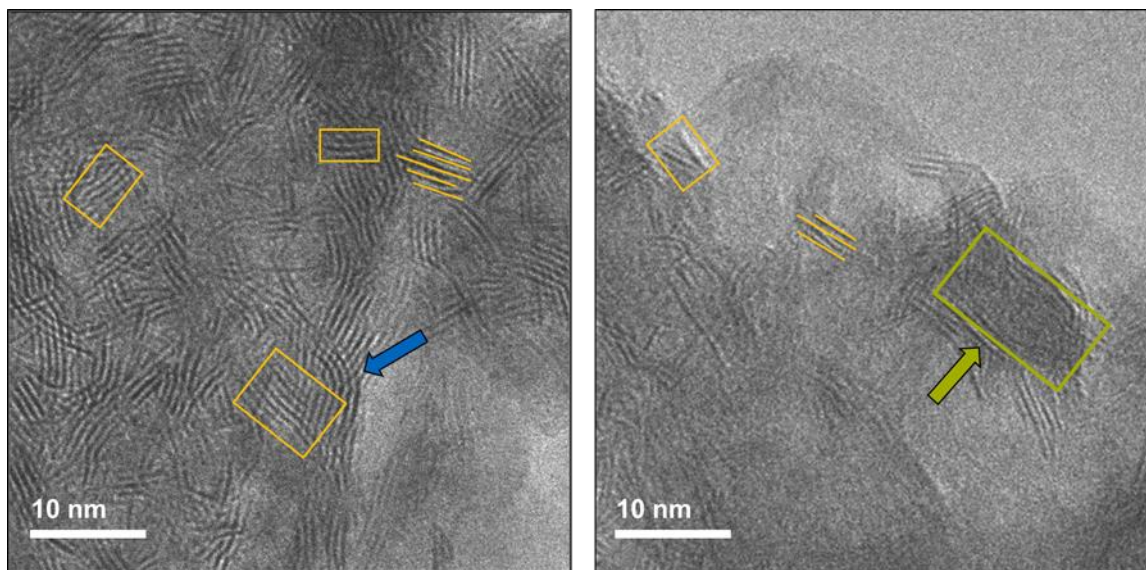


Figure 3-6. TEM images of unpromoted MoS₂ (left) and Ni_{0.6}MoS₂ (right). Domains with varying numbers of slabs and different slab length are identified. The blue arrow points on curved slabs found at the border of the particle. The catalyst with 60% Ni content shows a dense region which corresponds to a NiS particle (green box and arrow).

The images clearly show packages of stacked slabs randomly arranged. Some slabs are curved which speaks for default active sites created thereby. Generally, the oxide form of the catalysts is not revealed by TEM but oxygen poor oxysulfides (MoO_{0.2}S_{1.7}) still give contrast. Other phases detectable are crystals of Ni(Co) sulfides seen as dark, dense areas. Based on the images the sample can be quantified in stacking and slab length and further statistically analyzed. A rule of thumb is to analyze at least 200 slabs (better 500) to be achieve reproducibility of 15% of stacking and mean length of the slabs. Based on the slab length the dispersion of the MoS₂ given as the fraction, f_{Mo} , of Mo atoms located at the edges of a perfect hexagon is calculated via,^[99,113]

$$f_{Mo} = \sum_{i=1...t} 6n_i - 6 / \sum_{i=1...t} 3n_i^2 - 3n_i + 1$$

with the number of atoms at one edge $n_i = length/6.4 + 0.5$. For this work the software ImageJ was used to measure the slab length. Typically, the slab sizes varied in a small range. The spreading of the numbers was calculated via the covariance of sample mean and histograms were created:

$$Var = \sqrt{\frac{1}{n} \cdot \sum_{i=1}^n (X_i - \bar{X})^2}$$

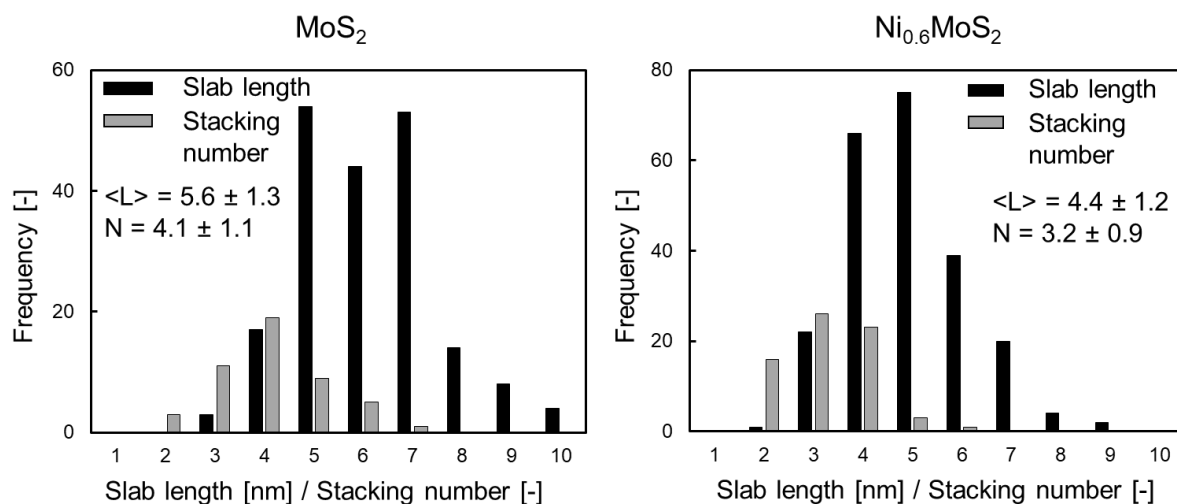


Figure 3-7. Histograms for the above presented TEM samples of unpromoted MoS_2 and promoted $\text{Ni}_{0.6}\text{MoS}_2$. The average length, $\langle L \rangle$, and stacking, N , are determined by counting and statistical analysis as presented above.

Scanning electron microscopy (SEM)

Scanning electron microscopy provides images of the surface topography of a material.^[295] Next, to crystalline structure the chemical composition and electrical behavior can be analyzed. For this study, images mainly give an impression of the effect of leaching, namely, the removal of large NiS_x phases.

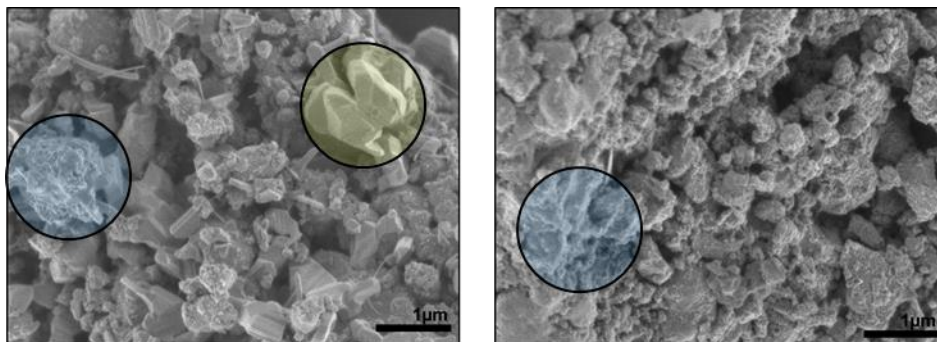


Figure 3-8. SEM images of a parent (left) and leached (right) TMS catalyst. The green area on the left indicates crystalline NiS_x phases which are almost no longer discernible on the right. The blue area represents the Mo(W)S_2 phase.

Other characterization techniques

In the field of sulfide catalysis some other important characterization techniques are widely applied, but not considered for this work. One method is X-ray absorption (EXAFS, XANES)^[296] which gives insights into the electron and atomic structure of a sample. Thereby, the intensity of X-ray photons impinging on a sample decrease by passing through it depending on the wavelength

or energy of the beam. The energy chosen corresponds to core-electron levels and is specific for each element. This allows to gather information about valence state and coordination environment. One advantage of this method is that structural information of mixed sulfide phases can be obtained in-situ. For example, it was proven that a Co(Ni)-Mo contribution is in the coordination sphere of Co(Ni) speaking for an edge substitution by the promoters. Anyhow, one drawback of the method is that synchrotron radiation is needed to get access to the x-ray radiation of this energy.

Another commonly used technique is X-ray-photoelectron spectroscopy (XPS)^[297] at which electrons released by photoemission after excitation by X-rays are detected. The energy for this process is directly linked to the nature of atom and its energetic level of the atomic orbital. XPS is considered as a surface technique (penetration depth of a few microns) and was, for example, used to identify mixed Co(Ni)MoS₂ phases, to study temperature effects on sulfidation or to measure Co(Ni) substitution and distribution at the slabs edges.

Laser Raman spectroscopy (LRS)^[298] is a surface technique which has the drawback of a bad signal to noise ratio due to the black color of the sulfides. The band position depends on the slab size, temperature and atmosphere and characteristic bands for MoS₂ and e.g. [S-S]²⁻ are observed.

2.2 Measuring active sites

One of the most important measures in heterogeneous catalysis research is the characterization of the active sites involved in the catalytic cycle. The quantitative and qualitative description of the arrangement at the materials surface allows to understand the influence of elements on the reaction mechanism as well the calculation of the turn-over frequency 'TOF', a quantitative intrinsic activity parameter for active site comparison. It is defined as molecules reacting per unit time per active site.^[168] As discussed above, the active sites of TMS catalysts are coordinatively unsaturated sites (CUS) with Lewis acidic character and sulfhydryl groups (SH) with Brønsted acid properties. According to the definition of acid-base concepts these sites can be 'titrated' or 'probed' with base molecules. Hence, some methods for testing the nature, density or strength of acid sites have been developed^[299] and transferred to TMS catalysts. A good method allows to distinguish between up to 4 type of sites present at the catalysts edges, namely, metal and sulfur edge, both promoted and unpromoted.

Infrared Spectroscopy

A commonly used technique is Fourier Transformed Infrared Spectroscopy (FTIR) analysis of the catalyst surface interacting with probe molecules. This method is very sensitive and selective to the chemical environment and geometry of the metallic state of the sample. It is

suitable for measuring the type of sites (Lewis and Brønsted acidity, location) and for quantifying the sites by a neat choice of probe adsorbents. The experiment is carried out at ultra-high vacuum and a transmissive sample is required. For this reason studies on sulfides can only be made with supported catalyst because of the black appearance of bulk materials.

Temperature Programmed Desorption

Temperature Programmed Desorption (TPD) is a technique to quantify sites interacting with a probe molecule. Typically, ammonia (but also amines and pyridine, NO, H₂S) is used to determine acid site concentration and strength of catalyst samples. A fully probe molecule covered sample is treated with a defined temperature increase and molecules leaving the surface are detected with GC or MS. Based on the temperature required for desorption the strength of a site is estimated and after full desorption the total amount of sites is analyzed. The method suffers from uncertainties because of readsorption of probe molecules during the desorption process and of being unselective regarding Brønsted or Lewis acidity.

Volumetric Pulsing

Volumetric pulsing of probe molecules allows to quantify sites where probe adsorbs strongly by chemisorption. Typically, a defined volume of the probe is pulsed over a catalyst bed located in a flow system and the molecules are monitored by quantification tools, e.g. a mass spectrometer. By measuring the difference of incoming and leaving concentration of the probe the amount adsorbed on the catalyst is quantified. This method cannot distinguish between the types of sites as well, but offers a possibility to study bulk TMS catalysts. In this study NO volumetric pulsing (chemisorption) was used. In a typical experiment 60-100 mg of sulfided catalyst was filled in a quartz tube held in place with glass wool and installed horizontally into a furnace. Helium, nitrogen, hydrogen and dihydrogen sulfide were connected to the reactor set-up and a sample loop (volume = 1.6887 mL) was filled with nitric oxide (10 vol.-% in He). For all experiments the same activation protocol was run prior to adsorption. First, the catalyst was treated with 10 vol.-% H₂S in H₂ at 400°C for 1h and allowed to cool down to 250°C at which the H₂S/H₂ flow was stopped and N₂ was introduced. The reactor was cooled down to 35°C and the pulsing program was started. Every 30 min 6.905 μmol NO were pulsed over the catalyst bed and the effluent stream monitored with a mass spectrometer. In total 24 pulses were recorded.

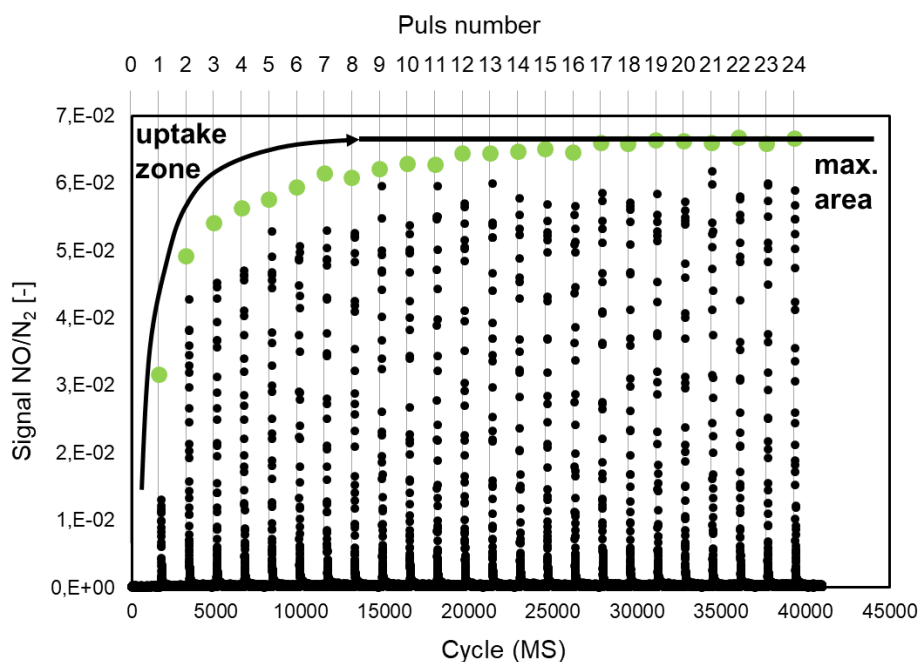


Figure 3-9. Experimental result of volumetric pulsing of NO on a sulfided catalyst. 24 pulses, hold for 30 min each, were recorded by MS. The values of the integrated areas are plotted as green dots. The noise wave-like MS signal is due to presentation in the diagram and do not fully cover the maximum of the signal.

Figure 3-9 shows an example on $\text{Ni}_{0.7}\text{MoS}_2$ catalyst. Full breakthrough of NO (= maximal area) is taken between pulses #12 and #14. The total amount of NO adsorbed on the sample corresponds to the sum of all NO not detected by MS signal.

$$n_{\text{NO},\text{total}} = \sum_{i=0}^{n=\text{breakthrough}} n_{\text{NO per puls } i} \cdot \left(1 - \frac{\text{area}_{\text{peak } i}}{\text{area}_{\text{peak breakthrough}}} \right)$$

In this case the sum of No adsorbed was $10.54 \mu\text{mol}$ on 67 mg catalyst. Therefore, a total uptake of $157 \mu\text{mol}_{\text{NO}} \text{ g}_{\text{cat}}^{-1}$ was determined and correlated to CUS sites.

Probe molecules

Independent of the method chosen a probe molecule should fulfill some criteria in order to give significant and robust results.^[300] It should be selective to either acid or base sites, small to have access to sites located in narrow pores or cavities, sterically hindered Lewis acid sites and not to adsorb on exposed surfaces randomly and have a low activity at the chosen experiment temperature to avoid surface changes during experiment. Ideally, the molecule has the appropriate acid or base strength according to the HSAB principle, e.g. NH_3 is a hard base probing hard acids and CO as a soft base probing soft acids. Several probes with varying hardness might be used for detailed understanding of the acid strength. Based on this considerations several probe molecules are suitable for characterizing surface sites on $\text{Ni}(\text{Co})\text{MoWS}_2$ formulations.^[301]

Dihydrogen sulfide, H_2S , was used in TPD experiments on $(\text{Co})\text{Mo}/\text{Al}_2\text{O}_3$ catalysts.^[302] It was shown that H_2S interacts with the support in a simple adsorption-desorption process and adsorbs on vacancies dissociatively.

Dioxygen, O_2 , was used in chemisorption or pulse experiments^[303–307] and it was found to adsorb fast and irreversible. Although the nature of active sites was speculated about based on O_2 chemisorption behavior no clear correlation between HDS and HDN activity (or change in promoter content) and O_2 uptake was established. One problem might be the reactivity with the sulfide surface, so that experimental conditions of low temperature and pressure have to be chosen to avoid bulk oxidation. This method might act as a measurement for dispersion.

Carbon monoxide, CO , is commonly used in FTIR studies.^[308–311] It is possible to distinguish between interactions of CO and active sites located at metal or sulfur edges and between support and bulk sulfide phases. The adsorption is totally reversible and only minor disruption in adjacent sites is observed. Experiments are directly linked to the oxidation degree of the probed site and the results are in alignment with catalyst properties. CO adsorption usually takes place at 77 K for IR studies, in chemisorption experiments (volumetric pulsing) 273 K to room temperature is applied. Both methods allow to establish activity–site correlations by the measure of active site concentration, but at higher promoter loading the CO uptake is overlain by contributions from $\text{Ni}(\text{Co})\text{S}$.

Nitric oxide, NO , offers a good complement to CO in FTIR studies (its adsorption frequencies are more sensitive to changes in catalyst structure) and can act as probe molecule for chemisorption as well, like demonstrated in this work. In general its reactivity with the surface is higher (strong adsorption) than CO and an oxidation reaction with the surface metal can occur even at low temperatures (>200 K).^[303,312,313] By using pulse and FTIR studies linear relations between Co atoms present in the Co-Mo-S phase and the NO uptake were established. The studies showed that the amount and mode of NO adsorption depend on various parameters whereof some should be discussed shortly. First, the uptake depends on the atmosphere present in the experiment. As discussed above the amount of CUS (to be probed by NO) depends on the partial pressures of H_2S and H_2 which influences the sulfidation degree (and extend of reduction) of the edges. Therefore, during NO adsorption experiments the atmosphere has to be controlled and reported accordingly. Additional to H_2S and H_2 other pre-adsorbed species influence the NO uptake. Further, NO might not only adsorb on edges of the CoMoS phase, but also on Co(Ni) sulfides which is indistinguishable by volumetric pulsing experiments.^[305,313–315] Next, the mode of adsorption was speculated about. On the one hand it was found that NO partially dissociates,^[312] on the other NO dimers or dinitrosyls were suggested in the 1980ties.^[305] This lead to a combined study of FTIR, STM and DFT of NO adsorption on MoS_2 and CoMoS.^[315,316] Based on this study a complex picture arose which is summed up in the following. Nitric oxide adsorption is suitable for measuring the nature and quantity of active edge sites, but strong adsorption induces edge reconstruction. On fully sulfided edges without hydrogen adsorption is very unlikely and only

vacancies offer adsorption sites. Thereby, mononitrosyls are possible at Mo-edges while dinitrosyls are likely at (Co)-S-edges. The authors suggested the so-called “push-pull” mechanism for the NO adsorption of edges with adsorbed hydrogen. NO adsorption is energetically favored (-500 kJ mol^{-1}) to overcome the energy needed for creation of S-vacancies. Hence, a concerted mechanism of edge-SH replacement by NO adsorption of the created vacancy takes place. With respect to the diverse factors influencing the amount and way of NO adsorption in this thesis the absolute number of NO molecules up taken by a sample is reported. There was no ambition or experiment conducted which allows to speculate about this topic. Interestingly, although correlations of HDS activity and NO uptake (or promoter / active site concentration) were established by other authors, no turn-over frequency was reported for polyaromatic hydrogenation on TMS catalysts, to the knowledge of this author.

Surface Titration during a catalytic reaction

Active sites in TMS catalysts are either of Lewis or Brønsted acidic character. Their nature is by definition to interact with bases and build surface complexes in defined stoichiometric ratios. This effect was used in zeolite and oxide catalysis before to quantify active sites by counting strongly adsorbed base molecules. This was not only demonstrated by spectroscopic methods, but also by titration of active sites during the catalytic reaction. The idea is to follow the decrease in substrate conversion while introducing a known number of molecules which do not convert and stick strongly and specifically on the active centers. Analyzing the amount of adsorbent allows a direct conclusion on the number of active sites. One key point of this work was to establish a method for quantifying active sites on TMS catalysts in an ‘operando’ mode (that is, during a reaction). The advantage is obvious that the catalyst analyzed is in the same condition as during the hydrotreatment reaction, which is in fact an important point for TMS catalysts (see above). In chapter 6, an exploratory work is presented in which N-heterocyclic aromatics (base molecules for titration) were used to quantify active sites under realistic hydrogenation conditions. The ring-cleavage, as expected to happen for HDS and HDN reactions was successfully suppressed.

3 Reaction Kinetics

Alongside the synthesis and characterization of catalytic active materials, their functions in a chemical reaction have to be investigated. The aim is to correlate material properties to fundamental steps of a chemical reaction. Therefore, kinetic studies of model compounds for real applications are conducted in model reactors. For analyzing the results some parameters are defined to draw conclusions about the system.^[317,318]

3.1 Primary measures – reaction rate, selectivity and yield

One of the most important property of a catalyst is its activity for converting the target molecule efficiently. A measure for this is the reaction rate, r_i , which is defined as the change of the amount of a molecule with time, dn_i/dt , normalized to its stoichiometric coefficient, ν , and active material, m_{cat} , (in heterogeneous catalysis). The differential ansatz is:

$$r_i = \frac{1}{\nu_i} \cdot \frac{1}{m_{cat}} \cdot \frac{dn_i}{dt}$$

In a laboratory scale tube reactor the initial amount of reactant fed is known and its concentration in the effluent stream can be detected (e.g., by GC in the case of phenanthrene). With the definition of the conversion, X , which relates the decline of the reactant at a time point t to the maximum possible,

$$X_t = \frac{\dot{n}_{i,0} - \dot{n}_{i,t}}{\dot{n}_{i,0}}$$

the rate equation for phenanthrene hydrogenation ($\nu=1$) is transformed to:

$$r_{Phe} = \frac{\dot{n}_{Phe,0} - \dot{n}_{Phe,t}}{m_{cat}} = \frac{X_t \cdot \dot{n}_{Phe,0}}{m_{cat}}$$

Note, that the differential was assumed to be the difference between reactant in and reactant out, what holds only true for small conversion values (initial rate). Additionally, the time normalization is done by the constant molecular flow of the reactant reasoned by stable (time independent) concentration profiles along the reactor tube at steady state conditions! The above formulation allows to determine the reaction rate at constant temperature by plotting the conversion vs. the set molecular flow. More precisely, during the experiment the volumetric flow of feed, \dot{V}_{feed} , is varied and the concentration of reactant and products is measured at the reactor outlet. By knowing the catalyst mass and feed properties (average density, $\bar{\rho}_{feed}$, reactant mass fraction, w_{Phe}) and calculation of the conversion the following plot is created.

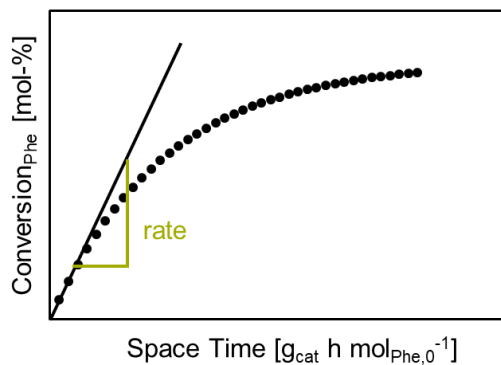


Figure 3-10. Space-Time – Conversion plot for the determination of initial reaction rates in tube reactors. Usually the linear part of the curve up to 5 % conversion corresponds to an initial rate under differential conditions. Hence the slope is the rate. Processes such as mass transfer through the reactor or thermodynamic equilibria of chemical reactions can cause a bending at higher space times. Here the plot is given for a first order kinetic equation.

Hence, the reaction rate is the slope of the line including the origin of the graph through the conversion – space time points. The space time is arbitrarily defined to:

$$ST = \frac{m_{cat}}{\dot{n}_{Phe,0}} = \frac{m_{cat} \cdot \dot{M}_{Phe}}{\dot{V}_{feed} \cdot \bar{\rho}_{feed} \cdot w_{Phe}}$$

Experimentally a bending of the curve can be found at higher conversion levels. This is either due to equilibrium (hydrogenation reactions are dominated by thermodynamic equilibria) and (product-) inhibition (adsorption of reaction intermediates on the same site as the reactant) effects or due to the natural behavior of positive order reactions in a tube reactor at high conversion (e.g. $X = 1 - \exp(-k\tau)$ for first order reaction). In summary, a rate determined in the described way in a tubular reactor is an initial reaction rate determined by varying space-time at constant temperature independent of the reaction order. The space-time range and temperature have to be given.

One important number in heterogeneous catalysis to give, is the *turn-over frequency (TOF)* or *turn-over rate*. It allows, for example, to compare activity data from different labs or helps to identify promoting effects by referring the reaction rate to the number of catalytic active sites:^[319]

$$TOF = \frac{rate}{catalytic\ active\ sites}$$

Phenanthrene hydrogenation follows two main paths. For each of them a formation rate of the products can be given by calculating the yield of the individual products and treating it the same way as described above, with the conversion, X , being exchanged by the yield, Y . The yield is defined as the amount of product produced, \dot{n}_p , normalized to the maximum possible (amount of reactant), \dot{n}_i , weighted by stoichiometric factors:

$$Y_{p,i} = \frac{v_i}{v_p} \cdot \frac{\dot{n}_{p,0} - \dot{n}_{p,t}}{\dot{n}_{i,0}}$$

The sum of all product yields equals the conversion of the reactant.

Another important measure for analyzing reaction networks is the selectivity, S . It is defined as the fraction of one product out of all products (or amount of reactant converted):

$$S_{p,i} = \frac{v_i}{v_p} \cdot \frac{\dot{n}_{p,0} - \dot{n}_{p,t}}{\dot{n}_{i,0} - \dot{n}_{i,t}} = \frac{Y_{p,i}}{X_i}$$

For deeper network analysis the so-called delplot ('del' for university of Delaware?) technique was established.^[320] It allows to separate secondary from primary products based on ranked delplots with respect to the reaction order. In this work first and second rank delplots were investigated and an example is given below.

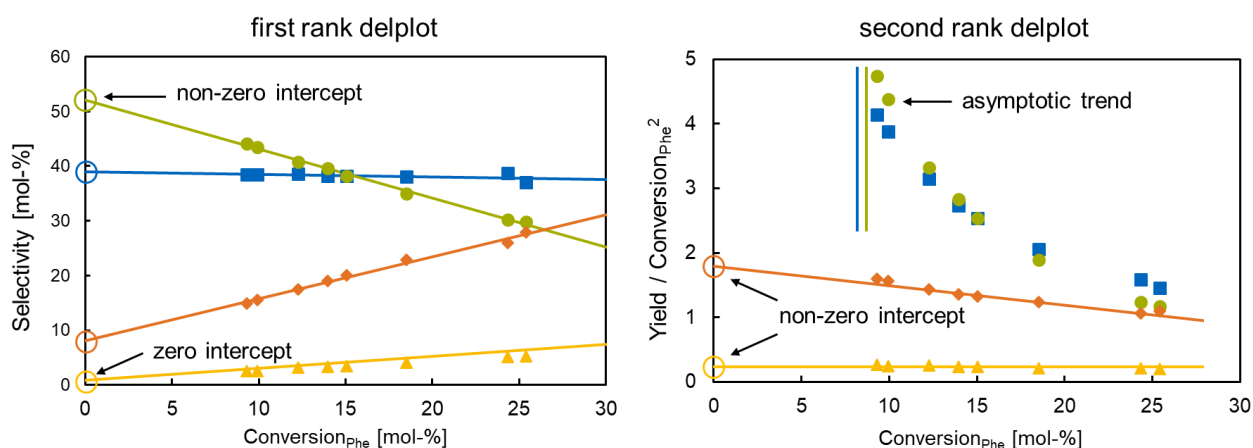


Figure 3-11. Example for delplot analysis. On the left: First rank delplot showing $Y/X = S$ vs. X . Every to zero conversion extrapolated curve with a non-zero intercept represents a primary product. In this case the blue and green products are clearly of primary nature while the yellow product is not. In the case of the orange product the case lies not that clear and selectivities at lower conversion levels should be measured. To help the situation a second rank delplot for the same experiment is shown on the right: On the ordinate Y/X^2 is given. Here an asymptotic behavior represents a primary product while positive intercepts with the ordinate speak for secondary product. In conclusion the yellow and orange products show a secondary nature.

3.2 Secondary measures – reaction order and activation energy

In heterogeneous catalysis reactants interact with the solids surface via adsorption before reaction. The dependency of the reaction rate is described by the amount adsorbed, the surface coverage. In general, the microkinetic rate equation (as power law) respects the concentration dependency of the rate with the reaction order, n .

$$r = k \cdot c_1^{n_1} \cdot c_2^{n_2} = k \cdot p_1^{n_1} \cdot p_2^{n_2}$$

For ideal systems the concentration of a compound can be expressed as its partial pressure, p_i . By changing the reactant concentration and measuring the resulting rate the reaction order with respect to the changed compound (the second reactant concentration should be kept constant) is determined by linearization of the power law rate equation:

$$\ln r = \ln k + n_1 \cdot \ln p_1 + n_2 \cdot \ln p_2$$

The reaction order of the changed compound is the slope of a line in a logarithmic plot rate vs concentration. The reaction order can be directly related to the surface coverage or even fundamental reaction step. Here, the simplest derivation of the rate-reaction-coverage dependency is presented to show the mathematical strategy:

The reaction



proceeds via a Langmuir type adsorption followed by a surface reaction being the rate determining step. The rate equation can be written as

$$r = \frac{k \cdot K_A \cdot p_A}{1 + K_A \cdot p_A}$$

The reaction order is the rate's exponential dependency of the partial pressure, therefore

$$n_A = \frac{\partial \ln(r)}{\partial \ln(p_A)} = \frac{\partial \ln\left(\frac{kK_A p_A}{1 + K_A p_A}\right)}{\partial \ln(p_A)}$$

Extending the quotient with ∂p_A and eliminating all terms not related to the partial pressure of A results in

$$\begin{aligned} n_A &= \frac{\frac{\partial \ln(r)}{\partial p_A}}{\frac{\partial \ln p_A}{\partial p_A}} = \frac{\frac{\partial \ln(kK_A)}{\partial p_A} + \frac{\partial \ln\left(\frac{p_A}{1 + K_A p_A}\right)}{\partial p_A}}{\frac{1}{p_A}} \\ &= p_A \cdot \frac{(1 + K_A p_A)}{p_A} \left[0 + \frac{1 \cdot (1 + K_A p_A) - p_A \cdot K_A}{(1 + K_A p_A)^2} \right] = 1 - \frac{K_A p_A}{1 + K_A p_A} \end{aligned}$$

With the Langmuir adsorption isotherm for the coverage of reactant A, θ_A ,

$$\theta_A = \frac{p_A K_A}{1 + p_A K_A}$$

the formalism for the reaction order is:

$$n_A = 1 - \theta_A$$

This correlation shows that for a reaction following a Langmuir type mechanism a reaction order between 1 and 0 can be measured (because of the definition of the coverage θ_A as the amount

adsorbed normalized to the maximum possible, the active centers ranging from 0 to 1). Hence, at low coverages the rate is under limitation of the concentration of the reactants, giving a first order dependency and at the other end of the scale at full coverage a further change in concentration does not influence the overall rate, so a zero order is measured. By formulating individual rate equations for different surface reaction steps in complicated mechanisms the range of reaction order for each individual compounds can be determined by applying the above mathematical treatment.

A catalyst reduces the activation energy, E_A , of a chemical reaction by influencing the energetic barrier of its rate determining step. The relation between reaction speed and the activation energy was formulated by Svante Arrhenius:

$$k = k_0 \cdot e^{-E_A/RT}$$

The reaction rate constant, k , as a factor in the rate equation describes the temperature dependency of the reaction rate in an exponential law. Hence, the activation energy can be measured by varying the reaction temperature and determining the rate. By transforming the Arrhenius equation into a logarithmic form the Arrhenius plot is created.

$$\ln k = \ln k_0 - \frac{1}{T} \cdot \frac{E_A}{R}$$

Alternatively, the rate equation is tried:

$$\ln r = \ln k_0 - \frac{1}{T} \cdot \frac{E_A}{R} + n_1 \cdot \ln p_1 + n_2 \cdot \ln p_2$$

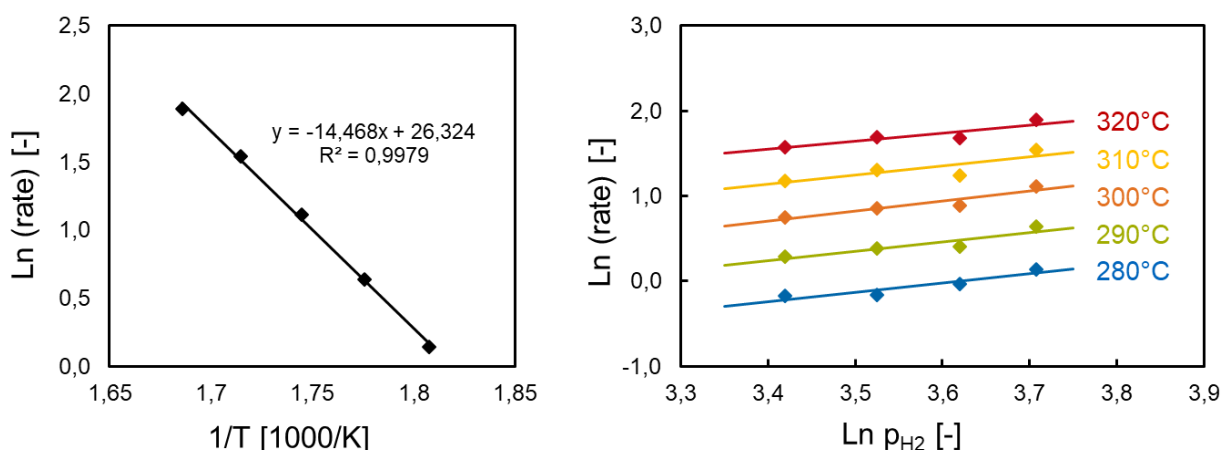


Figure 3-12. Examples for determining activation energy and reaction order experimentally. On the left Arrhenius-type plot created with 5 rates measured at 5 temperatures. The slope multiplied with the universal gas constant, R , gives the activation energy. $E_A = -\text{slope} \cdot R = 14.468 \cdot 8.314 \frac{\text{kJ}}{\text{mol}} = 120 \frac{\text{kJ}}{\text{mol}}$. On the right, the partial pressure of hydrogen was varied and the corresponding rates are plotted in a logarithmic form at 5 temperatures. The slope of the lines represent the reaction order in hydrogen, $n_{H_2} \approx 1$.

Knowing the activation energy of a reaction, the rate constants, k , can be estimated by intra- or extrapolation to another temperature under the assumption of no change in the rate determining step:

$$\frac{k_1(T_1)}{k_2(T_2)} = \frac{k_0}{k_0} \cdot \exp \left[\frac{-E_A}{R} \cdot \left(\frac{1}{T_1} - \frac{1}{T_2} \right) \right]$$

A very important tool for estimating rate constant comes with *transition-state-theory*.^[321-323] The assumption behind is, that molecules which react are in a quasi-equilibrium with an activated complex. This complex is the active species in transition (transition state ‘≠’) between reactants and products. According to this theory, the reaction rate constant is estimated by:

$$k_i = \frac{k_B T}{h} \cdot \exp \left(-\frac{\Delta G_i^\ddagger}{RT} \right) = \frac{k_B T}{h} \cdot \exp \left(\frac{\Delta S_i^\ddagger}{R} - \frac{\Delta H_i^\ddagger}{RT} \right)$$

3.3 Reaction kinetics experimental

Hereinafter, the reaction set-up as well as a detailed description of the phenanthrene hydrogenation reaction are presented.

3.3.1 Reaction set-up

The hydrogenation unit was planned and constructed in house in a scale suitable for microkinetic reaction studies. Designed for typical hydrotreatment applications, the set-up allowed pumping liquid feed out of a 1 L glass bottle with the help of a HPLC pump (flow range used: 0.05 to 0.5 mL min⁻¹). This feed was mixed with a gas stream before entering the tube reactor. The gases attached were hydrogen and nitrogen (80 bar pre-pressure) and dihydrogen sulfide (25 bar pre-pressure) and controlled by mass flow controllers (MFC, Wagner) up to a maximum volumetric flow of 200 mL min⁻¹. The reactants got in contact in a 1/16 inch tube so that a plug flow behavior was established. After mixing, the reactants were introduced into a stainless steel tube reactor sitting in a heating jacket.

The tube reactor (stainless steel tube coated with glass inside, inner diameter 4 mm, length 27 cm, brass heating coat of 17.5 cm) was packed with SiC and TMS catalyst the following way. Little amount of quartz wool was coiled up to block the bottom outlet of the tube loosely. Then, SiC (150-250 μm) was filled in from the top using a funnel until the cold part of the tube (when the heating coat begins) was packed. On top of this SiC (60-90 μm) was filled until the isothermal zone was reached (~15 cm from the top). The catalyst was shaped to 250-355 μm by pressing it to pellets (on Kapton® tape the smear effect of the sulfide is limited) and fractionated using a sieve tower. Then the catalyst was mixed in a 1 / 20 ratio with SiC (60-90 μm) and filled into the reactor.

Following to that, the reactor tube was filled with SiC (60-90 μm) until the end of the heated zone was reached and topped with SiC (150-250 μm). A small amount of quartz wool was coiled up to close the reactor.

After the reactor, a backpressure regulator (homemade) was placed and pressurized with nitrogen up to 60 bar. Then the reaction mixture was led into a washing system for acidic gases (two containers; one for collecting liquid, another filled with conc. NaOH solution) or switched to a 16-port valve with sampling vials (1.5 mL GC-vials) screwed in. Samples were taken automatically in defined time intervals, capped manually and analyzed in a GC system.

3.3.2 Experimental procedure

Phenanthrene hydrogenation was conducted in the trickle bed reactor system. Initial rates were measured at varying space times in a linear conversion-space time plot. For that the feed containing phenanthrene (reactant), tetradecane (internal standard), dimethyl disulfide (as S source) and decalin (solvent) was prepared in the following way. First, decalin (~916 g) was given into a 1 L glass bottle (brown, borosilicate, to prevent exposure to visible light) and tetradecane (~18.9 g, 2 wt.%) was dissolved. Then, phenanthrene (~9.45 g powder, 1 wt.%, low solubility in decalin!) was weight out in a plastic boat and filled into the decalin bottle. The system was ultra-sonicated (degassing and dissolution) until no phenanthrene particles were observed (hour time span). Before starting the reaction dimethyl disulfide (~1.311 mL, 1.39 g, 1.47 wt.% corresponds to 1000 ppmw S) was added using a 1000 μL Eppendorf pipette and the bottle was shaken for short time. Throughout this study the feed was prepared the way described. Small changes were made when the reaction order of phenanthrene (0.6 wt.%, 0.8 wt.% and 1.2 wt.%) was determined and for titration experiments where a titrant and another inert molecule as tracer were added.

Reaction gases used (H_2 , H_2S and N_2) were not further purified and used as delivered. A standard rate was measured at 300°C and 60 bar total pressure. The total gas flow to hydrocarbon liquid flow (complete feed) was set to 300 (v/v). For measuring the reaction order in hydrogen the total H_2 stream was lowered to 100 vol-%, 91.7 vol-%, 83.3 vol-% and 75.0 vol-% and filled up with N_2 (constant gas/HC ratio!) to obtain 5 bar steps concentration decrease. Typical flow rates were 0.1–0.5 mL min^{-1} (liquid) and 30–150 mL min^{-1} (gas) and space time varied between 5 and 140 $\text{g}_{\text{cat}} \text{h mol}_{\text{Phe},0}^{-1}$.

In order to simplify the calculation of partial pressures ideal gases were assumed for Phe and H_2 . Additionally, the decalin density of 880 g l^{-1} and molar mass of 138.25 g mol^{-1} are taken as averaged density and molar mass of the feed because of the low concentration of other compounds. The mass flow controllers are calibrated under standard conditions so that the molar gas density is calculated as:

$$V_m = \frac{RT_{std}}{p_{std}} = \frac{8.314 \frac{\text{J}}{\text{mol K}} \cdot 298.15 \text{ K}}{1.013 \cdot 10^5 \text{ Pa}} = 24.47 \frac{\text{l}}{\text{mol}}$$

For ideal substances the partial pressure is:

$$p_i = y_i \cdot p_{total}$$

And the molar fraction is:

$$y_i = \frac{\dot{n}_i}{\dot{n}_{total}}$$

For all gases in the system the molar flow is calculated via the ideal gas law:

$$pV = nRT \rightarrow \dot{n}_G = \frac{p_{std}}{RT_{std}} \cdot \dot{V}_G = \frac{\dot{V}_G}{V_m}$$

Individual gases are corrected by their concentration x_i :

$$\dot{n}_{i,G} = \dot{n}_G \cdot x_i = \frac{\dot{V}_G}{V_m} \cdot x_i$$

For all liquid hydrocarbons in the system, the following equations apply:

$$\dot{n}_L = \frac{\bar{Q}_L}{\bar{M}_L} \cdot \dot{V}_L$$

$$\dot{n}_{i,L} = \frac{w_i}{M_i} \cdot \bar{Q}_L \cdot \dot{V}_L$$

With this the total molar flow of the system is calculated and written as a function of total gas or liquid volumetric flow (with the ratio v of gas and liquid volume $\dot{V}_G = v \cdot \dot{V}_L$):

$$\dot{n}_{total} = \dot{n}_G + \dot{n}_L = \frac{\dot{V}_G}{V_m} + \frac{\bar{Q}_L}{\bar{M}_L} \cdot \dot{V}_L$$

For gases the molar fraction, $y_{i,g}$, for all gaseous compounds is calculated:

$$y_{i,g} = \frac{\dot{n}_{i,g}}{\dot{n}_{total}} = \frac{\dot{V}_G}{V_m} \cdot x_{i,g} \cdot \left[\dot{V}_G \cdot \left(\frac{1}{V_m} + \frac{\bar{Q}_L}{\bar{M}_L v} \right) \right]^{-1} = x_{i,g} \cdot \left[1 + \frac{V_m \bar{Q}_L}{\bar{M}_L v} \right]^{-1}$$

$$= x_{i,g} \cdot \left[1 + \frac{22.47 \frac{l}{mol} \cdot 880 \frac{g}{l}}{138.25 \frac{g}{mol} \cdot 300} \right]^{-1} = \frac{x_{i,g}}{1.476}$$

For liquids, the molar fraction, $y_{i,l}$, for all compounds in the liquid feed is calculated:

$$y_{i,l} = \frac{\dot{n}_{i,l}}{\dot{n}_{total}} = \frac{w_i}{M_i} \bar{Q}_L \dot{V}_L \cdot \left[\dot{V}_L \left(\frac{v}{V_m} + \frac{\bar{Q}_L}{\bar{M}_L} \right) \right]^{-1} = \frac{w_i}{M_i} \cdot \left[\frac{v}{V_m \bar{Q}_L} + \frac{1}{\bar{M}_L} \right]^{-1}$$

$$= \frac{w_i}{M_i} \cdot \left[\frac{300}{22.47 \frac{l}{mol} \cdot 880 \frac{g}{l}} + \frac{1}{138.25 \frac{g}{mol}} \right]^{-1} = w_i \cdot \frac{44.63 \frac{g}{mol}}{M_i}$$

With these formulas the molar fraction and partial pressures at 60 bar of all compounds can be calculated. Table 3-3 summarized values obtained according to above demonstrated calculations for a standard reaction rate measurement.

Table 3-3. Molar fraction and partial pressure of compounds for a standard reaction rate measurement at 300°C and 60 bar total pressure. Feed composition: 1 wt.% Phe, 2 wt.% TD and 0.14 wt.% DMDS (=1000 ppmw S) in decalin. Volumetric flow rate of H₂ / hydrocarbon feed = 300.

	Phe	TD	Dec	H ₂ S*	H ₂
$y_i[-]$	0.0025	0.0045	0.3131	0.00066	0.6772
$p_i[bar]$	0.15	0.27	18.79	0.04	40.63

*Under the assumption that DMDS is fully decomposed into H₂S.

3.4 H₂-D₂ scrambling

In literature H₂-D₂ scrambling or H₂-D₂ equilibration, which describes the plain exchange reaction of H₂ and D₂ to HD without aromatic structures present, is applied in studies dealing with H₂ activation on TMS catalysts sometimes combined with DFT studies to model active surface species. Main findings were that H₂ and H₂S exchange on the same Lewis acid sites and associated S atoms and therefore compete about adsorption on them. Further, it was suggested that hydrogen can be activated on cobalt sulfide or the catalyst support and spills over to the active TMS slab. Usually the reaction order for hydrogen measured indicates the rate limiting step for H₂ splitting at a specific active sites.^[82,216,324–326]

In this work H₂-D₂ scrambling was used to study the hydrogen activation capability of NiMo(W)S₂ catalysts and to estimate the adsorption rate constant on NiMoWS. The experiments were conducted in the TPS set-up. In the following a detailed experimental protocol and data analysis is given followed by the presentation and derivation of the formula used for an estimation of the adsorption constant of H₂.

3.4.1 Experimental and data analysis

Typically, 100 mg of sulfided catalyst were placed in the middle of a quartz tube reactor (4 mm inner diameter, 250 mm length) and hold in place with glass wool. The reactor was placed horizontal in a furnace (Horst, 5 cm isothermal zone) and attached to the gas supply system. The standard HD-formation rate was determined by varying the space time changing the total volumetric flow from 18 to 6 mL min⁻¹ at a constant gas stream of 16.67 vol-% H₂ and 16.67 vol-% D₂ in nitrogen in a temperature range between 50 and 110°C. The system was allowed to equilibrate for at least 30 minutes after each change of conditions. All gases were monitored by MS in a constant flow.

For the evaluation of the data the HD signal was normalized to the N₂ signal in order to correct for fluctuations. Figure 3-13 (left) shows the result of a typical experiment on NiMoS(L) at 100°C for 5 different space times. The horizontal level at steady state is taken to calculate the concentration of HD (see below).

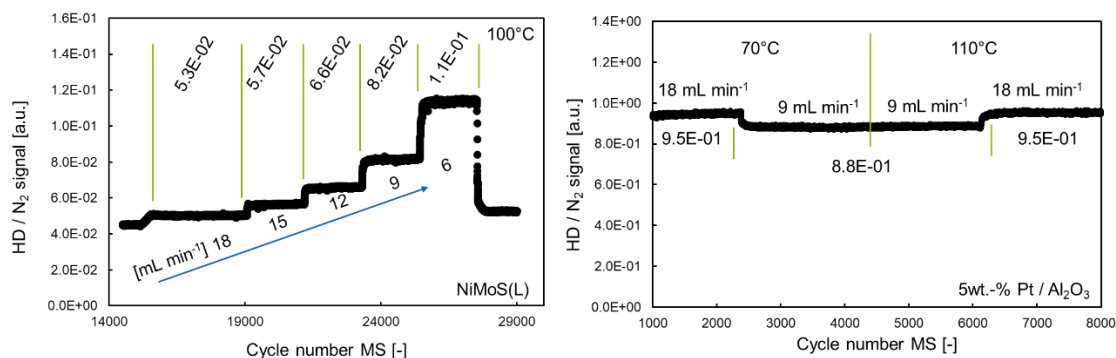


Figure 3-13. MS signals of a typical scrambling experiment at the example of NiMoS(L) (left) and on 5 wt.-% Pt on Al₂O₃ (right). The scale difference is about a factor of 10 from kinetic measurement to thermodynamic equilibrium, which allows to call the measured rate for HD of initial nature.

In order to quantify the HD concentration in the effluent stream it was calibrated via the thermodynamic equilibrium of the H₂-D₂ scrambling reaction. For this, 100 mg of 5 wt.-% Pt on Al₂O₃ (Sigma) were loaded into the same setup and the scrambling protocol was examined. In Figure 3-13 (right) the calibration of the HD signal is demonstrated. First, it can be seen that the temperature has no effect on the HD intensity which is directly linked to the fact that the catalyst established the equilibrium of the H₂-D₂ scrambling reaction. Second, the ratio of HD to N₂ is a factor of at least 8 higher than measured during the scrambling experiments on the Ni promoted MoS₂ catalyst. This is important to state that in the latter case the reaction is far from equilibrium and forward rates of H₂-D₂ scrambling were measured. Last, the change in volumetric flow caused a change in the steady state signal. This might be due to a pressure drop in the reactor, but could be calibrated out.

With this information a calibration line connecting the HD / N₂ signal to the HD concentration was determined. The equilibrium concentration of the reaction H₂+D₂→2HD is given by the following equation:^[327,328]

$$\log K_{eq} = -\left(155/4.57 \cdot \frac{T}{[K]}\right) + 0.6276$$

The equilibrium constant is defined as the ratio of the products to the reactants in equilibrium weighted with the exponent of their stoichiometric numbers. Hence, for the H₂-D₂ scrambling it follows (note that in equilibrium the concentration of H₂ and D₂ are identical):

$$K_{eq} = \frac{[HD]^2}{[H_2] \cdot [D_2]} = \frac{[HD]^2}{[H_2]^2}$$

The equilibrium concentration of HD, χ_{HD} , is defined as:

$$\chi_{HD} = \frac{[HD]}{[HD] + [D_2] + [H_2]} = \frac{[HD]}{[HD] + 2[H_2]} = \left(1 + 2 \frac{[H_2]}{[HD]}\right)^{-1}$$

And with $[H_2]/[HD] = 1/\sqrt{K_{eq}}$:

$$\chi_{HD} = \frac{\sqrt{K_{eq}}}{2 + \sqrt{K_{eq}}}$$

For the given example on NiMoS(L) at 100°C the equilibrium concentration is:

$$\chi_{HD,100^\circ C} = \frac{\sqrt{3.46}}{2 + \sqrt{3.46}} = 0.482 \frac{mol}{mol}$$

The concentration of HD for each steady state point of the scrambling experiment on NiMoS(L) can be calculated via:

$$\chi_{HD,100^\circ C, NiMoS(L)} = \frac{\frac{HD_{signal}}{N_{2,signal_{NiMoS(L)}}}}{\frac{HD_{signal}}{N_{2,signal_{Pt,100^\circ C}}}}$$

With this, an initial rate using the five space time points shown in Figure 3-13 can be calculated.

3.4.2 Derivation of equation for determining K_{ads}

One potential of H₂-D₂ scrambling experiments is to measure the adsorption constant for H₂ under ambient pressure and moderate temperatures. In order to do so, some basic equations are tried to achieve one formulation for fitting experimental data.

First the rate equations for H₂ and D₂ adsorption and desorption as well as the desorption of their product, HD, are formulated. The Greek symbols, α , β and γ , are parameters representing a kinetic isotope effect.

Adsorption

$$r_{H_2,ads} = p_{H_2} \cdot \theta_*^2 \cdot k_{ads}$$

$$r_{D_2,ads} = p_{D_2} \cdot \theta_*^2 \cdot k_{ads} \cdot \alpha$$

Desorption

$$r_{H_2,des} = \theta_{H_2}^2 \cdot k_{des}$$

$$r_{D_2,des} = \theta_{D_2}^2 \cdot k_{des} \cdot \gamma$$

$$r_{HD,des} = \theta_D \cdot \theta_H \cdot k_{des} \cdot \beta$$

Next, the mass balances in steady state for H and D are denoted:

$$p_{H_2} \cdot \theta_*^2 \cdot k_{ads} = \theta_D \cdot \theta_H \cdot k_{des} \cdot \beta + \theta_H^2 \cdot k_{des} \quad (I)$$

$$p_{D_2} \cdot \theta_*^2 \cdot k_{ads} \cdot \alpha = \theta_D \cdot \theta_H \cdot k_{des} \cdot \beta + \theta_D^2 \cdot k_{des} \cdot \gamma \quad (II)$$

Adding up (I) and (II) results in:

$$(p_{H_2} + \alpha \cdot p_{D_2}) \cdot \theta_*^2 \cdot k_{ads} = 2 \cdot \theta_D \cdot \theta_H \cdot k_{des} \cdot \beta + \theta_D^2 \cdot k_{des} \cdot \gamma + \theta_H^2 \cdot k_{des}$$

Under the assumption $\gamma \sim \beta^2$ (approximated by results and discussion published by Lercher *et al.*^[329]) the equation reduces to:

$$(p_{H_2} + \alpha \cdot p_{D_2}) \cdot \theta_*^2 \cdot k_{ads} = k_{des} \cdot (\theta_H + \beta \cdot \theta_D)^2$$

And with $K_{ads} = \frac{k_{ads}}{k_{des}}$ it follows:

$$\frac{\theta_H + \beta \cdot \theta_D}{\theta_*} = \sqrt{K_{ads} \cdot (p_{H_2} + \alpha \cdot p_{D_2})} \quad (III)$$

Under steady state the coverages of H and D are formulated via their equilibrium adsorption:

$$H_2 + 2 * \leftrightarrow 2H_* \quad \rightarrow \quad K_H = \frac{\theta_H^2}{p_{H_2} \cdot \theta_*^2}$$

$$D_2 + 2 * \leftrightarrow 2D_* \quad \rightarrow \quad K_D = K_H \cdot \frac{\alpha}{\gamma} = \frac{\theta_D^2}{p_{D_2} \cdot \theta_*^2}$$

$$H_2 + 2 \theta_D \leftrightarrow 2 \theta_H + D_2 \quad \rightarrow \quad K = \frac{K_H}{K_D} = \frac{\gamma}{\alpha} = \frac{\theta_H^2 \cdot p_{D_2}}{p_{H_2} \cdot \theta_D^2}$$

$$\frac{\theta_H}{\theta_D} = \sqrt{\frac{p_{H_2} \cdot \beta^2}{p_{D_2} \cdot \alpha}} \quad \rightarrow \quad \theta_H = \theta_D \cdot \sqrt{\frac{p_{H_2} \cdot \beta^2}{p_{D_2} \cdot \alpha}}$$

Site balance

$$\theta_* = 1 - \theta_H - \theta_D = 1 - \theta_D \cdot \left(\sqrt{\frac{p_{H_2} \cdot \beta^2}{p_{D_2} \cdot \alpha}} + 1 \right)$$

The coverages are included into equation (III):

$$\frac{\left(\sqrt{\frac{p_{H_2} \cdot \beta^2}{p_{D_2} \cdot \alpha}} + \beta\right) \cdot \theta_D}{1 - \theta_D \left(\sqrt{\frac{p_{H_2} \cdot \beta^2}{p_{D_2} \cdot \alpha}} + 1\right)} = \sqrt{K_{ads}} \cdot \sqrt{p_{H_2} + \alpha \cdot p_{D_2}}$$

$$\left(\sqrt{K_{ads}} \cdot \sqrt{p_{H_2} + \alpha \cdot p_{D_2}}\right)^{-1} = \frac{1}{\left(\sqrt{\frac{p_{H_2} \cdot \beta^2}{p_{D_2} \cdot \alpha}} + \beta\right) \cdot \theta_D} - \frac{\sqrt{\frac{p_{H_2} \cdot \beta^2}{p_{D_2} \cdot \alpha} + 1}}{\sqrt{\frac{p_{H_2} \cdot \beta^2}{p_{D_2} \cdot \alpha}} + \beta} \quad (\text{IV})$$

$$P = \frac{\sqrt{\frac{p_{H_2} \cdot \beta^2}{p_{D_2} \cdot \alpha}} + 1}{\sqrt{\frac{p_{H_2} \cdot \beta^2}{p_{D_2} \cdot \alpha}} + \beta}$$

During the scrambling experiment the HD-formation rate is determined. Hence, the rate equation for HD formation is used to express the surface coverage of deuterium, θ_D :

$$r_{HD} = 2k_{des} \cdot \beta \cdot \theta_D \cdot \theta_H$$

$$r_{HD} = 2k_{des} \cdot \beta \cdot \theta_D^2 \cdot \sqrt{\frac{p_{H_2} \cdot \beta^2}{p_{D_2} \cdot \alpha}} \quad \rightarrow \quad \frac{1}{\theta_D} = \sqrt{\frac{2k_{des} \cdot \beta}{r_{HD}}} \cdot \sqrt[4]{\frac{p_{H_2} \cdot \beta^2}{p_{D_2} \cdot \alpha}}$$

With this (IV) turns into the final equation:

$$\frac{\sqrt{\frac{2k_{des} \cdot \beta}{r_{HD}}} \cdot \sqrt[4]{\frac{p_{H_2} \cdot \beta^2}{p_{D_2} \cdot \alpha}}}{\left(\sqrt{\frac{p_{H_2} \cdot \beta^2}{p_{D_2} \cdot \alpha}} + \beta\right)} = \frac{\sqrt{k_{des}}}{\sqrt{k_{ads}}} \cdot \left(\sqrt{p_{H_2} + \alpha \cdot p_{D_2}}\right)^{-1} + P$$

Which is with separated adsorption and desorption rate constants:

$$\frac{1}{\sqrt{r_{HD}}} \cdot \frac{\sqrt{2\beta} \cdot \sqrt[4]{\frac{p_{H_2} \cdot \beta^2}{p_{D_2} \cdot \alpha}}}{\left(\sqrt{\frac{p_{H_2} \cdot \beta^2}{p_{D_2} \cdot \alpha}} + \beta\right)} = \frac{1}{\sqrt{k_{ads}}} \cdot \left(\sqrt{p_{H_2} + \alpha \cdot p_{D_2}}\right)^{-1} + \frac{P}{\sqrt{k_{des}}}$$

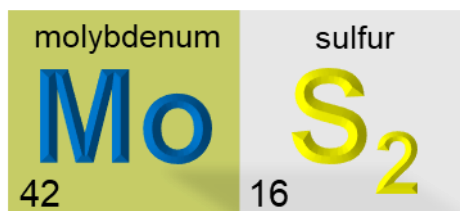
For given kinetic isotope factors α and β , the left hand side of the equation is determined by a measured HD-formation rate at set partial pressures of deuterium and hydrogen. The right hand side could be fitted to the experimental data to determine adsorption and desorption rate constants of hydrogen.

Chapter 4

Comparison of Ni promoted Mo and W sulfides in HDA

“Why using MoS₂, you ask? Well,

‘Sulfur – Part of the ‘tria prima’, sal, sulphur and mercury; the essential elements of Paracelsus’ medicine doctrine.’



*‘The answer to the ultimate question of life, the universe and everything is 42.’
from ‘The Hitchhiker’s Guide to the Galaxy’, Douglas Adams, 1979.’*

Heard at the MACSVIII (Molecular Aspects in Catalysis of Sulfides) conference, 2019 in Cabourg, France.

1 Preface

Transition metal catalysis is a complex and challenging field to investigate because of the many unique concepts and methods applied in science and industry. Hence, it is a must for each researcher to get familiar with the particular topics of precursor synthesis, sulfidation methods and protocols and finally the demanding kinetic reaction investigation.

However, this chapter is designed for presenting some aspects of the Ni-promoted Mo(W) sulfides and phenanthrene hydrogenation catalyzed thereof. It mainly deals with catalysts obtained by the conventional route of precipitation of metal salts and sequential sulfidation. First, the focus is placed on the in-house developed ‘leaching’ method, i.e., a post-synthetic treatment with HCl, and demonstrates rate improvement by this method. Additionally, a short statement on the application of organo-acids for leaching is given. A very important task for catalysis research in general, and of great interest in particular for bulk TMS catalysts, is the determination and quantification of active sites that catalyze the hydrogenation reaction. Therefore, a method is presented to estimate sulfhydryl groups located at the edges of the Mo(W)S₂ slabs in order to calculate turnover frequencies (TOFs). This is done by comparing the hydrogen activation ability of bulk TMS against a supported catalyst formulation with known SH-concentration.

After that, key aspects of the hydrogenation reaction are discussed. A brief investigation of the pathways of phenanthrene hydrogenation on the in-house synthesized catalysts is presented, followed by a preliminary attempt to calculate adsorption constants of H₂ on a trimetallic NiMoWS₂ catalyst via H₂-D₂-scrambling experiments. Finally, alternative protocols for precursor synthesis and sulfidation are suggested.

2 Experimental

2.1 Characterization of bulk NiMo(W) sulfides

For the following aspects of TMS catalysis some standard characterization techniques (see chapter 3) were applied, namely elemental analysis, X-ray diffraction, and SEM and TEM imaging. Combining the data of BET surface area, NO uptake by volumetric pulsing and H₂-D₂ scrambling, a geometric estimate for the active site density was obtained for the TMS catalysts.

2.2 Synthesis and characterization of bulk NiMoW sulfides

Parent catalysts

NiMoS, NiWS and NiMoWS formulations were synthesized by co-precipitation (see chapter 3, 1.1). The ammonium heptamolybdate and metatungstate salts were dissolved in 120 mL, nickel nitrate hexahydrate in 7.5 mL and the maleic acid in 90 mL of deionized water.

Table 4-1. Net weight of Ni, Mo and W oxide salts for the synthesis of oxidic TMS precursors.

	Ni(NO ₃) ₂ ·6H ₂ O	(NH ₄) ₆ Mo ₇ O ₂₄ ·4H ₂ O	(NH ₄) ₆ W ₁₂ O ₄₀ H ₂ ·H ₂ O	C ₄ H ₄ O ₄
NiMoO _x	8.7323	5.7374		0.5250
NiWO _x	8.7156		8.3001	0.5233
NiMoWO _x	8.7342	2.6488	3.7003	0.5275

The oxidic precursors were sulfided in-situ in liquid phase. Typically, 300 mg of powder were mixed with SiC (500–1000 mg; 1 / 5) and loaded into the tubular reactor. The sulfidation protocol was a multistep process and conducted in liquid phase using dimethyl disulfide as sulfiding agent. The H₂ to sulfur ratio was fixed to 10 for each individual sulfidation step. After sulfidation, the reactor was flushed with toluene (0.3 mL min⁻¹) for 4 hours, then with hexane (0.3 mL min⁻¹) for another 4 hours and finally dried in a N₂ flow. Finally, the catalyst was separated from SiC by sieving. The industrial catalyst was sulfided with an optimized sulfidation procedure as presented in Figure 4-4 and discussed later, but the washing protocol remained the same.

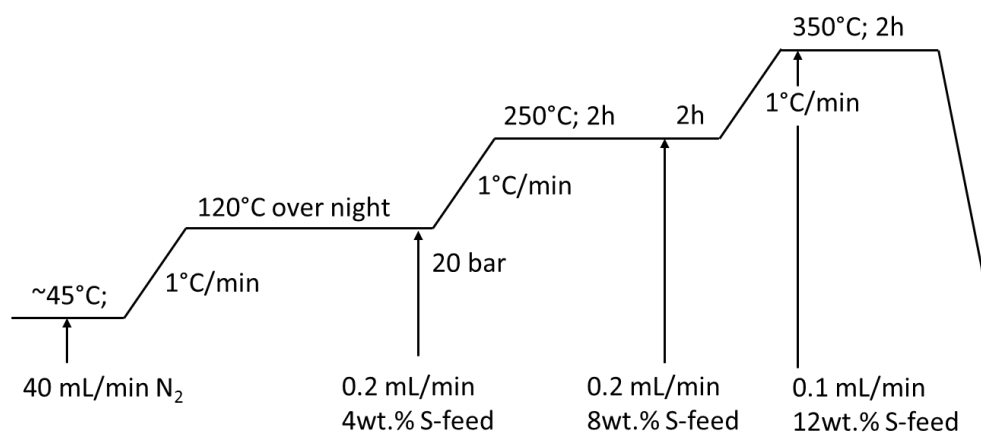


Figure 4-1. Sulfidation protocol for transition metal mixed oxides in liquid phase. The sulfur for 3 individual feeds was added as dimethyl disulfide. During the complete procedure the H_2 / S ratio was kept constant at 10 mol mol^{-1} .

Leached catalysts

A key step toward forming an active TMS catalyst is the removal of inactive matter for catalytic hydrogenation. Hence, the so-called ‘leaching’ procedure was applied to the ‘parent’ sulfides. Here, the protocol was different (see also previous publication of the group)^[330] to the one described in chapter 3 and applied for the study in chapter 5. Mainly, the temperature (80°C vs. R.T.) and the leaching time respectively the iteration (10 vs. 3) was differed. For this treatment, 130 mg of NiMo(W)S were boiled at 80°C in 3 mL concentrated HCl in a 5 mL glass vial. After 10 minutes, the catalyst particles were allowed to settle and the green supernatant was removed and the HCl replenished. This procedure was repeated until no green color was observed (ca. 9-10 times). Then the catalyst was washed with deionized water for at least 3 times and dried in dynamic vacuum in a desiccator.

2.3 H_2 - D_2 scrambling

Hydrogen activation on the TMS catalysts was followed by the HD-formation rate for comparison of bimetallic NiMoS and NiWS as well as the trimetallic NiMoWS and industrial catalyst. The HD-formation rate was determined as described in chapter 3.

Additional to that, an experiment used to obtain the adsorption rate constant of H_2 on TMS catalyst was designed. Figure 4-2 shows the related equation. The experiment was carried out on a sulfided trimetallic catalyst obtained by the ‘one-pot’ synthesis method (see below).

$$\frac{1}{\sqrt{r_{HD}}} \cdot \frac{\sqrt{2\beta} \cdot \sqrt[4]{\frac{p_{H_2}}{p_{D_2}} \cdot \frac{\beta^2}{\alpha}}}{\left(\sqrt{\frac{p_{H_2}}{p_{D_2}} \cdot \frac{\beta^2}{\alpha}} + \beta\right)} = \frac{1}{\sqrt{k_{ads}}} \cdot \left(\sqrt{p_{H_2} + \alpha \cdot p_{D_2}}\right)^{-1} + \frac{P}{\sqrt{k_{des}}}$$

↑ ↑ ↑ ↑ ↑ ↑ ↑ ↑

Measure HD-formation rate guess factors for KIE vary partial pressure of H₂ and D₂ in the scrambling experiment fit adsorption / desorption rate constants with the method of least squares

Figure 4-2. Equation on which the H₂-D₂-scrambling experiment was designed as derived in chapter 3. On the left-hand side of the equation, parameters which were either set or guessed in the experiment and the corresponding measured rate are found. On the right-hand side, the adsorption and desorption rate constant to be fitted are pictured.

According to this equation, the partial pressures of H₂ and D₂ were alternated with holding the H₂ pressure constant at three different values, 0.13, 0.20 and 0.20 bar. Deuterium was added in ratios of H₂/D₂ of 0.7, 1.0, 1.5, 2.0 and 3.0 while N₂ was added as a diluent gas. The total pressure was 1 bar. Initial rates of HD-formation were measured as described in chapter 3 at varying space times of H₂ and D₂. The total volumetric flow rates were between 3 and 25 mL min⁻¹ on 110 mg of catalyst at 80°C. After collecting all HD-formation rates the Excel® solver was used to fit the above equation with the method of least squares.

2.4 Reaction kinetics

Reaction kinetic studies were performed as described in chapter 3 for phenanthrene hydrogenation in the hydrotreatment set-up. For analyzing the reaction network, one additional experiment using dihydrophenanthrene (DiHPhe, Sigma, 94%) instead of phenanthrene as reactant was conducted. This experiment was examined the same way as described for phenanthrene. The partial pressures of hydrogen and phenanthrene were calculated according to the equations derived there.

A second set of experiments was to identify the reaction orders in hydrogen and phenanthrene as well as the activation energy for this reaction. Therefore, initial rates were determined by varying space times for 4 partial pressures of Phe (0.09 to 0.18 bar) and H₂ (30 to 40 bar) at 4 temperatures between 290 and 320°C. Nitrogen was added to the gas stream to keep a constant gas flow to liquid flow ratio of 300 v/v.

2.5 Alternative protocols

Most of the catalysts studied in this thesis were synthesized, sulfided and leached as described in chapter 3. However, some protocols were revised or designed in order to improve or simplify the experiments. Here, an alternative way to synthesize the oxidic precursors of the TMS catalysts, an optimized sulfidation protocol and a leaching variation are presented.

2.5.1 Synthesis of oxidic precursor by a 'one-pot' method

Compared to the method for precursor oxide synthesis applied above a second protocol was chosen in order to simplify and control the pH in a more proper way. The oxide salts nickel nitrate hexahydrate, $\text{Ni}(\text{NO}_3)_2 \cdot 6\text{H}_2\text{O}$, ammonium heptamolybdate tetrahydrate, $(\text{NH}_4)_6\text{Mo}_7\text{O}_{24} \cdot 4\text{H}_2\text{O}$, and ammonium metatungstate, $(\text{NH}_4)_6\text{H}_2\text{W}_{12}\text{O}_{40}$, were dissolved simultaneously in 120 mL of deionized water. Then, maleic acid (optionally oxalic acid) was added in the same stoichiometry as above. Before heating to 90°C under reflux and stirring (300 rpm) urea was giving to the solution in a urea / Ni ratio of 3. During the process the pH was measured by universal pH paper. After 22.5 h the green precipitate was filtered and washed with water and dried in air.

Component	$(\text{NH}_4)_6\text{Mo}_7\text{O}_{24} \times 4 \text{ H}_2\text{O}$	$(\text{NH}_4)_6\text{W}_{12}\text{O}_{40} \times \text{H}_2\text{O}$	$\text{Ni}(\text{NO}_3)_2 \times 6 \text{ H}_2\text{O}$	$\text{CH}_4\text{N}_2\text{O}$	$\text{C}_4\text{H}_4\text{O}_4$	H_2O	
Mass	2.67g	3.72g	8.71g	5.44g	0.52g	120 g	
Time	0	15 min	30 min	35 min	90 min	150 min	22.5 h
pH	3	3, T= 60°C	3.5, T= 85°C	3.5, T= 90°C	5.5	6	pH filtrate = 8.5

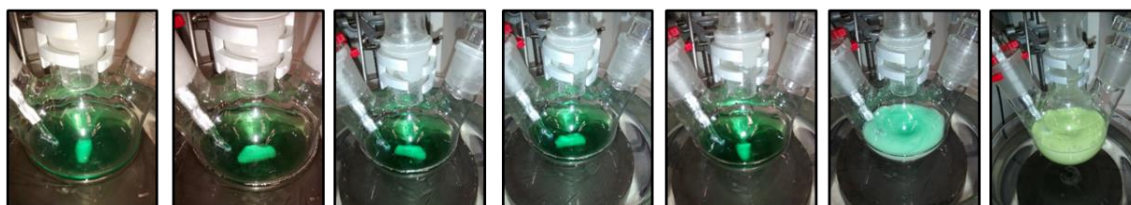


Figure 4-3. Experimental data on 'one-pot' synthesis including pictures of the suspension at different time points. The pH given was measured by taking a sample with a micro pipette and universal indicator paper.

2.5.2 Changing the sulfidation protocol

The trimetallic catalysts were sulfided in two different ways, one as described above, and the other with a higher H_2/S molar ratio and constant sulfur content in liquid phase. After a drying step in nitrogen (120°C) overnight a liquid feed of decalin containing 4 wt.% of sulfur as DMDS was introduced (0.2 mL min^{-1}) and H_2 ($123.2 \text{ mL min}^{-1}$) was added in a H_2 / S molar ratio of 25 and the pressure was increased to 20 bar. Then the temperature was increased to 250°C (1°C min^{-1} ramp) and hold for 4 hours followed by a second heating ramp (1°C min^{-1}) to 350°C and a hold time of 2 h. Finally, the reactor was allowed to cool to room temperature, the pressure was released,

the gaseous flow stopped and the catalyst was first washed with toluene (0.3 mL min^{-1}) for 3-4 hours and then with hexane for 3-4 h (0.3 mL min^{-1}) before drying in N_2 and unloading.

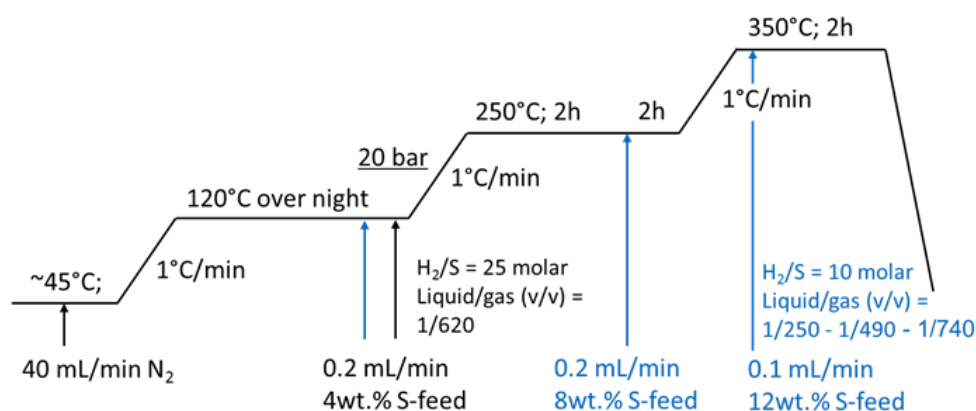


Figure 4-4. Variation of sulfidation protocol for transforming oxidic precursors to sulfide catalysts. In blue the original protocol is presented. In black changes regarding the feed S concentration (constant during complete sulfidation at a low level) and most importantly the H_2 / S ratio (25 mol mol^{-1}) are demonstrated. The temperature was not changed between both protocols.

2.5.3 Usage of organic acids for leaching

Next to the leaching protocol described above, a $\text{Ni}_{0.5}\text{MoS}_2$ catalyst prepared by the thiosalt impregnation route was treated with organic acids. Therefore, 0.1 mol L^{-1} solutions of trifluoroacetic acid (TFA, $\text{pH} = 1.73$), oxalic acid (OA, $\text{pH} = 1.76$), succinic acid (SA, $\text{pH} = 2.77$) and maleic acid (MA, $\text{pH} = 1.84$) were prepared and 100 mg of catalyst were exposed to 3 mL of the acidic solutions each for 24 h. Then the catalyst was extensively washed with water and dried in dynamic vacuum.

3 Results

In the following the results on investigations of bulk TMS catalysts obtained by co-precipitation are discussed. First, the effect of ‘leaching’ on the activity of these catalysts is presented followed by a method for estimating surface concentration of active sites. Then, the focus is directed to phenanthrene hydrogenation and hydrogen activation on these samples and finally, alternative methods for synthesis and sulfidation are presented.

3.1 Effect of leaching

From precursor synthesis to the choice of a promising sulfidation protocol, many parameters influence the activity of TMS catalysts. After all, both Ni(Co)-promoted Mo/WS₂ slabs and Ni(Co)S_x particles, which are typically regarded as being inactive for hydrogenation, are formed under HDS conditions. Hence, a post-synthetic treatment of the so-called ‘parent’ sulfides was developed by Wagenhofer *et al.* and further investigated by others in our group.^[286,330] The catalysts were exposed to concentrated HCl, a treatment that was found to result in two main benefits. One was an increase in activity due to the removal of essentially inactive NiS_x particles and the cleaning of the slabs’ surface. A second finding was, that it became possible to quantify the Lewis acid sites (S-vacancies, or CUS) of the ‘cleaned’ up surface by NO probe molecules, which was previously impossible on parent samples, leading to a good correlation between the HDS (NiMoS) and HDN (NiMo(W)S) activities of the bulk catalysts and the concentration of sites probed by NO. Based on these findings, an immediate question, from the standpoint of the current thesis, was if the same observations could be made for phenanthrene hydrogenation on NiMo(W)S catalysts. Hence, three unsupported NiMoWS catalysts were synthesized, sulfided and leached as described above. Additionally, an industrial trimetallic formulation (Ind.S) was sulfided and leached. In the following, the influence of HCl treatment on the hydrogenation of phenanthrene is presented.

The most important characterization techniques are elemental analysis and the XRD pattern of the formulations. Additional to that, N₂-physisorption was used to measure the BET surface areas of parent and leached samples, and SEM images were taken to visualize effects on the morphology of the catalyst surface after ‘leaching’ of NiS_x; the results are presented in the appendix (Figure S 6-1). Table 4-2 summarizes the characteristics of these catalysts and Figure 4-5 shows the corresponding XRD patterns.

For all four formulations, HCl leaching removed nickel sulfides effectively and selectively while the sulfide slab stayed intact as directly seen in the XRD patterns. Elemental analysis of the samples showed a drop in relative Ni content of NiMoS (58%) > Ind.S (48%) > NiMoWS (46%) > NiWS (39%). The BET area slightly increased for all samples after leaching but remained below 20 m² g⁻¹ for the in-house prepared samples and the pore volume (Gurvich) increased by a factor

Comparison of Ni promoted Mo and W sulfides in HDA

of 1.5 to 2 for all formulations. The higher surface area of the industrial formulation might be attributed to a better defined precursor and an optimized sulfidation protocol (as discussed below).

Table 4-2. Elemental composition, BET surface area and pore volume of bi- and trimetallic TMS catalysts obtained by co-precipitation of metal salts. Data obtained for oxidic precursors (Ox), a parent sulfided (P) and leached catalyst (L). The last three entries show an industrial formulation.

	Atomic content [mmol g _{cat} ⁻¹]					Ni / metal [mol mol ⁻¹]	BET surface area [m ² g _{cat} ⁻¹]	Pore volume (Gurvich) [cm ³ g _{cat} ⁻¹]
	Ni	Mo	W	S	C+H+N			
NiMoOx	3.9	4.0		-	4.7	0.49	-	-
NiMoS(P)	3.1	3.4		10.8	3.4	0.48	10.08	0.0197
NiMoS(L)	1.1	4.4		11.3	3.5	0.20	13.25	0.0334
NiWOx	2.4		3.0	-	2.0	0.44	-	-
NiWS(P)	2.2		2.8	7.4	2.3	0.44	10.82	0.0142
NiWS(L)	1.2		3.3	7.6	1.8	0.27	19.32	0.024
NiMoWOx	3.5	1.3	1.9	-	2.1	0.52	-	-
NiMoWS(P)	3.2	1.2	2.0	9.3	2.4	0.50	5.28	0.0094
NiMoWS(L)	1.3	1.4	2.2	9.0	2.6	0.27	14.08	0.0185
Ind.Ox*	5.7	0.7	2.7	-	6.2	0.62	-	-
Ind.S(P)*	4.3	0.5	2.0	8.7	4.6	0.63	48.01	0.0454
Ind.S(L)*	1.6	0.7	2.6	9.2	5.9	0.33	53.60	0.0636

All three in-house synthesized formulations showed an increase in activity with factors of 3.58 (NiWS), 2.87 (NiMoWS) and 2.45 (NiMoS), while the industrial formulation was not influenced by the removal of Ni (see Figure 4-6). Figure 4-6. Conversion-Space-Time plots of NiMo(W)S catalysts comparing leached and parent formulations. The in-house catalysts benefited from HCl treatment on a mass basis while the industrial formulation was unaffected. The hydrogenation rates presented are on a catalyst mass basis. Hence, removing inactive mass led to a higher mass-specific rate except for the industrial catalyst. Therefore, mass loss factors were compared to the activity increase. The factors were 1.18 (NiWS), 1.13 (NiMoWS), 1.3 (NiMoS) and 1.32 (Ind.S). For all three formulations the activity increase was higher than the expected for mass loss. This indicates that upon inert mass removal additional active sites are available after leaching. Large NiS_x might have blocked active centers located at the edges of the Mo(W)S₂ slab which were freed up during HCl treatment.

Comparison of Ni promoted Mo and W sulfides in HDA

Table 4-3. Comparison of Phenanthrene hydrogenation rates for parent and leached transition metal sulfides. For all in-house prepared formulations the rate increase was higher than the expected increase of rate due to mass loss.

Catalyst	Mass loss factor* ($n_{\text{Mo/W,leached}} / n_{\text{Mo,W parent}}$)	Activity increase ($r_{\text{leached}} / r_{\text{parent}}$)	HDA rate (parent) [mmol _{Phē} g _{cat} ⁻¹ h ⁻¹]	HDA rate (leached) [mmol _{Phē} g _{cat} ⁻¹ h ⁻¹]
NiMoS	1.29	2.45	1.41	3.46
NiWS	1.18	3.58	1.74	6.23
NiMoWS	1.13	2.87	1.06	3.04
Ind.S	1.32	0.98	10.63	10.45

*equivalent to 'expected factor for H₂ addition rate increase due to the removal of inert mass' in Table 5-4.

After 'leaching' an increase in catalytic activity was expected due to removal of inert mass (NiS_x) and unblocking of active sites (e.g., CUS). This effect was tested by the hydrodearomatization of phenanthrene on parent and leached formulations. Figure 4-6 shows the phenanthrene conversion plotted as a function of space time for the parent and leached catalysts (rate numbers are presented in Table 4-3).

However, this picture is not entirely valid for the industrial formulation. Although a substantial amount of Ni was removed, the activity did not increase. The reasons have remained unclear so far, but this observation led to the question as to whether NiS_x particles actually participate in the catalytic mechanism and if so, to what extent. Therefore, another study was designed and executed with the aim to elucidate the role(s) of nickel sulfides in the hydrogenation of phenanthrene, presented in chapter 5 of this thesis.

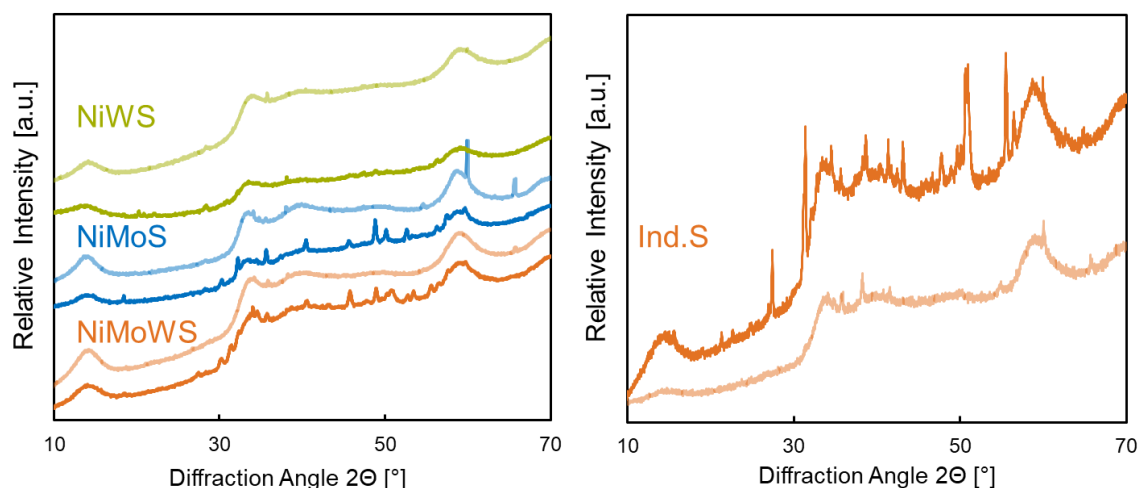


Figure 4-5. XRD pattern of parent (solid) and leached (pale) catalysts. Leaching diminished the crystalline NiS_x particles while the underlying slab structured remained intact. The spike in the leached NiMoS catalyst is caused by SiC (diluent) present originated from sulfidation in the HDA reactor and incomplete separation.

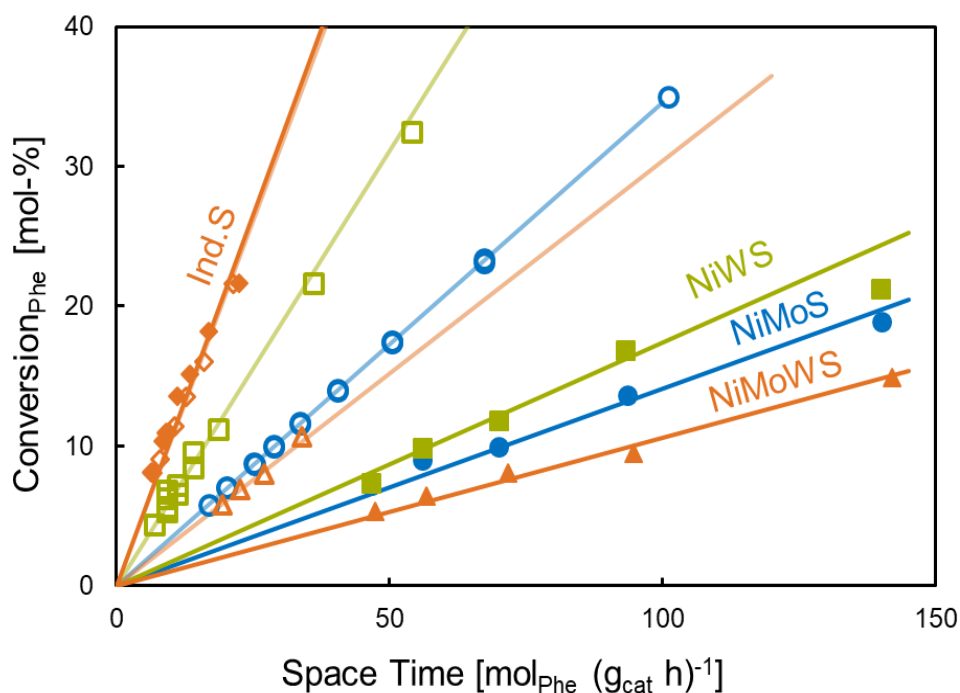


Figure 4-6. Conversion-Space-Time plots of NiMo(W)S catalysts comparing leached and parent formulations. The in-house catalysts benefited from HCl treatment on a mass basis while the industrial formulation was unaffected.

The rate improvement and the observation that the leaching treatment did not negatively influence an industrial catalyst inspire the idea of Ni recycling by leaching. In principle, a feed containing a leaching agent could be introduced into a freshly sulfided catalyst bed to dissolve inactive Ni species (while Ni-incorporated in the slabs would be marginally affected), which could be recovered at the reactor outlet. However, the protocol detailed above explored the use of concentrated HCl as a leaching agent, which is very corrosive. In a refinery, more gentle options would have to be sought. Hence, the idea of using mild organic acids for leaching was investigated. These mildly acidic substances might have an additional benefit of redispersing Ni during the process owing to their complexing ability.

A Ni_{0.5}MoS₂ catalyst was synthesized via the thiosalts impregnation route and leached according to the R.T. protocol using 4 different compounds, oxalic, maleic, succinic acid and trifluoro acetic acid, were tested. After that, elemental analysis and XRD patterns were taken and phenanthrene hydrogenation rates measured. Table 4-4 summarizes the elemental composition of the samples as well as the corresponding phenanthrene hydrogenation rate. While trifluoroacetic acid (TFA), maleic and succinic acid removed Ni to the same extent from 0.54 (parent) to 0.23 mol_{Ni} mol_{metal}⁻¹, oxalic acid relatively increased the Ni content to 0.61 mol_{Ni} mol_{metal}⁻¹, likely due to the more preferential removal of components other than Ni. At the same time, the hydrogenation rate increased with a decrease in Ni content and was a bit lower for the oxalic acid sample compared to the parent Ni_{0.5}MoS₂. This shows that complexing organic acids are able to remove NiS_x particles and cause an increase in rate due to a loss in inert mass as well as unblocking

of active sites, although the pH (1.5–3) was higher than suggested by the Pourbaix diagram (Figure 3-3). Oxalic acid might have a too short chain to create a Ni^{2+} complex or simply redisperse it again without pulling it into solution. Figure S 6-2 shows the XRD patterns of the samples. For maleic, succinic and trifluoroacetic acids, no sharp NiS_x reflections were observed after leaching while the oxalic acid treated sample still showed the NiS_x . This also indicates that those particles, if they had been attacked, were redispersed and not removed.

All this would point to a promising way to leach TMS catalysts and enhance their mass-specific activity on an industrial scale, if there were not the following observation. Figure 4-7 depicts pictures taken during typical leaching experiments in the laboratory. For succinic, maleic and trifluoroacetic acid, the solution turned blue or dark blue. This is a strong indication for oxidic molybdenum species in the aqueous solution (e.g., ‘molybdenum blue’, $\text{Mo}_4\text{O}_{10}(\text{OH})_2$). Further, the mass loss during leaching was much higher, in the range of 70-80%, than that expected solely based on NiS_x removal. This means that not only nickel was removed, but also the MoS_2 slab was attacked and partly dissolved by the acids.

As already shown in experiments with HCl leaching, a little loss of Mo is unavoidable because of partial oxidation of the slabs while handling the samples in air atmosphere. It seems that complexing acids interact much stronger with the surface Mo oxide and therefore are able to sequentially leach out the metal. Hence, the usage of organic acids for leaching is to be advised against.

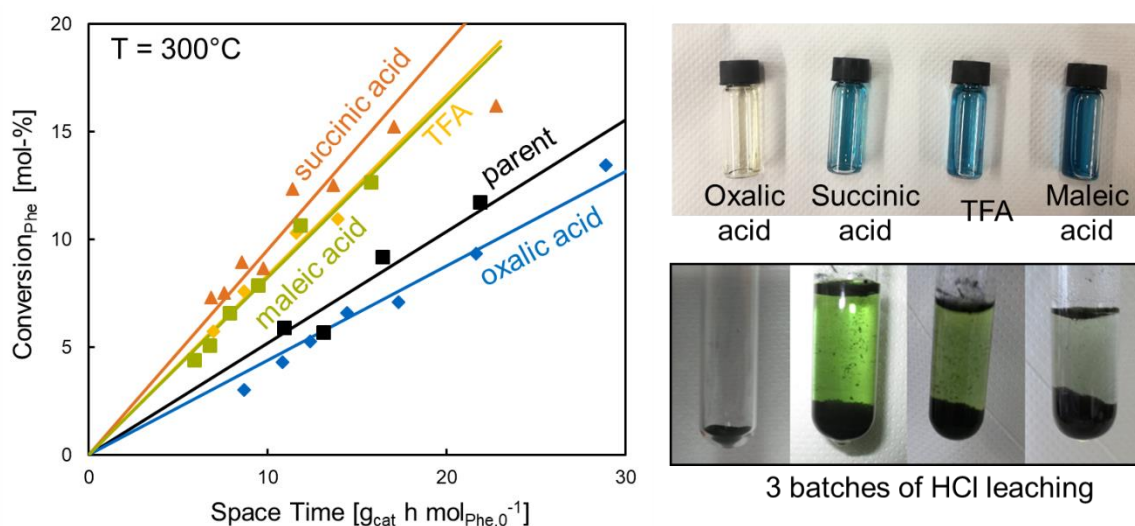


Figure 4-7. Left: Conversion-Space Time plot for $\text{Ni}_{0.5}\text{MoS}_2$ catalyst leached with different organic acids; Right: Comparison of experimental leaching. Succinic, maleic and trifluoro acetic acid caused a blue coloring of the solution. Oxalic acid showed a pale green color. Classical HCl leaching follows a declining strength in green coloring (Ni^{2+}) with multiple leaching steps.

Table 4-4. Elemental composition of Ni_{0.5}MoS₂ catalyst before and after leaching with different leaching agents. Last column gives initial phenanthrene hydrogenation rates at 300°C and 60 bat hydrogen pressure obtained by space-time depending conversion plots.

Catalyst (leaching agent)	Elemental content [mmol g _{cat} ⁻¹]				Ni/metal [mol mol ⁻¹]	Rate [mmol _{Phe} g _{cat} ⁻¹ h ⁻¹]
	Ni	Mo	S	C+H+N		
Ni _{0.5} MoS ₂ (P)	4.28	3.71	10.97	12.3	0.54	5.2
Ni _{0.5} MoS ₂ (oxalic)	4.86	3.13	8.68	11.3	0.61	4.4
Ni _{0.5} MoS ₂ (TFA)	1.50	5.14	11.61	14.5	0.23	8.4
Ni _{0.5} MoS ₂ (maleic)	1.56	5.14	11.46	13.2	0.23	8.2
Ni _{0.5} MoS ₂ (succinic)	1.57	5.11	11.52	14.9	0.24	9.6

3.2 Estimation of surface SH-groups

In-situ site quantification of bulk TMS catalysts suffers from their black appearance and therefore poor light-transmissivity as needed for IR studies. Hence, alternative methods for the estimation of active sites, in particular SH-groups, are sought after. Here, a method using the hydrogen activation activity (determined via H/D exchange rates) as a comparable measure between a sample of known SH-concentration and of samples to be investigated is presented. The catalysts studied were leached formulations obtained from co-precipitation of oxide salts as described above, NiMoS(L), NiWS(L) and NiMoWS(L) ('Effect of leaching'); their characteristics are summarized in Table 4-2.

In order to estimate the H₂ activation ability, H₂-D₂ scrambling experiments were performed between 70 and 100°C to determine the activation energy and subsequently extrapolate

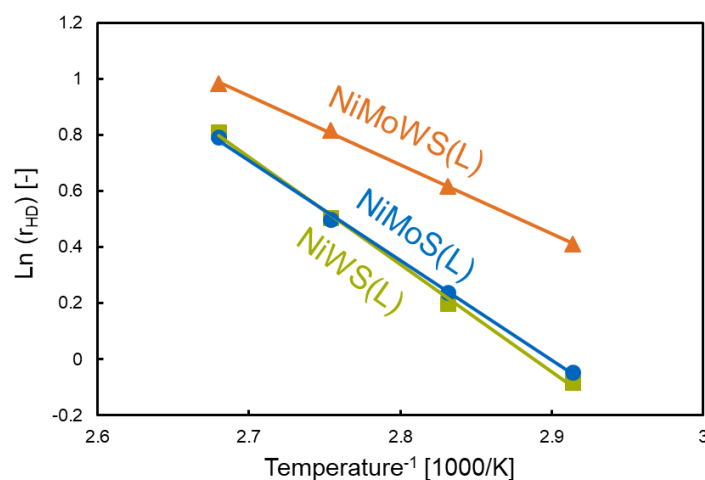


Figure 4-8. Arrhenius-type plot for leached NiMoS, NiWS and NiMoWS catalyst for H₂-D₂ exchange reaction.

the HD-formation rate as a measure for H₂ activation to 300°C (i.e., reaction temperature). Figure 4-8 gives the Arrhenius-type plot of the H₂-D₂-exchange reaction.

The two bimetallic formulations showed similar HD-formation rates and activation energies for this process while the trimetallic formulation had higher rates but a lower activation energy. Hence, extrapolating to 300°C, the activity changed to follow the order of NiWS(L) (80.0 mmol_{HD} g_{cat}⁻¹ h⁻¹) > NiMoS(L) (61.2 mmol_{HD} g_{cat}⁻¹ h⁻¹) > NiMoWS(L) (26.6 mmol_{HD} g_{cat}⁻¹ h⁻¹). The NO-uptake of the samples as a measure for available active sites was NiMoS(L) (101 μmol_{NO} g_{cat}⁻¹) > NiMoWS(L) (71 μmol_{NO} g_{cat}⁻¹) > NiWS(L) (64 μmol_{NO} g_{cat}⁻¹). These site densities were estimated in combination with the fraction of metal atoms exposed at the slab edges, *f*_{Mo}, compared to a sample with a known active site concentration.

In previous studies, a γ-Al₂O₃ supported Ni(3)MoS₂ catalysts was investigated in IR to estimate SH concentration in IR using dimethyl pyridine (DMP) as a titrant. Additional to that, the NO uptake by volumetric pulsing was determined in the same way as for this work. It was reported^[192] that 107 μmol_{DMP} g_{cat}⁻¹ was adsorbed on a sulfided catalysts after exposure to hydrogen. In another work,^[152] the NO uptake on the same sample was determined to 298 μmol_{NO} g_{cat}⁻¹. On the identical sample H₂-D₂ scrambling was performed with the same method as for the leached bulk formulations. All data are compiled in Table 4-5.

In order to estimate surface SH concentration of the bulk materials, the known concentration of the reference was related to the measured HD-formation rate:

$$C_{SH-HD} = \frac{q_{DMP,ref}}{r_{HD,300^{\circ}C,ref.}} = \frac{107 \frac{\mu mol_{DMP}}{g_{cat}}}{292 \frac{mmol_{HD}}{g_{cat}h}} = 0.3664 \frac{h \mu mol_{SH}}{mmol_{HD}}$$

Then, a reference factor for the availability of sites by NO was defined as:

$$F_{NO} = \frac{q_{NO,ref.}}{q_{NO,sample}}$$

With this, the surface concentration of SH groups for the three bulk TMS catalysts was calculated with respect to edge sites only:

$$SH_{edge} = C_{SH-HD} \cdot r_{HD,300^{\circ}C,sample} \cdot F_{NO} \cdot \frac{1}{f_{Mo/W}}$$

The highest SH concentration was found for NiWS(L) (471 μmol_{SH} g_{cat}⁻¹), followed by NiMoS(L) (254 μmol_{SH} g_{cat}⁻¹) and NiMoWS(L) (120 μmol_{SH} g_{cat}⁻¹).

Table 4-5. Characteristics of TMS catalysts for estimation of surface sulfhydryl groups (SH) via a known reference^[152,192] (last entry.) The edge fraction of metal atoms, $f_{\text{Mo/W}}$, was determined by TEM, the NO uptake by volumetric pulsing and the HD-formation rate via H₂-D₂-scrambling at 70 to 100°C.

	$f_{\text{Mo/W}}$ [-]	NO uptake [$\mu\text{mol g}_{\text{cat}}^{-1}$]	F_{NO} [-]	$E_{\text{A,HD}}$ [kJ mol ⁻¹]	HD formation rate _{300°C} [mmol g _{cat} ⁻¹ h ⁻¹]	SH (edge) [$\mu\text{mol g}_{\text{cat}}^{-1}$]
NiMoS(L)	0.26	101	2.95	29.5	61.2	254
NiWS(L)	0.29	64	4.66	31.8	80.0	471
NiMoWS(L)	0.34	71	4.20	20.4	26.6	120
Ni(3)MoS ₂ /Al ₂ O ₃ - reference		298	1.00	32.2	292.0	107 ^[a]

^[a]DMP uptake after H₂ adsorption on the fresh sulfided sample. Corresponds to sulfhydryl groups which protonated DMP.

With this, the *turn-over frequency* (TOF) of the SH groups was determined from the plot of phenanthrene hydrogenation rates as a function of SH concentration.

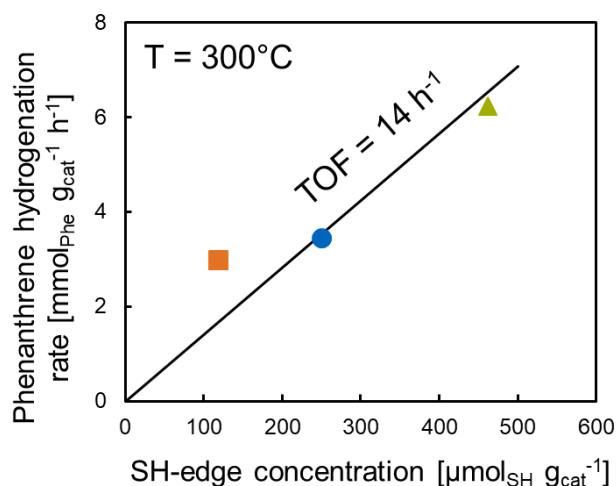


Figure 4-9. Phenanthrene hydrogenation rate plotted against the SH-concentration at the edges of the TMS slab. The slope gives the TOF of these active sites.

Figure 4-9 shows that all three catalysts almost had the same slope in the rate vs. active site concentration diagram, so that a $\text{TOF}_{\text{SH}} = 14 \text{ h}^{-1}$ was determined independent of the formulation. Consequently, one could argue that the activity difference of a W-based catalyst compared to a Mo-based catalyst lies not in the intrinsic difference of SH-groups located at the edges but on their amount, which is higher for NiWS(L) than for NiMoS(L).

3.3 Phenanthrene hydrogenation on bulk NiMoWS₂

In the following, the reaction network of phenanthrene hydrogenation on a leached NiWS catalyst is investigated by the Delplot analysis of space time depending selectivity-conversion plots for the two substrates phenanthrene and dihydrophenanthrene. In the second part, a pathway analysis with respect to the activation energies and orders of hydrogen and phenanthrene is presented.

3.3.1 Reaction network analysis on the example of leached NiWS

Reaction network analysis of phenanthrene hydrodearomatization may allow to get insights into fundamental reaction steps during the course of sequential hydrogenation. Equally important is that a shift in pathway selectivity can be used to differentiate between promoted and unpromoted active sites, as shown earlier^[236], and is a key argument for the discussion in Chapter 5. For addressing the situation in the present chapter, a more detailed analysis was undertaken for NiWS(L) and compared to the other formulations of NiMoS(L) and Ind.S(L).

The reaction network for hydrogenation of phenanthrene as presented in Figure 2-7 shows complete equilibrium situation between all products and the reactant. This study was mainly conducted in a kinetic regime at 300°C where not all equilibria were reached. Hence, the simple network with a clear differentiation between the asymmetric and symmetric pathways without interference between them was assumed in the first place. This network (N.I.) was suggested earlier by Gutiérrez et al.^[152] Later a more detailed study improved the model (N.II.) by assuming Langmuir-Hinshelwood kinetics and allowed to determine rate constants for individual reaction steps for NiMoS₂/Al₂O₃.^[236] Figure 4-10 shows the reaction network.

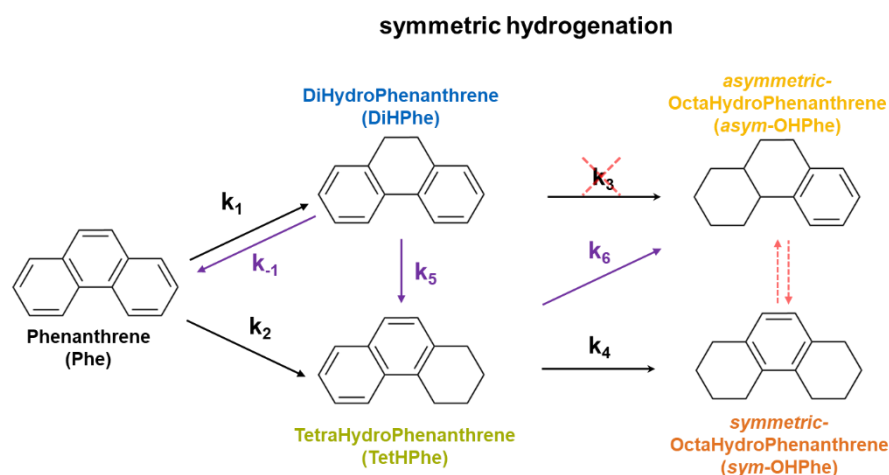


Figure 4-10. Reaction network (N.I., black arrows) for phenanthrene hydrogenation on Ni promoted Mo/WS₂ catalysts. Purple reaction pathways represent (N.II.) the augmented reaction steps after kinetic modeling by Gutiérrez et al.^[236] The pathways are named after the nature of the primary products; symmetric hydrogenation based on the symmetric molecule DiHPhe and asymmetric hydrogenation based on the asymmetric molecule TetHPhe. The red cross and arrows are possibilities considered in this work.

N.II. identified the equilibrium between Phe and DiHPhe ($K_1 = 0.72$) to be established and on the side of Phe under the reaction conditions studied (300°C, 40 bar H_2) and added additional crossways between symmetric and asymmetric hydrogenation for DiHPhe \rightarrow TetHPhe (k_5) and TetHPhe \rightarrow *asym*-OHPhe (k_6). For the supported NiMoS₂ catalyst the forward rate constants of the primary products were approx. 6 times higher than for the secondary reaction step. In all cases, the initial selectivities for the primary products were about 50 mol-% and for the secondary products OHPhe were below 1 mol-%.

Targeting the pathway ratios two experiments varying the space time were performed on NiWS(L) catalyst, i) using Phe as reactant and ii) using DiHPhe as reactant. Based on the obtained data, first and second rank delplots (see 3.1 in Chapter 3) were created and plotted in Figure 4-11.

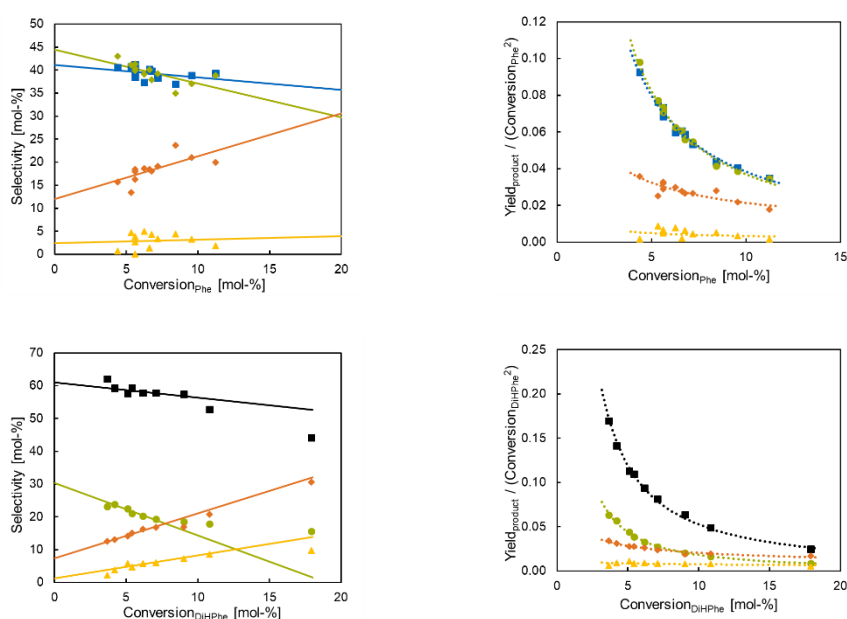


Figure 4-11. First (left) and second (right) rank delplot for hydrogenation of phenanthrene (top) and dihydrophenanthrene (bottom) on NiWS(L). Blue squares: DiHPhe; green circles: TetHPhe; orange diamonds: *sym*-OHPhe; yellow triangles: *asym*-OHPhe; black squares: Phe.

A first rank delplot for Phe hydrogenation showed DiHPhe and TetHPhe to have a non-zero intercept ($X \rightarrow 0$) which identifies those products as of kinetically primary nature, while the close to zero intercept of *asym*-OHPhe speaks for a higher product rank. Although *sym*-OHPhe has a non-zero intercept as well, its nature should be analyzed further. With the help of the second rank delplot DiHPhe and TetHPhe are clearly identified as primary products since their curves diverge. *Sym*-OHPhe might have a positive intercept and therefore be of secondary rank, rather than suggested by the first rank delplot. Because of its very low appearance it is hard to judge on the rank nature of *asym*-OHPhe, but it might show a zero intercept in the second rank delplot, hence speaking for a higher rank ($r > 2$). Rather than increasing the number of the rank in the delplot, the second experiment, starting with DiHPhe, is analyzed in the same way.

Phenanthrene clearly appears as a primary product, along with TetHPhe (positive zero intercept!). While *asym*-OHPhe shows a zero intercept (non-primary product), the case of *sym*-OHPhe stays vague. The second rank delplot confirms the primary nature of Phe and TetHPhe (diverging curves!) and hints to a zero intercept of *asym*-OHPhe as well (higher rank!). *Sym*-OHPhe shows a positive zero intercept in the second rank delplot, identifying it to be of second rank.

Based on this analysis the following network is suggested. Phe and DiHPhe quickly establish their interconversion equilibrium since both are primary products to each other and their initial selectivities are very high (see Table 4-6 and Table 4-7). TetHPhe is a primary product for both, Phe and DiHPhe, so that the reaction 5 has to be considered. For this study *asym*-OHPhe could not be identified as a primary product to DiHPhe which would exclude reaction 3 (which also had a very small k in the previous study). *Sym*-OHPhe is of secondary nature for DiHPhe as reactant and has to be of secondary nature for Phe as well. The question remains how *asym*-OHPhe is produced. There are two pathways open, one formed by hydrogenation of TetHPhe ('6') and the isomerization of *sym*-OHPhe. The latter one could neither be studied nor confirmed in this work, but remains a possibility. However, the existence of *asym*-OHPhe was very low among all catalysts tested in this work (< 5 mol-%) so that its impact on the pathway analysis was very low as well. Note that for the step $\text{DiHPhe} \rightarrow \text{asym-OHPhe}$, 6 H atoms have to be added at the same active center while the equilibrium drives the reaction towards the lower hydrogenated Phe. This result is more in line with the work published for larger scale processes.^[237,239,244]

In a less detailed manner, the analysis was done for NiMoS(L) and Ind.S(L) as well. It was found that the above analysis holds true for these catalysts as well (plots see Figure S 6-4). Typically, a ratio of DiHPhe to TetHPhe of close to 1 (slightly on the side of TetHPhe) was found. Deeper hydrogenation accumulated to 25 mol-% selectivity with a large surplus in *sym*-OHPhe. Temperature increase had no effect on the reaction network, while shifting the selectivity slightly to deeper hydrogenation. Table 4-6 and Table 4-7 summarize the initial selectivities obtained from a first rank delplot for Phe and DiHPhe hydrogenation.

Comparison of Ni promoted Mo and W sulfides in HDA

Table 4-6. Initial selectivities (290/300/310/320°C) of the products dihydrophenanthrene (DiHPhe), tetrahydrophenanthrene (TetHPhe), symmetric Octahydrophenanthrene (Sym-OHPhe) and asymmetric Octahydrophenanthrene (Asym-OHPhe) for phenanthrene (Phe) hydrogenation on leached NiWS, NiMoS and the industrial formulation. The values are obtained by extrapolating to zero contact time (delplot). The last column gives the close to unity ratio of the two primary products DiHPhe and TetHPhe.

	Initial selectivities [mol-%]				DiHPhe / TetHPhe
	DiHPhe	TetHPhe	Sym-OHPhe	Asym-OHPhe	
NiWS(L)	46/41/43/48	48/45/43/43	6/12/11/8	0/2/3/1	1.0/0.9/1.0/1.1
Ind.S(L)	38/38/38/36	40/36/34/32	19/22/24/28	3/4/4/4	1.0/1.1/1.1/1.1
NiMoS(L)	40/39/41/41	45/37/39/39	13/20/17/17	2/4/3/3	0.9/1.1/1.1/1.1

Table 4-7. Initial selectivities of the products phenanthrene (Phe), tetrahydrophenanthrene (TetHPhe), symmetric Octahydrophenanthrene (*sym*-OHPhe) and asymmetric Octahydrophenanthrene (*asym*-OHPhe) for dihydrophenanthrene (DiHPhe) hydrogenation on leached NiWS and the industrial formulation. The values are obtained by extrapolating to zero contact time (delplot).

	Initial selectivities [mol-%]			
	Phe	TetHPhe	Sym-OHPhe	Asym-OHPhe
NiWS(L)	61	30	7	2
Ind.S(L)	67	23	7	3

3.3.2 Pathway analysis

The reaction network of phenanthrene hydrogenation on NiWS catalysts discussed above shows that the network can be divided into two main paths, the symmetric path with DiHPhe and the asymmetric one with TetHPhe as the primary products. Hence, the reaction orders and activation energies measured for hydrogen and phenanthrene on leached NiMo(W)S catalysts were separately determined for these pathways and presented in Table 4-8.

The order in phenanthrene was nearly one for the industrial catalyst indicating a low surface coverage by phenanthrene and surface intermediates derived from it for both paths. The phenanthrene order was smaller on NiWS and NiMoS, suggesting a higher coverage of phenanthrene and its derived surface species on these catalysts than the industrial one. Earlier experiments suggested that phenanthrene mainly adsorbs via π -interaction with the basal plane of the slab and is unaffected by the nature of the sulfide.^[236] Note, however, that the phenanthrene order for the symmetric and asymmetric routes was similar on NiMoS and the industrial catalysts, whereas on NiWS, the symmetric and asymmetric paths exhibited different reaction orders in phenanthrene, being somewhat higher for the asymmetric hydrogenation path.

The reaction order in H_2 was close to or larger than 1 in all cases, suggesting that the rate-determining step (r.d.s.) is not the first addition of an H atom to the hydrocarbon. In that case an order of 0.5 would be expected. Indeed, the order of unity points to an r.d.s lying in the addition of the second H atom to the surface monohydrated phenanthrene. Further, the hydrogen coverage was low on all active sites during the reaction. Temperature affected neither the reaction order nor the ratio of initial selectivities to the primary products DiHPhe / TetHPhe (Table S 6-2-3) in an appreciable manner. Hence, the rate equation for DiHPhe and TetHPhe formation are noted:

$$r_{DiHPhe} = k_2 K_1 K_{Phe} K_{H_2} [Phe] [H_2]$$

$$r_{TetHPhe} = k_2' K_1' K_{Phe} K_{H_2} [Phe] [H_2]$$

where K_{Phe} and K_{H_2} are the adsorption equilibrium constants for phenanthrene and hydrogen. K_1 and K_1' are the thermodynamic constants for the first H-addition (assumed to be quasi-equilibrated) along the formation pathway for DiHPhe and TetHPhe, respectively.

Activation energies (Table S 6-5 and Table S 6-6) hardly varied over the pathways and concentration changes of phenanthrene and hydrogen on the three catalysts. The bimetallic leached NiMoS and NiWS offered values of 111 to 115 kJ mol^{-1} while the activation energy of the industrial catalysts was lower at around 94 kJ mol^{-1} . This is in agreement with the two rate equations shown above, which further show that the measured $E_{A,app}$ is, in essence, a sum of reaction and activation enthalpies related to reactant adsorption, the first H-addition, and the rate-determining H-addition elementary step.

In addition, the grouping of kinetic and thermodynamic constants reflects the difference in standard Gibbs free energies, ΔG_{eff}^\ddagger , between the transition state, TS , for the kinetically relevant step of DiHPhe / TetHPhe formation and the gaseous phenanthrene, G_{Phe} , H_2 , G_{H_2} , and three vacancies sites, G_* :

$$k_2 K_1 K_{Phe} K_{H_2} = \exp\left(-\frac{\Delta G_{eff}^\ddagger}{RT}\right)$$

$$\Delta G_{eff}^\ddagger = G^\ddagger - (3G_* + G_{Phe} + G_{H_2})$$

The ratio of formation rates of the two major products, DiHPhe and TetHPhe, reflects the difference in standard Gibbs free energies for the relevant transition states involved in the r.d.s along the two formation routes:

$$\frac{r_{DiHPhe}}{r_{TetHPhe}} = \frac{k_2 K_1}{k_2' K_1'} = \exp\left(-\frac{G_{DiHPhe}^\ddagger - G_{TetHPhe}^\ddagger}{RT}\right)$$

where G_{DiHPhe}^\ddagger and $G_{TetHPhe}^\ddagger$ correspond to the standard free energies of the TS formed along the reaction coordinate of the second H-addition elementary step (rate-determining) leading to DiHPhe and TetHPhe formation.

According to the initial selectivities of the bulk NiMo(W)S catalysts (Table 4-6 and Table S 6-2-4) as well as NiMoS catalysts supported on γ -Al₂O₃,^[152,236] this ratio was close to one for the leached NiMoS, NiWS and industrial catalysts for all temperatures between 290 and 320°C and in the partial pressure range of 30 to 40 bar hydrogen and 0.09 to 0.18 bar phenanthrene. This suggests that the two kinetically relevant TS for DiHPhe and TetHPhe formation are nearly the same in energy and by inference, structure. With the temperature independent ratio, the two TS enthalpies are also similar. Together, nearly identical free energies and enthalpies for the kinetically relevant TS along the paths to DiHPhe and TetHPhe, the corresponding TS entropies should also be very close.

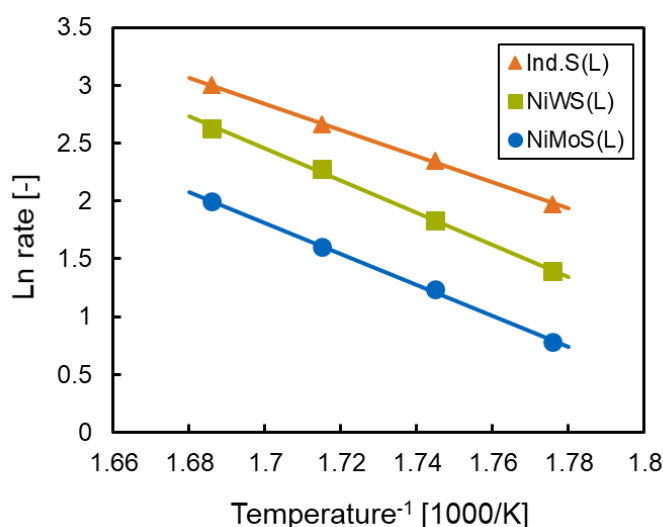


Figure 4-12. Arrhenius type plot for the three leached formulations, Ind.S(L), NiWS(L) and NiMoS(L) for the temperatures 290, 300, 310 and 320 °C.

Table 4-8. Reaction (symmetric / asymmetric hydrogenation) order in Phe and H₂ for the temperature range 290-320°C. The partial pressure range for H₂ was 30.48-40.65 bar and 0.09-0.18 bar for Phe.

Temperature [°C]	Reaction order phenanthrene (sym/asym)				Reaction order hydrogen (sym/asym)			
	290	300	310	320	290	300	310	320
NiMoS(L)	0.45 / 0.43	0.61 / 0.64	0.62 / 0.61	0.63 / 0.54	0.76 / 0.95	0.94 / 1.18	0.92 / 1.05	0.80 / 0.86
NiWS(L)	0.77 / 0.91	0.47 / 0.75	0.60 / 0.82	0.70 / 0.81	0.86 / 1.70	0.87 / 1.01	0.86 / 0.93	0.89 / 0.84
Ind.S(L)	0.93 / 0.92	0.90 / 0.94	0.93 / 0.92	1.02 / 0.96	1.09 / 1.42	0.82 / 1.15	0.80 / 1.20	0.74 / 1.09

3.4 Hydrogen activation on TMS

H₂-D₂ scrambling offers the possibility to determine the adsorption equilibrium constant of H₂ using the following equation derived in chapter 3.

$$\frac{1}{\sqrt{r_{HD}}} \cdot \frac{\sqrt{2\beta} \cdot \sqrt[4]{\frac{p_{H_2}}{p_{D_2}} \cdot \frac{\beta^2}{\alpha}}}{\left(\sqrt{\frac{p_{H_2}}{p_{D_2}} \cdot \frac{\beta^2}{\alpha}} + \beta\right)} = \frac{1}{\sqrt{k_{ads}}} \cdot \left(\sqrt{p_{H_2} + \alpha \cdot p_{D_2}}\right)^{-1} + \frac{P}{\sqrt{k_{des}}}$$

A simple approach allows to obtain the rate constants from regression of the HD-formation rates, measured under varying partial pressures of H₂ and D₂ on a trimetallic NiMoWS catalyst, to the equation shown in Figure 4-2. The parameters associated with the isotope effect (*IE*, here α and β) were allowed to vary.

HD-formation rates at 80°C were found to be in the range of 0.85 to 1.45 mmol_{HD} (g_{cat} h)⁻¹ for hydrogen partial pressures of 0.13, 0.20 and 0.29 bar and concentration ratios of H₂/D₂ between 0.7 and 3. Based on this set of experiments, the desorption rate constant of hydrogen was found to be at least a factor of 200 larger than its adsorption rate constant, independent of IE parameters chosen in the interval of 1 to 1.4. The sum of least squares was in the range of 2E-03 to 3E-03. As an example, the parity plot and the magnitude of the adsorption constant at 80°C is given below. Additional to the adsorption equilibrium constant, the order in deuterium and hydrogen was determined based on the accumulated data. They are similar for H₂ and D₂; n_{H₂} = 0.59 and n_{D₂} = 0.54.

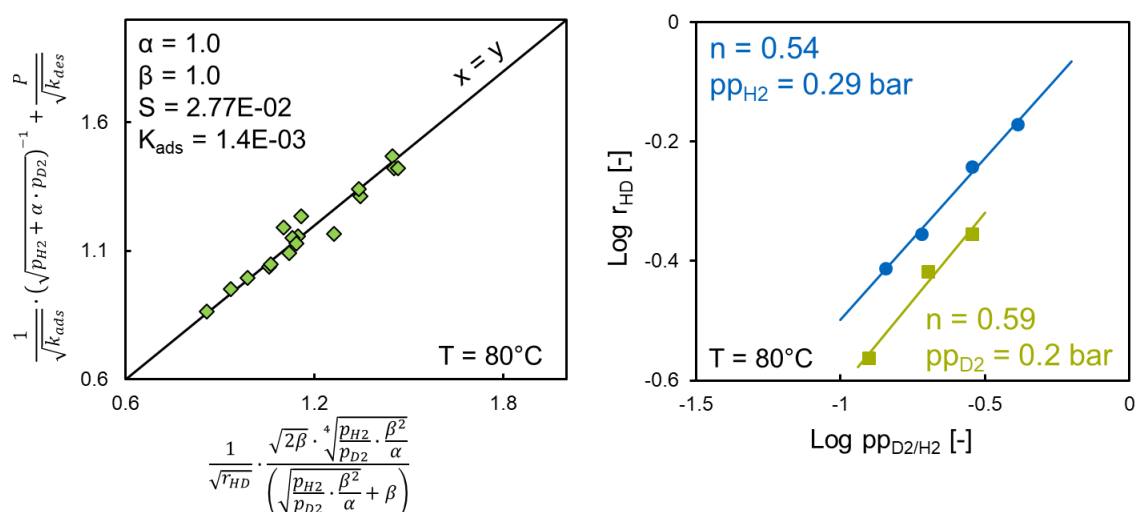


Figure 4-13. H₂-D₂ scrambling on trimetallic NiMoWS catalyst at 80°C with varying partial pressures of H₂ and D₂. On the left, a parity plot for fitting the adsorption constant is given. On the right, the reaction orders of hydrogen and deuterium are presented.

An order of about 0.5 for hydrogen activation reflects a low coverage on the catalytic surface. In line with this finding the desorption rate constant is an order of magnitude larger than the adsorption rate constant, reflecting a fast desorption process compared to the adsorption of H₂ or D₂. As a result, the population of H on the surface is low. With the rate limiting step being the adsorption or activation of H₂ for the H₂-D₂ exchange, the active site involved is related to a Mo(W)-Mo(W) Lewis site. According to DFT^[216] calculations, a Ni-S pair is not stable and cannot activate H₂ without the loss of H₂S and activity. Experimentally it was shown that the hydrogen scrambling does not depend on the Ni loading in these catalysts.^[198] The authors claimed that hydrotreatment reactions are of higher complexity, involving aromatic activation and interaction of the catalyst surface with the gas phase and consequently the overall rate limiting step might not be hydrogen activation in this case.

3.5 Precursor synthesis and S-protocol

Due to difficulties in maintaining experimental consistency during the synthesis of oxidic precursors for TMS catalysts and perception of the importance of the sulfidation thereof, both protocols were adjusted and tested. One method for co-precipitation of trimetallic (NiMoW) precursors followed the ‘dropping’ procedure at which Ni(NO₃)₂ solution was dropped into a pH adjusted solution of Mo/W oxides over a time span under stirring. The second way of synthesis was a ‘one-pot’ method where all metals were provided together with urea in one batch and stirred for long time to allow the oxide precursor to precipitate (see above). These precursors, as well as the industrial formulation, were sulfided in liquid phase with DMDS in two different ways, i) a three-step protocol with increasing S content and ii) without changing S concentration during the T-protocol, which was kept constant in magnitude and time for both protocols. The main difference between the protocols was the hydrogen to sulfur molar ratio. According to the patent by Kuperman *et al.*^[253] the hydrogen to DMDS ratio was much higher for sulfidation in an industrial process than adopted in this work. Hence the H₂/S ratio was increased from 10 to 25 mol mol⁻¹.

The response of the catalytic activity to the changes in the sulfidation protocol made, were demonstrated by the test reaction of the hydrogenation of phenanthrene. Initial rates at 300°C and 60 bar total pressure are presented and compiled in Figure 4-14 and Table 4-9.

Based on the reaction rate for phenanthrene hydrogenation, keeping the pH high for longer time during oxidic precursor synthesis results in a more active catalyst after sulfidation. For the example of a trimetallic formulation the rate increased by a factor of 1.9 from 1.24 to 2.39 mmol_{Phe} (g_{cat} h)⁻¹. This effect might be caused by a more uniform co-precipitation in a one-pot synthesis compared to the ‘dropping’ method. This dropping method was not optimized for pH and dropping speed control, and mainly suffered from the fact that the optical observation of particle formation and disappearance during precipitation was used in order to set the time intervals for the drops. Further, the dropwise addition of Ni(NO₃)₂ solution into the solution containing

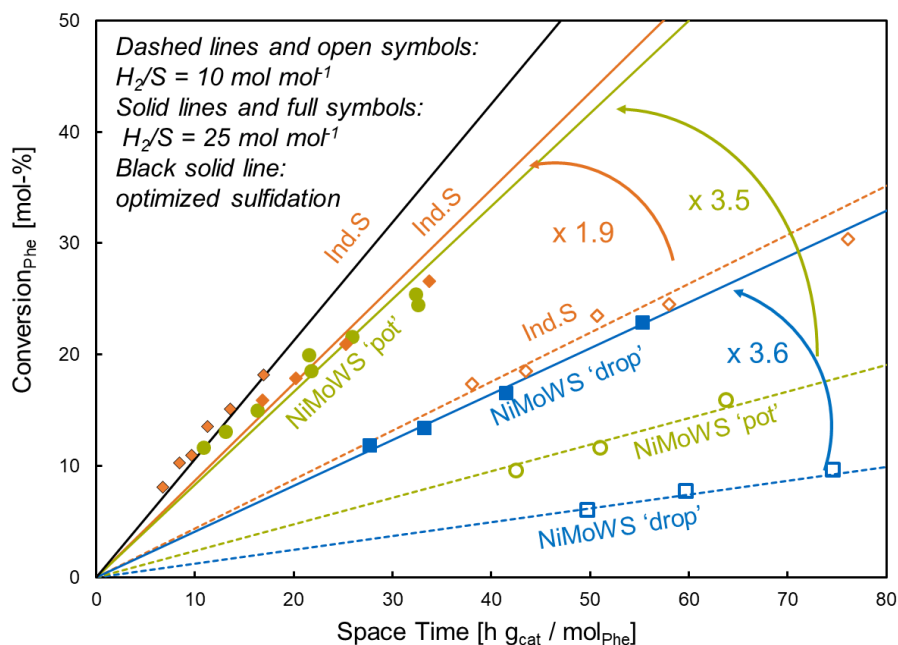


Figure 4-14. Hydrogenation activity of trimetallic NiMoWS catalysts obtained by different synthesis methods and with varying sulfidation protocols.

Mo/W salts was not calibrated well by an automatic syringe. At the same time this protocol lacked pH control during the synthesis, so that the formation of NiO and Ni(OH)₂ was not controlled, too. This resulted in mainly small-surface-area catalysts after sulfidation with a high content of nickel sulfides. Using urea, which decomposes into ammonia at the synthesis temperature, buffers the solution at a high pH (the pH increased over the first 3 hours). This seems to be beneficial for creating a better Ni-Mo/W mixed oxide compared to the former synthesis.

More important than the precursor synthesis was the sulfidation treatment. By drastically increasing the H₂/S molar ratio from 10 to 25, a large boost in hydrogenation activity was achieved. For both synthesis methods, the rates increased by a factor of ~3.5 from 1.24 to 4.11 mmol_{Phe} (g_{cat} h)⁻¹ ('dropping') and from 2.39 to 8.35 mmol_{Phe} (g_{cat} h)⁻¹ ('one-pot'). The industrial formulation showed a more modest increase of a factor of 1.9 from 4.4 to 8.7 mmol_{Phe} (g_{cat} h)⁻¹.

Transformation of a transition metal oxide into its sulfide requires a tremendous structural change of the crystal. Additionally, this process is of high exothermicity. Therefore, a mild and 'smooth' sulfidation allows the transformation into stacked slabs with a high sulfidation degree. One step to achieve this situation is to sulfide in liquid phase whereas the solvent (here decalin) dissipates the heat released by the process better than in gas phase (using a mixture of H₂ and H₂S).

However, after sulfidation a fully sulfided catalyst with a high degree of Ni incorporation/substitution at the slab edge or at least small and well distributed NiS_x clusters are targeted. Additionally, a high edge dispersion of the Mo(W)S₂ phase is beneficial to expose as

many as possible active sites. These parameters are influenced by the sulfidation treatment. Above 277°C no difference in activity was found for DMDS sulfided or H₂S sulfided Ni(Co) promoted Mo/Al₂O₃ catalysts. However, the actual sulfiding agent in both cases was H₂S because of the decomposition of DMDS to H₂S and DMS and a potential benefit remains the heat dissipation capacity of the liquid organosulfide solvent mixture.^[331]

The sulfidation protocol was chosen out of the following reasons. After drying (removal of adsorbed water) in nitrogen at 120°C, a 4 wt.-% S containing feed was introduced together with hydrogen and the system pressurized to 20 bar. A higher pressure than atmospheric typically leads to more active HDS catalysts due to higher edge decoration of Co in the MoS₂ phase by redispersion of CoS_x and the higher sulfidation rate enables sulfidation of tungsten oxide phases.^[264,332,333] Then, the temperature was slowly increased to 250°C and held for 4 h. This temperature is clearly above the decomposition temperature of DMDS,^[331] and the O-S exchange reaction proceeds at a relatively high rate (>245°C).^[260] At the same time the reduction process of the oxide by H₂, which competes with sulfidation, occurred at a low rate below 300°C.^[267,268,334] The following step of increasing the S concentration to 8 wt.-% was based on the assumption that deeper sulfidation would be boosted by the higher S potential. Accordingly, it was further increased at the next temperature step. After 4 hours the temperature was further increased to 350°C. This step was indispensable to fully sulfide W based oxides. Additionally, segregated NiS_x particles began to redisperse on the Mo(W)S₂ phase and allow incorporating more Ni into the Ni-Mo-S phase.^[260,265] This might be the strongest enhancing effect on the HDS activity by a temperature treatment.

As demonstrated in Figure 4-14 this protocol was improved by increasing the H₂/S ratio and keeping the S level low. Although a high H₂ content increases the reduction rate and therefore lowers the sulfidation rate, this effect is minimal at temperatures below 300°C. Thus, the beneficial role of high H₂ pressures might be to suppress coking.^[268] An increase in the S potential at this level does not have a beneficial effect. It is suspected that a too high level of S in the sulfidation feed would lead to large Mo(W)S₂ particles and a large proportion of segregated NiS_x particles.

Comparison of Ni promoted Mo and W sulfides in HDA

Table 4-9. Phenanthrene hydrogenation rates at 300°C and 60 bar total pressure. Upper part shows the rates for trimetallic catalysts with different precursor synthesis and sulfidation protocols. Bottom part compares the rates of parent and leached formulations of NiMoS, NiWS, NiMoWS and the industrial NiMoWS formulations. The numbers in parentheses reflect the leached catalysts.

Catalyst	Precursor synthesis	H ₂ /S ratio during sulfidation [mol mol ⁻¹]	Phe hydrogenation rate	
			[mmol (g _{cat} h) ⁻¹]	[mol (mol _{metal} h) ⁻¹]
NiMoWS	dropping	10	1.24	0.22
		25	4.11	0.65
NiMoWS	one-pot	10	2.39	0.37
		25	8.35	1.31
Ind. NiMoWS	n.a.	10	4.40	0.65
		25	8.70	1.29
Ind. NiMoWS		25 ^[a]	10.63 (10.45)	1.56 (2.13)
NiMoS	dropping	10	1.41 (3.46)	0.18 (0.63)
NiWS	dropping	10	1.74 (6.23)	0.31 (1.39)
NiMoWS	dropping	10	1.06 (3.04)	0.19 (0.62)

^[a] Optimized sulfidation protocol.

Based on these findings, an optimized sulfidation protocol (Figure 4-15) regarding practicability and toward the goal of obtaining a more active catalyst was suggested. The hydrogen to sulfur ratio was kept at 25 mol mol⁻¹ and the temperature steps were the same, 250°C (decomposition of DMDS and O-S exchange) and 350°C (deep sulfidation and redispersion of NiS_x) at 20 bar total pressure. The main idea was to minimize the heat release rate of the sulfidation reaction by decreasing its reaction rate. Hence, the S content was slightly lowered to 3 wt.-% and the volumetric flow rate increased. For compensating the low rate, the reaction time was prolonged from 4 to 8 hours at 250°C and from 2 to 3 hours at 350°C. In total 7 times more sulfur was fed than stoichiometrically needed for a complete sulfidation of the Mo(W) phase. However, this sulfidation protocol successfully increased the hydrogenation rate of the industrial formulation by 20%.

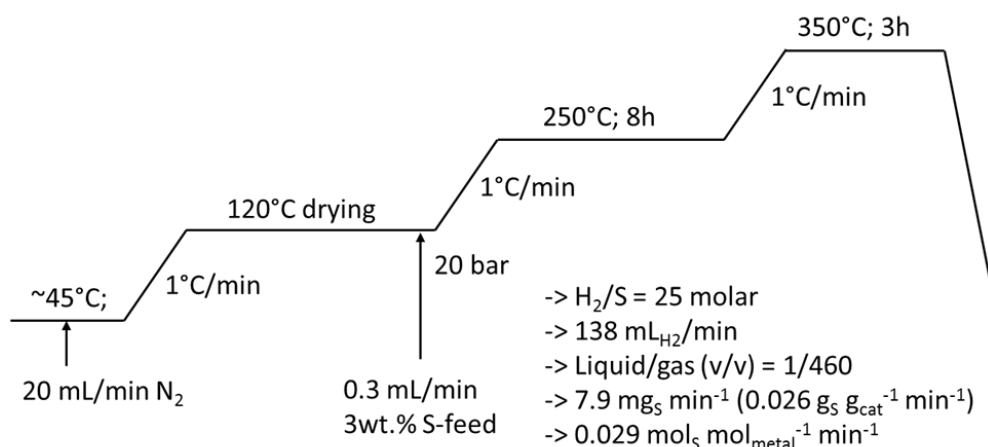


Figure 4-15. Optimized sulfidation protocol for TMS catalysts.

The reaction network and pathway selectivity were hardly changed (see Table S 6-10) by neither the synthesis method, nor the sulfidation protocol with one small exception. The formulation from the one-pot synthesis under the low H₂ sulfidation protocol showed a slight shift to dihydrophenanthrene as the main product. Here, the hydrogen uptake might be a bit smaller than for the other formulation.

4 Conclusion

In the first part of this chapter the synthesis and post-synthetic acidic treatment of NiMoS and NiWS was discussed. When using concentrated HCl as a ‘leaching’ agent, NiS_x phases were selectively removed while the concomitant WS₂ or MoS₂ structures remained intact, even at 80°C and multiple repetitions of the treatment. In the case of complexing/chelating organo-acids (and dicarboxylic acids) as leaching agent the catalysts disappeared by time and a blue coloring of the solution occurred. Partially oxidized Mo/WS₂ phases were attacked and could dissolve. However, on a mass basis, the removal of NiS_x phases increased the reaction rate of phenanthrene hydrogenation due to unblocking of active sites and elimination of chemically inert mass.

An industrial trimetallic formulation was exposed to the leaching as well. Although nickel sulfides were removed to a large extent, no increase in reaction rate was observed. Up to this point there is no satisfying explanation for this observation, but it led to speculations about the role of these formerly inactive NiS_x species. Leaching might have negative and positive influence on the catalytic properties the sulfides and could balance out. This was discussed later and the work is presented in chapter 5 of this thesis.

A second topic was the estimation of surface SH-groups as active sites for hydrogenation. It was shown that independent of the formulation, the SH concentration on the leached samples was the lowest for NiMoWS followed by NiMoS and NiWS. However, the turnover frequency on all formulations was almost identical at 14 h⁻¹. This means that SH-group has the same activity independent of the surrounding metal atoms and only the site density depends on the identity of the transition metal (Mo, W or mixed Mo/W). This finding is in line with previously published findings on supported TMS catalysts.^[193]

Hydrogenation of phenanthrene followed mainly two reaction pathways on the leached formulations, one with DiHPhe and another with TetHPhe as primary products. However, both transition states for the products were nearly the same in energy. A direct hydrogenation of DiHPhe to asym-OHPhe was essentially excluded based on the Delplot analysis. Hydrogen activation on the formulation was found to be adsorption-limited as the desorption equilibrium constant for H₂ was high in comparison to the adsorption constant. In line with this, an order of 0.5 was found for pure hydrogen scrambling experiments.

Last, the synthesis and sulfidation protocol for TMS catalysts was discussed. In general, a slow sulfidation of oxides with temperature steps at 250°C and above 320°C was beneficial to balance sulfidation and reduction rates during this process.

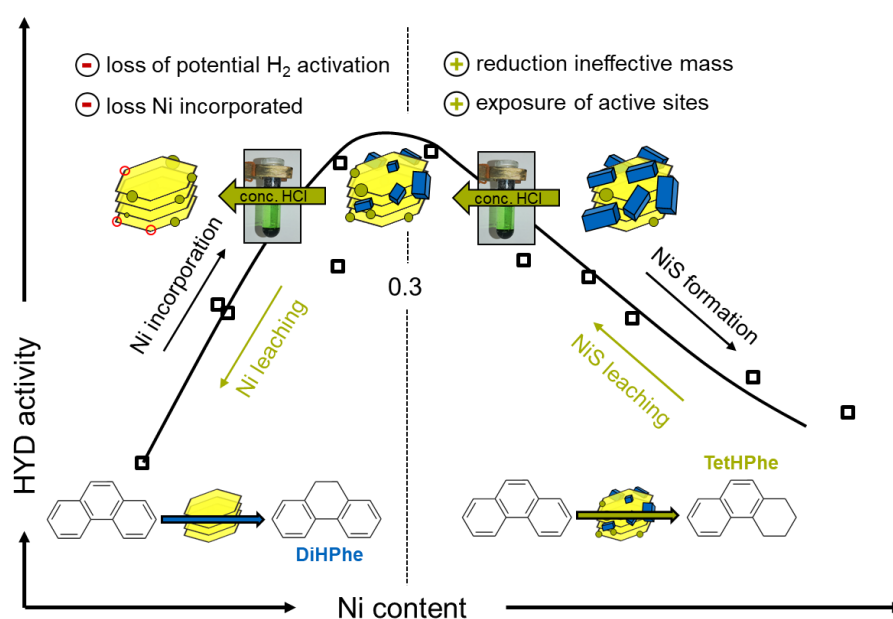
Chapter 5

On the multifaceted roles of NiS_x in hydrodearomatization reactions catalyzed by unsupported Ni-promoted MoS₂

This chapter is based on:

Ferdinand Vogelgsang, Yinjie Ji, Hui Shi, Johannes A. Lercher, 'On the multifaceted roles of NiS_x in hydrodearomatization reactions catalyzed by unsupported Ni-promoted MoS₂.' *Journal of Catalysis* 391 (2020) 212-223.

DOI: 10.1016/j.jcat.2020.08.026



1 Abstract

A series of unsupported Ni-Mo sulfide catalysts with varying Ni contents (0.13-0.72 mol_{Ni} mol_{Ni+Mo}⁻¹) was post-synthetically treated with concentrated HCl to remove large crystallites of accessible NiS_x. These sulfide particles inevitably form and grow at Ni concentrations required for the synthesis, but generally have very low activities. In all cases, Ni concentrations were greatly reduced by the HCl treatment. While this ‘leaching’ strategy successfully improved the reaction rates of high Ni-content (> 0.4 mol_{Ni} mol_{metal}⁻¹) catalysts for the hydrogenation of phenanthrene, modest to drastic decreases in catalytic rates (×0.1–0.8) were registered for catalysts with lower Ni concentrations. For the lowest Ni-loaded catalyst (0.05 mol_{Ni} mol_{metal}⁻¹), HCl treatment caused a dramatic loss of specific surface area and catalytic activity by more than a factor of 6 and shifted the selectivity pattern to that of pure MoS₂. These observations allow us to conclude that Ni atoms incorporated at the slab edges are inherently susceptible to HCl attack. NiS_x, however, are the preferential sites at which HCl induces dissolution. Experiments with inter-particle mixtures and segregated beds of NiS_x and MoS₂ demonstrate that NiS_x not only activates H₂, but also acts as a reservoir to dynamically incorporate Ni in the MoS₂ slabs at reaction conditions. These beneficial effects are reduced, as nickel sulfide particles become excessively abundant as typical for high Ni-content catalysts, for which edge substitution by Ni is near or at its maximum. The areal activity and concentration of chemisorbed nitric oxide (NO) are well correlated for the leached catalysts, with the exception of the lowest Ni-containing catalyst that has a low degree of Ni edge substitution (< 20% of total edge atoms) and predominantly unpromoted sites. This linear correlation shows that the Ni-promoted sites are more than five-fold as active as the unpromoted sites.

Keywords: Hydrodearomatization, polynuclear aromatic compounds, phenanthrene, NO chemisorption, nickel sulfides, unsupported sulfide catalysts.

2 Introduction

Binary and ternary transition metal sulfides (TMS) are promising catalysts for the hydrogenation of heavier crudes with high polyaromatics and heteroatom contents.^[18,33,338,53,65,77,128,230,335–337] These supported and bulk mixed-phase sulfide catalysts contain a primary active structure (i.e., Ni(Co)-Mo(W)-S) with varying degrees of substitution at the edge of the slabs, often together with segregated sulfide phases of the promoter element (e.g., Ni or Co).^[50,51,53,147–150,173] The formation of segregated promoter sulfides (NiS_x or CoS_x) is thermodynamically favored and inevitable in TMS catalysts with high promoter

concentrations,^[147,151,339] because the edge surface area is insufficient to accommodate all Ni (or Co). Such segregated promoter phases alone typically have low to moderate catalytic activities in hydrotreating reactions,^[20,151,340,341] and are generally considered to be detrimental because they reduce the mass-specific and metal-based reaction rates. Yet their ubiquitous presence requires a more comprehensive understanding of their roles in hydrogenation and hydrogenolysis reactions beyond their own limited catalytic propensity.

Various models have been advanced to elucidate the chemical structure and function of the promoter.^[44,46,343–345,47,49–51,117,173,341,342] The majority of the community nowadays describe the hydrotreating TMS catalysts with the “Co-Mo-S” model and its analogues.^[50,51,173,345] However, there is sufficient evidence supporting alternative theories, such as the “remote control/contact synergy” model, in which the catalytic synergy is attributed to an intimate contact and cooperative action between the Mo(W)S₂ and NiS_x or CoS_x phases without necessarily forming a mixed “Ni(Co)-Mo(W)-S” phase.^[49,343,344]

Eijsbouts consolidated the various models into a unified depiction of structural evolution that reflects the dynamic nature of the multi-component TMS catalyst in its working state.^[147] At low Ni(Co)-to-Mo(W) ratios, promoter atoms are atomically dispersed at the edges of Mo(W)S₂, while at very high ratios, particles of segregated promoter sulfides are in intimate contact with and “decorate” the Mo(W)S₂-slabs, corresponding structurally to the contact synergy model. While the presence of CoS_x and NiS_x crystals in the close vicinity of the primary active structure partially limits the accessibility of edge sites in the slab, this spatial proximity could also enable more efficient spillover of hydrogen (contact synergy model), necessitated by the short diffusion path, from CoS_x or NiS_x crystals to the adjacent promoted Mo(W)S₂ phase. Moreover, the dispersion and segregation of the promoter likely occurs in a dynamic fashion under reaction conditions.^[147] It is therefore conceivable that the manifestations of the promoter effect in a given reaction, e.g., the variations of rates and selectivities to the changes in the promoter concentration, should depend on the quantity, size, location, and nature of the segregated phases, the degree of Ni substitution in the Ni(Co)-Mo(W)-S phase, as well as the interactions among these phases and with the support.

Inspired by the work of Eijsbouts et al.^[151,339] on the roles of nickel sulfides (NiS_x) and interested in exploiting the higher hydrogenation activity of Ni-promoted MoS₂/WS₂ compared to the Co-promoted counterparts, we recently undertook a major effort to reduce the concentrations of NiS_x in high-Ni-content mixed Ni-Mo and Ni-W sulfides supported on γ -Al₂O₃ and in self-supported forms.^[286,330,346] This was enabled by a ‘leaching’ procedure, which relied on a selective reaction between concentrated HCl and accessible NiS_x phases, but not Mo(W)S₂. While these studies proved the efficacy of this strategy in enhancing catalytic rates of highly Ni-loaded catalysts, the detailed impact of the HCl treatment on the catalysis with unsupported sulfide catalysts of lower nickel contents was not explored.

Thus, we address here the consequences of removing NiS_x by HCl treatment for the physicochemical properties and catalytic rates of unsupported Ni-Mo sulfide catalysts containing low to high Ni contents (Ni/(Ni+Mo) = 0.13-0.72 mol/mol). We started with two hypotheses, i.e., (i) NiS_x and Ni incorporated at the slab edge are in dynamic equilibrium and (ii) removing NiS_x will improve the structure-activity correlation using probe molecules that adsorb on both the primary phase and NiS_x. To address the first hypothesis, hydrogenation of phenanthrene was chosen as the model hydrodearomatization reaction. The regioselectivity of this reaction exhibits a marked sensitivity to Ni promotion,^[152,193] allowing us to gain insights into the changes induced by HCl to the edge substitution degree in the primary slabs. To test the second hypothesis, we employed chemisorption of nitric oxide (NO) as a means to quantify the concentration of coordinatively unsaturated sites (CUS) that mediate H₂ activation and hydrogen addition.

3 Experimental

3.1 Synthesis of catalysts

The parent Ni_aMoS₂ ('a' represents the nominal molar fraction of Ni among total metals, i.e., Ni/(Ni+Mo) in the synthesis mixture) catalysts were synthesized via a thiosalt method to allow a good control over the Ni content. First, ammonium tetrathiomolybdate ((NH₄)₂MoS₄, abbreviated as ATM hereafter) was synthesized following a method reported by de Brimont et al.^[280] Specifically, 8 g of ammonium heptamolybdate tetrahydrate, (NH₄)₆Mo₇O₂₄·4 H₂O (Merck, 99%), were dissolved in 20 g of ammonium hydroxide solution (Merck, 32 wt% in water), and 72 g of a (NH₄)₂S solution (Alfa Aesar, 40-44% w/w aq. solution) were added in excess (S/Mo = 10). The mixed solution was stirred at 60°C for 1 h. After that, the dark red solution was put on ice for 3 h to allow complete precipitation of dark red ATM crystals, which were then filtered off and washed with cold isopropanol. Next, the tetraalkylammonium thiomolybdate precursor was synthesized via a co-precipitation method described by Alonso- et al.^[278] The ATM crystals previously obtained were dissolved in deionized water and a solution containing stoichiometric amounts (1:1 with respect to Mo) of hexamethonium bromide, (CH₃)₃N(Br)(CH₂)₆N(Br)(CH₃)₃ (Alfa Aesar, 98%) was added. Once the two solutions came in contact, an orange water-insoluble precipitate (hexamethonium tetrathiomolybdate) formed immediately, which upon full sedimentation was filtered off and washed with copious amounts of water to remove Br⁻. The solid was dried in dynamic vacuum in a desiccator and kept there before use. The choice of hexamethonium tetrathiomolybdate was originally intended for achieving higher surface areas of the sulfides (upon decomposition) than in a previous work by Alonso et al., where (R₄N)₂Mo^VS₄ (R = H, CH₃, n-C₄H₉) was used.^[160] As shown later, this precursor eventually led to unsupported MoS₂ with a specific surface area of 140 m² g⁻¹, exceeding the conventional range of surface areas

(up to 100 m² g⁻¹) reported for (NH₄)MoS₄-derived MoS₂ while being less than that (250 m² g⁻¹) of ((C₄H₉)₄N)₂MoS₄-derived MoS₂.

MoS₂ and Ni-containing MoS₂ catalysts were obtained by thermal decomposition of the thiomolybdate in organic solvent in a high pressure batch reactor (300 mL, Parr instruments) using a method adapted from that described elsewhere.^[279] First, 3 g of the precursor, hexamethonium tetrathiomolybdate, were loaded into the batch reactor and 100 mL of decalin were added. For Ni-containing catalysts, additionally a solution of nickel naphthenate, Ni(C₁₁H₇O₂)₂ (Alfa Aesar, 8.09 wt% Ni according to the certificate of this specific batch of chemical) in decalin was added in a quantity corresponding to the target ratio of Ni/(Ni+Mo) (varying from 0 to 0.7). The batch reactor was purged three times with 45 bar H₂ and pressurized to that pressure. Subsequently, it was heated to 350°C and maintained at that temperature and H₂ pressure for 3 h. After cooling down to room temperature overnight, the liquid was decanted and the separated solid was put into a 50 mL centrifuge tube. Then, it was washed with 40 mL of n-hexane, centrifuged and decanted again. This procedure was repeated 5 times. Finally, the catalyst was dried in dynamic vacuum. Before pelletizing and packing into the reactor, the Ni_aMoS₂ was re-sulfided with a 10 mL min⁻¹ flow of 10 vol% H₂S in H₂ (Westfalen, certified mixture of 98% purity H₂S and 99.999% purity H₂) at 400°C for 8 h. Those catalysts are denoted as Ni_aMoS₂-P ('P' stands for 'parent', while 'a' represents the molar fraction of Ni among total metals, i.e., Ni/(Ni+Mo)).

In addition, a series of catalysts was prepared by treating the parent samples with aqueous concentrated HCl (~37 wt. %, 12 M). Specifically, 400 mg of the parent Ni_aMoS₂ were put into a 5 mL glass tube and 3 mL of concentrated HCl solution were added. After 1 h of vigorous reaction, the solution was centrifuged and the green aqueous phase was removed. This procedure was repeated twice to the remaining solid; no further sign of dissolution (coloring of the aqueous phase, gas evolution) was observable after the third HCl treatment. Then, the solid sample was washed with copious amounts of deionized water to remove remaining chloride ions, dried in dynamic vacuum overnight and stored in a desiccator. Before pelletizing, the samples were re-sulfided with a 10 mL min⁻¹ flow of 10 vol. % H₂S in H₂ at 400°C for 8 h. These 'leached' samples are denoted with an 'L' as the suffix.

A nickel sulfide sample (denoted as Ni_mS_n hereafter) was synthesized by a method described by Bezverkhy et al., according to which mixtures of Ni₃S₂ and NiS would be synthesized.^[347] Nickel nitrate hexahydrate, Ni(NO₃)₂·6H₂O (Acros Organics, 99%), was dissolved in water and Na₂S·9H₂O (VWR, 98%) was added. The solution was stirred at room temperature for 1 h and the precipitate was filtered off. The precipitate was washed several times with water and once with acetone before leaving it over night to dry. Finally, the dried sample was re-sulfided in a 10 mL min⁻¹ flow of 10 vol. % H₂S/H₂ at 400°C for 8 h prior to catalytic use; the catalytic activity was hardly measurable. This sample could be completely dissolved by the same HCl treatment.

3.2 Characterization

The contents of H, C, N and S were quantified by oxidative combustion using an automated element analyzer instrument (Vario EL CHN Analyzer, ELEMENTAR). The gases CO₂, H₂O, N₂ and SO₂ were detected by gas chromatography. The concentrations of Ni and Mo were photometrically measured after digestion of the solids.

Physisorption of N₂ at -196°C was performed on an automated nitrogen adsorption analyzer Sorptomatic 1990 Series (Thermo Finnigan), where BET surface areas and total pore volumes (Gurvich method) of ~250 mg of sample were determined. The samples were outgassed in vacuum at 250°C for 2 h prior to adsorption.

Powder X-ray diffraction (XRD) patterns were recorded on an Empyrean system from PANalytical equipped with a Cu X-ray tube (Cu-K_α radiation, 0.154 nm), a nickel K_β-filter, and solid-state detector (PIXcel1D) operated at 45 kV and 40 mA with step size of 0.017° and scan time of 115 s per step. The peaks were identified using the Highscore software.

Transmission electron microscopy (TEM) images were taken on a JEOL JEM 2010 instrument equipped with a LaB₆-cathode with an accelerating voltage of 120 kV. The samples were prepared by grinding a small amount of specimen and dispersing it ultrasonically in absolute ethanol. Subsequently, drops of this suspension were applied on a Cu grid (200 mesh) with a lacey carbon film and ethanol was evaporated at room temperature. For each sample, >100 of slabs were measured to allow a statistical analysis of the average slab length and stacking degree.

Nitric oxide (NO) chemisorption was carried out at ambient temperature and pressure on a continuous flow reactor connected to a mass spectrometer (Pfeiffer Vacuum QME 200). The catalyst (80 mg) was packed into a quartz tube (4 mm inner diameter, isothermal zone 5 cm) and re-sulfided in a flow of H₂S (10 vol % in H₂, 100 mL min⁻¹ g⁻¹) by heating to 400°C (10°C min⁻¹) and holding at this temperature for 1 h. Subsequently, the reactor was cooled to 250°C at which the H₂S/H₂ flow was stopped, and then was cooled to 35°C in a constant flow of 8 mL min⁻¹ N₂ (i.e., 100 mL min⁻¹ g⁻¹). For the pulsing experiments, a loop with a defined volume (1.69 mL) was filled with 10 vol. % NO in helium, which was pulsed (6.9 μmol of NO per pulse) through an automated valve into the reactor. This was repeated 24 times in 30 min intervals and the breakthrough of NO was detected with a mass spectrometer (monitoring the signal at m/z = 30). Total NO uptakes were calculated by subtracting each residual peak area (i.e., NO not adsorbed) from the averaged peak area after saturation with NO and adding up the differences.

3.3 Catalytic evaluation

Phenanthrene hydrogenation was carried out in a down-flow trickle bed reactor system equipped with an HPLC pump (Gilson 302) and mass flow controllers (Wagner Mess- und

Regeltechnik GmbH), to control the volumetric flows of the liquid feed, H₂ (Westfalen, 99.999%) and N₂ (Westfalen, 99.999%). The liquid feed contained 1 wt% phenanthrene (Alfa Aesar, 98%), 2 wt% tetradecane (Alfa Aesar, 99%) as internal standard and 1000 ppmw sulfur as dimethyl disulfide (DMDS, Aldrich, 98%) in decalin (Merck, cis- and trans-isomeric mixture, 99.0%) as the solvent. In a typical experiment, 15 mg of catalyst (250-355 μm pellets, resulfided) were diluted with SiC (sieved to mesh sizes of 63-90 μm) in a 1:20 w/w ratio. The filling pattern is shown in Figure 1 (left panel). After conditioning the catalyst at 360°C for 21 h, the hydrodearomatization reaction was carried out at 300°C and 60 bar total pressure and steady-state catalytic rates were measured by varying the space time from 10 to 30 (g_{cat} h) mol_{Ph_e}⁻¹. Deactivation was <5% of the initial activity over time on stream. Liquid samples were taken in a time interval of 30 min and analyzed with an offline GC (Shimadzu 2010, flame ionization detector, 50 m HP-1 column with 32 μm inner diameter).

Conversion rates of phenanthrene were obtained from the conversion-space time plots. H₂-addition rates were determined using the following equation using initial rates and selectivities (extrapolated to zero contact time):

$$\text{H}_2\text{-addition rate} = \text{Phenanthrene hydrogenation rate} \times [\text{Sel}_{\text{DiHPh}} (\%) + 2 \times \text{Sel}_{\text{TetHPh}} (\%) + (4 \times (\text{Sel}_{\text{sym-OHPh}} + \text{Sel}_{\text{asym-OHPh}}) (\%)]$$

3.4 Experiments with physical mixtures and stacked beds of Ni_mS_n and MoS₂

The as-obtained Ni_mS_n sample was mixed with MoS₂ (synthesized from thermal decomposition of hexamethonium tetrathiomolybdate, Section 2.1), both in powder form and the total mass being ~120 mg, in a 5 mL glass tube where n-hexane was added. The slurry was ultrasonicated to mix the powders until the n-hexane evaporated. Typically, 15 mg of the pelletized and sieved (250-355 μm) physical mixture was loaded into the trickle bed reactor described above. The filling pattern in such experiments is illustrated in Figure 5-1 (right panel). Variations of catalyst mix were positioned within the isothermal zone of the reactor furnace: diluted MoS₂, undiluted MoS₂, Ni_mS_n/MoS₂ mixtures with mass ratios of 1:1, 3:1, 6:1 and 9:1, as well as stacked Ni_mS_n and MoS₂ beds in a mass ratio of 3:1 separated by an intervening bed of 4 mm of γ-Al₂O₃.

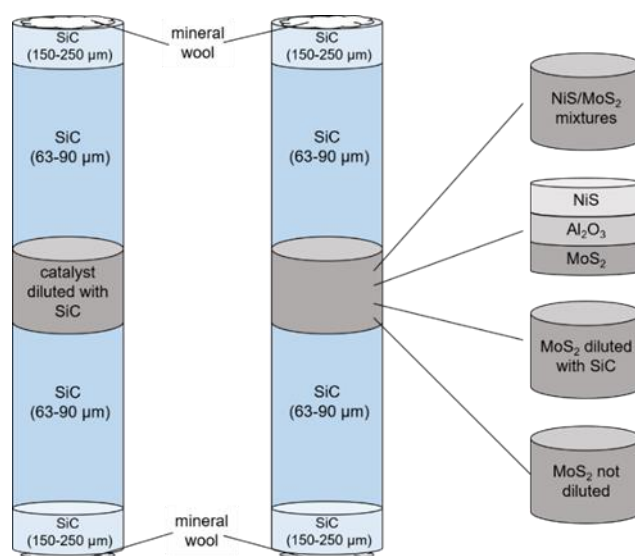


Figure 5-1. Illustration of the filling patterns in conventional operation (left) and experiments with physical mixtures and stacked beds (right).

4 Results and Discussion

4.1 Elemental and phase compositions of Ni_aMoS₂ catalysts before and after leaching

The contents of Ni, Mo and S in the parent Ni_aMoS₂ (where “a” refers to the molar fraction of Ni among all metals) and those after HCl treatment are compiled in

Table 5-1. The total contents of C, H and N from organic residues were < 5 wt% for most cases (Table S 6-9, SI). The Ni content in Ni_aMoS₂ was close to the nominal value in the synthesis mixture, and the residual carbon in the parent sample was lower (C/Mo = 0.89 mol mol⁻¹ for MoS₂ and 0.04-0.31 mol mol⁻¹ for Ni-containing MoS₂ samples) with the synthesis method employed here than with (R₄N)₂MoS₄ precursors (C/Mo = 1.2-2.0 in MoS₂).^[160] The molar ratios of S to metals (Ni and Mo) varied between 1.3-2.0 for the parent series. The S/metal ratio decreased monotonically with increasing Ni content. This is attributed to a much lower average stoichiometric ratio of S to Ni (< 2 or even < 1) in various NiS_x phases (e.g., Ni₃S₂, Ni₉S₈), present in increasing concentrations as the overall Ni content increased.

By adding concentrated HCl to the suspension containing solid particles, the supernatant turned green, indicating the presence of Ni²⁺ in the solution. In parallel, H₂S evolved. The loss of Ni is evident when comparing the parent and leached samples (

Table 5-1). The Ni concentration decreased in the order: 62.5% (Ni_{0.1}MoS₂) > 50.0% (Ni_{0.2}MoS₂) > 44.4% (Ni_{0.6}MoS₂) > 37.5% (Ni_{0.7}MoS₂) ≈ 37.0% (Ni_{0.4}MoS₂) ≈ 34.3% (Ni_{0.5}MoS₂).

In contrast, the Mo concentration generally increased with the original Ni content: 13% (Ni_{0.1}MoS₂), 7% (Ni_{0.2}MoS₂), 28% (Ni_{0.4}MoS₂), 23% (Ni_{0.5}MoS₂), 38% (Ni_{0.6}MoS₂) and 52% (Ni_{0.7}MoS₂). Without applying an electric potential or strong oxidative driving force, pure MoS₂ does not react with concentrated HCl (even at 12 M) at these conditions, according to the thermodynamic data (for bulk phase).^[285] Thus, we hypothesized that the (Ni)MoS₂ slab structure stayed largely intact during the treatment, while crystalline NiS_x reacted with HCl to produce H₂S and dissolved. Independent analysis of the filtrate solution after leaching of parent MoS₂ revealed a relatively minor loss of Mo (~0.5% of total Mo), suggesting a small extent of destruction (~2-3% of edge Mo) at the slab edge. However, this level of Mo leaching did not seem to be substantial. As a result, the observed increase in Mo content after leaching, for the Ni-containing samples, must be due to the loss of mass in the form of NiS_x. Consequently, also the overall ratio of S/metal should increase. This was observed experimentally for the majority of samples except Ni_{0.1}MoS₂ and Ni_{0.4}MoS₂. Aside from possible measurement errors (e.g., ±10% for Mo) in elemental analysis, the minor decrease in this ratio for Ni_{0.1}MoS₂ and Ni_{0.4}MoS₂ suggests that some phases with a S/Me ratio of >2 have also been involved in the dissolution. It is, however, unclear as to why these two samples differ from the others. It should be mentioned at this point that Ni incorporated in the slabs might also be attacked by HCl, a possibility that will be examined in detail later. While the elemental analysis results reveal the variations in the bulk fractions of segregated NiS_x and Ni-promoted slabs, we note that a careful XPS study combined with a well-advised peak decomposition approach could provide a means to resolve and quantify the different Ni species on the surface in the parent and leached samples, which would be worthwhile to explore in future studies.

On the multifaceted roles of NiS_x in hydrodearomatization reactions catalyzed by unsupported Ni-promoted MoS₂

Table 5-1. Elemental compositions of the parent and HCl-treated Ni_aMoS₂.

Catalysts	Ni ^[a] [mmol g _{cat} ⁻¹]	Mo ^[a] [mmol g _{cat} ⁻¹]	S ^[a] [mmol g _{cat} ⁻¹]	S/metal [mol/mol]	Atomic Ni fraction [mol _{Ni} mol _{metal} ⁻¹]
Ni _{0.1} MoS ₂	0.8 (0.3)	5.3 (6.0)	12.3 (11.8)	2.0 (1.9)	0.13 (0.05)
Ni _{0.2} MoS ₂	1.6 (0.8)	5.1 (5.5)	12.1 (12.9)	1.8 (2.0)	0.24 (0.13)
Ni _{0.4} MoS ₂	2.7 (1.7)	4.2 (5.4)	11.8 (11.2)	1.7 (1.6)	0.39 (0.24)
Ni _{0.5} MoS ₂	3.5 (2.3)	3.9 (4.8)	11.6 (12.5)	1.6 (1.8)	0.48 (0.33)
Ni _{0.6} MoS ₂	5.4 (3.0)	3.1 (4.3)	11.5 (12.5)	1.4 (1.7)	0.63 (0.41)
Ni _{0.7} MoS ₂	6.4 (4.0)	2.5 (3.8)	11.9 (12.1)	1.3 (1.6)	0.72 (0.52)
MoS ₂	0	5.3	12.4	2.3	0
Ni _m S _n	11.3	0	10.1	0.89	1

[a] Values in the parentheses correspond to the leached samples.

Figure 5-2 (a) and (b) depict the powder X-ray diffraction patterns of the parent and leached Ni_aMoS₂ catalysts, respectively. Every formulation shows the underlying diffraction pattern of MoS₂, with peaks at $2\theta = 14^\circ, 32^\circ, 40^\circ$ and 59° corresponding to the reflections of (002), (010), (013) and (110) planes. Conventionally, the (002) plane is used to calculate the stacking degree of the MoS₂ slabs by determining the d-spacing of the slabs and their crystal size by the Scherrer equation. Note, however, that the curvature and imperfect stacking (i.e., turbostraticity and disorder) of sulfide slabs also causes the loss of scattering coherency, thus, resulting in asymmetric broadening and precluding the observation of sharp reflections. The sharp reflections in the patterns of high-Ni content catalysts are attributed to NiS_x phases (primarily Ni₉S₈ and Ni₃S₂), which were hardly detectable at Ni contents up to 0.4 mol_{Ni} mol_{metal}⁻¹. While the absence of sharp reflections in the XRD patterns of other low-Ni-content Ni_aMoS₂ ($a = 0.1-0.4$) samples does not necessarily indicate the absence of segregated nickel sulfide phases,^[155] they are most likely small in size and become undetectable by XRD.

The patterns of the ‘leached’ Ni_aMoS₂ catalysts evidence a successful removal of a majority of large nickel sulfide crystallites originally present in the parent samples. Some sharp reflections of NiS_x remained in the XRD patterns of formulations with Ni contents higher than 0.5 mol_{Ni} mol_{metal}⁻¹, albeit showing a smaller number of peaks at lower intensities. Their persistence could reflect that the severity and duration of the present leaching protocol is insufficient to remove all leachable NiS_x or that some is present at inaccessible locations (e.g., entrapped or ingrown). Note that the leached samples had been sulfided before measurements and we cannot exclude the formation of new crystallites of NiS_x during that re-sulfidation process.

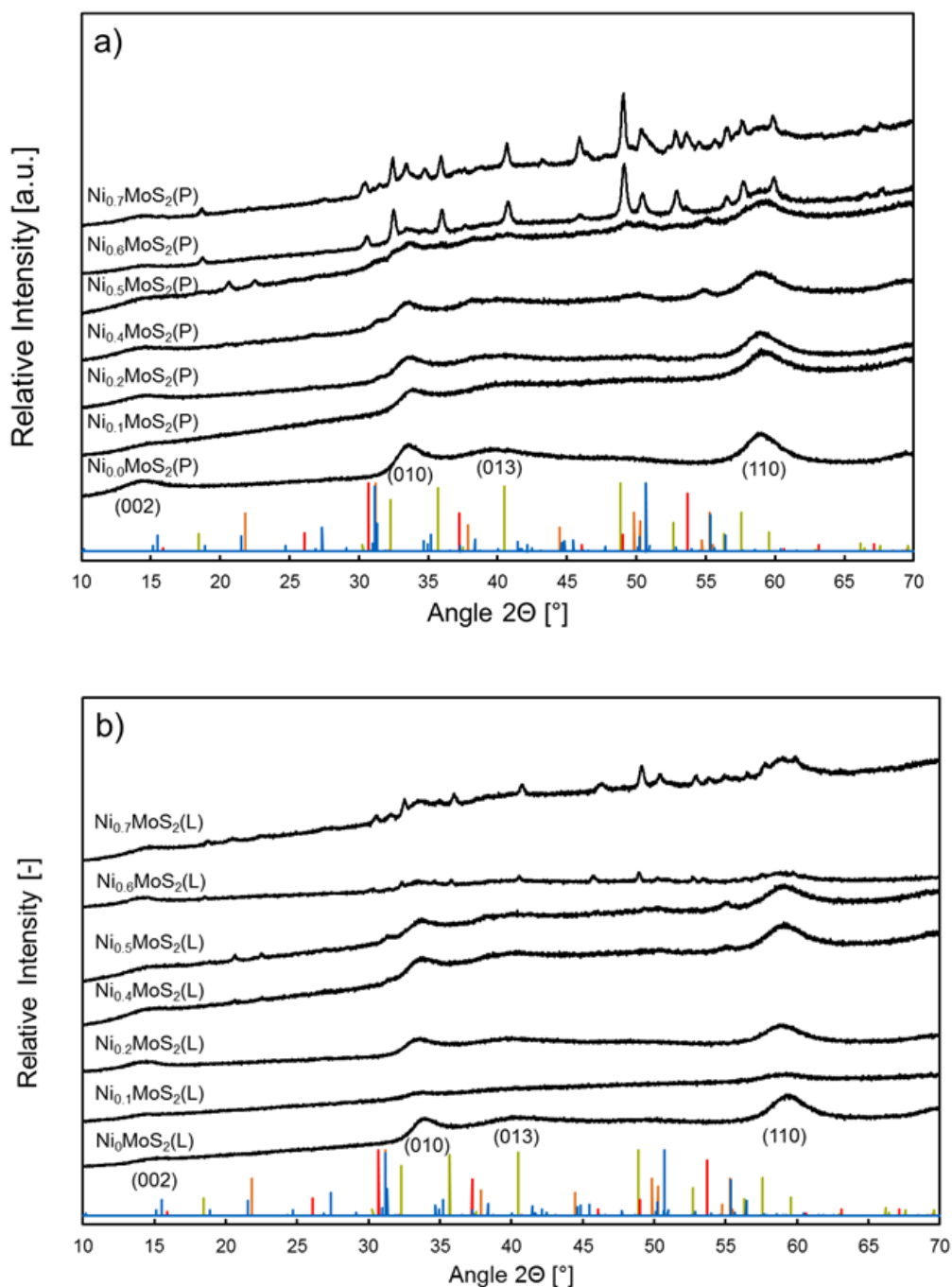


Figure 5-2. (a) XRD patterns of the parent Ni_aMoS₂ formulations with increasing Ni content ordered from bottom to top. The stick patterns of four reference substances (obtained from Highscore database) are shown at the bottom: blue, godlevskite (Ni₉S₈); green, millerite (NiS); orange, heazlewoodite (Ni₃S₂); red, polydymite (Ni₃S₄). (b) XRD patterns of the 'leached' formulations. The reflections of MoS₂ are denoted along with indices of lattice planes.

4.2 Textural and slab properties of Ni_aMoS₂ catalysts before and after leaching

BET surface areas and total pore volumes (Gurvich method) are compiled in Table 5-2; the corresponding N₂ sorption isotherms and pore size distribution histograms are presented in Figure S 6-6 and Figure S 6-6. Pure MoS₂ displayed a specific surface area of 140 m² g⁻¹ and a pore volume of 0.538 cm³ g⁻¹, comparable to those of the parent Ni_{0.1}MoS₂. Increasing the Ni content led to a decrease in the specific surface area and pore volume of the parent samples. Up to 0.5 mol_{Ni} mol_{metal}⁻¹, the surface area and pore volume remained no lower than 90 m² g⁻¹ and 0.2 cm³ g⁻¹, respectively. For Ni_{0.6}MoS₂ and Ni_{0.7}MoS₂ in their parent form, the surface areas were rather low at 26 and 34 m² g⁻¹ and their pore volumes were also much lower than catalysts containing less Ni. Because NiS_x domains in parent samples with lower Ni contents are less abundant and significantly smaller in size, these smaller entities do not block the pores to the extent that large crystallites do and, hence, the variations in pore volumes and specific surface area is less drastic than for materials with larger NiS_x domains.

Table 5-2. Physicochemical characteristics of Ni_aMoS₂, MoS₂ and Ni_mS_n.

Catalysts	BET surface area [m ² g _{cat} ⁻¹]	Pore volume [cm ³ g _{cat} ⁻¹]	Average number of slabs in stacks (TEM) [-]	Slab length (TEM) [nm]	f _{Mo} ^[a] [-]
Ni _{0.1} MoS ₂	140 (22)	0.394 (0.061)	4.1±0.9 (3.8±1.1)	5.3±1.4 (4.0±1.1)	0.21 (0.27)
Ni _{0.2} MoS ₂	129 (106)	0.384 (0.278)	3.5±0.9 (3.7±1.5)	4.9±1.6 (4.8±1.7)	0.22 (0.23)
Ni _{0.4} MoS ₂	91 (45)	0.256 (0.095)	3.7±1.2 (3.5±0.9)	6.6±3.0 (4.9±1.6)	0.15 (0.22)
Ni _{0.5} MoS ₂	90 (80)	0.224 (0.166)	3.9±1.3 (3.8±1.1)	5.3±1.7 (4.8±1.4)	0.21 (0.23)
Ni _{0.6} MoS ₂	26 (44)	0.049 (0.077)	3.2±0.9 (3.8±0.8)	4.4±1.2 (4.3±1.4)	0.25 (0.25)
Ni _{0.7} MoS ₂	34 (61)	0.081 (0.153)	3.8±1.0 (3.5±1.2)	5.2±2.4 (6.2±2.7)	0.19 (0.17)
MoS ₂	140 (160)	0.538 (0.400)	4.1±1.1 (4.3±1.0)	5.6±1.3 (4.7±1.5)	0.20 (0.23)
Ni _m S _n	11	0.0455	— ^[b]	— ^[b]	— ^[b]

^[a] Calculated via $f_{Mo} = \frac{\sum_{i=1}^m 6n_i - 6}{\sum_{i=1}^m 3n_i^2 - 3n_i + 1}$ with the number of Mo atoms along the edge $n_i = L/6.4 \text{ \AA} - 0.5$ ^[99,348]. ^[b] Not applicable.

The effect of HCl treatment on the specific surface area and pore volume of the Ni_aMoS₂ varied with the Ni content. For the two highest-Ni-loaded samples, which, according to XRD, contained a larger number of nickel sulfide crystallites, the specific surface areas and pore volumes increased substantially after leaching. This is in agreement with our most recent work also showing a significant increase in pore volume and specific surface area upon HCl treatment^[330] for a series of high-Ni-content (0.67-0.77 mol_{Ni} mol_{metal}⁻¹) Mo(W) sulfide materials prepared by coprecipitation. Such increase is attributed to the removal of a large quantity of NiS_x with low surface area and pore volume (see the last entry of Table 5-2). The deleterious effect of this leaching on the textural properties at lower Ni contents is, however, not understood at this stage and may point to a complex action of the HCl treatment that goes beyond the simple removal of NiS_x. While we speculate that agglomeration of the (Ni)MoS₂ phase occurred to a significant extent for the low-Ni-content materials during the HCl treatment, TEM and SEM pictures did not provide strong support, nor did they evidence any morphological changes (e.g., NiS_x obstructing the edges, or amorphization of the slabs) that could be held responsible for the loss of specific surface area in these samples.

There appears to be a ‘zigzag’ trend in the variation of specific surface area caused by the HCl treatment: the most drastic loss was exhibited by Ni_{0.1}MoS₂ (a factor of 6 decrease), followed by Ni_{0.4}MoS₂ that lost more than a half of its original pore volume and surface area, whereas such decreases were much less pronounced for Ni_{0.2}MoS₂ and Ni_{0.5}MoS₂ (Table 5-2). The varying extents of losses and gains in BET surface area for the individual samples after HCl treatment reflect a complex interplay of multiple factors (e.g., removal of NiS_x with different sizes and surface areas in the parent sample, the different amounts of retained organics in the parent samples and the removal of organic residues during HCl treatment). It appears plausible that organic residues in some of the parent samples (Ni_{0.1}MoS₂, Ni_{0.4}MoS₂ and Ni_{0.5}MoS₂) helped in resisting agglomeration of particles and thus their removal during HCl treatment (Table S 6-9) caused the particles to agglomerate. Although the exact reason is not quantitatively understood at present, the ‘zigzag’ trend across the series could be a result of removing organics and NiS_x during the HCl treatment, which have opposing consequences for the surface area and textural properties, and thus the variations in surface area might depend on the quantities of these species removed and perhaps also the agglomeration of the Ni-promoted MoS₂ primary particles and the intimacy of NiS_x and NiMoS₂ in the parent samples.

These parent and leached samples were investigated by TEM to see if the leaching process had caused any major modifications of the slab characteristics. Representative images are shown in Figure S 6-8. For the parent series of catalysts, the average slab length varied between 4 and 5 nm, while the average stacking degree was between 3 and 4 slabs per particle, both being marginally affected by the Ni content. The primary slab structure was not significantly affected by HCl treatment. The fraction of edge atoms among all atoms in a slab was estimated from the average slab length by assuming an equilateral hexagon shape for the slab (see the last column of

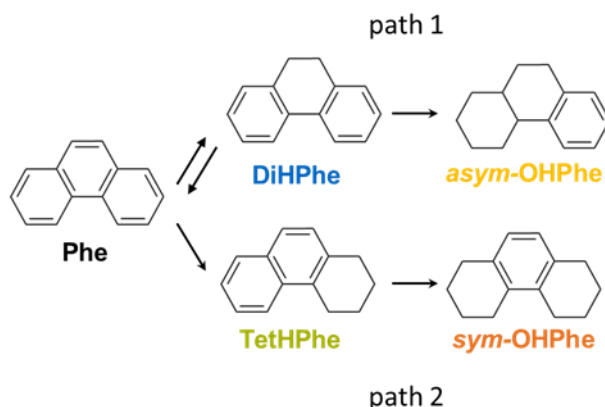
Table 5-2). According to these estimates, the total number of Ni atoms before leaching should exceed the total number of edge atoms (decreasing from 1.0 to 0.5 mmol_{edge atom} g⁻¹ with Ni concentration increasing from 0.8 to 6.4 mmol_{Ni} g⁻¹) on all parent samples except Ni_{0.1}MoS₂, which means that NiS_x must be present in those samples. For the leached samples, the total amount of Ni in both Ni_{0.1}MoS₂ and Ni_{0.2}MoS₂ would not be sufficient to attain a full substitution at the edge. In particular, the calculated Ni edge substitution degree would be less than 20% of the total edge atoms for the leached Ni_{0.1}MoS₂ sample, thus, leaving a high statistical probability (> 60%) of exposing unpromoted sites (i.e., neighboring Mo-Mo) on this sample.

4.3 Phenanthrene hydrogenation on Ni_aMoS₂ catalysts

4.3.1. Reaction pathways and initial selectivities

Ni-promoted MoS₂ catalysts with different Ni contents, before and after HCl treatment, were examined in the hydrogenation of phenanthrene. In all reactions, four products were identified, namely 9,10-dihydrophenanthrene (DiHPhe), 1,2,3,4-tetrahydrophenanthrene (TetHPhe), 1,2,3,4,5,6,7,8-octahydrophenanthrene (*sym*-OHPhe) and 1,2,3,4,4a,9,10,10a-octahydrophenanthrene (*asym*-OHPhe). Perhydrophenanthrene, the fully hydrogenated product, was not observed at the reaction temperature of 300°C and no lighter products were observed so the carbon balance was always closed within ±5%.

A delplot analysis of first and second rank^[320] allowed us to identify the nature of the detected products. Two primary products were observed on all catalysts, DiHPhe (two H-added) and TetHPhe (four H-added), while *sym*- and *asym*-OHPhe (eight-H added) were secondary kinetic products. Therefore, a reaction network including two routes for hydrogenation is proposed (Scheme 5-1). Along path 1, phenanthrene first undergoes the hydrogenation across the olefin-like 9,10-bond to DiHPhe followed by further hydrogenation of a lateral ring to *asym*-OHPhe, while along path 2, hydrogenation of one of the lateral rings forms TetHPhe first, followed by the hydrogenation of the other lateral ring to form *sym*-OHPhe. The DiHPhe formation is reversible ($K_{eq} = 1.6$ for this step at 60 bar of H₂ and 300°C; calculated from thermodynamic data in ref^[349]). Other hydrogenation reactions remain essentially irreversible at typical conditions (e.g., $K_{eq} = 50$ and larger for [TetHPhe]/[Phe] and [OHPhe]/[Phe] at 60 bar H₂ and 300°C).



Scheme 5-1. Simplified reaction pathways of phenanthrene hydrogenation.

The initial selectivities of the products, obtained by extrapolation to zero contact time in a selectivity-conversion plot, are shown in Figure 5-3. Detailed values are compiled in Table S 6-10, which also includes the ratio of selectivities along the two paths (i.e., Sel._{DiHPhe} + Sel._{asym-OHPhe} for path 1 and Sel._{TetHPhe} + Sel._{sym-OHPhe} for path 2). For all parent and HCl-treated formulations, the two primary products DiHPhe and TetHPhe accounted for a selectivity of more than 90% combined. Of the ‘deeper’ hydrogenated products, *asym*-OHPhe was hardly observed, while *sym*-OHPhe was found for catalysts with Ni contents higher than 0.15 mol_{Ni} mol_{metal}⁻¹. Here, for non-promoted bulk MoS₂ the initial selectivities were 86% for DiHPhe and 14% for TetHPhe, respectively, while no deep hydrogenation was observed. On the parent Ni_aMoS₂, the selectivities to DiHPhe and TetHPhe became comparable, a greater extent of deep hydrogenation (OHPhe formation) was observed and the overall reaction shifted in favor of path 2, in contrast to the unpromoted MoS₂. As previously observed for Ni-promoted MoS₂ supported on γ -Al₂O₃, the ratio of initial selectivities in phenanthrene hydrogenation is a strong indication for the Ni promotion of the MoS₂ slab;^[192] specifically, the selectivity shifts in favor of DiHPhe with decreasing degree of Ni incorporation at the slab edge. Selectivities were quite similar among Ni-promoted samples, irrespective of the Ni content.

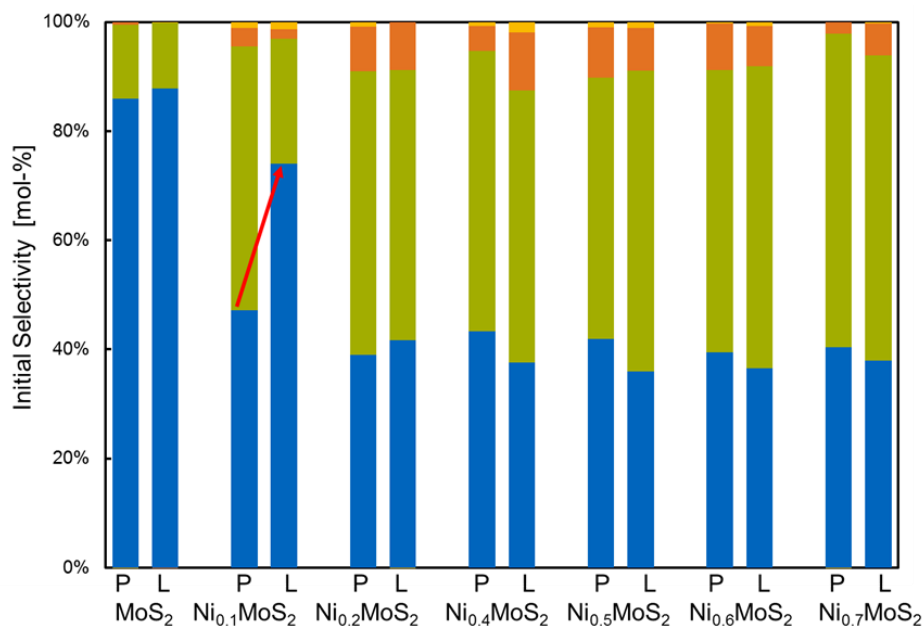


Figure 5-3. Initial selectivities obtained from extrapolation of product selectivities (measured at phenanthrene conversion of 10 – 20%) to zero contact time at 300°C and 60 bar total pressure. The arrow indicates a significant shift in the pathway ratio on the HCl-treated Ni_{0.1}MoS₂ toward that of a pure MoS₂ catalyst. Blue bar: DiHPhe; green bar: TetHPhe; yellow bar: *asym*-OPhe; orange bar: *sym*-OPhe.

For most catalysts, HCl treatment hardly changed the pathway ratio or slightly shifted it towards path 2, whereas the ‘leached’ Ni_{0.1}MoS₂ catalyst showed a marked shift towards path 1, moving closer to that of MoS₂ (Figure 5-3). Given the relation between Ni promotion and product distribution,^[192] the observation for Ni_{0.1}MoS₂ suggests that most of the promoted active sites have been eliminated after ‘leaching’ of this catalyst. This, in turn, strongly suggests that HCl is able to attack Ni²⁺ in the slab structure, in addition to segregated NiS_x. The same treatment, however, did not seem to cause the loss of Ni-promoted edge sites in other Ni_aMoS₂ catalysts. Thus, we hypothesize that HCl preferentially attacks NiS_x, unless the amount of such entities is small as in the case of Ni_{0.1}MoS₂. In this connection, we would like to point to the statistically less than 20% Ni edge substitution for Ni_{0.1}MoS₂, being much lower than for the other samples.

4.3.2. Effects of Ni content and HCl treatment on the hydrogenation rates

Table 5-3 lists the conversion rates of phenanthrene and the hydrogen-addition rates for the parent and HCl-treated Ni_aMoS₂ catalysts. Hydrogen addition rates plotted against the molar fraction of Ni among total metal are illustrated in Figure 5-4 for both sets of catalysts, while other plots are shown in Figure S 6-9 – Figure S 6-12. The rates follow a volcano-shaped curve for both parent and HCl-treated series of catalysts, with the maximum rate appearing at 0.32 mol_{Ni} mol_{metal}⁻¹ (Ni_{0.5}MoS₂-L). The maximum rate was rather close to that measured on Ni_{0.2}MoS₂-P. In terms of conversion rates normalized to total Mo content, the bulk Ni_aMoS₂ catalysts peaked at 1.9 mol_{Phe} mol_{Mo}⁻¹ h⁻¹, similar to the maximum rate (1.6 mol_{Phe} mol_{Mo}⁻¹ h⁻¹, also appearing at 0.33 mol_{Ni}

mol_{metal}⁻¹) measured for Al₂O₃-supported NiMoS₂ catalysts (with similar average slab lengths) at the same conditions.^[192] Similarly, other normalized rates at the maximum were also comparable on bulk and Al₂O₃-supported NiMoS₂ catalysts.

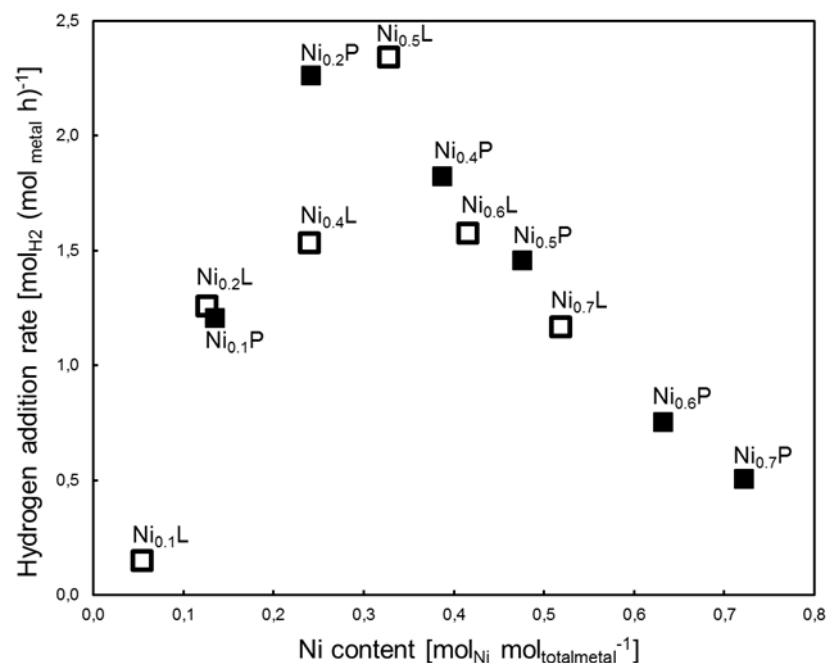


Figure 5-4. Hydrogen addition rates (calculated from the phenanthrene consumption and the moles of hydrogen consumed along each route) over the parent and HCl-treated Ni_aMoS₂ as a function of Ni content. Full squares represent the parent samples, while open squares correspond to the HCl-treated formulations.

On the multifaceted roles of NiS_x in hydrodearomatization reactions catalyzed by unsupported Ni-promoted MoS₂

Table 5-3. Hydrogenation rates of phenanthrene on the parent and HCl-treated formulations. The rates are obtained at 300°C and 60 bar H₂ pressure by varying the space time between 7-40 (h·g_{cat})/mol_{Phe,0}. The feed contained 1 wt.% Phe, 1000 ppmw S as dimethyl disulfide (DMS) and 2 wt% tetradecane as the internal standard in decalin. The ratio of H₂/hydrocarbons was 300 (v/v).

Catalysts	Conversion rates			H ₂ addition rates ^a	
	[mmol _{Phe} g _{cat} ⁻¹ h ⁻¹]	[mol _{Phe} mol _{metal} ⁻¹ h ⁻¹]	[mol _{Phe} mol _{Mo} ⁻¹ h ⁻¹]	[mol _{H2} mol _{Mo} ⁻¹ h ⁻¹]	[mol _{H2} mol _{metal} ⁻¹ h ⁻¹]
Ni _{0.1} MoS ₂ -P	4.6	0.7	0.9	1.4	1.2
Ni _{0.1} MoS ₂ -L	0.7	0.1	0.1	0.1	0.1
Ni _{0.2} MoS ₂ -P	8.6	1.3	1.7	3.0	2.3
Ni _{0.2} MoS ₂ -L	4.6	0.7	0.8	1.5	1.3
Ni _{0.4} MoS ₂ -P	7.5	1.1	1.8	3.0	1.8
Ni _{0.4} MoS ₂ -L	5.8	0.8	1.1	2.0	1.5
Ni _{0.5} MoS ₂ -P	6.0	0.8	1.6	2.8	1.5
Ni _{0.5} MoS ₂ -L	9.1	1.3	1.9	3.5	2.3
Ni _{0.6} MoS ₂ -P	3.6	0.4	1.1	2.0	0.8
Ni _{0.6} MoS ₂ -L	6.4	0.9	1.5	2.7	1.6
Ni _{0.7} MoS ₂ -P	2.7	0.3	1.1	1.8	0.5
Ni _{0.7} MoS ₂ -L	5.2	0.7	1.4	2.4	1.2

Let us now take a closer look at the individual series. Within the parent samples, the total-metal-based H₂-addition rate increased from 1.2 mol_{H2} mol_{metal}⁻¹ h⁻¹ (Ni_{0.1}MoS₂) to 2.3 mol_{H2} mol_{metal}⁻¹ h⁻¹ (Ni_{0.2}MoS₂). After passing the maximum, the rate decreased with increasing Ni content in the order of Ni_{0.4}MoS₂ (1.8 mol_{H2} mol_{metal}⁻¹ h⁻¹) > Ni_{0.5}MoS₂ (1.5 mol_{H2} mol_{metal}⁻¹ h⁻¹) > Ni_{0.6}MoS₂ (0.8 mol_{H2} mol_{metal}⁻¹ h⁻¹) > Ni_{0.7}MoS₂ (0.5 mol_{H2} mol_{metal}⁻¹ h⁻¹). This trend is explained by the presence of both active and inactive Ni-associated phases, the relative population of which changes with the Ni concentration. Increasing the Ni content initially increases the edge substitution by Ni and the number of promoted sites at the edge, leading to a better hydrogenation activity. Here, the fraction of metal atoms located at the slab edges is ~0.2 on average (Table 5-2). Therefore, a full Ni substitution of the edges was reached on Ni_{0.2}MoS₂ (0.24 mol_{Ni} mol_{metal}⁻¹), which was the most active formulation. Upon further increasing the amount of Ni in the catalysts, more and larger NiS_x crystallites form and segregate from the original slabs. Al₂O₃-supported nickel sulfide phase was previously shown to be inactive for the hydrogenation of phenanthrene^[192] and bulk NiS_x (at least the large crystallites) were found in this study to be inactive as well. Thus, these segregated Ni species contribute negligibly to the hydrogenation activity and represent

On the multifaceted roles of NiS_x in hydrodearomatization reactions catalyzed by unsupported Ni-promoted MoS₂

undesired inert mass, leading to an eventual drop of reaction rates on a mass or total metal basis. A fraction of (promoted) sites of the (Ni)MoS₂ slabs may be blocked by NiS_x, if they are located nearby, leading to a decrease in reaction rates even on a Mo basis.

Our prior study showed that HCl treatment of Al₂O₃-supported NiWS₂ catalysts selectively removed NiS_x and increased the mass-specific catalytic activity at high Ni loadings, while at low Ni loadings, HCl treatment did not change the overall activity.^[346] In the present work on unsupported NiMo sulfide catalysts, the effect of HCl treatment appears to be more intricate, depending on the nature of the parent samples, especially the original Ni concentration. For parent catalysts with Ni concentrations higher than 0.4 mol_{Ni} mol_{metal}⁻¹, H₂-addition rates (total metal based) increased on their HCl-treated counterparts, by 53% for Ni_{0.5}MoS₂, 100% for Ni_{0.6}MoS₂ and 140% for Ni_{0.7}MoS₂. For catalysts with original Ni contents lower than 0.4 mol_{Ni} mol_{metal}⁻¹, the HCl treatment had a negative impact on the reaction rate, which dropped by 17% on Ni_{0.4}MoS₂, 43% on Ni_{0.2}MoS₂ and 83% on Ni_{0.1}MoS₂ (Table 5-4).

Table 5-4. Comparison of the observed rate enhancement due to ‘leaching’ and the expected enhancement due to the loss of inactive mass.

Catalysts	Observed rate enhancement for H ₂ addition (r _{leached} /r _{parent})	Expected factor of H ₂ -addition rate increase due to the removal of inert mass (n _{Mo,leached} /n _{Mo,parent})
Ni _{0.1} MoS ₂	0.17	1.13
Ni _{0.2} MoS ₂	0.57	1.08
Ni _{0.4} MoS ₂	0.83	1.29
Ni _{0.5} MoS ₂	1.53	1.23
Ni _{0.6} MoS ₂	2.00	1.39
Ni _{0.7} MoS ₂	2.40	1.52

As discussed above, increases in reaction rates are partially due to the loss of inactive phases in the TMS catalysts. While a direct measurement of the mass loss during leaching was subject to large errors because of the difficulty in quantitative recovery of solids, the extent of mass loss can be calculated based on the elemental composition, by assuming the mass conservation of Mo that is minimally leachable in concentrated HCl. Since the removed mass is almost only composed of NiS_x, this factor (Table 5-4) also reflects a theoretical correction for the rate of a catalyst after removing (a portion of) these inactive phases.

Following this rationale, the reaction rate is expected to increase for all catalysts after HCl treatment. This is experimentally observed for Ni contents higher than 0.4 mol_{Ni} mol_{metal}⁻¹, yet the expected extents of rate enhancement merely due to inert mass removal are always smaller than the observed changes (Table 5-4). Therefore, we conclude that high Ni-loaded catalysts benefit

from leaching, by way of losing inactive large NiS_x particles and unblocking of active sites. In contrast, the effect of HCl treatment was more destructive for those with lower Ni contents, likely caused by the removal of small NiS_x clusters located at the edges of the (Ni)MoS₂ slabs or even the removal of promoting Ni atoms. Thus, we hypothesize that NiS_x has positive as well as negative roles in the hydrogenation of phenanthrene.

4.4 Phenanthrene hydrogenation on physical mixtures and stacked beds of Ni_mS_n and MoS₂

To better understand the roles of NiS_x particles in the hydrogenation of phenanthrene, the reaction was carried out on various physical mixtures of a homemade Ni_mS_n sample and MoS₂. These experiments were designed in a way akin to earlier works by Delmon and coworkers.^[120,350–352] Note that this Ni_mS_n sample was not active for this reaction. Mo-based H₂-addition rates (Table 5-5) were substantially enhanced (by a factor of 3.0-3.1 compared to pure MoS₂) on inter-particle mixtures containing Ni_mS_n and MoS₂ in mass ratios of 1:1 and 3:1. More remarkably, all physical mixtures showed a selectivity pattern similar to that of the Ni-promoted catalysts, with comparable selectivities to DiHPhe and TetHPhe and a lower-than-unity ratio (0.9) of path 1 and path 2 (Table 5-6). This means that a promotional effect arises even by physical contact of Ni_mS_n and MoS₂ particles, reminiscent of the “remote control/contact synergy” model.^[49,343,344]

Several NiS_x phases exhibit Tammann temperatures lower than 270°C. Thus, nickel sulfide particles are hypothesized to be highly mobile at the reaction temperature of 300°C. We hypothesize that nickel sulfide particles in an interparticle mixture provide a means to dynamically incorporate Ni into MoS₂ slabs under reaction conditions, accounting for the observed rate enhancement and selectivity shifts with physical mixtures of Ni_mS_n and MoS₂. At even higher mixing ratios of Ni_mS_n and MoS₂, H₂-addition rates normalized to Mo decreased and approached that of pure MoS₂, likely due to potential blockage of active sites with excessive presence of nickel sulfides in the vicinity of MoS₂.

Additionally, an experiment with separated beds of Ni_mS_n and MoS₂ by 4 mm of γ -Al₂O₃ was carried out (see Experimental). Separating Ni_mS_n from MoS₂ increased the H₂-addition rate by 83% (from 0.6 to 1.1 mol_{H2} mol_{Mo}⁻¹ h⁻¹), indicating that H₂ can be activated on Ni_mS_n and spill over to separated MoS₂ placed downstream. At the same time, the pathway ratio remained essentially the same as for the pure MoS₂, which indicates that no direct promotion occurred without physical contact and that the modest rate enhancement is only due to the increased supply of H-species via spillover. Since nickel sulfide particles are unable to traverse the long distance (4 mm) of the Al₂O₃ bed,^[120] this experiment serves to substantiate the local effect of NiS_x on the dynamic formation of Ni-promoted sites as observed for intimately mixed particles.

On the multifaceted roles of NiS_x in hydrodearomatization reactions catalyzed by unsupported Ni-promoted MoS₂

Table 5-5. Reaction rates of phenanthrene hydrogenation at 300°C and 60 bar total pressure on physical mixtures and stacked beds of Ni_mS_n and MoS₂.

Catalysts ^a	Ni/Mo [mol mol ⁻¹]	Reaction rates		
		[mol _{Phe} /(mol _{metal} h)]	[mol _{Phe} /(mol _{Mo} h)]	[mol _{H₂} mol _{Mo} h ⁻¹]
MoS ₂	0	0.53	0.53	0.61
MoS ₂ (undiluted)	0	0.54	0.54	0.63
Ni _m S _n /MoS ₂ (1:1)	2.0	0.39	1.17	1.9
Ni _m S _n /MoS ₂ (3:1)	6.2	0.16	1.16	1.8
Ni _m S _n /MoS ₂ (6:1)	12.2	0.04	0.47	0.7
Ni _m S _n /MoS ₂ (9:1)	22.7	0.03	0.61	0.9
Ni _m S _n -Al ₂ O ₃ - MoS ₂ (3:1) ^b	6.3	0.13	0.93	1.1

Table 5-6. Initial product selectivities of phenanthrene hydrogenation at 300°C and 60 bar total pressure obtained by extrapolating to zero contact time. Pathway ratio (path 1/path 2) is constant for Ni_mS_n/MoS₂ mixtures. For stacked beds of Ni_mS_n and MoS₂ separated by 4 mm γ-Al₂O₃, the ratio was shifted to that measured for pure MoS₂.

Catalysts ^a	Initial selectivities (%)				Pathway ratio
	DiHPhe	TetHPhe	sym-OHPhe	asym-OHPhe	
Ni _m S _n /MoS ₂ (1:1)	45	52	2	1	0.9
Ni _m S _n /MoS ₂ (3:1)	47	52	1	0	0.9
Ni _m S _n /MoS ₂ (6:1)	48	52	0	0	0.9
Ni _m S _n /MoS ₂ (9:1)	47	53	0	0	0.9
Ni _m S _n -Al ₂ O ₃ - MoS ₂ (3:1) ^b	84	16	0	0	5.3

^a Values in parentheses are the mass ratio of Ni_mS_n and MoS₂. The total mass of the catalyst bed was kept identical in all experiments. ^b Ni_mS_n and MoS₂ was separated by a 4 mm bed of γ-Al₂O₃.

4.5 Structure-activity correlations for promoted and unpromoted sites in bulk Ni_aMoS₂

Transmission infrared (IR) spectroscopy was previously applied to determine the surface density of (potentially) catalytically relevant sites on supported sulfide samples with good IR light transmissibility.^[193,346] However, for bulk sulfide catalysts, we failed to obtain IR spectra. In this final section, we attempt to correlate the hydrogenation rates of the HCl-treated Ni_aMoS₂ catalysts with the concentrations of coordinatively unsaturated sites (CUS) determined using the chemisorption of nitrogen monoxide (NO).^[173,353]

Values of NO uptakes are compiled in Table S 6-11. As described earlier, HCl treatment caused varying degrees of changes to the textural properties of the bulk catalysts, especially Ni_{0.1}MoS₂ and Ni_{0.4}MoS₂, though the primary slab structure was not significantly affected. For a fair comparison of activities of different parent and HCl-treated formulations, H₂-addition rates and NO uptakes were normalized by the specific surface area (Figure 5-5).

The Ni_mS_n sample had a small BET surface area (11 m² g⁻¹) but showed a considerable NO uptake (35 μmol g⁻¹). This sample was inactive for phenanthrene hydrogenation under the conditions studied. Since parent catalysts with high Ni contents, especially Ni_{0.6}MoS₂ and Ni_{0.7}MoS₂, contain a great number of nickel sulfide crystallites, the correlation between catalytic activity and NO uptake was poor among the parent samples (filled squares in Figure 5-5). HCl treatment removes a substantial portion of the large nickel sulfide crystallites and allows gaining increased access of reactant and site-specific probe molecules (such as NO) to the active sites located at the edge of the (Ni)MoS₂ slab. Given that NiS_x at accessible surfaces had been successfully removed by HCl, an improved correlation between catalytic activity and NO uptake was expected for the leached series, as was indeed observed, except for the leached Ni_{0.1}MoS₂ (Figure 5-5). Parent samples without too many nickel sulfide particles, Ni_aMoS₂ (a = 0.1-0.5), appear to lie along the same trend line, albeit with pronounced scatter.

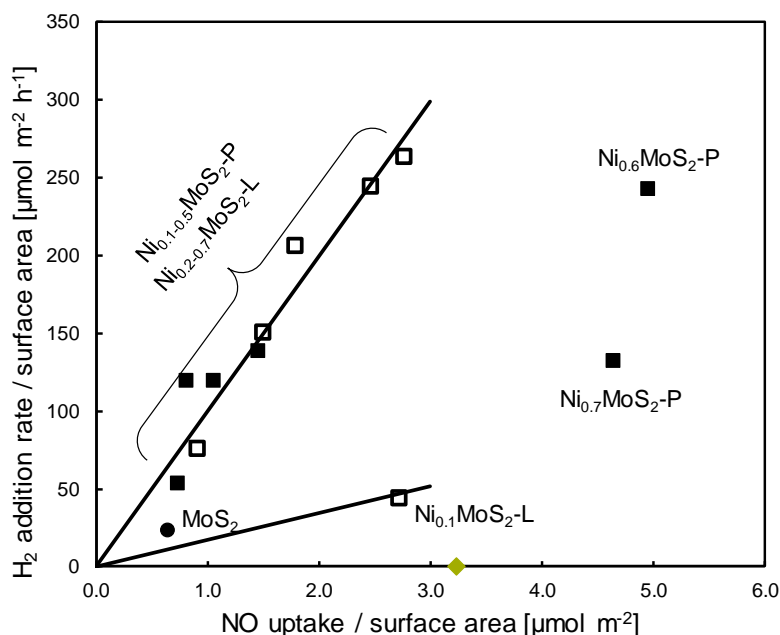


Figure 5-5. Hydrogen addition rate (calculated from the phenanthrene consumption and the moles of hydrogen consumed along each route) as a function of NO uptake, both normalized to the specific surface area. Open squares represent the leached versions of the parent samples (filled squares), unpromoted MoS₂ is identified via the filled circle. The slopes of the lines can be interpreted as quasi-TOFs for the promoted (100 h⁻¹) and non-promoted sites (17 h⁻¹), respectively.

By normalizing the measured rates against the corresponding NO uptakes, we were able to obtain quasi-TOF (“TOF”), a site-specific activity that does not take into account the dependence of site density on the conditions (primarily, temperature, pressure and H₂S/H₂ ratio). For all leached samples except Ni_{0.1}MoS₂-L, a steeper slope is observed, corresponding to an estimated “TOF” of 100 h⁻¹ that represents the H₂-addition activity of Ni-promoted CUS at the slab of MoS₂. It is likely that the degree of Ni edge substitution is high in those samples and the activity is predominantly contributed by promoted CUS, which is probed by NO and not heavily blocked by NiS_x. The Ni_{0.1}MoS₂-L catalyst can be readily identified as an outlier in the leached series, exhibiting a significantly smaller H₂-addition “TOF” of 17 h⁻¹ that is comparable to that of pure MoS₂. Recall that this catalyst behaved kinetically similar to a non-promoted MoS₂ catalyst in terms of the pathway ratio. Together, these results speak strongly for the fact that a majority of Ni atoms incorporated at the slab edge have been removed in this particular sample. The TOFs calculated based on phenanthrene conversion are 55 and 8.7 h⁻¹ for promoted and non-promoted CUS, respectively. Notably, the 6-time difference in the “TOFs” between promoted and unpromoted sites is similar in magnitude to that reported previously for Al₂O₃-supported Ni-Mo sulfide catalysts at the same reaction conditions,^[193] in that work, TOFs of the Ni-promoted and non-promoted sites were 40 and 6 h⁻¹, respectively, albeit with a different method (based on SH counts and IR spectroscopy) to enumerate active sites.

4.6 On the complexity of the HCl treatment

In a most recent study,^[286] we applied the HCl treatment to a series of unsupported NiMo sulfides containing high concentrations of Ni (0.48-0.60 atomic metal fraction). For those compact (less porous) NiMo sulfides, a significant portion (but not all) of NiS_x was found to be selectively removed by the HCl extraction whereas the decorated NiMoS phase stayed intact. Unsupported NiMo sulfides studied in the present work exhibited very different textural properties and morphologies (Figure S 6-6 – S 3); in general, the samples used here were a lot more porous, and the Ni contents varied in a much wider range (0.13-0.72 atomic metal fraction). For all Ni-loaded samples except for Ni_{0.1}MoS₂, we reached the same conclusion as in the previous work for unsupported NiMo sulfide samples with relatively high Ni loadings, i.e., the edge-incorporated Ni remained intact upon HCl attack.

However, the effects of HCl treatment turned out to be more intricate than we had thought. Two distinct observations have surfaced from this study: (1) HCl treatment caused the removal of edge-incorporated Ni from the slab for the lowest-Ni-content sample (Ni_{0.1}MoS₂); (2) HCl treatment caused the decrease in catalytic activity for less Ni-loaded catalysts. It appears that removing NiS_x on high-Ni-loaded samples universally increases the accessible surfaces; this is seen from the generally increased surface areas and pore volumes after HCl treatment of such samples in our previous and this work. This is the main driver behind the rate enhancement. On the other hand, for parent catalysts with lower Ni contents (i.e., < 0.4 mol_{Ni} mol_{metal}⁻¹) and less (and likely smaller) NiS_x, the accessibility of the NiMoS phase is most likely no longer the limiting factor, and the major consequence of removing NiS_x turns detrimental, probably because (i) sites on NiS_x surfaces can serve to dissociate H₂ and (ii) structural stability against HCl attack is compromised, the cause of which remains unclear. In the extreme case of Ni_{0.1}MoS₂, without enough NiS_x at the periphery, a loss of edge-incorporated Ni even occurred, leading to a drastic rate loss (Table 5-3).

Summarizing, only high-Ni-loaded unsupported sulfides were used in our previous works,^[286,330] while this study expanded the range of Ni contents to encompass those compositions that corresponded to less-than-complete edge substitution. The added value of this work lies in this extension and the implications of the complex trends as discussed above, providing a more comprehensive view on the roles of NiS_x. Admittedly, there is a lot more to understand about this leaching procedure and a more systematic investigation of the process variables (duration, temperature, exposure to air, etc.) needs to be carried out in the future.

5 Conclusion

We have shown for the catalytic hydrogenation of phenanthrene that the ubiquitous presence of separate NiS_x phases in unsupported Ni-Mo binary sulfide catalysts has multiple consequences, some being detrimental to catalytic activity, some being beneficial. These phases are inherently much less active than unpromoted and promoted sites in (Ni)MoS₂ slabs, but under reaction conditions, they are potentially able to dynamically incorporate Ni into slabs originally without Ni or with low edge substitution degrees. NiS_x can also activate H₂, and because of the higher surface-to-volume ratios, small particles, which are more prevalent in low Ni-content samples, do so more efficiently than large particles, which are more frequently found on high Ni-content samples. Therefore, the combined effects of nickel sulfide phases on the hydrogenation activity depend on the Ni content, which determines the abundance and size of these entities.

Post-synthetic treatment of high Ni-content (e.g., > 0.4 molNi mol_{metal}⁻¹ as investigated in this work) bulk sulfide catalysts with concentrated HCl successfully dissolves large crystallites of NiS_x at accessible surfaces, leading to a reduction of catalytically inactive sulfides and an increased exposure of active sites. These two primary positive consequences overcompensate the loss of some entities that are able to provide additional H₂ activation sites, and, thus, the mass-specific and total-metal-based reaction rates of these catalysts are significantly enhanced. This leaching strategy, however, is associated with the risk of leaching Ni-promoted active sites within the slabs of the main active phase, particularly when the amount of NiS_x is insufficient to retard the attack of HCl on the primary slab structure. For the lowest Ni-loaded catalyst studied here (0.05 molNi mol_{metal}⁻¹), HCl treatment caused a catastrophic loss of catalytic activity by a factor of > 6, and even shifted the selectivity pattern to that of pure MoS₂. Such selectivity shifts were not captured on other catalysts. These observations, together with the sensitivity of the regioselectivity to Ni promotion for this reaction, lead us to conclude that Ni atoms incorporated at the slab edges are inherently susceptible to HCl attack, but NiS_x appear to be the preferential sites where HCl attack and dissolution starts. Disrupting the Ni-promoted sites and reducing the small NiS_x are the two major causes for the substantially decreased rates on low Ni-content samples upon the HCl treatment.

Finally, we have demonstrated that HCl treatment leads to a greatly improved correlation between areal activity and the areal concentration of chemisorbed NO on the leached catalysts, with the exception of the lowest Ni-containing one. By estimating its Ni content and the fraction of edge atoms, we conclude that this catalyst has a low edge substitution degree of Ni (< 30% at the slab edge) and contains a predominant fraction of edge sites as unpromoted sites. The slope of the linear correlation indicates that the Ni-promoted active sites in NiMoS₂ are more than five times as active as the unpromoted sites, a similar enhancement factor compared to that observed earlier for the Al₂O₃-supported counterparts.

6 Acknowledgement

This work was financially supported by the Chevron Energy Technology Company. The authors would like to especially thank Dr. Alexander Kuperman, Dr. Axel Brait, and Prof. Roel Prins for fruitful discussions. We are also grateful to the members of TU München for their support in different ways, especially Ulrike Ammari (Elemental Analysis), Roland Weindl (TEM) and Xaver Hecht (technical support).

7 Addendum to ‘multifaceted roles of NiS_x’

7.1 Preface

In the above study, Ni_aMoS₂ catalysts were exposed to HCl treatment, the so-called ‘leaching’. One characteristic of the applied protocol was that the time span was fixed to 3 times in an hour independent of the formulation (Ni content of the material). In each case the third batch of leaching was colorless (Ni²⁺ in water appeared green) indicating a final state of NiS_x removal. According to XRD pattern analysis (Figure 5-2) high Ni-content catalysts still showed NiS_x phases after leaching. Further, the activity of Ni_{0.5}MoS₂-L, Ni_{0.6}MoS₂-L and Ni_{0.7}MoS₂-L in hydrogenation was still on the declining side of the H₂-addition-rate vs. Ni content plot (Figure 5-4). Therefore two questions were open, one if it was possible to further leach high-Ni content catalysts to remove large NiS_x particles still present at the slab blocking active sites and to obtain an optimal activity, and second if a catalyst could be ‘over-leached’ meaning that too harsh leaching removes promoting Ni atoms out of the slab even for parent formulations with Ni content >50%.

Last but not least the study was extended to Ni_aWS₂ catalysts. Its aim was to amplify the concept of leaching and site quantification (NO uptake) to a larger set of catalysts and to compare the site specific activity of Mo and W based sulfides. Although Ni promoted W-based sulfides are more active in hydrogenation reaction than their NiMoS counterparts the two formulations are isostructural (chapter 2, section 1.3) and therefore similar site specific activity is expected.^[46,193,264,308,354,355]

In the following experimental conditions and basic characterization of prolonged leaching of Ni_{0.5}MoS₂ and Ni_{0.7}MoS₂ and leaching of some Ni_aWS₂ is presented and their catalytic activity for phenanthrene hydrogenation is evaluated.

7.2 Experimental and characterization

All Ni_aWS₂ were synthesized via the thiosalts method described in Chapter 3. The Mo based catalyst parent formulations are identical to the ones presented in the *Journal of Catalysis* publication reprinted above. For ‘leaching’ of the W-based catalysts the same method as described in the publication was applied while leaching of high Ni molybdenum sulfides was extended. First, 400 mg of Ni_{0.7}MoS₂-P and Ni_{0.5}MoS₂-P were put into a 5 mL glass tube and 3 mL conc. HCl were added. After 1 h the HCl was replenished. After 5 repetitions the catalysts were once more exposed to HCl and kept overnight. Then, the catalyst was washed several times with water and re-sulfided as described above. The obtained formulations are denoted as Ni_{0.7}MoS₂-L_{long} and Ni_{0.5}MoS₂-L_{long} respectively.

Another experiment was conducted using the resulfided Ni_{0.5}MoS₂-L_{long} formulation. About 150 mg of the catalyst were treated with 3 mL HCl again. Although the solution was clear after the last step during the first leaching, after resulfidation a green color appeared again. The catalyst was leached 5 times and one additional over-night step again and resulfided. It is further denoted as Ni_{0.5}MoS₂-L_{over leached}.

The studied catalysts were characterized by elemental analysis, XRD and N₂-physisorption as well as NO pulsing in the same way as described in the publication above. Phenanthrene hydrogenation was studied in the same set-up and under the same reaction conditions as above (300 °C, 60 bar total pressure, 1 wt.-% in decalin, 300 (v/v) gas to hydrocarbons) and initial hydrogen addition rates as well as initial selectivities (delplot technique) were obtained accordingly.

7.3 Over leaching of Ni_{a>0.5}MoS₂

7.3.1 Results

Additional HCl treatment affected the Ni concentration in Ni_aMoS₂ in the following way (elemental analysis data compiled in Table 5-7): a long-duration leaching of NiS_x caused a further drop in Ni content of 0.48 (P) – 0.33 (L) – 0.14 (L_{long}) mol_{Ni} mol_{total metal}⁻¹ for Ni_{0.5}MoS₂ and 0.72 (P) – 0.52 (L) – 0.18 (L_{long}) mol_{Ni} mol_{total metal}⁻¹ for Ni_{0.7}MoS₂. In the case where the resulfided Ni_{0.5}MoS₂-L_{long} catalyst was leached again, the Ni content even dropped further to 0.09 mol_{Ni} mol_{total metal}⁻¹. This additional decrease of NiS_x phases is represented by the XRD patterns in Figure 5-6. The samples Ni_aMoS₂-L (leached for 3 h) still exhibit NiS_x phases indicating an unfinished leaching. The long time leached samples show a pattern similar to unpromoted MoS₂ and no sharp reflections for NiS_x are found. Further, the fluorescence (constant increase of the baseline) of these samples is much lower than for high Ni containing ones.

For Ni_{0.7}MoS₂-L_{long} the measured BET surface area of 38 m² g_{cat}⁻¹ was lower than obtained after 3 h leaching (61 m² g_{cat}⁻¹). A NO uptake by volumetric pulsing was determined to 130 μmol g_{cat}⁻¹ (Table 5-8).

On the multifaceted roles of NiS_x in hydrodearomatization reactions catalyzed by unsupported Ni-promoted MoS₂

Table 5-7. Elemental composition of long time leached Ni_aMoS₂ and synthesized Ni_aWS₂ catalysts parent and leached.

Catalysts	Ni ^[a] [mmol g _{cat} ⁻¹]	Mo/W ^[a] [mmol g _{cat} ⁻¹]	S ^[a] [mmol g _{cat} ⁻¹]	S/metal [mol/mol]	Atomic Ni fraction [mol _{Ni} mol _{metal} ⁻¹]
Ni _{0.5} MoS ₂ -P ^[b]	3.5 (2.3)	3.9 (4.8)	11.6 (12.5)	1.6 (1.8)	0.48 (0.33)
Ni _{0.5} MoS ₂ -L _{long}	0.9	5.6	12.1	1.9	0.14
Ni _{0.5} MoS ₂ -L _{over leached}	0.6	5.9	12.3	1.9	0.09
Ni _{0.7} MoS ₂ -P ^[b]	6.4 (4.0)	2.5 (3.8)	11.9 (12.1)	1.3 (1.6)	0.72 (0.52)
Ni _{0.7} MoS ₂ -L _{long}	1.2	5.4	12.4	1.9	0.18
WS ₂ ^[c]	0	3.6	8.7	2.4	0
Ni _{0.2} WS ₂ ^[c]	1.1 (1.0)	3.4 (3.5)	8.3 (8.3)	1.8 (1.8)	0.24 (0.22)
Ni _{0.5} WS ₂	3.1 (2.3)	2.6 (2.8)	8.0 (8.9)	1.4 (1.7)	0.54 (0.45)
Ni _{0.7} WS ₂	4.4 (4.0)	1.7 (2.0)	5.8 (8.7)	1.0 (1.5)	0.72 (0.67)

^[a]Values in parenthesis correspond to the leached material (3 h).

^[b]Data obtained from Table 5-1.

^[c]See also next chapter, Table 5-8.

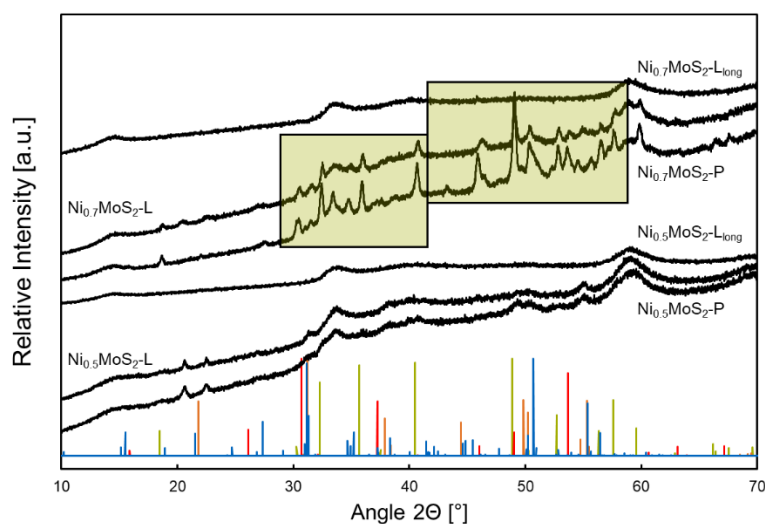


Figure 5-6. XRD patterns of the parent and leached Ni_aMoS₂ formulations. The green boxes indicate large NiS_x particles present and clearly observable in the high Ni content catalysts. The stick patterns of four reference substances (obtained from Highscore database) are shown at the bottom: blue, godlevskite (Ni₉S₈); green, millerite (NiS); orange, heazlewoodite (Ni₃S₂); red, polydymite (Ni₃S₄).

On the multifaceted roles of NiS_x in hydrodearomatization reactions catalyzed by unsupported Ni-promoted MoS₂

Table 5-8. Hydrogenation rates of phenanthrene on the parent and HCl-treated formulations. The rates are obtained at 300°C and 60 bar H₂ pressure by varying the space time between 7-40 (h·g_{cat})/mol_{Phe,0}. The feed contained 1 wt.% Phe, 1000 ppmw S as dimethyl disulfide (DMDS) and 2 wt% tetradecane as the internal standard in decalin. The ratio of H₂/hydrocarbons was 300 (v/v). Additionally, initial selectivities and physical characteristics of the formulations are presented.

Catalysts	Phe conversion ^[a] rates		H ₂ addition rates ^[a]	Observed rate enhancement for H ₂ addition (r _{leached} /r _{parent})	Expected factor of H ₂ -addition rate increase due to the removal of inert mass (n _{Mo/W,leached} /n _{Mo/W,parent})	NO uptake ^[a] [μmol g _{cat} ⁻¹]	BET surface area ^[a] [m ² g _{cat} ⁻¹]	Initial selectivities ^[c] [%]				Pathway ratio
	[mmol _{Phe} g _{cat} ⁻¹ h ⁻¹]	[mol _{Phe} mol _{metal} ⁻¹ h ⁻¹]	[mol _{H₂} mol _{metal} ⁻¹ h ⁻¹]					DiHPhe	TetHPhe	<i>sym</i> -OHPhe	<i>asym</i> -OHPhe	
Ni _{0.5} MoS ₂ ^[b]	6.0 (9.1)	0.8 (1.3)	1.5 (2.3)	1.53	1.23	73 (143)	90 (80)	42 (36)	48 (55)	9 (8)	1 (1)	0.7 (0.6)
Ni _{0.5} MoS ₂ -L _{long}	11.4	1.7	3.0	2.0	1.44	n.a.	n.a.	39	56	4	1	0.7
Ni _{0.5} MoS ₂ -L _{over leached}	1.9	0.3	0.4	0.27	1.51	n.a.	n.a.	57	43	0	0	1.3
Ni _{0.7} MoS ₂ ^[b]	2.7 (5.2)	0.3 (0.7)	0.5 (1.2)	2.40	1.52	157 (91)	34 (61)	41 (38)	57 (56)	2 (6)	0 (0)	0.7 (0.6)
Ni _{0.7} MoS ₂ -L _{long}	8.0	1.2	2.3	4.60	2.16	130	38	36	52	11	1	0.6
MoS ₂ ^[b]	2.8	0.5	0.6	-	-	90	140	86	14	0	0 (0)	6.1
WS ₂	1.1	0.3	0.4	-	-	68	35	85	15	0	0	5.8
Ni _{0.2} WS ₂	4.1 (8.1)	0.9 (1.8)	1.9 (3.7)	2.58	1.02	122 (136)	109 (91)	36 (42)	42 (34)	21 (21)	3 (3)	0.6 (0.8)
Ni _{0.5} WS ₂	9.3 (10.9)	1.6 (2.1)	3.4 (4.3)	1.26	1.08	78 (243)	36 (81)	41 (40)	34 (38)	21 (18)	4 (4)	0.8 (0.8)
Ni _{0.7} WS ₂	8.1 (8.9)	1.3 (1.5)	2.6 (2.9)	1.11	1.18	24 (185)	77 (96)	38 (37)	46 (48)	15 (13)	1 (2)	0.6 (0.6)

^[a]Values in parenthesis correspond to leached formulations (3 hours).

^[b]Data obtained from Table 5-3, Table 5-4 and Table 5-2.

^[c]Determined by extrapolation of product selectivities measured at phenanthrene conversions of 10–20% to zero contact time.

Table 5-8 compares the reaction rates of Ni_aMoS₂ leached for phenanthrene hydrogenation and the thereof calculated H₂-addition. Long time leaching increase the catalysts activity in both cases from 1.5 (P) – 2.3 (L) – 3.0 (L_{long}) mol_{H₂} mol_{metal}⁻¹ h⁻¹ for Ni_{0.5}MoS₂ and from 0.5 (P) – 1.2 (L) – 2.3 (L_{long}) mol_{H₂} mol_{metal}⁻¹ h⁻¹ for Ni_{0.7}MoS₂. The calculated expected factor of H₂-addition rate increase due to the removal of inert mass was lower than the observed rate enhancement. This situation changed when Ni_{0.5}MoS₂-L_{long} after resulfidation was further exposed to HCl for overnight. The rate dropped to 0.4 mol_{H₂} mol_{metal}⁻¹ h⁻¹ and the rate enhancement, 0.27, was much lower than an expected one, 1.51, due to ‘inert’ mass removal.

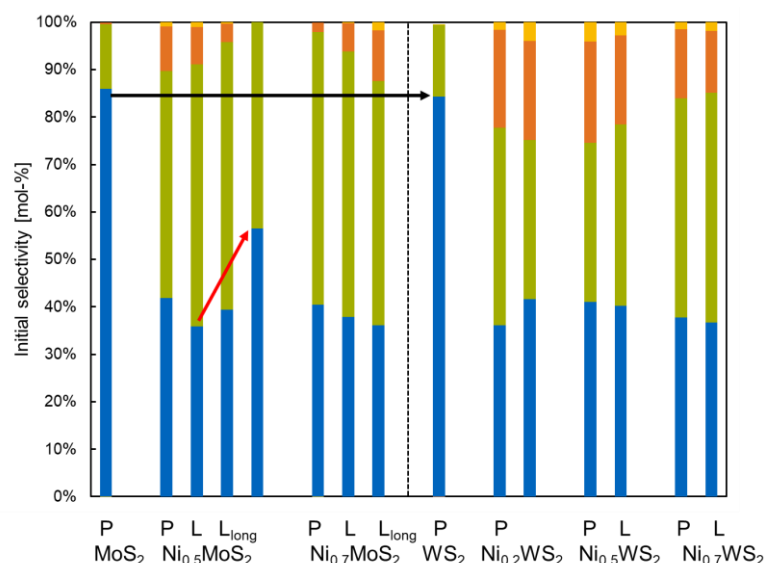


Figure 5-7. Initial selectivities obtained by extrapolation of S – X plots to zero contact time (delplot technique). Colors: Blue, DiHPhe; green, TetHPhe; orange, *sym*-OHPhe and yellow, *asym*-OHPhe. Left: Comparison of long time leached Ni_aMoS₂ catalysts. The red arrow indicates a shift of pathway to DiHPhe (symmetric hydrogenation) a typical pattern for unpromoted Mo/WS₂ catalysts as seen on the very left and the first bar on the right side of the presentation. Right: Initial selectivities for Ni_aWS₂ formulations parent and leached. Here, leaching does not affect the reaction pathway.

Reaction pathway analysis for phenanthrene hydrogenation using the delplot technique showed that long time leaching does not change the pathway ratio which is constant at 0.6 to 0.7 symmetric to asymmetric hydrogenation. Over-leaching shifts the ratio to 1.3 in favor to formation of DiHPhe (Table 5-8 and Figure 5-7).

7.3.2 Discussion

In order to support the conclusions drawn in the above presented publication the experiments of long time (additional) leaching and over-leaching were conducted. It was shown that longer (better: more repetitions) of HCl treatment removed more Ni present as NiS_x (see XRD patterns) at the MoS₂ slabs edges compared to a 3 h leaching. This is still beneficial for the hydrogenation of phenanthrene since more active sites were opened up due to the removal of large inert particles. This had no effect on the reaction pathway and is in line with previous results and

proves that the Ni incorporated in the slab stayed untouched. The selectivity pattern is typical for Ni promoted MoS₂ catalysts. However, the catalysts fit into the volcano type shape of the activity vs. Ni content diagram (Figure 5-8). Ni_{0.7}MoS₂-l_{long} already is located on the left hand side of the curve which represents the attack of incorporated Ni by HCl. Anyhow, the effect is not severe and the catalyst ends up in the area of high active catalysts (Ni content around 0.2–0.3 mol_{Ni} mol_{metal}⁻¹). Although the Ni_{0.5}MoS₂-l_{long} catalyst falls on the left hand side of the diagram as well, the activity is the highest measured in this study. Here, the optimum ‘leaching’ is applied so that most of the ‘inert’ NiS_x phases are removed while the slab incorporated Ni is present and can offer its full potential for hydrogenation.

This situation changes when the resulfided catalysts is further leached. Its activity drastically drops down the decreasing line in Figure 5-8. Here, the additional (too often) leaching attacks the active centers (Ni = 0.09 mol_{Ni} mol_{metal}⁻¹) of the catalyst resulting in an activity similar to the leached Ni_{0.1}MoS₂-L (Ni = 0.05 mol_{Ni} mol_{metal}⁻¹). The samples also share the selectivity shift to DiHPhe (compare Figure 5-3 and Figure 5-7) which is a strong indication for a loss in Ni promoted sites.

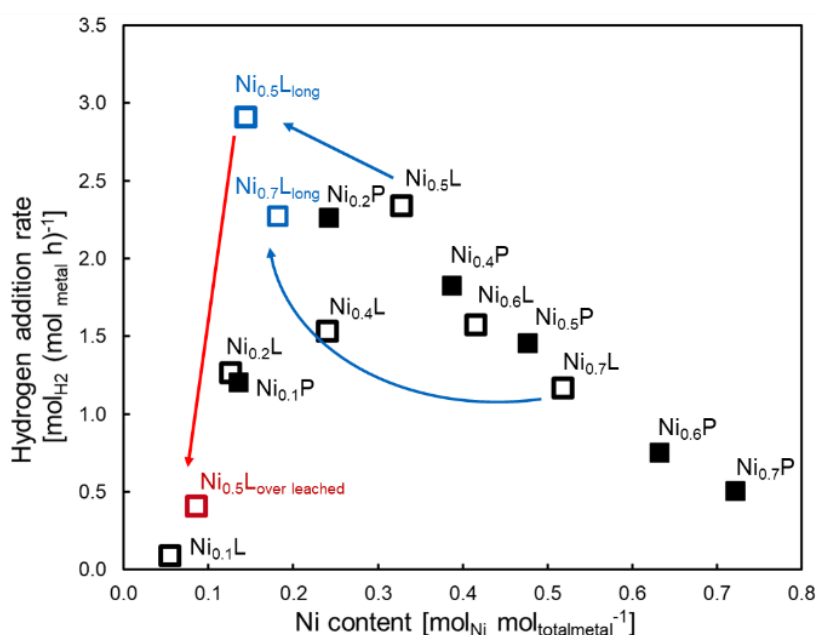


Figure 5-8. Extended Figure 5-4 by long time and over-leached samples. Hydrogen addition rates over the parent and HCl-treated Ni_aMoS₂ as a function of Ni content. Full squares represent the parent samples, while open squares correspond to the HCl-treated formulations. Blue open squares show the increase of activity for long time leached samples while the red open square represents the over leached sample with a low activity similar to disrupted Ni_{0.1}L.

To sum up these experiments, it is clearly shown that leaching of Ni_aMoS₂ has two effects on the activity for hydrogenation reactions. First, the removal of inert mass has to be controlled up to the point where no innocent NiS_x particles are left. Second, when this point is reached, additional leaching is disadvantageous to the activity because incorporated Ni is removed. All formulations

should be able to ‘move’ along the volcano shaped curve of activity vs. Ni content. The selectivity pattern of phenanthrene hydrogenation is an excellent hint for Ni removal out of the MoS₂ slab due to its sensitive response to promoted and unpromoted sites.

7.4 Leaching of Ni_aWS₂

7.4.1 Results

Four different Ni_aWS₂ were successfully synthesized by the thiosalt synthesis route in order to obtain formulations comparable to Ni_aMoS₂ studied before. The Ni content of the parent sulfides (Table 5-7) was determined to $a = 0.0, 0.24, 0.54$ and $0.72 \text{ mol}_{\text{Ni}} \text{ mol}_{\text{metal}}^{-1}$. The BET surface area of the samples was in the range of Ni_aMoS₂ catalysts in the order of Ni_{0.2}WS₂ ($109 \text{ m}^2 \text{ g}_{\text{cat}}^{-1}$) > Ni_{0.7}WS₂ ($77 \text{ m}^2 \text{ g}_{\text{cat}}^{-1}$) > Ni_{0.5}WS₂ ($36 \text{ m}^2 \text{ g}_{\text{cat}}^{-1}$) \approx Ni_{0.0}WS₂ ($35 \text{ m}^2 \text{ g}_{\text{cat}}^{-1}$). Note, that the unpromoted Ni_{0.0}WS₂ exhibited a much smaller area than the unpromoted Ni_{0.0}MoS₂ ($140 \text{ m}^2 \text{ g}_{\text{cat}}^{-1}$) counterpart. Volumetric pulsing of nitric oxide resulted in uptake values of Ni_{0.2}WS₂ ($122 \mu\text{mol}_{\text{NO}} \text{ g}_{\text{cat}}^{-1}$) > Ni_{0.5}WS₂ ($78 \mu\text{mol}_{\text{NO}} \text{ g}_{\text{cat}}^{-1}$) > Ni_{0.0}WS₂ ($68 \mu\text{mol}_{\text{NO}} \text{ g}_{\text{cat}}^{-1}$) \approx Ni_{0.7}WS₂ ($24 \mu\text{mol}_{\text{NO}} \text{ g}_{\text{cat}}^{-1}$).

Initial reaction rates of Ni_aWS₂-P for hydrogenation of phenanthrene were determined at 300°C and 60 bar total pressure and compared to Ni_aMoS₂-P. The activity order was Ni_{0.5}WS₂ ($3.4 \text{ mol}_{\text{H}_2} \text{ mol}_{\text{metal}}^{-1} \text{ h}^{-1}$) > Ni_{0.7}WS₂ ($2.6 \text{ mol}_{\text{H}_2} \text{ mol}_{\text{metal}}^{-1} \text{ h}^{-1}$) > Ni_{0.2}WS₂ ($1.9 \text{ mol}_{\text{H}_2} \text{ mol}_{\text{metal}}^{-1} \text{ h}^{-1}$) \gg Ni_{0.0}WS₂ ($0.4 \text{ mol}_{\text{H}_2} \text{ mol}_{\text{metal}}^{-1} \text{ h}^{-1}$) and initial selectivity analysis gave a pathway ratio of 0.6 to 0.8 for promoted and 5.8 for unpromoted Ni_aWS₂ (Figure 5-7).

Leaching reduced the Ni content to $a = 0.22, 0.45$ and 0.67 respectively. This decrease was smaller than for the Mo based sulfides. The low Ni content Ni_{0.2}WS₂ lost 9 % (Ni_{0.2}MoS₂: 50%), Ni_{0.5}WS₂ lost 26 % (Ni_{0.5}MoS₂: 34%) and Ni_{0.7}WS₂ lost 9 % (Ni_{0.7}MoS₂: 38%) of nickel. Anyhow, the XRD pattern (Figure 5-9) of the W based sulfides did not show large particles of NiS_x neither for parent nor for leached samples. With the loss of NiS_x the BET surface area of Ni_{0.7}WS₂ and Ni_{0.5}WS₂ increased to $96 \text{ m}^2 \text{ g}_{\text{cat}}^{-1}$ and $81 \text{ m}^2 \text{ g}_{\text{cat}}^{-1}$, respectively while the area of Ni_{0.2}WS₂ slightly decreased to $91 \text{ m}^2 \text{ g}_{\text{cat}}^{-1}$. The NO uptake for all formulations increased to Ni_{0.5}WS₂-L ($243 \mu\text{mol}_{\text{NO}} \text{ g}_{\text{cat}}^{-1}$) > Ni_{0.7}WS₂-L ($185 \mu\text{mol}_{\text{NO}} \text{ g}_{\text{cat}}^{-1}$) > Ni_{0.2}WS₂-L ($136 \mu\text{mol}_{\text{NO}} \text{ g}_{\text{cat}}^{-1}$).

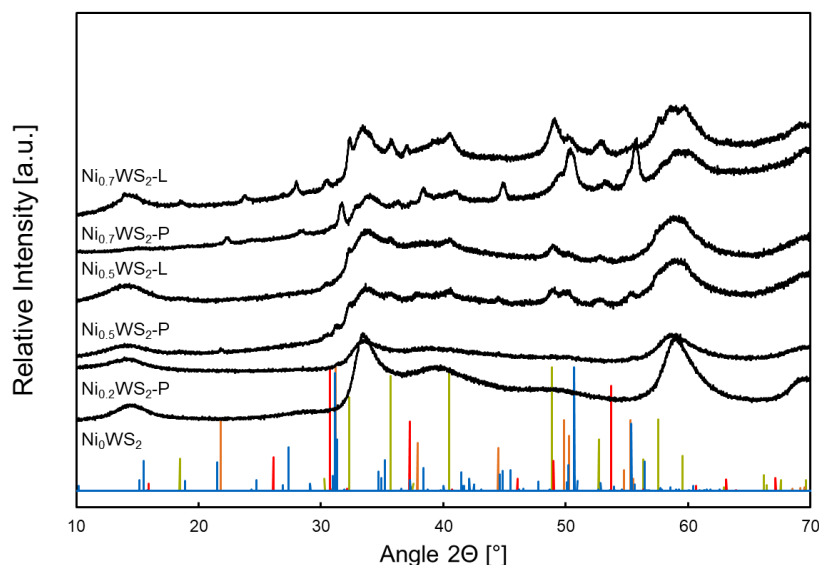


Figure 5-9. XRD patterns of the parent and leached Ni_aWS₂ formulations. The stick patterns of four reference substances (obtained from Highscore database) are shown at the bottom: blue, godlevskite (Ni₉S₈); green, millerite (NiS); orange, heazlewoodite (Ni₃S₂); red, polydymite (Ni₃S₄).

Leaching increased the reaction rates for all three formulations with the highest benefit for Ni_{0.2}WS₂-P. The activity order was Ni_{0.5}WS₂-L (4.3 mol_{H₂} mol_{metal}⁻¹ h⁻¹) > Ni_{0.2}WS₂-L (3.7 mol_{H₂} mol_{metal}⁻¹ h⁻¹) > Ni_{0.7}WS₂-L (2.9 mol_{H₂} mol_{metal}⁻¹ h⁻¹) and the initial selectivities remained unchanged (Figure 5-7 and Table 5-8). Rate enhancement was higher than the rate increase due to loss of ‘inert’ mass for Ni_{0.5}WS₂ and Ni_{0.2}WS₂ and almost identical for Ni_{0.7}WS₂.

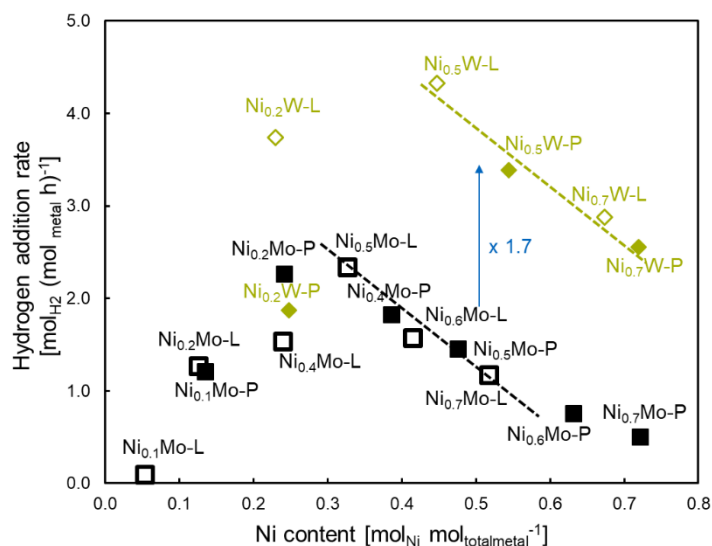


Figure 5-10. Hydrogen addition rates (calculated from the phenanthrene consumption and the moles of hydrogen consumed along each route) over the parent and HCl-treated Ni_aMoS₂ and Ni_aWS₂ as a function of Ni content. Full squares represent the parent samples, while open squares correspond to the HCl-treated formulations. The blue arrow depicts the higher activity of Ni_aWS₂ catalysts by a factor of 1.7 compared to the Ni_aMoS₂ counterparts.

Figure 5-10 depicts the combined H₂-addition rate vs. Ni content plot for Ni_aMo/WS₂ parent and leached formulations. The W based catalysts follow a similar volcano shaped trend as the Mo based ones, shifted upwards in activity by a factor of approximately 1.7 at the increasing right hand side of the diagram. In contrast to the Ni_{0.2}MoS₂ pair, Ni_{0.2}WS₂-L showed a significant higher activity than Ni_{0.2}WS₂-P, but might be located in the activity declining left hand side of the diagram. While Ni_aWS₂ in general showed a higher hydrogenation activity than the Ni_aMoS₂ the unpromoted Ni_{0.0}WS₂ only reached 67% of the Ni_{0.0}MoS₂ on a total metal basis.

7.4.2 Discussion

Highly active NiMo/WS₂ catalysts show a large proportion of Ni-Mo/W-S phase while the formation of NiS_x particles is suppressed. The exact distribution of the promotor Ni to each of these phases depends on several parameters such as sulfidation temperature and the usage of chelating agents during synthesis to shift it.^[154,356-362] For Ni promoted WS₂ it was shown that redispersion of NiS_x is an important step during the synthesis^[265] and a high sulfidation degree leads to higher activity. This process is described by a migration of bulk NiS_x to the edge sites and the formation of Ni-W-S phase. However, the catalysts in this study did not show large NiS_x phases in their XRD patterns which speaks for a high dispersion of small (X-ray amorphous) particles. Additionally, the effect of Ni loss after HCl treatment is not that pronounced as in their Ni_aMoS₂ counterparts. During the leaching process NiS_x partially go into solution as Ni²⁺ and H₂S evolves. This solution is allowed to settle for 1 h which allows ions to adsorb on the sulfide phase. This process somehow mimicking the redispersion of Ni using chelating agents. If the Ni²⁺ adsorb too strongly on the WS₂ phase and water is not able to remove them again, highly dispersed Ni is present during the final sulfidation step after drying of the catalyst. This may lead allow to form more Ni incorporated active sites according to the Ni-Mo-S. Hence, Ni_aWS₂ are ‘hard’ to leach in comparison to Ni_aMoS₂ and a relative higher activity for hydrogenation is achieved due to more active sites present.

Anyhow, the question about the quality of active sites is unanswered by the above statements. To deal with this task the NO uptake and BET surface area experiments are exerted. Figure 5-11 shows the combined data of H₂-addition rates normalized by surface area and NO uptake normalized by surface area on Ni_aMoS₂ and Ni_aWS₂ parent and leached samples. Similar to the effects discussed in the publication above parent Ni_aWS₂ catalysts fall off the correlation drawn as a straight line in the diagram while leached catalysts match. Further, the unpromoted WS₂ exhibits a lower ‘quasi-TOF’ than the promoted. It also falls on the line drawn by the very sparse promoted Ni_{0.05}MoS₂ and unpromoted MoS₂.

Therefore, the nature of active sites in NiMoS₂ and NiWS₂ catalysts is identical and the same TOF for hydrogenation of phenanthrene is found on both systems. Hence, the higher activity

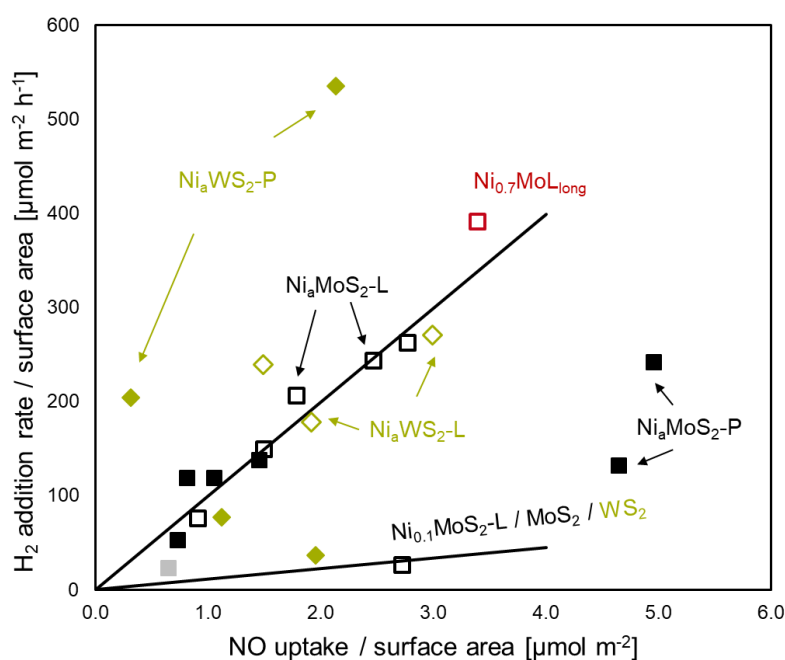


Figure 5-11. Extended hydrogen addition rate (calculated from the phenanthrene consumption and the moles of hydrogen consumed along each route) as a function of NO uptake, both normalized to the specific surface area. Open symbols represent the leached versions of the parent samples (filled symbols). Squares stand for Mo-based sulfides and diamonds represent W-based sulfides. Unpromoted MoS₂ is identified via the filled grey square. The slopes of the lines can be interpreted as quasi-TOFs for the promoted (100 h⁻¹) and non-promoted sites (17 h⁻¹), respectively. This plot clearly indicates that NiMoS₂ and NiWS₂ show the same intrinsic activity based on NO site quantification. Long time leached high Ni content MoS₂ catalyst also falls in line with other leached samples.

of promoted W-based sulfides is caused by a higher density of active sites (CUS and SH) per gram of catalyst or mole of transition metal as shown for supported systems before.^[193] The lower activity of unpromoted WS₂ compared to MoS₂ is compensated by a much lower surface area and therefore site density, but the quality of these sites is the same as seen by the ‘quasi-TOF’ and supported by the same product distribution (DiHPhe / TetHPhe ≈ 80/20).

Figure 5-11 includes the additional information for the long time leached Ni_{0.7}MoS₂ catalyst. Remember, this sample was more active than the 3 h leached Ni_{0.7}MoS₂ and falls on the left hand side of the volcano curve activity vs. Ni content (Figure 5-8). However, it also fits the ‘quasi-TOF’ of promoted and leached Ni_aMo/WS₂ catalysts which proves that at this point of leaching incorporated Ni atoms are not attacked and the surface is further freed by NiS_x particles.

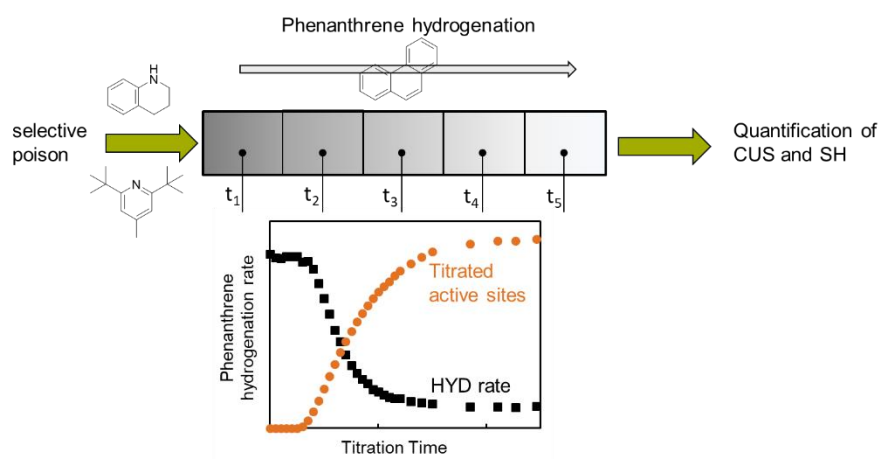
Chapter 6

Toward quantification of active sites and site-specific activity for polyaromatics hydrogenation on transition metal sulfides

This chapter is based on:

Ferdinand Vogelgsang, Hui Shi, Johannes A. Lercher, 'On the multifaceted roles of NiS_x in hydrodearomatization reactions catalyzed by unsupported Ni-promoted MoS₂.' *Journal of Catalysis* 403 (2021) 98-110.

DOI: 10.1016/j.jcat.2021.02.034



1 Abstract

Quantification of active sites is indispensable for understanding a catalytic material, ultimately enabling meaningful comparisons across different catalysts and discerning the underlying intrinsic kinetics. At present, however, few methods are available for quantitatively probing the catalytic surface of transition metal sulfides (TMS) during catalysis. TMS catalysts expose Brønsted acidic (sulfhydryls, SH) and Lewis acidic sites (coordinatively unsaturated sites, CUS) at their surfaces and, thus, are conceptually amenable to in situ acid-base titration with judicious choices of bases that strongly bind to the acidic entities. In this proof-of-concept study, in situ titration using several N-containing organic bases allowed us to determine the surface concentration of active sites and their specific activities for polyaromatics hydrogenation on unsupported TMS catalysts. Ni-promoted sulfide catalysts were more active than the unpromoted ones, because of a modest increase in the site density and a 2- to 3-fold enhancement in the TOF averaged over all titrated sites. By further discriminating between the titrated CUS and SH with site-selective titrants, a substantial difference in the TOF was found between CUS and SH among the titrated pool of sites. In addition to the titrated sites that contributed to the majority (80-95%) of the hydrogenation activity, some active sites remained unoccupied by the studied base molecules. The contribution of these residual sites, likely inaccessible to large-sized and less mobile titrants, depended on the temperature, H₂ pressure and the catalyst, but was unaffected by the space time, titrant concentration, and the type or concentration of the polyaromatic reactant, for a given catalyst. This work leads to several emerging opportunities to better understand complex TMS catalysts.

Keywords:

In situ titration; transition metal sulfides; polyaromatics; hydrogenation; active sites

2 Introduction

Transition metal sulfide (TMS) catalysts used in refineries are inherently anisotropic materials, primarily composed of stacks of two dimensional slabs featuring basal planes and edges. This intrinsic site heterogeneity is exacerbated by the varying extents of intralayer-mixing of metal elements, slab stacking, and the co-existing phases of the promoters, as well as by interactions with the underlying support. The ‘Co-Mo-S’ model along with its analogs for other binary and ternary TMS systems, advanced first by Henrik Topsøe 40 years ago,^[50,51] remains to be the most successful microscopic description for these catalysts, and the type of model has been continuously refined and popularized by numerous research groups over the past decades.^[96,102,124,128,200,363–365]

If we focus our attention on the smallest repetitive chemical entities that constitute the sulfide domains, two primary types of surface functionalities exist: coordinatively unsaturated sites (CUS) and sulfhydryl groups (SH). Regardless of the exact atomistic arrangements in the TMS slabs, general agreement exists on the key roles of CUS and SH in the diverse forms of catalysis. For the majority of cases relevant to hydrotreating catalysis, we are only concerned with these sites located at the edge of the slabs, but not on the basal planes, whereas recent studies also indicated the presence of basal plane vacancies albeit in unconventional coordination environments.^[366,367]

The existence of CUS (S^{2-} anion vacancies) and SH-groups (Figure 6-1) has been long recognized,^[45,172,202,205] but their site concentrations and specific activity have been scarcely assessed in the literature. Among the probe molecules used in the infrared (IR) spectroscopic studies of unsupported and supported TMS, CO and NO have been shown to be able to distinguish among CUS residing at different locations (metal edge or sulfur edge), on different phases and in different coordination environments.^[173,316,368–375] Discrimination of SH and CUS by IR spectroscopy is also possible with the adsorption of basic molecules (e.g., 2,6-dimethylpyridine). The spectra allow differentiating between protonated and coordinatively bound species.^[189,190,376] By following the variation of their intensity with temperature, the strength of the binding sites can be qualitatively investigated. However, in addition to the often unclear stoichiometries for the adsorption of probe molecules (e.g., mononitrosyl/dinitrosyl for NO), there has been a dearth of either molar extinction coefficients (except for those determined for CO and NO by Maugé and coworkers^[368,370,374,377]) or robust calibration protocols, largely precluding a reliable quantitative analysis of individual bands in the spectra. Moreover, most spectroscopic tools (e.g., Mössbauer, XPS, IR, EPR) are faced with a common problem that the catalysts under such measurements are not exposed to the actual reaction conditions applied in hydrotreating, let alone the additional complex interactions between a catalyst and various carbon- and sulfur-containing molecules in the liquid phase.

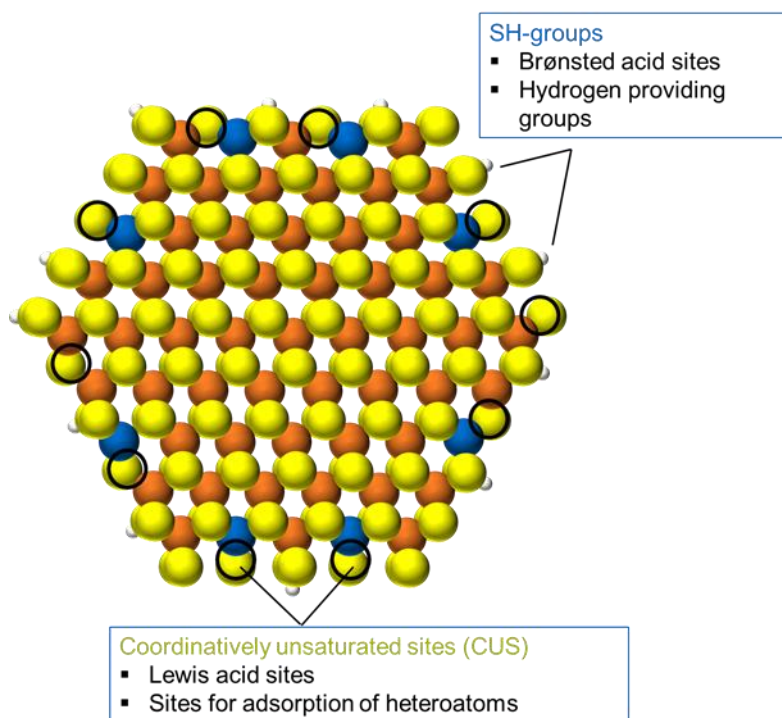


Figure 6-1. Illustration of coordinatively unsaturated sites (CUS) and sulfhydryl (SH) groups as two major classes of acidic sites on a binary TMS catalyst (top view). Ni (blue), Mo (orange), sulfur (yellow), and hydrogen (white).

Although correlations between catalytic activity and CUS concentration were previously established for certain catalysts (mainly supported systems) and reactions,^[371] information on the concentration of active sites for bulk TMS materials has been lacking. This is associated with the higher stacking, agglomeration, and tendency to form segregated promoter phases,^[65] compared to supported counterparts. These complications make unsupported TMS catalysts particularly challenging to characterize, especially with regard to their surfaces (X-ray absorption techniques fall largely short for the large domain size of bulk TMS). Moreover, only limited success has been achieved in the quantitative detection of the surface entities and adsorbed species on unsupported TMS samples by both transmission and diffuse reflectance IR spectroscopy.^[378,379]

To circumvent this problem, our recent works made the first attempt to correlate the catalytic activities in hydrodearomatization (HDA), hydrodesulfurization (HDS) and hydrodenitrogenation (HDN) with either H₂-D₂ exchange rates or the volumetric NO uptake for series of bulk TMS catalysts post-synthetically treated with aqueous acids to remove site-blocking phases and to improve the quality of correlations.^[286,330,380] Note, however, that both methods to probe the active sites have always been performed at conditions far from those in hydrotreating reactions,^[324,381] ignoring the dynamic restructuring that may occur with changing reaction environments.^[98,111]

Considering this background, it is not surprising that only a small portion of experimental studies on TMS catalysts have attempted to characterize and quantify active sites, among which only few were able to acquire turnover frequency (TOF) estimates for a given reaction catalyzed by TMS.^[193,286,380] Thus, it is highly important to develop in situ methods to qualitatively and quantitatively characterize active sites on bulk (unsupported) TMS materials during catalysis, which would in turn allow us to evaluate the site-specific activity.

In this context, it is helpful to first recall that various types and concentrations of Brønsted acidic (SH) and Lewis acidic (CUS) sites exist that are associated with the catalytic activity. For example, the Brønsted acidic character of the SH-groups was investigated by several authors, including Nan-Yu and Henrik Topsøe, for catalytic systems of Co(Ni)Mo(W)S₂.^[93,201,204,376,382] The acidic nature of these surface sites should make them amenable to an acid-base titration approach, with a judicious choice of bases, for determining the concentration of active sites and their site-specific activity during catalysis. Early in the 1950, Mills studied the poisoning effect of organic nitrogen compounds on cracking catalysts by controlled adsorption of the N-poison.^[383] Later, Santiesteban used a sterically hindered base, 2,6-dimethylpyridine, to titrate and distinguish between (strong) Brønsted acid sites and Lewis acid sites, which enabled a comparison of site-based activity (TOF) for n-pentane isomerization on WO_x/ZrO₂ and β-zeolites.^[384] Iglesia et al. further promoted this approach to the enumeration of active sites on a broader set of materials including zeolites, Keggin-type heteropolyacids and metal oxides, enabling in-depth structure-function relations for a multitude of acid-catalyzed reactions.^[385–390] In these experiments, small quantities of nitrogenous organic bases were added to the reaction feed and the reaction rate decreased with time on stream. The cumulative titrant uptake allowed the surface density of active sites to be estimated and by normalizing the specific rate to the site counts, a TOF estimate was obtained. In the field of TMS catalysis, there has been plenty of literature on the inhibition of HDS and hydrogenation reactions by basic nitrogen compounds,^[391–394] some studies showed that the poisoning effect of N-compounds on hydrogenation correlated with their gas-phase basicities/proton affinities,^[392,393] suggesting the critical role of Brønsted acidic sites for hydrogenation.

Inspired by these earlier contributions, we present here a proof-of-concept study on the use of N-base titrants for the quantification of active sites for polyaromatics hydrogenation on several bulk TMS catalysts based on MoS₂ and WS₂ with and without Ni. By quantitatively assessing site concentrations during catalysis, site-specific activities in phenanthrene hydrogenation are

compared and new insight into the heterogeneity of sites and their unequal catalytic contributions is gleaned.

3 Experimental

3.1 Catalyst preparation

The catalysts denoted as MoS₂ and Ni_{0.2}MoS₂ were the same as used in a previous study.^[380] WS₂, Ni_{0.2}WS₂, and Ni_{0.6}WS₂ were synthesized via the same thiosalt impregnation method. Only the first step in synthesis, the formation of (NH₄)₂WS₄, was slightly modified due to a low yield of this thiosalt precursor, when using ammonium paratungstate as the oxidic precursor. First, 5.0 g of tungstic acid, H₂WO₄ (Aldrich, 99%), was dissolved in 40 mL of an ammonium hydroxide solution, NH₄OH (Merck, 32 wt% in water), in a three neck round bottle flask (250 mL) and 10 vol% H₂S in H₂ (Westfalen, certified mixture of 98% purity H₂S and 99.999% purity H₂) was bubbled through the stirred solution at a flow rate of 20 mL min⁻¹.^[277,283] The blue suspension was heated to 60 °C in an oil bath for 30 minutes after which a dark blue solid was filtered off. The remaining yellow and clear filtrate was heated to 60 °C and kept overnight under 20 mL min⁻¹ 10 vol.% H₂S/H₂ (Westfalen, certified mixture of 98% purity H₂S and 99.999% purity H₂) bubbling. Then, the solution was cooled to room temperature without precipitation of a solid. Next, a solution of 7.0 g of hexamethonium bromide, (CH₃)₃N(Br)(CH₂)₆N(Br)(CH₃)₃ (Alfa Aesar, 98%), in 10 mL water was added and a yellow solid immediately precipitated. This solid was hexamethoniumtetrathiotungstate according to previous literature, which was filtrated off and washed several times with water before drying it in vacuum. Finally, to obtain the Ni_aWS₂ catalyst the same procedure as described for the Ni_aMoS₂ counterparts was applied.^[380]

A trimetallic formulation, denoted as NiMoWS₂, was provided by the industrial partner as extrudates in an oxidic form, which was ground to powder and sulfided in house in the following way. About 400 mg of the powder were diluted 1:4 (w/w) with SiC (ESK-SIC GmbH, sieved to mesh sizes of 355-500 μm) to increase heat conductivity and avoid local hot spots and temperature runaways during the exothermic sulfidation. The physical mixture was loaded into the same tubular reactor as used for hydrogenation reactions (Section 3.3). After drying in 40 mL min⁻¹ N₂ at 120°C overnight, a feed containing decalin (Merck, cis- and trans-isomeric mixture, 99.0%) and 3 wt% of S in the form of dimethyl disulfide (DMDS, Aldrich, 98%) was introduced together with a H₂ flow in a molar ratio of H₂/S = 25. The total pressure was adjusted to 20 bar and the reactor was heated to 250°C at a heating rate of 1°C min⁻¹ and held at that temperature for 8 h, followed by another temperature ramp to 350°C (1°C min⁻¹) and dwelling for 3 h. After the reactor was cooled to 60°C, the pressure was released and liquid toluene, then n-hexane, was pumped through the reactor to rinse the sulfided sample. Due to the volatility of n-hexane, the sulfided sample was

apparently dry after being unloaded from the reactor. The sample was then stored under ambient conditions prior to use in catalysis. All the catalysts used in this study were characterized by N₂ physisorption, elemental analysis and X-ray diffraction, the experimental details and results of which are presented in the SI (Table S 6-12, Table S 6-13 and Figure S 6-13). Some catalysts were subjected to NO adsorption measurements, which were performed in a pulsing manner at ambient temperature and pressure on a continuous flow reactor connected to a mass spectrometer (Pfeiffer Vacuum QME 200).

3.2 Feed preparation for phenanthrene hydrogenation and titration experiments

A standard feed for phenanthrene hydrogenation consisted of 1 wt% phenanthrene (Alfa Aesar, 98%), 2 wt% tetradecane (Alfa Aesar, 99%, as the internal standard for offline GC analysis) in decalin (Merck, cis- and trans-isomeric mixture, 99.0%) mixed in a 1 L round bottom bottle (amber borosilicate, VWR). Additionally, 1000 ppmw S in the form of dimethyl disulfide (DMDS, Aldrich, 98%) were added. Then, the bottle was ultra-sonicated to dissolve phenanthrene and to degas the solution. The feed used for titration experiments was prepared by adding the titrant to the standard phenanthrene feed in a 0.5 L round bottom bottle (amber borosilicate, VWR) with the addition of 0.2 wt% hexadecane (abbreviated as HXD, VWR, >95%) as the tracer molecule and the titrant (a N-containing aromatic compound, typically tetrahydroquinoline) in a concentration range corresponding to 7-13 ppmw total nitrogen content. Titrant molecules in this study included quinoline (Q, Sigma, 98%), tetrahydroquinoline (THQ, Sigma, 98%), 2,6-di-tert-butyl-4-methylpyridine (DitBMP, Sigma, 98%), 2,6-di-tert-butylpyridine (DitBP, Sigma, >97%), and pyridine (Sigma, 99.8%). The organic bases are all soluble in the reaction feed primarily composed of decalin and phenanthrene.

3.3 Reaction and titration in the trickle bed reactor system

Reactions were carried out on a trickle bed reactor system consisting of gas supply (Bronkhorst mass flow controllers, purchased from Wagner Mess- und Regeltechnik GmbH), liquid feed delivery (HPLC pumps, Agilent) and a stainless steel tubular reactor (glass coated inner wall). The pressure of the system was adjusted with a stainless steel back-pressure regulator and for reactions, liquid samples were periodically taken at the reactor outlet with a 16 port valve. For titration, a three-way valve with an extra dipping line was installed directly after the back pressure regulator. Liquid samples of 0.05 mL were manually taken every 5 minutes to measure the conversion changes as a function of time.

In a typical titration experiment, 50-100 mg of a sulfide catalyst (powder) was diluted with SiC (ESK-SiC GmbH, sieved to mesh sizes of 63-90 μm) by a factor of 5 (w/w) and the physical

mixture was filled in the reactor right within its isothermal zone and held in place with additional SiC stuffed at the top and bottom. The hydrogenation reaction was first performed with a standard reaction feed (i.e., containing Phe, DMDS that provides a constant S chemical potential and tetradecane as the internal standard, all dissolved in decalin). For all experiments, the total pressure was 60 bar and a gas (pure H₂, or balanced with N₂ in measurements of H₂ reaction order) to hydrocarbon (total liquid feed) ratio of 300:1 (v/v) was applied. Each experimental run started with an initiation period for 21 h at 360°C, after which the reaction conditions were adjusted to the settings for titration experiments. After the reaction reached a steady-state conversion at the set temperature (typically 250-270°C), the feed was changed to a titrant-containing one and the change in conversion was monitored in 5-10 min intervals at a constant space time. Analysis of the phenanthrene conversion and product distribution was done by quantification of phenanthrene, its hydrogenated products, titrant, and hexadecane (tracer) in the collected aliquot of liquid sample using an offline GC (Shimadzu, GC-2010). The titration was kept running until a second steady state (at a lower level of activity) was reached. In some experiments, at the end of titration, the standard feed was introduced again and the temperature was increased to 340°C to remove the titrant from the catalyst surface. This temperature was kept for about 8 h before it was decreased to the reaction temperature, which was kept for 6 h. It was found that this re-activation protocol could recover the catalyst activity completely. Then a new titration cycle could be started. In all experiments, the carbon balance was found to be better than 95%.

Because our previous work established that the reaction rates did not change with conversion (up to 30%) or space time, the rates calculated in this study are one-point conversion rates at differential conditions, i.e., the measured sum of product yields ($\sum Y_{products}$, which is almost identical to the Phe conversion as nearly 100% carbon balance was observed in this work) divided by the space time (ST) to correct for small fluctuations in the volumetric flow (see below). The volumetric flow was measured for each titration cycle individually.

$$r_{Phe} = \frac{\sum Y_{products}}{ST}$$
$$ST = \frac{m_{cat}}{\dot{n}_{Phe,0}}$$

4 Results and Discussion

4.1 Phenanthrene hydrogenation

The temperature range (240-270°C) for phenanthrene (Phe) hydrogenation was slightly lower than that previously used (300°C). Under the studied conditions, Phe hydrogenation proceeds on TMS catalysts via two reaction pathways as described by us^[192,193,236,346,380] and shown in Figure 6-2. Along Path 1, 9,10-dihydrophenanthrene (DiHPhe) is formed as the primary product, followed by its consecutive hydrogenation to 1,2,3,4,4a,9,10,10a-octahydrophenanthrene (asym-OHPhe). Along Path 2, 1,2,3,4-tetrahydrophenanthrene (TetHPhe) and 1,2,3,4,5,6,7,8-octahydrophenanthrene (sym-OHPhe) are formed as the primary and the secondary product, respectively. Neither the fully hydrogenated product, perhydrophenanthrene, nor any lighter products were detected at the reaction conditions and conversion levels studied.

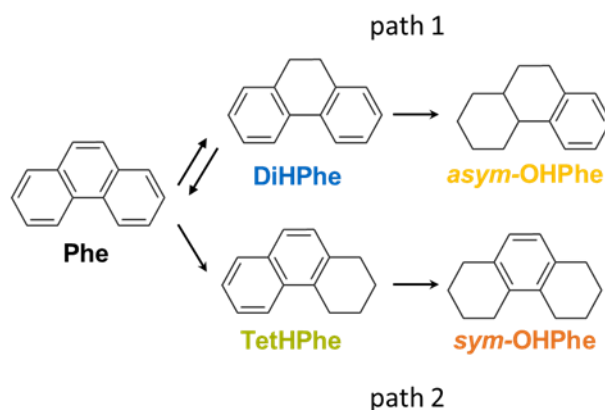


Figure 6-2. A simplified reaction network of phenanthrene hydrogenation.

Note that the characteristic selectivity pattern of an unpromoted Mo(W)S₂ catalyst fundamentally differs from that of a Ni-promoted catalyst.^[193,236,380] For the unpromoted Mo(W)S₂ catalyst, DiHPhe is produced with a selectivity up to 80% with almost no secondary products formed at typical conversions (< 30%) in this study, while the Ni-promoted catalyst shows a drastic shift to lateral ring hydrogenation producing TetHPhe and sym-OHPhe at a combined selectivity nearly equal to that of the DiHPhe and asym-OHPhe. Although the reactions were performed at a lower temperature than in our previous studies, the pathway ratios and product selectivities did not appreciably differ from those of prior studies.

The molecular level details for Phe hydrogenation on (Ni)MoS₂ catalysts have been presented previously.^[236] Briefly, the reaction proceeds through quasi-equilibrated adsorption of the reactants followed by consecutive addition of hydrogen pairs to the adsorbed Phe, with the rate-determining step differing along Path 1 (DiHPhe formation) and Path 2 (TetHPhe formation). Density functional theory (DFT) calculations indicated that Phe is preferentially adsorbed parallel

to the basal planes, while H is located at the edges. Moreover, experiments and theory both showed that the Ni addition does not significantly affect the coverage of the hydrocarbon species.^[236] As discussed later, the basic quinoline and pyridine titrants inhibit the Phe hydrogenation rates mainly by occupying H₂ activation and transfer sites (CUS and SH), rather than competition with Phe for basal plane sites. In this context, the active sites for Phe hydrogenation, as determined by titration, are synonymous with sites for H₂ activation and transfer, while not including those available for Phe adsorption.

4.2 Breakthrough of titrant and tracer in a blank reactor and during a titration experiment

The breakthrough behavior of the titrant and tracer in a blank reactor (same packing as for titration experiments but without a catalyst) was checked in preliminary tests. Figure S 6-14 shows the concentration profiles of the reactant (Phe), the tracer hexadecane (HXD), and the titrant, tetrahydroquinoline (THQ), in the reactor effluent upon switching from the standard Phe feed (i.e., reactant, internal standard, and DMDS in decalin) to a feed additionally containing the titrant and the tracer but with otherwise identical concentrations as the standard feed (see Experimental for the detailed feed compositions).

Phe was not converted in the absence of catalyst, as demonstrated by the unchanged level of Phe concentrations after switching and the absence of products from GC analysis. It took about 20 minutes (at the liquid flow rate of 0.2 mL min⁻¹) for HXD and THQ to reach the reactor outlet. Additionally, the breakthrough patterns of HXD and THQ were identical in the blank reactor (Figure S 6-14), indicating that a delay in the breakthrough of the THQ titrant in an actual titration experiment (Figure 6-3) must be linked to the fact that the titrant is held up by the catalyst and keeps accumulating on its surface. Only after surface sites on the catalyst are saturated, the titrant elutes and is detected in the reactor effluent. Next, we describe how we used the information about the breakthrough behavior of titrant and tracer in a blank reactor to correct the titrant uptake during an actual titration experiment with a sulfide catalyst loaded.

Figure 6-3 shows a typical titration experiment on a Ni_{0.6}WS₂ catalyst as an example, in which the Phe conversion rate (at 240°C), tracer (HXD) breakthrough and titrant (THQ) breakthrough were monitored over time on stream. The onset of tracer elution corresponds to the start of titration, because the tracer and the titrant reach the catalyst bed and elute in parallel (Figure S 6-14). The conversion rate of Phe decreased as more and more titrant traversed the catalyst bed and became adsorbed, until all sites that were able to retain THQ were saturated. After THQ became detectable in the effluent again, the slope of the titrant curve was smaller than that of the tracer (in contrast to the same curvature in a blank test shown in Figure S 6-14), indicating that the titration was still proceeding. Based on this experiment, the titrant uptake (normalized to the mass of catalyst m_{cat}), q , was calculated according to Eq. (1).

$$q = \frac{1}{m_{cat}} \cdot \sum_{i=1}^n \dot{n}_{titrant} \cdot (t_i - t_{i-1}) \cdot (1 - Y_{titrant}) \cdot Y_{tracer} \quad (1)$$

where q is the titrant uptake in the unit of $\mu\text{mol g}_{cat}^{-1}$, $\dot{n}_{titrant}$ is the constant molar flow of the titrant in the unit of $\mu\text{mol min}^{-1}$, t is the time interval for one measured conversion in the unit of min, $Y_{titrant}$ is the relative breakthrough of the titrant ($\frac{area_{titrant,sample\ i}}{area_{titrant,feed}}$) which is dimensionless, and Y_{tracer} is the relative breakthrough of the tracer ($\frac{area_{tracer,sample\ i}}{area_{tracer,feed}}$) which is also dimensionless.

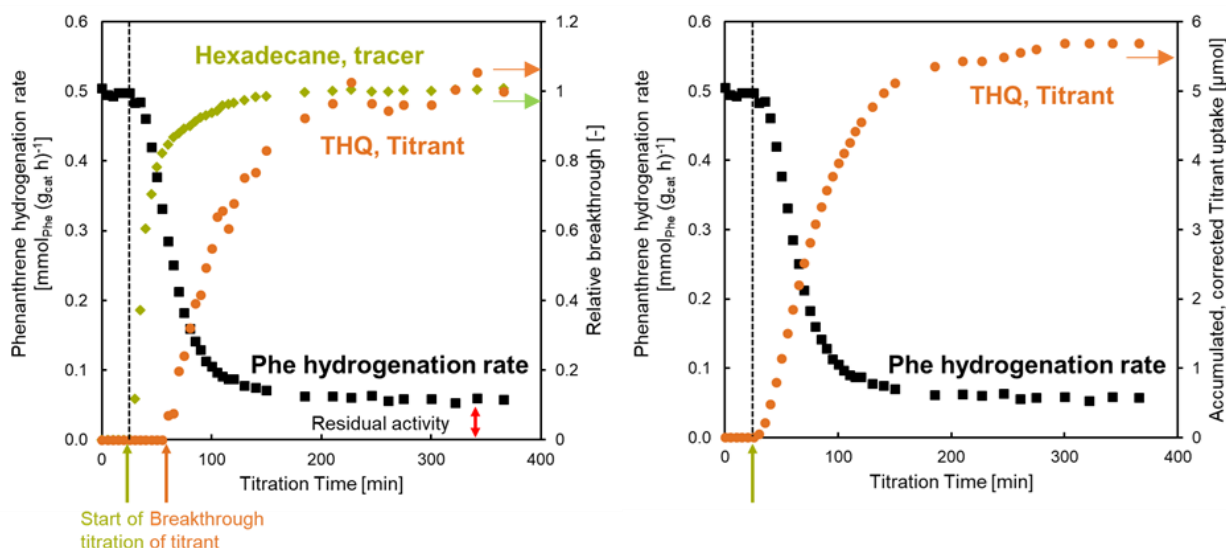


Figure 6-3. A typical titration experiment on a $\text{Ni}_{0.6}\text{WS}_2$ catalyst as an example, in which the Phe conversion rate (at 240°C), tracer (hexadecane) breakthrough and titrant (tetrahydroquinoline, THQ) breakthrough were monitored over time on stream (left panel). The right panel (orange trace) shows the cumulative titrant uptake as a function of time on stream.

The uptake (q) over the course of the experiment is the sum of all discrete uptake points within a time interval Δt , $\dot{n}_{titrant} \cdot (t_i - t_{i-1})$, where the counting starts with the first data point after the breakthrough of the tracer. Each individual summand has to be corrected for the titrant feed breakthrough indicated by the tracer (HXD) concentration profile, $Y_{tracer} = \frac{n_{HXD,i}}{n_{HXD,feed}}$, and the breakthrough of the titrant as measured, $Y_{titrant} = \frac{n_{titrant,i}}{n_{titrant,feed}}$. In this specific example, the total uptake of THQ was $53 \mu\text{mol g}_{cat}^{-1}$ ($5.7 \mu\text{mol}$ of THQ on 108 mg of $\text{Ni}_{0.6}\text{WS}_2$). When the conversion rates are plotted as a function of cumulative titrant uptake, it is apparent that titration with THQ led to an almost linear decrease in rates until the near-end of titration (Figure S 6-15(a)). This linear decrease in rates, however, does not unequivocally point to the presence of sites uniform in catalytic behavior, because strong binding leads to sequential titration of all sites along the catalyst bed, irrespective of their reactivity.^[388] Thus, the total titrant uptake may comprise titrant molecules adsorbed on more than one type of sites exposed at the sulfide surface.

At the end of titration, the catalyst became stable at a different level of activity (Figure 6-3). A conceptually plausible explanation for the decrease in rate over time-on-stream could be that the

titrant competes with the reactant for the active sites and another steady-state is established over time as the surface becomes equilibrated with the titrant. In this case, however, the residual activity would be affected by the concentration of the titrant. As shown later in Section 4.3, changing the titrant concentration in the feed affected neither the cumulative titrant uptake nor the residual activity. Therefore, we hypothesize that the residual rate of Phe conversion, after THQ concentration was back to its original value in the titration feed, mainly reflects the presence of sites on sulfide surfaces that are unable to bind THQ under reaction conditions (for strength or steric reasons), but which are active for Phe conversion. More discussions about the residual activity are presented in Section 4.6.

In previous studies focused on the poisoning effect of 3-ethylcarbazole on the HDS of S-heterocycles, Ho and Nguyen observed similar curves of the HDS activity and total N-concentration at reactor exit as functions of elapsed time after the introduction of 3-ethylcarbazole.^[395,396] They showed that the usual quasi-equilibrium or quasi-steady-state models failed to describe the observed curves properly. Instead, these results demonstrated that a large fraction of the adsorbed N compounds adsorb near-irreversibly at their conditions (265°C, 1.83 MPa H₂, H₂/liquid = 116 (v/v), 80 ppmw N).

Note in passing that the denitrogenation of the N-containing bases (e.g., THQ) was avoided, even in the presence of the most active sulfide catalyst, by the low temperature applied (typically 240-270°C). In this temperature range, hydrogenation proceeds at measurable rates while denitrogenation (N removal) of the base titrant does not occur. The absence of nitrogen removal as NH₃ ensures that the titrant, even if it is hydrogenated, remains strongly held at the active sites at these temperatures. For example, when using quinoline (Q) as the titrant, its hydrogenated product THQ was detected at the reactor outlet. Figure S 6-16 shows that the titration behavior, i.e., decrease of Phe hydrogenation rate as a function of time and the level of residual activity, was identical regardless of whether Q or THQ was used as the starting titrant, because of the rapid conversion of Q to THQ on the time scale of the hydrogenation reaction and titration.

4.3 Validation of the titration method for site quantification

Figure 6-4 depicts the titration profiles for two catalysts, a home-made MoS₂ and an industrial trimetallic sulfide, NiMoWS₂. In the case of MoS₂, the concentration of THQ in the titration feed was varied from 88 to 44 ppmw in two titration experiments with fresh or re-activated (several hours at 340°C to desorb the titrant) catalysts. For the NiMoWS₂ catalyst, two independent titration experiments were carried out first at 227 ppmw and then 77 ppmw of THQ. For both catalysts, the residual rate at the end of titration was nearly the same at both titrant concentrations. The residual rate also did not change when a poisoned catalyst was subjected to another titration feed containing a doubled concentration of THQ (Figure S 6-17). This independence of post-titration activity on the titrant concentration was verified for other catalysts and with a couple of

other titrants (e.g., pyridine). Moreover, we estimated that the total THQ uptake (270°C) on MoS₂ was very similar at 51 (±5) and 45 (±5) μmol g_{cat}⁻¹ at the titrant concentrations of 88 and 44 ppmw, respectively, while for NiMoWS₂, this uptake also hardly changed with the titrant concentration, being 66 (±6) μmol g_{cat}⁻¹ at 227 ppmw of THQ and 72 (±6) μmol g_{cat}⁻¹ at 77 ppmw of THQ, respectively (Table 6-1).

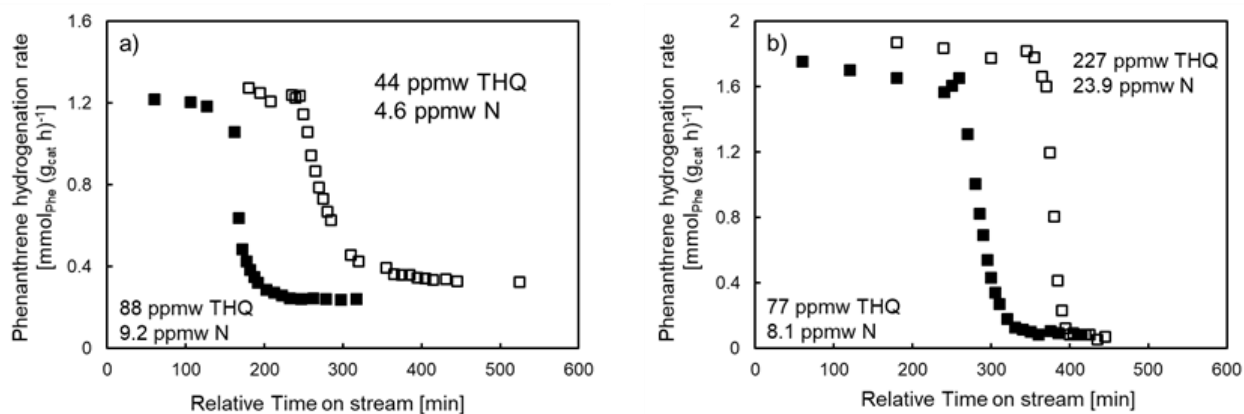


Figure 6-4. Titration profiles with varying titrant concentrations in the feed. a) MoS₂ (90 mg) titrated with a feed containing 88 ppmw THQ (filled squares) or 44 ppmw THQ (open squares). Reaction temperature was 270°C and a space time of 138 g_{cat} h mol_{Phe,0}⁻¹ was set. b) Industrial trimetallic catalyst titrated with a feed containing 77 ppmw THQ (filled squares) or 227 ppmw THQ (open squares). Reaction temperature was 250°C and a space time of 170 g_{cat} h mol_{Phe,0}⁻¹ was set. The two traces are offset in the graphs by some arbitrary value to be separated.

Table 6-1. Independence of titrant uptake on space time, titrant concentration and temperature.

Catalyst	Temperature [°C]	Space time [(g _{cat} h) mol _{Phe} ⁻¹]	THQ concentration in the feed [ppmw]	Titrant uptake [μmol _{THQ} g _{cat} ⁻¹] ^a
MoS ₂	270	138	88	50 (±5)
			44	45 (±5)
	260	141	54 (±5)	
		267	88	51 (±5)
250	141	88	53 (±5)	
NiMoWS ₂	250	170	77	66 (±6)
			227	72 (±6)
		103	77	67 (±6)

^a The uncertainties in the titrant uptake, rounded up to the nearest integer, mainly originate from the integration errors in area under the breakthrough curves and in the fluctuations of the measured space time.

It has been shown that Phe primarily adsorbs (physisorption) on the basal plane,^[236] while it appears plausible that THQ is strongly adsorbed on CUS and SH located at slab edges.^[397,398] By blocking these sites, THQ shuts off the supply of hydrogen to Phe and quenches the hydrogenation activity. Consistent with this conjecture, one test using DiHPhe as the reactant gave the same site count as measured for Phe hydrogenation, both using THQ as the titrant (Figure 6-5, the last cycle). This would be expected, if the titrant does not bind to sites where the aromatic reactant (Phe or DiHPhe) is adsorbed and if the same active sites/entities (SH and CUS) are involved for aromatic ring hydrogenation.

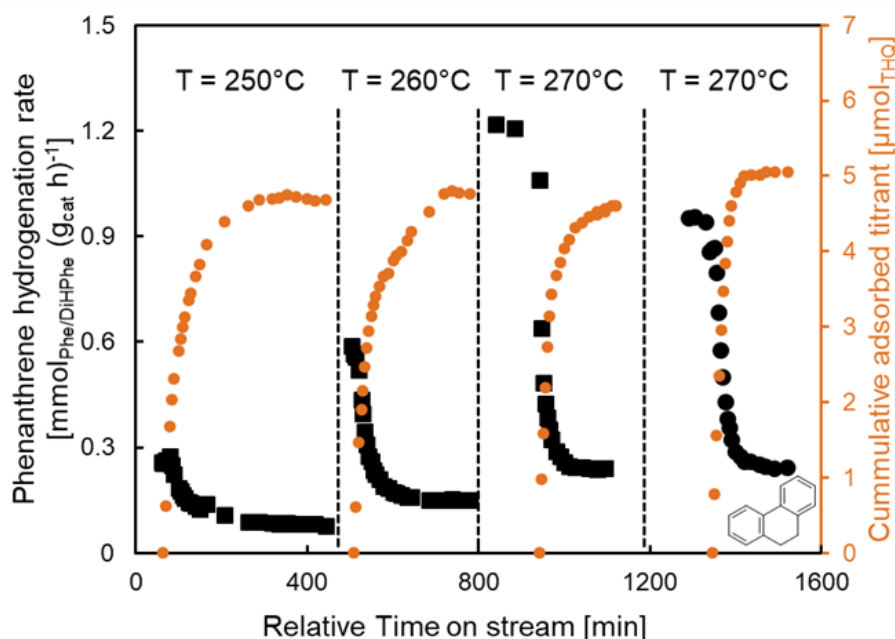


Figure 6-5. Titration cycles during phenanthrene hydrogenation (the first three cycles) and dihydrophenanthrene hydrogenation (the last cycle) on MoS₂ catalyst at 250-270°C. Desorption treatments are omitted and the time scales are re-adjusted, not reflecting the actual time-on-stream. Titrant: THQ (1000 ppmw); space time: 141-145 (g_{cat} h) mol_{Phe or DiHPhe}⁻¹; H₂ pressure: 40 bar.

In order to test for consistency of the titration technique, we performed experiments on the above two catalysts at different space times (ST) by changing the catalyst mass and the liquid flow rate. Consistent THQ uptakes were determined for a given catalyst: 66-67 μmol g_{cat}⁻¹ using 57 (ST = 103 g_{cat} h mol_{Phe}⁻¹) and 99 mg of NiMoWS₂ (ST = 170 g_{cat} h mol_{Phe}⁻¹) and 51-54 μmol g_{cat}⁻¹ using 90 mg of MoS₂ at two different liquid flow rates (0.21 mL min⁻¹ liquid flow, ST = 141 g_{cat} h mol_{Phe}⁻¹ and 0.11 mL min⁻¹ liquid flow, ST = 267 g_{cat} h mol_{Phe}⁻¹). Additionally, repeated cycles of titration, intervened by re-activation of the catalyst at 300°C for several hours in between titration cycles, were performed on NiMoWS₂. The results (Figure S 6-18) show that the titration experiments were fully reproducible in terms of both the titrant uptake and the residual

activity, which, in turn, suggest that THQ as titrant does not cause significant irreversible structural changes that cannot be recovered by high temperature desorption. Thus, various titration experiments (e.g., differing in the experimental settings) can be performed on the same catalyst without having to re-load a fresh aliquot of catalyst and re-start the experiment, thus enhancing the reproducibility and reliability of data analysis and comparison.

4.4 Comparison of site counts and average site-based activities across different catalysts

Blocking sites by stoichiometric base adsorption allows not only to quantify the concentration of sites, but also to differentiate between sites. THQ blocks surface sites for H₂ activation and the subsequent H-addition, because it potentially binds to both CUS and SH, as inferred from the work of Lauritsen and coworkers.^[397] Assuming that THQ adsorbs in a 1:1 stoichiometry on all plausible types of surface sites (CUS and SH in different coordination environments and at different locations), its total uptake can be considered to be equal to the surface sites that retain THQ during steady-state catalysis. Given the above understanding, the turnover frequency averaged over all the THQ-titrated sites ($TOF_{total,THQ}$) can be obtained from Eq. (2):

$$TOF_{total,THQ} = \frac{r_{Phe,initial} - r_{Phe,residual}}{q_{THQ}} \quad (2)$$

The calculated TOFs, along with the total THQ uptake, initial (before titration) and residual (after titration) rates, are compiled in Table 6-2 for different sulfide catalysts. Importantly, average TOFs were determined to be identical for Ni-promoted MoS₂ and WS₂ catalysts, while being marginally higher on pure MoS₂ than on WS₂. Given the experimental uncertainties, we conclude that Ni-promotion leads to a nearly 2- to 3-fold enhancement in the average TOF compared to unpromoted catalysts. This enhanced hydrogenation activity on Ni-promoted sites is qualitatively consistent with our recent study of phenanthrene hydrogenation on bulk sulfide catalysts, though the previously reported TOFs (a 6-time difference in the site-specific activity between Ni-promoted and nonpromoted sites) were based on rate data measured at 300°C and NO uptake measured at room temperature.

In view of the different sizes and chemical nature of NO and THQ, their site accessibility and specificity were anticipated to be dissimilar, especially considering that the measurement conditions widely differed for the two site probes. Interestingly, however, the NO uptakes measured for the two previously studied catalysts, MoS₂ and Ni_{0.2}MoS₂, were both about a factor of 2 (90 and 135 $\mu\text{mol}_{NO} \text{ g}^{-1}$, room temperature) as high as the corresponding THQ uptakes (51 and 73 $\mu\text{mol}_{THQ} \text{ g}^{-1}$) measured under reaction conditions. Considering that for typical sulfided catalysts with SH groups present at the edge, NO adsorption is thought to proceed via a “push-pull” type mechanism involving simultaneous vacancy creation, NO adsorption and H₂S

release,^[316] one conjecture may be that this factor of 2 difference points to a dinitrosyl species for NO adsorption on a CUS (preexisting or created upon adsorption). If such an adsorption complex were indeed predominant, it would imply a negligible restructuring of these bulk sulfides from room temperature up to the reaction conditions, at least not in a way affecting the total site concentration. At present, this remains speculative, as we do not yet have a dataset large enough to assess the possibility of a coincidental match between these uptakes; it would be interesting to examine whether ex situ NO uptake can be used as a reliable proxy for active site counts under reaction conditions, an enduring question that requires more careful scrutiny in future studies.

Both NO and THQ uptakes are much smaller than the surface concentration of available Mo atoms at the edge ($1.0\text{-}1.1 \text{ mmol}_{\text{edge Mo}} \text{ g}_{\text{cat}}^{-1}$), estimated from a hexagonal slab geometry and the slab properties measured from TEM. Therefore, it can be concluded that only a small fraction (<10%) of edge atoms is associated with active sites responsible for the major portion of hydrogenation activity on bulk MoS₂ and Ni_{0.2}MoS₂, in line with DFT calculations and experimental studies where it was also shown that only a fraction of total edge atoms forms stable S vacancies.^[176,178,405,212,216,399–404] Besides chemical reasons, it is also possible that the agglomeration of particles rendered some edge sites inaccessible to THQ or NO.^[286] Notably, according to both site counts, Ni-promoted catalysts exhibited a higher site density than the nonpromoted counterparts, in accordance with the expectation that Ni promotion enhances the ability of a sulfide catalyst to generate vacancies.

For all catalysts studied, a fraction of sites active for hydrogenation remained untitrated by THQ. The contribution of this fraction of sites to the total activity varied among the catalysts ($\frac{r_{\text{Phe,residual,THQ}}}{r_{\text{Phe,initial}}} = 0.11\text{-}0.20$, Table 6-2) and with reaction temperature and H₂ pressure (Section 4.6). For Phe hydrogenation on a given catalyst, the residual activity at the end of titration is not a function of space time (catalyst mass and flow rate), concentration of a titrant, or the type or concentration of the reactant, while it depends on the temperature (Section 4.6), the H₂ pressure (Section 4.6), and the type of titrant. Using a weaker base pyridine (gas-phase proton affinity = 930 kJ mol⁻¹ vs. 941 kJ mol⁻¹ for THQ and ~983 kJ mol⁻¹ for DitBP) to titrate a Ni_{0.2}MoS₂ catalyst, an even lower residual rate was found (Figure S 6-20(a)). Temel et al. reported that the adsorption of pyridine not only consumes atomically adsorbed hydrogen, which potentially could be used in hydrogenation, but also blocks active sites for hydrogenation by binding strongly to the MoS₂ brim sites.^[406] Thus, we tentatively hypothesize that the non-THQ-titrated sites are either geometrically so constrained that they are not accessible by THQ, or the relatively short distance between sites precludes a full titration with THQ, while allowing the access of smaller titrants (e.g., pyridine).

Toward quantification of active sites and site-specific activity for polyaromatics
hydrogenation on transition metal sulfides

Table 6-2. THQ uptakes, average turnover frequencies ($TOF_{total, THQ}$) of the THQ-titrated sites on different sulfide catalysts. Conditions for hydrogenation and titration: 1 wt% Phe in decalin, $T = 270^{\circ}\text{C}$, 60 bar total pressure (40 bar partial pressure of H_2), 76-88 ppmw THQ (8-9 ppmw N) as titrant. The liquid flow rate was about 0.2 mL min^{-1} corresponding to a space time range of $ST = 70 - 173 (\text{g}_{cat} \text{ h}) \text{ mol}_{Phe,0}^{-1}$.

	MoS ₂	Ni _{0.2} MoS ₂	WS ₂	Ni _{0.2} WS ₂
$q_{THQ} \left[\frac{\mu\text{mol}}{\text{g}_{cat}} \right]^a$	51 (± 5)	73 (± 7)	28 (± 4)	38 (± 5)
$r_{Phe,initial} \left[\frac{\text{mmol}}{\text{g}_{cat} \text{ h}} \right]$	1.22	2.59	0.38	1.49
$r_{Phe,residual,THQ} \left[\frac{\text{mmol}}{\text{g}_{cat} \text{ h}} \right]$	0.24	0.30	0.054	0.23
$\frac{r_{Phe,residual,THQ}}{r_{Phe,initial}}$	0.20	0.11	0.14	0.13
$TOF_{total,THQ} [\text{h}^{-1}]$	19 (± 3)	31 (± 3)	12 (± 3)	34 (± 4)

^a The uncertainties in the titrant uptake, rounded up to the nearest integer, mainly originate from the integration errors in area under the breakthrough curves and in the fluctuations of the measured space time.

^b The uncertainties in the $TOF_{total, THQ}$, rounded up to the nearest integer, mainly originate from errors in the uptake and modest errors (not shown) in the measured rates before and after titration.

4.5 Insights into the heterogeneity of active sites

During steady-state catalysis on TMS, both SH and CUS (i.e., S-vacancies) with varying electronic and steric environments are present on slab edges. In order to better understand the steric requirements, we also used titrants with substantial steric hinderance around the nitrogen atom, e.g., 2,6-di-tert-butyl-4-methylpyridine (DitBMP) and 2,6-di-tert-butylpyridine (DitBP), which served as very selective titrants for SH groups. Because the formation of the dative bonds between Lewis acidic metal centers and the electron pair donor site (the N atom) requires a close approach of the N-base to the surface site, CUS (and even some SH that are at inaccessible locations or are spatially too close to each other) cannot be accessed by these sterically hindered bases. With this in mind, it is not surprising to see that the residual rate of Phe hydrogenation was higher when titrated with the bulkier DitBMP than with THQ on various sulfide catalysts (Figure 6-6). DitBMP titrates Brønsted acidic SH-groups only, while THQ is adsorbed on Lewis acidic CUS as well. This, in turn, allows us to calculate the individual site densities of SH and CUS among the titrated sites and their corresponding site-specific activities (TOFs).

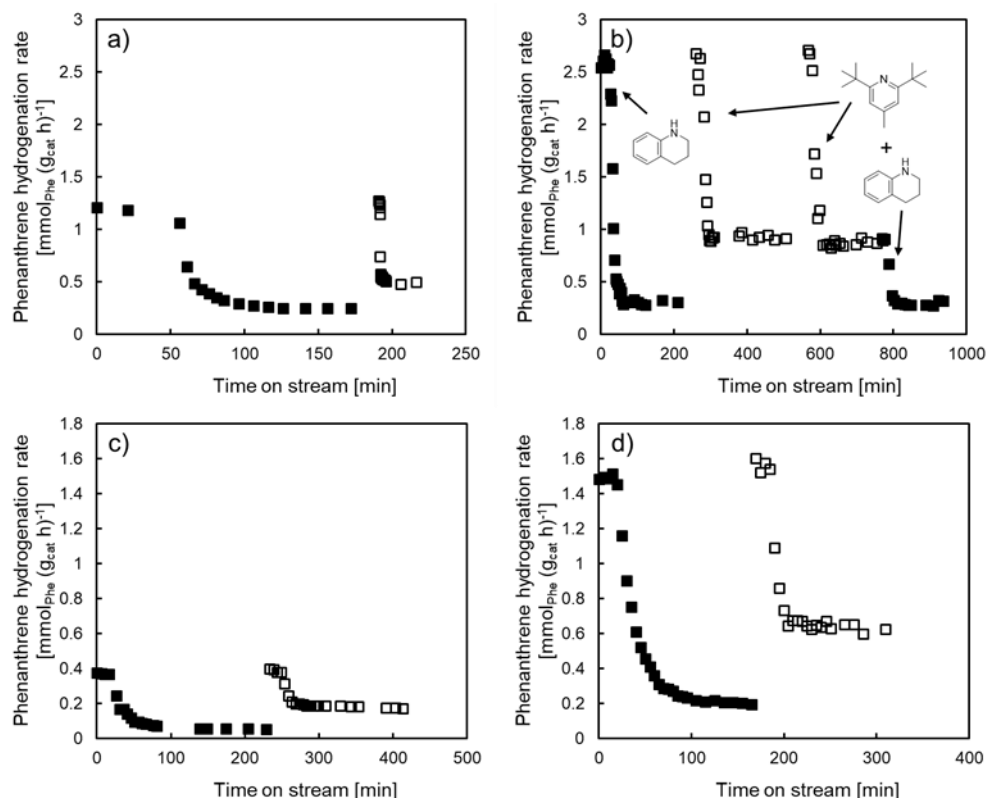


Figure 6-6. Phenanthrene hydrogenation rates at 270°C as a function of time after introducing the titrants THQ (filled squares) and DitBMP (open squares) on unpromoted a) MoS₂ and c) WS₂ and promoted b) Ni_{0.2}MoS₂ and d) Ni_{0.2}WS₂ catalysts. In panel b) the experiment on the right shows a sequential titration with DitBMP followed by a mixture of DitBMP and THQ. The re-activation stage was omitted and the time-on-stream values of different titration cycles were offset by some value.

Several sulfide catalysts were titrated by THQ in the first titration cycle and, after removing the titrant at 300°C, titrated by DitBMP in the second titration cycle (note: DitBMP was used instead of DitBP to avoid overlapping GC peaks). Using the same approach illustrated for the THQ titrant to correct for the breakthrough behavior, the total uptake (q) of DitBMP was obtained. For all the studied catalysts, the DitBMP uptake was approximately half the THQ uptake, which appears to reflect that the SH and CUS are present at comparable concentrations. We note in passing that Lauritsen et al. suggested that quinoline prefers to be strongly adsorbed through SH groups on the active S-edge of both unpromoted and Co-promoted MoS₂ nanoparticles, rather than on the CUS.^[397]

At almost equal site density of CUS, SH sites titrated by DitBMP consistently contributed to $60 \pm 5\%$ of the total activity, or $70 \pm 5\%$ of the overall activity of the THQ-titrated sites (refer to f_{SH} values in Table 6-3), indicating a higher site-based activity of the THQ-titrated SH than the remaining fraction of THQ-titrated sites (primarily including CUS, but possibly also some SH that cannot be accessed by DitBMP). The TOF of the DitBMP-titrated SH groups is calculated by:

$$TOF_{SH} = \frac{r_{Phe,initial} - r_{Phe,residual,DitBMP}}{q_{DitBMP}} \quad (3)$$

Assuming that DitBMP titrates all the SH among the pool of sites titrated by THQ, the TOF of the CUS can be calculated by:

$$TOF_{CUS} = \frac{r_{Phe,residual,DitBMP} - r_{Phe,residual,THQ}}{q_{THQ} - q_{DitBMP}} \quad (4)$$

However, the bulky and sterically hindered DitBMP may not be able to access SH at certain locations, and it is likely that more SH will become difficult or impossible for DitBMP to access, as the titration progresses and the surface crowdedness increases. If not all the SH are titrated by DitBMP for such steric reasons, Eq. (4) would express the TOF averaged over the SH and CUS untitrated by DitBMP.

The results in Table 6-3 show that the SH sites titrated by DitBMP are generally more active than the THQ-titrated CUS, regardless of the amount of SH sterically inaccessible to DitBMP. Both TOF_{SH} and TOF_{CUS} were very similar between the two Ni-promoted MoS_2 and WS_2 catalysts, while TOF_{CUS} was much less different than TOF_{SH} between the two unpromoted catalysts. When THQ was used to further titrate the remaining sites on a DitBMP-titrated $Ni_{0.2}MoS_2$ (the last cycle in Figure 6-6b; in this cycle, the DitBMP uptake was $39 \mu\text{mol g}^{-1}$), the additional THQ uptake was $33 \mu\text{mol g}^{-1}$, i.e., matching the difference between the total THQ uptake ($73 \mu\text{mol g}^{-1}$) and the DitBMP uptake ($35 \mu\text{mol g}^{-1}$) determined independently on $Ni_{0.2}MoS_2$ (the first and second cycles in Figure 6-6b). This indicates that the titration first with a bulkier base (DitBMP) does not cause additional steric hindrance to the second, smaller titrant (THQ). Consequently, the TOF calculated from the first ($0.90 \text{ mmol g}_{cat} \text{ h}^{-1}$) and second ($0.30 \text{ mmol g}_{cat} \text{ h}^{-1}$) residual rates (in the last titration cycle in Figure 6-6b) and the THQ uptake was the same as the TOF_{CUS} (16 h^{-1}) calculated from Eq. (4). It is important to note that the individual TOFs of CUS and SH can be also obtained from the slopes of rate-uptake curves, in this case not requiring specific knowledge about the precise titrant uptake.

Ni-promotion appeared to generate SH and CUS with a higher activity, with the enhancement being somewhat greater for SH-sites than for CUS (1.8-3.6 times vs. 1.5-2.2 times). Distinct activities of CUS and SH were not totally expected, especially if one presumed that all SHs are generated by quasi-equilibrated H_2 and H_2S dissociation on CUS.^[216,217,221] This is apparently not the case. Although the exact reason why SH and CUS present different site-specific activities remains to be understood, we can name several factors including the location (e.g., metal edge or sulfur edge), the metal coordination (e.g., single or double anion vacancies),^[407] and their ability to activate H_2 and mediate H-atom transfer (different energetics). One possible explanation is that the SH and CUS titrated by these bases are not cognate and more specifically, they may exist at different locations. For example, Lauritsen et al. showed that pyridine and quinoline molecules adsorb strongly on the S-edges of reduced MoS_2 and $CoMoS$ nanoparticles through the

Toward quantification of active sites and site-specific activity for polyaromatics
hydrogenation on transition metal sulfides

Table 6-3. DitBMP uptake and individual TOFs of CUS and SH on different sulfide catalysts. Conditions for hydrogenation and titration: 1 wt% Phe in decalin, T = 270°C, 60 bar total pressure (H₂ partial pressure 40 bar), 108-148 ppmw DitBMP (7-10 ppmw N) as titrant. The liquid flow rate was about 0.2 mL min⁻¹ corresponding to a space time range of ST = 74 - 173 (g_{cat} h) mol_{Phe,0}⁻¹.

	MoS ₂	Ni _{0.2} MoS ₂	WS ₂	Ni _{0.2} WS ₂
$q_{DitBMP} \left[\frac{\mu\text{mol}}{\text{g}_{\text{cat}} \text{h}} \right]^a$	28 (±4)	35 (±5)	15 (±3)	19 (±3)
$r_{Phe,initial} \left[\frac{\text{mmol}}{\text{g}_{\text{cat}} \text{h}} \right]$	1.22	2.59	0.38	1.49
$r_{Phe,residual,DitBMP} \left[\frac{\text{mmol}}{\text{g}_{\text{cat}} \text{h}} \right]$	0.49	0.91	0.18	0.64
$\frac{r_{Phe,residual,DitBMP}}{r_{Phe,initial}}$	0.40	0.34	0.45	0.39
f_{SH}^b	0.75	0.74	0.64	0.70
$TOF_{SH} [h^{-1}]^c$	26 (±3)	48 (±6)	13 (±2)	46 (±7)
$TOF_{CUS} [h^{-1}]^d$	11 (±2)	16 (±2)	10 (±2)	23 (±4)

^a The uncertainties in the DitBMP uptake, rounded up to the nearest integer, mainly originate from the integration errors in area under the breakthrough curves and in the fluctuations of the measured space time.

$$^b f_{SH} = \frac{r_{Phe,initial} - r_{Phe,residual,THQ}}{r_{Phe,residual,DitBMP} - r_{Phe,residual,THQ}}$$

^c The uncertainties in the TOF_{SH}, rounded up to the nearest integer, mainly originate from errors in the DitBMP uptake and modest errors (not shown) in the measured rates before and after titration.

^d The uncertainties for the TOF_{CUS}, rounded up to the nearest integer, mainly originate from errors in the uptakes of both THQ and DitBMP and modest errors (not shown) in the measured rates before and after titration. It should be borne in mind that the sites untitrated by DitBMP may comprise not only CUS (inherently inaccessible to DitBMP) but also some SH; as a consequence, the difference should be even greater between the TOF of SH and that of CUS.

formation of protonated pyridinium/quinolinium ions.^[397] It could be speculated that the titrated SH are mainly located at the S-edge, while the titrated CUS are mainly at the metal edge. Additional systematic studies would be required that combine controllable synthesis that fine-tune molecular-level structural features of sulfides with the in situ titrations and kinetic evaluations.

4.6 Effects of temperature and H₂ pressure on the titrant uptake and residual activity

For sulfide catalysts, the surface densities of CUS and SH that bind the base titrant may be altered by temperature and the chemical potentials of H₂ and H₂S. Our results with THQ titrant for MoS₂ as an example (Table 6-1 and the first three cycles in Figure 6-5) show that in the limited temperature range (240-270°C) chosen for titration experiments, the total THQ uptake, or the

equivalent site density (CUS + SH), did not significantly change with temperature (50-54 $\mu\text{mol}_{\text{THQ}} \text{g}_{\text{cat}}^{-1}$ at the same space time and THQ concentration) for this catalyst. H_2 pressure (20-40 bar) also hardly affected the total titrant uptake, which varied between 44 and 51 $\mu\text{mol}_{\text{THQ}} \text{g}_{\text{cat}}^{-1}$ without systematic variations as the H_2 pressure was increased (Figure 6-7). The insensitivity of the total THQ uptake to both temperature and H_2 pressure suggests that the total number of sites (CUS and SH) that are available for H_2 activation and account for the majority of catalytic hydrogenation activity is unaffected by these two parameters, at least in the range explored.

The steady-state activity at the end of THQ titration (relative to the initial activity before THQ titration), however, was significantly affected by both temperature and H_2 pressure. The relative residual activity decreased from 30% to 19% as temperature increased from 250 to 270°C at a H_2 pressure of 40 bar. This temperature effect suggests that the residual sites catalyze Phe hydrogenation with a lower activation energy than the average sites titrated by THQ. As the H_2 pressure was increased from 20 to 40 bar at 270°C, the relative residual activity also decreased from 30% to 19%. This can be rationalized by a much smaller reaction order in H_2 for the catalytic route on residual sites (~ 0.10 vs. 0.98) than on the titrated sites. Thus, both temperature and H_2 pressure effects on the post-titration activity support a different reaction mechanism (e.g., a different rate-determining H-addition step) for Phe hydrogenation on the residual sites that are not titrated by THQ.

Currently, there are more than one way to explain the residual activity after titration with THQ. For one, there might be sites at a different location than the titrated sites. For instance, based on DFT calculations of reaction pathways for both the hydrogenation (HYD) and direct desulfurization (DDS) routes in thiophene hydrodesulfurization over different equilibrium MoS_2 edge structures, Moses et al. concluded that the HYD route could occur either at the S(1010) edge, where S vacancies must be created to become active for HYD, or at the Mo(1010) edge without the need to create edge Mo-CUS.^[179] They also found that the effective energy barrier for vacancy creation depended on the H_2 partial pressure. Other possible candidate proposals for the location of residual sites include the less accessible metallic-like brim sites on the basal plane, and the corner sites where the quinolinic titrants may not bind as effectively as on slab edges.^[397] Alternatively, it could also be that some active sites become weaker in binding strength and/or less accessible when vicinal sites are covered by the titrants. A third possibility is associated with the known ability of decalin (solvent) and THQ in transferring hydrogen to unsaturated compounds. Thus, one could posit that some transfer hydrogenation pathway (more likely from decalin, which was present at concentrations several orders of magnitude higher than that of THQ, to Phe) might be responsible for the remaining activity. In this regard, the absence of reaction without catalysts clearly excludes a non-catalytic transfer hydrogenation route, but whether or not there is a catalyzed transfer hydrogenation route remains to be addressed. Detailed investigations would be required to determine the precise origin(s) of the pressure and temperature effects, the nature of

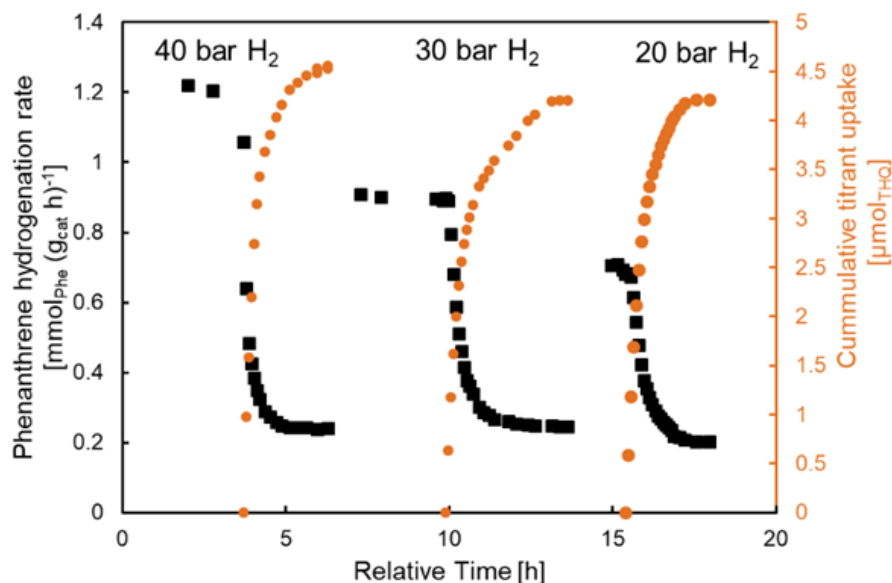


Figure 6-7. Effect of H₂ pressure on the titration behavior and cumulative THQ uptake on MoS₂. The re-activation stage was omitted and the time-on-stream scale (x-axis) was offset for successive cycles.

the residual sites, and the alternative hydrogenation mechanism on post-titration sites, which are beyond the scope of the present study.

4.7 On the potential and limitations of the in situ titration methods for studying sulfide catalysts

We have presented an exploratory study using basic N-containing heteroaromatic compounds as a class of titrants that can probe the vast majority of active sites for hydrogenation reactions on TMS catalysts, essentially CUS and SH at the slab edge that are both acidic (Figure 6-1). Unlike previous techniques such as IR spectra of probe molecules (much less successful for bulk sulfides), H₂-D₂ exchange and volumetric NO pulsing that have been employed at far-from-reaction conditions, the in situ titration is applicable to supported and unsupported sulfide catalysts at working states and less restricted in its operating conditions. Thus, it allows one to quantitatively understand and rationalize differences in the measured activity among catalysts, for reactions beyond phenanthrene hydrogenation discussed in this work (perhaps even encompassing electrocatalytic reactions, if the titrant is properly chosen).

There are limitations at the present stage to the proposed approach. For one, it may be that not all the titrated sites contribute to the hydrogenation catalysis, considering the complex phase composition and surface structures for sulfide materials. Consequently, the site counts may represent an upper bound for the actual concentration of active sites, while the corresponding TOFs calculated may provide a lower bound for the actual TOFs. For the unpromoted catalysts and low Ni-loading counterparts (those in Table 6-2 and 3), there was no or only a minimal quantity of NiS_x phases where additional sites may exist for the titrant to adsorb. But as the Ni loading

increases, more sites for titrant binding would be exposed on the surface of NiS_x particles. As NiS_x itself is conventionally regarded as inactive phase for Phe hydrogenation but contributes to the activation of H₂, it would be rather complicated to determine the TOFs of the main active phase (MoS₂ or WS₂) based on the convoluted site counts.

Another limitation is the suitable range of conditions for conducting these titration experiments. In this study, hydrogenation reactions were carried out at relatively low temperatures (up to 280°C) to avoid the decomposition of the titrants, because it was presumed that denitrogenation, if it occurred, would form a base (NH₃) that is much weaker and more reversibly adsorbed. But if NH₃ adsorption were sufficiently strong, then the temperature range for the presented titration approach could be further expanded.

Despite the current limitations, we may begin to address the unresolved issue of site heterogeneity (metal edge vs. sulfur edge, single vacancy vs. double vacancies,^[407] etc.) for such complex materials. In addition, apparent kinetic data can also be interpreted with more rigor so as to better guide the theoretical assessments. The approach also allows one to address support, promoter and additive effects,^[102,113,408–415] as well as other effects associated with changes in synthesis conditions (sulfiding and reductive treatments,^[220,370,416] chelating agent,^[370,417] etc.). For example, it was shown using the in situ titration that a decrease in S content in the reaction feed from 1000 to 500 ppm brought forth a 2-fold increase in the site concentration and a 1.5-fold increase in the site-specific activity, leading to a 3-fold enhancement in the mass-specific rate of WS₂ (Figure S 6-19). Another enduring question in the research of TMS hydrotreating catalysts concerns the origin of the different dependences of apparent (i.e., not site-based) catalytic activities on the stacking degree in hydrogenation and hydrogenolysis.^[97,286,418–421] In this regard, it would be highly relevant to explore the impact of stacking degree on the TOFs (i.e., site-based) of unsupported and supported TMS catalysts in various hydrotreating reactions using the in situ site counting method for rate normalization.

5 Conclusions

We have presented unambiguous evidence demonstrating that the stoichiometric, strong binding of the quinolinic titrant (primarily THQ) on active sites of either a Brønsted or Lewis acidic nature, rather than the competitive adsorption of the titrant and the reactant, is the primary cause for the rate decrease as a function of titrant uptake on transition metal sulfide catalysts. The in situ site counting method developed and validated herein allowed us to assess and compare site densities on unsupported TMS catalysts and site-specific activities in phenanthrene hydrogenation at working conditions. We find that Ni-promoted sulfide catalysts are more active than the unpromoted ones, because of a modest increase in the site density and a 2-3 fold enhancement in the TOF averaged over all the titrated sites.

By further discriminating between CUS and SH sites by site-selective titrants, a substantial difference has been discerned for the first time in the TOF between CUS and SH among the titrated pool of sites. There appears to be at least one more set of surface sites that are active for hydrogenation yet with a kinetic behavior distinct from the titrated pool of sites. The contribution of these residual sites, which may be inaccessible to the organonitrogen titrants, depends on the temperature, H₂ pressure and the catalyst, but is unaffected by the space time, titrant concentration, and the type or concentration of the polyaromatic reactant.

6 Acknowledgement

This work was financially supported by the Chevron Energy Technology Company. The authors would like to especially thank Dr. Alexander Kuperman, Dr. Axel Brait, Prof. Roel Prins and Prof. Enrique Iglesia for fruitful discussions. We are also grateful to the members of TU München for their support in various ways, especially Ulrike Ammari (Elemental Analysis), Xaver Hecht (technical support), Yinjie Ji, Sicong Ren and Dr. Yong Wang (titration experiments).

Summary and Final Conclusions

Nickel-promoted molybdenum or tungsten sulfides are the work horses in refining industry for hydrotreatment reactions. Although they were first described in the 1930s and have been extensively studied over the last decades, some questions remain open. Knowledge has been accumulated about the TMS's general structure, reaction mechanisms catalyzed by them and the detailed structure-function relations. Although the nature of active sites has been identified and largely agreed upon, especially for supported systems, there is limited information about the exact role of the promoting Ni (sulfides) species/phase and whether there is a difference in Ni promotion for MoS₂ or WS₂ phases. This dissertation aims to add a piece to the large 'tart' of TMS catalysis research to aid in the fundamental understanding of mechanisms and processes involved.

For this purpose, phenanthrene hydrogenation was used as a test reaction for investigating the catalytic properties. In a first step, the reaction network consisting of parallel and consecutive reaction pathways was analyzed. The Delplot analysis suggested that dihydro- and tetrahydrophenanthrene were primary products of phenanthrene while both sym- and asym-octahydrophenanthrene were secondary products consecutive to tetrahydrophenanthrene. One important observation was the shift in dihydrophenanthrene selectivity from 40% on Ni-promoted catalysts to 80% for unpromoted catalysts. This feature was very valuable for the investigation of the nature of active sites.

In order to investigate the function of Ni (sulfides) during phenanthrene hydrogenation, a set of Ni promoted Mo/WS₂ bulk catalysts was prepared via a co-precipitation method to obtain oxidic precursors, which underwent an in-situ sulfidation to form the final sulfides. The first obtained oxides were exposed to different sulfidation protocols to optimize for highest activity in phenanthrene hydrogenation. Based on the literature information and experimental results of this brief exploration, a protocol of slow sulfidation with implemented temperature dwell steps at around 250 and 320°C under high H₂ content resulted in sulfides with decent hydrogenation properties. A good balance of reducing and sulfiding rates had to be maintained.

However, the control of Ni content in the sulfides from co-precipitation turned out to be complex. Hence, a second set of Ni promoted Mo/WS₂ bulk catalysts was prepared by a thiosalt based route which allowed to control the Ni content in the formulations effectively. Additionally, these formulations exhibited a higher surface area than the co-precipitation based sulfides due to the introduction of a spacer cation during the synthesis.

During the synthesis of Ni promoted Mo/W sulfides Ni was not only incorporated into the slabs structure but also formed separated NiS_x phases. At higher Ni concentrations those phases that were large in size and poorly dispersed were largely inactive for hydrotreatment reactions, which led to the common phenomenon in sulfide catalysis of an 'ideal' Ni content of around 30% in metal. In order to investigate the activity of Ni promoted sites in Mo or W sulfides a 'leaching' protocol was established. In short, it is a post-synthetic treatment of sulfides with an acid, here HCl, in water under air atmosphere either at room temperature or under boiling conditions. For all

synthesized formulations with detectable (XRD) nickel sulfide phases the reaction rate for phenanthrene hydrogenation increased after this treatment. The usage of organo-acids led to a loss of NiS_x as well, but also attacked the slab structure of Mo/WS_2 so that a substantial mass loss was detected. This might be due to the high water solubility of a partially oxidized and complexed Mo/WS_2 phase. When using HCl as leaching agent the catalyst slab structure stayed intact and only a very low portion of Mo was lost. This loss was higher for Ni-promoted MoS_2 , most likely because of an easier oxidation by air of the Mo atoms next to Ni atoms at the slabs edges.

HCl leaching increased the BET surface area and selectively removed NiS_x for Ni concentrations larger than 40% in metal content. This removal increased the phenanthrene hydrogenation reaction rate due to loss of inactive matter and the increased accessibility of Ni-promoted sites at the catalyst slabs. At low Ni contents, HCl was able to remove Ni^{2+} cations incorporated in the Mo/WS_2 slabs/edges, which led to a drastic drop in activity. Multiple leaching of originally high-Ni-content MoS_2 catalysts and prolonged leaching time eventually resulted in the same observation of activity loss. In conclusion, highly active sulfide catalysts were obtained by choosing a synthesis protocol which allowed a high Ni edge decoration (high Ni content during synthesis) followed by a post-synthetic HCl treatment which removed excess NiS_x phases, thermodynamically stable phases under hydrotreatment conditions. Leaching time and repetition of the protocol controlled the final Ni concentration.

By removing the virtually inactive, relatively large NiS_x crystals from the sulfide slabs an almost ‘cleaned up’ Mo/WS_2 surface evolved. Accordingly, the majority of all remaining Ni atoms decorated the edges of the slabs and contributed as promoters to the catalytic activity. Those active sites were titrated by NO in volumetric pulsing experiments to quantify their amount. For all Ni- MoS_2 or Ni- WS_2 catalysts with an edge decoration of >20% Ni, a linear correlation between the areal hydrogen addition rate to phenanthrene and the areal NO uptake was established. Catalysts with Ni edge decoration <10% showed the same activity–NO uptake correlation as pure MoS_2 or WS_2 . For those formulations, the majority of the edge sites were unpromoted. They showed a typical product selectivity pattern of 80% dihydrophenanthrene and 20% tetrahydrophenanthrene without deeper hydrogenation compared to promoted edge sites which usually led to 40% di- and tetrahydrophenanthrene each and 20% sym-octahydrophenanthrene in the conversion range studied. However, the slope of the two linear correlations corresponded to the site specific activity (TOF) of promoted and unpromoted edge sites of the sulfide catalysts, where promoted sites were 5 times more active than unpromoted sites.

In a next set of experiments where a bed of Ni_xS_y was stacked on top of (upstream of) unpromoted MoS_2 , the hydrogen addition rate was higher than for pure MoS_2 . Thus, Ni_xS_y particles were not innocent spectators during the hydrogenation of polyaromatics. They activated and allowed a spill-over of H_2 to the MoS_2 slab where the polyaromatic molecule was adsorbed. This finding together with the volcano shaped curve of the activity–Ni concentration relation fitted into the model of ‘symmetrical synergy’ suggested by Chianelli. For Ni contents up to ~25 % the

classical Topsøe model best described the nature of active sites. At higher Ni contents when Ni_xS_y particles grew and segregated, the overall hydrogenation activity is a combination of ‘synergy by contact’ and the Topsøe model.

A general phenomenon in TMS catalysis is the dependency of edge site CUS formation on the surrounding reaction conditions. Especially the composition of the atmosphere, reducing (H_2 concentration) and sulfiding (H_2S concentration), is of high importance. Typically applied measurements for CUS or SH sites are carried out in vacuum (IR) or at ambient temperature and pressure (e.g., volumetric pulsing of NO), i.e., conditions far from those used in practical operations. Further, a so-called push-pull mechanism of NO with the sulfides edges is discussed in literature which would lead to additional site creation during such site counting practices. Hence, the surface arrangement of the catalysts studied with these techniques differs from that of catalyst surfaces under operating conditions.

To tackle this problem an operando technique for site titration was established. Quinolinic titrants, mainly THQ, caused a significant drop of phenanthrene hydrogenation rate when added to the phenanthrene feed. They acted as poisons for active sites present on the sulfide slab edges, namely CUS and sulfhydryl groups (SH). By changing the titrant to a sterically hindered one (DitBMP), the extent of rate inhibition was diminished. Four Mo/ WS_2 catalysts, unpromoted and Ni-promoted (<30%), were investigated by this method. In all cases three different type of sites were identified and quantified, SH groups, CUS and non-titratable sites. Therefore, THQ titrated almost all sterically accessible sites while DitBMP adsorbed selectively only onto SH-groups due to steric hindrance. Independent of the titrant used, a residual activity was measured. The contribution of those titrant-inaccessible sites to the hydrogenation activity depended on temperature and hydrogen pressure.

With this method, TOFs of SH groups and CUS sites of promoted and unpromoted sites of MoS_2 and WS_2 bulk catalysts were differentiated. Sulfhydryl groups turned out to be somewhat more active than CUS, and Ni-promoted sites were a factor of 2-3 more active than unpromoted sites. Further, this method, combined with the previous work on leached catalysts with varying Ni concentrations and our earlier TOF estimates of SH-groups, suggested the same activity of active sites on Mo and W based sulfides for phenanthrene hydrogenation.

In conclusion, this work offers insights into the nature of Ni-promoted, self-supported Mo/ WS_2 catalysts and the origin of Ni promotion for the hydrogenation of phenanthrene and adds to the existing large body of research on transition metal sulfides. With help of the elaborate technique ‘leaching’, a detailed catalytic study uncovered the multiple roles of the Ni promoter including the function of segregated NiS_x phase. In order to address the lack of information on the site-specific activity under realistic hydrotreating conditions, this work explored the utility of an operando titration approach for the first time in the quantification of active sites on sulfide catalysts. Despite the method being experimentally demanding, the obtained results particularly delighted

this author. Altogether, this thesis has addressed several novel aspects in the wide and mature field of transition metal sulfide catalysis.

References

- [1] P. Méda, *Innov. Copilots*. (2019). <https://www.icopilots.com/innovation-mindset/the-stone-age-did-not-end-because-the-world-ran-out-of-stones-16887> (accessed February 24, 2021).
- [2] Aoghs.org (American Oil & Gas Historical Society), (2019). <https://aoghs.org/petroleum-pioneers/american-oil-history> (accessed March 24, 2020).
- [3] Encyclopaedia Britannica, Petroleum, in: *Encycl. Br. - Vol. XXI, Eleventh edition*, The Encyclopaedia Britannica Company, 1911.
- [4] A. Gesner, *Gesner's Patent Kerosene Gas*, in: *Gesner's Pat. Kerosene Gas - Obtained from Bitumen, Asph. or Miner. Pitch*, New-York, 1860.
- [5] The Editors of Encyclopaedia Britannica, *Encycl. Br. Inc.* (2020).
- [6] I. Tarbell, *The History of the Standard Oil Company*, Belt Publishing, Cleveland, Ohio, 2018.
- [7] L. Maugeri, *The Age of Oil: The Mythology, History, and Future of the World's Most Controversial Resource*, First Edit, Praeger Publishers, Westport, CT, 2006.
- [8] T. Toyoda, *Osaka Keidai Ronshu*. 54 (2003) 187–218.
- [9] P.A. Dickey, *J. Pet. Technol.* 11 (1959) 14–26.
- [10] D.S. Painter, *Hist. Soc. Res.* 39 (2014) 186–208.
- [11] Chevron (see where we've been and where we're going), (2019). <https://www.chevron.com/about/history> (accessed August 12, 2020).
- [12] BP, *BP Statistical Review of World Energy 2019*, London, 2019.
- [13] J.G. Speight, *The Chemistry and Technology of Petroleum*, Fifth Edit, CRC Press, Boca Raton, FL, 2014.
- [14] A. Demirbas, H. Alidrisi, M.A. Balubaid, *Pet. Sci. Technol.* 33 (2015) 93–101.
- [15] A. Quinard, *An Overview of Refining*, in: Hervé Toulhoat, Pascal Raybaud (Eds.), *Catal. by Transit. Met. Sulphides*, IFP Energies nouvelles, Paris, France, 2013: pp. 523–546.
- [16] P. Sarrazin, C. Baudouin, G. Martino, *Perspectives in oil Refining*, in: J.W. Gerhard Ertl, Helmuth Knözinger, Ferdi Schüth (Ed.), *Handb. Heterog. Catal., Second Edition*, Wiley VCH Verlag GmbH & Co KGaA, Weinheim, Germany, 2008: pp. 2677–2695.
- [17] J.G. Speight, B. Özüm, *Petroleum Refining Processes*, Marcel Dekker, Inc., New York, Basel, 2002.
- [18] H. Toulhoat, P. Raybaud, *Catalysis by Transition Metal Sulfides: From Molecular Theory to Industrial Application*, Éditions Technip, Paris, 2013.
- [19] R. Prins, *Hydrotreating*, in: Garhard Ertl, Helmuth Knözinger, Ferdi Schüth, Jens Weitkamp (Eds.), *Handb. Heterog. Catal., Second Edition*, Wiley VCH Verlag GmbH & Co. KGaA, Weinheim, Germany, 2008: pp. 2695–2718.
- [20] H. Topsøe, B.S. Clausen and, F.E. Massoth, *Hydrotreating Catalysis in CATALYSIS-Science and Technology*, Vol 11, Springer, Berlin, 1996.
- [21] I. Maritime Organization, *Resolution MEPC.251(66) (Adopted on 4 April 2014) Amendments to the annex of the protocol of 1997 to amend the international convention for the prevention of pollution from ships, 1973, as modified by the protocol of 1978 relating thereto*, 2015.
- [22] J.D. Miller, C. Façanha, *The state of clean transport policy*, ICCT, Washington DC, 2014.
- [23] UNEP, *Diesel Sulphur Levels: Global Status*, 2018.
- [24] The European Parliament and the Council of the European Union, *Directive 2009/30/EC*, 2009.
- [25] Environmental Protection Agency, *Control of Air Pollution From Motor Vehicles: Tier 3 Motor Vehicle Emission and Fuel Standards*, 2014.

References

- [26] X. Yue, Y. Wu, J. Hao, Y. Pang, Y. Ma, Y. Li, B. Li, X. Bao, *Energy Policy*. 79 (2015) 87–98.
- [27] *Hydrocarb. Technol.* (2013). <https://www.hydrocarbons-technology.com/features/feature-top-ten-largest-oil-refineries-world/> (accessed August 13, 2020).
- [28] T.G. Kaufmann, A. Kaldor, G.F. Stuntz, M.C. Kerby, L.L. Ansell, *Catal. Today*. 62 (2000) 77–90.
- [29] T. Chapus, D. Hudebine and, V. Souchon, Deep Desulphurization of Middle Distillates, in: Hervé Toulhoat, Pascal Raybaud (Eds.), *Catal. by Transit. Met. Sulphides*, IFP Energies Nouvelles, Paris, France, 2013: pp. 547–578.
- [30] M.S. Rana, V. Sámano, J. Ancheyta, J.A.I. Diaz, *Fuel*. 86 (2007) 1216–1231.
- [31] J. Ancheyta, J.E. Speight, *Hydroprocessing of Heavy Oils and Residua*, CRC Press, Boca Raton, FL, 2007.
- [32] J.A.R. van Veen, *Catal. Today*. 292 (2017) 2–25.
- [33] R.R. Chianelli, G. Berhault, B. Torres, *Catal. Today*. 147 (2009) 275–286.
- [34] O. Weisser, S. Landa, *Sulphide Catalysts, Their Properties and Applications*, Pergamon Press, Oxford, NY, 1973.
- [35] C. Krauch, M. Pier, *Zeitschrift Für Angew. Chemie*. 44 (1931) 953–958.
- [36] A.C. Byrns, W.E. Bradley, M.W. Lee, *Ind. Eng. Chem.* 35 (1943) 1160–1167.
- [37] E.E. Donath, *Adv. Catal.* 8 (1956) 239–292.
- [38] T.A. Pecoraro, R.R. Chianelli, *J. Catal.* 67 (1981) 430–445.
- [39] H. Beuther, R.A. Flinn, J.B. McKinley, *Ind. Eng. Chem.* 51 (1959) 1349–1350.
- [40] C. Marcilly, *J. Catal.* 216 (2003) 47–62.
- [41] R.R. Chianelli, T.A. Pecoraro, T.R. Halbert, W.-H. Pan, E.I. Stiefel, *J. Catal.* 86 (1984) 226–230.
- [42] H. Toulhoat, P. Raybaud, *Periodic Trends in Catalysis by Sulphides*, in: *Catal. by Transit. Met. Sulphides*, IFP Energies Nouvelles, Paris, France, 2013: pp. 3–23.
- [43] J.M.J.G. Lipsch, G.C.A. Schuit, *J. Catal.* 15 (1969) 163–173.
- [44] J.M.J.G. Lipsch, G.C.A. Schuit, *J. Catal.* 15 (1969) 174–178.
- [45] J.M.J.G. Lipsch, G.C.A. Schuit, *J. Catal.* 15 (1969) 179–189.
- [46] R.J.H. Voorhoeve, J.C.M. Stuijver, *J. Catal.* 23 (1971) 228–235.
- [47] R.J.H. Voorhoeve, *J. Catal.* 23 (1971) 236–242.
- [48] P. Grange, *Catal. Rev. - Sci. Eng.* 21 (1980) 135–181.
- [49] B. Delmon, *Bull. Soc. Chim. Belg.* 88 (1979) 979–987.
- [50] H. Topsøe, B.S. Clausen, R. Candia, C. Wivel, S. Mørup, *J. Catal.* 68 (1981) 433–452.
- [51] C. Wivel, R. Candia, B.S. Clausen, S. Mørup, H. Topsøe, *J. Catal.* 68 (1981) 453–463.
- [52] N.-Y. Topsøe, H. Topsøe, O. Sørensen, B.S. Clausen, R. Candia, *Bull. Soc. Chim. Belg.* 93 (1984) 727–733.
- [53] H. Topsøe, B.S. Clausen, *Catal. Rev.* 26 (1984) 395–420.
- [54] H. Toulhoat, P. Raybaud, *J. Catal.* 216 (2003) 63–72.
- [55] P. Raybaud, G. Kresse, J. Hafner, H. Toulhoat, *J. Phys. Condens. Matter*. 9 (1997) 11085–11106.
- [56] P. Raybaud, J. Hafner, G. Kresse, H. Toulhoat, *J. Phys. Condens. Matter*. 9 (1997) 11107–11140.
- [57] R.R. Chianelli, G. Berhault, P. Raybaud, S. Kasztelan, J. Hafner, H. Toulhoat, *Appl. Catal. A Gen.* 227 (2002) 83–96.
- [58] P. Afanasiev, I. Bezverkhyy, *Appl. Catal. A Gen.* 322 (2007) 129–141.
- [59] I. Shafiq, S. Shafique, P. Akhter, W. Yang, M. Hussain, *Catal. Rev. - Sci. Eng.* (2020) 1–86.

References

- [60] S.L. Soled, S. Miseo, R. Krycak, H. Vroman, T.C. Ho, Ke.L. Riley, (2001), US 6,299,760 B1.
- [61] F.L. Plantenga, R. Cerfontain, S. Eijsbouts, F. Van Houtert, G.H. Anderson, S. Miseo, S. Soled, K. Riley, K. Fujita, Y. Inoue, *Stud. Surf. Sci. Catal.* 145 (2003) 407–410.
- [62] Y. Gochi, C. Ornelas, F. Paraguay, S. Fuentes, L. Alvarez, J.L. Rico, G. Alonso-Núñez, *Catal. Today*. 107–108 (2005) 531–536.
- [63] Albemarle, STAX Technol. (2021).
<https://www.albemarle.com/businesses/catalysts/hydroprocessing-catalysts/stax-technology> (accessed March 1, 2021).
- [64] B. Leliveld and, B. Slettenhaar, *Albemarle Catal. Cour.* 89. (2019).
- [65] S. Eijsbouts, S.W. Mayo, K. Fujita, *Appl. Catal. A Gen.* 322 (2007) 58–66.
- [66] R.G. Leliveld, S.E. Eijsbouts, *Catal. Today*. 130 (2008) 183–189.
- [67] K.J. Laidler, *Pure Appl. Chem.* 68 (1996) 149–192.
- [68] R.R. Chianelli, M.H. Siadati, M. Perez De la Rosa, G. Berhault, J.P. Wilcoxon, R. Bearden, B.L. Abrams, *Catal. Rev. - Sci. Eng.* 48 (2006) 1–41.
- [69] M. Breyse, E. Furimsky, S. Kasztelan, M. Lacroix, G. Perot, *Catal. Rev. - Sci. Eng.* 44 (2002) 651–735.
- [70] A. Stanislaus, B.H. Cooper, *Catal. Rev. Sci. Eng.* 36 (1994) 75–123.
- [71] R.R. Chianelli, M. Daage, M.J. Ledoux, *Adv. Catal.* 40 (1994) 177–232.
- [72] B. Delmon, *Catal. Letters*. 22 (1993) 1–32.
- [73] P.T. Vasudevan, J.L.G. Fierro, *Catal. Rev. - Sci. Eng.* 38 (1996) 161–188.
- [74] J.N.D. de León, C.R. Kumar, J. Antúnez-García, S. Fuentes-Moyado, *Catalysts*. 9 (2019) 1–26.
- [75] M. Che, *Catal. Today*. 218–219 (2013) 162–171.
- [76] P. Sabatier, *Berichte Der Dtsch. Chem. Gesellschaft.* (1911) 1984–2001.
- [77] M. Lacroix, N. Boutarfa, C. Guillard, M. Vrinat, M. Breyse, *J. Catal.* 120 (1989) 473–477.
- [78] J.P.R. Vissers, C.K. Groot, E.M. Van Oers, V.H.J. De Beer, R. Prins, *Bull. Soc. Chim. Belg.* 93 (1984) 813–821.
- [79] M.J. Ledoux, O. Michaux, G. Agostini, P. Panissod, *J. Catal.* 102 (1986) 275–288.
- [80] J.K. Nørskov, B.S. Clausen, H. Topsøe, *Catal. Letters*. 13 (1992) 1–8.
- [81] S. Harris, R.R. Chianelli, *J. Catal.* 86 (1984) 400–412.
- [82] E.J.M. Hensen, H.J.A. Brans, G.M.H.J. Lardinois, V.H.J. De Beer, J.A.R. Van Veen, R.A. Van Santen, *J. Catal.* 192 (2000) 98–107.
- [83] P. Raybaud, *Appl. Catal. A Gen.* 322 (2007) 76–91.
- [84] C. Thomazeau, C. Geantet, M. Lacroix, M. Danot, V. Harlé, P. Raybaud, *Appl. Catal. A Gen.* 322 (2007) 92–97.
- [85] N. Guernalec, C. Geantet, P. Raybaud, T. Cseri, M. Aouine, M. Vrinat, *Oil Gas Sci. Technol. IFP.* 61 (2006) 515–525.
- [86] N. Guernalec, T. Cseri, P. Raybaud, C. Geantet, M. Vrinat, *Catal. Today*. 98 (2004) 61–66.
- [87] J. Bénard, J. Oudar, N. Barbouth, E. Margot, Y. Berthier, *Surf. Sci.* 88 (1979) L35–L41.
- [88] J.C. Duchet, E.M. Van Oers, V.H.J. De Beer, R. Prins, *J. Catal.* 80 (1983) 386–402.
- [89] S. Harris, R.R. Chianelli, *J. Catal.* 98 (1986) 17–31.
- [90] H. Toulhoat, P. Raybaud, S. Kasztelan, G. Kresse, J. Hafner, *Catal. Today*. 50 (1999) 629–636.
- [91] J.C. Wildervanck, F. Jellinek, *Zeitschrift Für Anorg. Und Allg. Chemie. Band* 328 (1964) 309–318.
- [92] P. Ehrlich, *Zeitschrift Für Anorg. Chemie. Band* 257 (1948) 247–253.

References

- [93] E. Payen, S. Kasztelan, J. Grimblot, *J. Mol. Struct.* 174 (1988) 71–76.
- [94] R.G. Dickinson, L. Pauling, *V.* 45, R.G. Dick, 45 (1923) 1466–1471.
- [95] J.A. Wilson, A.D. Yoffe, *Adv. Phys.* 18 (1969) 193–335.
- [96] J. V. Lauritsen, M. V. Bollinger, E. Lægsgaard, K.W. Jacobsen, J.K. Nørskov, B.S. Clausen, H. Topsøe, F. Besenbacher, *J. Catal.* 221 (2004) 510–522.
- [97] M. Daage, R.R. Chianelli, *J. Catal.* 149 (1994) 414–427.
- [98] H. Schweiger, P. Raybaud, G. Kresse, H. Toulhoat, *J. Catal.* 207 (2002) 76–87.
- [99] S. Kasztelan, H. Toulhoat, J. Grimblot, J.P. Bonnelle, *Appl. Catal.* 13 (1984) 127–159.
- [100] F. Pedraza, J. Cruz-Reyest, D. Acosta, M.J. Yanez, M. Avalos-Borja, S. Fuentes, *J. Phys. Condens Matter* . 5 (1993) A219–A220.
- [101] M. Salmeron, G.A. Somorjai, A. Wold, R. Chianelli, K.S. Liang, *Chem. Phys. Lett.* 90 (1982) 105–107.
- [102] L.S. Byskov, J.K. Nørskov, B.S. Clausen, H. Topsøe, *J. Catal.* 187 (1999) 109–122.
- [103] J.G. Kushmerick, P.S. Weiss, *J. Phys. Chem. B.* 102 (1998) 10094–10097.
- [104] J. Bulicz, L. Morales De La Garza, S. Fuentes, *Surf. Sci.* 365 (1996) 411–421.
- [105] T.F. Hayden, J.A. Dumesic, *J. Catal.* 103 (1987) 366–384.
- [106] S. Helveg, J. V. Lauritsen, E. Laegsgaard, I. Stensgaard, J.K. Nørskov, B.S. Clausen, H. Topsøe, F. Besenbacher, *Phys. Rev. Lett.* 84 (2000) 951–954.
- [107] S. Kasztelan, *Langmuir.* 6 (1990) 590–595.
- [108] S. Cristol, J.F. Paul, E. Payen, D. Bougeard, S. Clémendot, F. Hutschka, *J. Phys. Chem. B.* 104 (2000) 11220–11229.
- [109] G. Plazenet, S. Cristol, J.F. Paul, E. Payen, J. Lynch, *Phys. Chem. Chem. Phys.* 3 (2001) 246–251.
- [110] S. Cristol, J.F. Paul, E. Payen, D. Bougeard, S. Clémendot, F. Hutschka, *J. Phys. Chem. B.* 106 (2002) 5659–5667.
- [111] P. Raybaud, J. Hafner, G. Kresse, S. Kasztelan, H. Toulhoat, *J. Catal.* 189 (2000) 129–146.
- [112] E. Payen, R. Hubaut, S. Kasztelan, O. Poulet, J. Grimblot, *J. Catal.* 147 (1994) 123–132.
- [113] E.J.M. Hensen, P.J. Kooyman, Y. Van der Meer, A.M. Van der Kraan, V.H.J. De Beer, J.A.R. Van Veen, R.A. Van Santen, *J. Catal.* 199 (2001) 224–235.
- [114] K.-I. Tanaka, T. Okuhara, *J. Catal.* 78 (1982) 155–164.
- [115] T.C. Ho, *Catal. Rev.* 30 (1988) 117–160.
- [116] H. Topsøe, B.S. Clausen, N.-Y. Topsøe, E. Pedersen, W. Niemann, A. Müller, H. Bögge, B. Lengeler, *J. Chem. SOC., Faraday Trans. I.* 83 (1987) 2157–2167.
- [117] R.J.H. Voorhoeve, J.C.M. Stuiver, *J. Catal.* 23 (1971) 243–252.
- [118] G. Hagenbach, P. Courty, B. Delmon, *J. Catal.* 31 (1973) 264–273.
- [119] S. Göbölös, Q. Wu, P.G. Delannay, P. Grange, B. Delmon, J. Ladriere, *Polyhedron.* 5 (1986) 219–224.
- [120] P. Baeza, M.S. Ureta-Zañartu, N. Escalona, J. Ojeda, F.J. Gil-Llambías, B. Delmon, *Appl. Catal. A Gen.* 274 (2004) 303–309.
- [121] R.W. Phillips, A.A. Fote, *J. Catal.* 41 (1976) 168–172.
- [122] R.R. Chianelli, G. Berhault, *Catal. Today.* 53 (1999) 357–366.
- [123] M. Ramos, G. Berhault, D.A. Ferrer, B. Torres, R.R. Chianelli, *Catal. Sci. Technol.* 2 (2012) 164–178.
- [124] J. V. Lauritsen, J. Kibsgaard, G.H. Olesen, P.G. Moses, B. Hinnemann, S. Helveg, J.K. Nørskov,

- B.S. Clausen, H. Topsøe, E. Lægsgaard, F. Besenbacher, *J. Catal.* 249 (2007) 220–233.
- [125] O. Sørensen, B.S. Clausen, R. Candia, H. Topsøe, *Appl. Catal.* 13 (1985) 363–372.
- [126] R. Candia, B.S. Clausen, H. Topsøe, *J. Catal.* 77 (1982) 564–566.
- [127] P. Raybaud, J. Hafner, G. Kresse, S. Kasztelan, H. Toulhoat, *J. Catal.* 190 (2000) 128–143.
- [128] J. V. Lauritsen, S. Helveg, E. Lægsgaard, I. Stensgaard, B.S. Clausen, H. Topsøe, F. Besenbacher, *J. Catal.* 197 (2001) 1–5.
- [129] H. Schweiger, P. Raybaud, H. Toulhoat, *J. Catal.* 212 (2002) 33–38.
- [130] M. Sun, A.E. Nelson, J. Adjaye, *J. Catal.* 226 (2004) 32–40.
- [131] W. Niemann, B.S. Clausen, H. Topsøe, *Catal. Letters.* 4 (1990) 355–364.
- [132] S.M.A.M. Bouwens, J.A.R. Van Veen, D.C. Koningsberger, V.H.J. De Beer, R. Prins, *J. Phys. Chem.* 95 (1991) 123–134.
- [133] S.P.A. Louwers, R. Prins, *J. Catal.* 133 (1992) 94–111.
- [134] E.F. Gallei, M. Hesse, E. Schwab, Development of Industrial Catalysts, in: G. Ertl, H. Knözinger, F. Schüth, J. Weitkamp (Eds.), *Handb. Heterog. Catal.*, Second Edition, Wiley VCH Verlag GmbH&Co KGaA, Weinheim, Germany, 2008: pp. 57–66.
- [135] F. Maugé, J.C. Duchet, J.C. Lavalley, S. Houssenbay, E. Payen, J. Grimblot, S. Kasztelan, *Catal. Today.* 10 (1991) 561–577.
- [136] B. Hinnemann, J.K. Nørskov, H. Topsøe, *J. Phys. Chem. B.* 109 (2005) 2245–2253.
- [137] H. Topsøe, *Appl. Catal. A Gen.* 322 (2007) 3–8.
- [138] H. Topsøe, R. Candia, N.-Y. Topsoe, B.S. Clausen, *Bull. Soc. Chim. Belg.* 93 (1984) 783–806.
- [139] H. Topsøe, B.S. Clausen, *Appl. Catal.* 25 (1986) 273–293.
- [140] J.P.R. Vissers, V.H.J. De Beer, J.A. Moulijn, R. Prins, *J. Catal.* 105 (1987) 277–284.
- [141] R.I. Decierck-Grimee, P. Canesson, R.M. Friedman, J.J. Fripiat, *J. Phys. Chem.* 82 (1978) 889.
- [142] V.M. Kogan, N.N. Rozhdestvenskaya, I.K. Korshevets, *Appl. Catal. A Gen.* 234 (2002) 207–219.
- [143] A.N. Startsev, *Catal. Rev. Sci. Eng.* 37 (1995) 353–422.
- [144] Y.C. Park, H.-K. Rhee, *Korean J. Chem. Eng.* 15 (1998) 411–416.
- [145] V.H.J. De Beer, T.H.M. Van Sint Fiet, J.F. Engelen, A.C. Van Haandel, M.W.J. Wolfs, C.H. Amberg, G.C.A. Schuit, *J. Catal.* 27 (1972) 357–368.
- [146] J. Mijoin, V. Thévenin, N. Garcia Aguirre, H. Yuze, J. Wang, W.Z. Li, G. Pérot, J.L. Lemberon, *Appl. Catal. A Gen.* 180 (1999) 95–104.
- [147] S. Eijsbouts, *Appl. Catal. A Gen.* 158 (1997) 53–92.
- [148] B. Guichard, M. Roy-Auberger, E. Devers, C. Legens, P. Raybaud, *Catal. Today.* 130 (2008) 97–108.
- [149] E. Krebs, B. Silvi, P. Raybaud, *Catal. Today.* 130 (2008) 160–169.
- [150] J. Hein, O.Y. Gutiérrez, E. Schachtl, P. Xu, N.D. Browning, A. Jentys, J.A. Lercher, *ChemCatChem.* 7 (2015) 3692–3704.
- [151] S. Eijsbouts, X. Li, J. Bergwerff, J. Louwen, L. Woning, J. Loos, *Catal. Today.* 292 (2017) 38–50.
- [152] E. Schachtl, L. Zhong, E. Kondratieva, J. Hein, O.Y. Gutiérrez, A. Jentys, J.A. Lercher, *ChemCatChem.* 7 (2015) 4118–4130.
- [153] M. Breyse, B.A. Bennett, D. Chadwick, M. Vrinat, *Bull. Soc. Chim. Belg.* 90 (1981) 1271–1277.
- [154] P.P. Minaev, P.A. Nikulshin, M.S. Kulikova, A.A. Pimerzin, V.M. Kogan, *Appl. Catal. A Gen.* 505 (2015) 456–466.
- [155] S. Eijsbouts, L.C.A. Van den Oetelaar, R.R. Van Puijenbroek, *J. Catal.* 229 (2005) 352–364.

References

- [156] X. Zhao, J. Wei, *J. Catal.* 147 (1994) 429–440.
- [157] F.B. Garreau, H. Toulhoat, S. Kasztelan, R. Paulus, *Polyhedron*. 5 (1986) 211–217.
- [158] T.A. Pecoraro, R.R. Chianelli, N.J. Somerville, (1985), U.S. Patent 4,528,089.
- [159] R.R. Chianelli, T.A. Pecoraro, (1981), U.S. Patent 4,288,422.
- [160] G. Alonso, M. Del Valle, J. Cruz, V. Petranovskii, A. Licea-Claverie, S. Fuentes, *Catal. Today*. 43 (1998) 117–123.
- [161] G. Berhault, L. Cota Araiza, A. Duarte Moller, A. Mehta, R.R. Chianelli, *Catal. Letters*. 78 (2002) 1–4.
- [162] G. Berhault, A. Mehta, A.C. Pavel, J. Yang, L. Rendon, M.J. Yácaman, L. Araiza Cota, A. Moller Duarte, R.R. Chianelli, *J. Catal.* 198 (2001) 9–19.
- [163] M. Ramos, D. Ferrer, E. Martinez-Soto, H. Lopez-Lippmann, B. Torres, G. Berhault, R.R. Chianelli, *Ultramicroscopy*. 127 (2013) 64–69.
- [164] V. Schwartz, S.T. Oyama, *J. Mol. Catal. A Chem.* 163 (2000) 269–282.
- [165] J.C. Schlatter, S. Ted Oyama, J.E. Metcalfe, III., J.M. Lambert, Jr., *Ind. Eng. Chem. Res.* 27 (1988) 1648–1653.
- [166] S. Ramanathant, S.T. Oyama, *J. Phys. Chem.* 99 (1995) 16365–16372.
- [167] J.S. Lee, M. Boudart, *Appl. Catal.* 19 (1985) 207–210.
- [168] R.L.J. Burwell, *Pure Appl. Chem.* 46 (1976) 71–90.
- [169] K. Piszczatowski, G. Łach, M. Przybytek, J. Komasa, K. Pachucki, B. Jeziorski, *J. Chem. Theory Comput.* 5 (2009) 3039–3048.
- [170] G. Herzberg, *J. Mol. Spectrosc.* 33 (1970) 147–168.
- [171] S.J. Tauster, T.A. Pecoraro, R.R. Chianelli, *J. Catal.* 63 (1980) 515–519.
- [172] F.E. Massoth, *J. Catal.* 36 (1975) 164–184.
- [173] N.-Y. Topsøe, H. Topsøe, *J. Catal.* 84 (1983) 386–401.
- [174] P. Raybaud, J. Hafner, G. Kresse, H. Toulhoat, *Surf. Sci.* 407 (1998) 237–250.
- [175] F.E. Massoth, C.L. Kibby, *J. Catal.* 47 (1977) 300–315.
- [176] J.F. Paul, E. Payen, *J. Phys. Chem. B*. 107 (2003) 4057–4064.
- [177] T. Kabe, W. Qian, A. Ishihara, *Catal. Today*. 39 (1997) 3–12.
- [178] W. Qian, A. Ishihara, G. Wang, T. Tsuzuki, M. Godo, T. Kabe, *J. Catal.* 170 (1997) 286–294.
- [179] P.G. Moses, B. Hinnemann, H. Topsøe, J.K. Nørskov, *J. Catal.* 248 (2007) 188–203.
- [180] L.S. Byskov, B. Hammer, J.K. Nørskov, B.S. Clausen, H. Topsøe, *Catal. Letters*. 47 (1997) 177–182.
- [181] L.S. Byskov, J.K. Nørskov, B.S. Clausen, H. Topsøe, *Catal. Letters*. 64 (2000) 95–99.
- [182] P. Faye, E. Payen, D. Boudgeard, *J. Mol. Model.* 5 (1999) 63–71.
- [183] G.L. Schrader, C.P. Cheng, *J. Catal.* 80 (1983) 369–385.
- [184] M. V. Bollinger, K.W. Jacobsen, J.K. Nørskov, *Phys. Rev. B - Condens. Matter Mater. Phys.* 67 (2003) 085410.
- [185] J. V Lauritsen, M. Nyberg, R.T. Vang, M. V Bollinger, B.S. Clausen, H. Topsøe, K.W. Jacobsen, E. Laegsgaard, J.K. Nørskov, F. Besenbacher, *Nanotechnology*. 14 (2003) 385–389.
- [186] M. V. Bollinger, J. V. Lauritsen, K.W. Jacobsen, J.K. Nørskov, S. Helveg, F. Besenbacher, *Phys. Rev. Lett.* 87 (2001) 196803.
- [187] A.B. Anderson, Z.Y. Al-Saigh, W.K. Hall, *J. Phys. Chem.* 92 (1988) 803–809.
- [188] N.-Y. Topsøe, H. Topsøe, *J. Catal.* 139 (1993) 641–651.
- [189] C. Petit, F. Maugé, J.-C. Lavalley, *Stud. Surf. Sci. Catal.* 106 (1997) 157–166.

References

- [190] A. Travert, F. Maugé, *Stud. Surf. Sci. Catal.* 127 (1999) 269–277.
- [191] O.Y. Gutiérrez, A. Hrabar, J. Hein, Y. Yu, J. Han, J.A. Lercher, *J. Catal.* 295 (2012) 155–168.
- [192] E. Schachtl, E. Kondratieva, O.Y. Gutiérrez, J.A. Lercher, *J. Phys. Chem. Lett.* 6 (2015) 2929–2932.
- [193] W. Luo, H. Shi, E. Schachtl, O.Y. Gutiérrez, J.A. Lercher, *Angew. Chemie - Int. Ed.* 57 (2018) 14555–14559.
- [194] F. Bataille, J.L. Lemberon, P. Michaud, G. Pérot, M. Vrinat, M. Lemaire, E. Schulz, M. Breysse, S. Kasztelan, *J. Catal.* 191 (2000) 409–422.
- [195] A. Müller, R. Jostes, W. Hellmann, C. Römer, H. Bögge, U. Schimanski, B. Zhuang, L.D. Rosenheim, J.W. McDonald, W.E. Newton, *Z. Anorg. Allg. Chem.* 533 (1986) 125–145.
- [196] P.G. Moses, B. Hinnemann, H. Topsøe, J.K. Nørskov, *J. Catal.* 268 (2009) 201–208.
- [197] H. Topsøe, B.S. Clausen, N.-Y. Topsøe, J.K. Nørskov, C.V. Ovesen, C.J.H. Jacobsen, *Bull. Soc. Chim. Belg.* 104 (1995) 283–291.
- [198] C. Thomas, L. Vivier, M. Lescanne, S. Kasztelan, G. Pérot, *Catal. Letters.* 58 (1999) 33–35.
- [199] M. Sun, J. Adjaye, A.E. Nelson, *Appl. Catal. A Gen.* 263 (2004) 131–143.
- [200] F. Besenbacher, M. Brorson, B.S. Clausen, S. Helveg, B. Hinnemann, J. Kibsgaard, J. V. Lauritsen, P.G. Moses, J.K. Nørskov, H. Topsøe, *Catal. Today.* 130 (2008) 86–96.
- [201] P.C.H. Mitchell, D.A. Green, E. Payen, A.C. Evans, *J. Chem. Soc. Faraday Trans.* 91 (1995) 4467–4469.
- [202] P. Ratnasamy, J.J. Fripiat, *Trans. Faraday Soc.* 66 (1970) 2897–2910.
- [203] T.L. Slager, C.H. Amberg, *Can. J. Chem.* 50 (1972) 3416–3423.
- [204] P. Sundberg, R.B. Moyes, J. Tomkinson, *Bull. Soc. Chim. Belg.* 100 (1991) 967–976.
- [205] C. Sampson, J.M. Thomas, S. Vasudevan, C.J. Wright, *Bull. Soc. Chim. Belg.* 90 (1981) 1215–1224.
- [206] P.N. Jones, E. Knözinger, W. Langel, E.B. Moyes, J. Tomkinson, *Surf. Sci.* 207 (1988) 159–176.
- [207] C.J. Wright, C. Sampson, D. Fraser, R.B. Moyes, P.B. Wells, *J.C.S. Faraday I.* 76 (1980) 1585–1598.
- [208] N. Topsøe, *J. Catal.* 64 (1980) 235–237.
- [209] L.S. Byskov, M. Bollinger, J.K. Nørskov, B.S. Clausen, H. Topsøe, *J. Mol. Catal. A Chem.* 163 (2000) 117–122.
- [210] M.H. Farias, A.J. Gellman, G.A. Somorjai, R.R. Chianelli, K.S. Liang, *Surf. Sci.* 140 (1984) 181–196.
- [211] B.H. Upton, C. Chen, N.M. Rodriguez, R.T.K. Baker, *J. Catal.* 141 (1993) 171–190.
- [212] P.Y. Prodhomme, P. Raybaud, H. Toulhoat, *J. Catal.* 280 (2011) 178–195.
- [213] W.P. Dianis, *Appl. Catal.* 30 (1987) 99–121.
- [214] J. Polz, H. Zeilinger, B. Müller, H. Knözinger, *J. Catal.* 120 (1989) 22–28.
- [215] V. Alexiev, R. Prins, T. Weber, *Phys. Chem. Chem. Phys.* 3 (2001) 5326–5336.
- [216] A. Travert, H. Nakamura, R.A. Van Santen, S. Cristol, J.F. Paul, E. Payen, *J. Am. Chem. Soc.* 124 (2002) 7084–7095.
- [217] M. Sun, A.E. Nelson, J. Adjaye, *J. Catal.* 233 (2005) 411–421.
- [218] N. Dinter, M. Rusanen, P. Raybaud, S. Kasztelan, P. da Silva, H. Toulhoat, *J. Catal.* 267 (2009) 67–77.
- [219] P. Afanasiev, H. Jobic, C. Lorentz, P. Leverd, N. Mastubayashi, L. Piccolo, M. Vrinat, *J. Phys. Chem. C.* 113 (2009) 4139–4146.

References

- [220] P. Afanasiev, *J. Catal.* 269 (2010) 269–280.
- [221] M. Sun, A.E. Nelson, J. Adjaye, *Catal. Today.* 105 (2005) 36–43.
- [222] R.G. Leliveld, A.J. Van Dillen, J.W. Geus, D.C. Koningsberger, *J. Catal.* 171 (1997) 115–129.
- [223] P. Raybaud, J. Hafner, G. Kresse, H. Toulhoat, *Stud.Surf.Sci.Catal.* 127 (1999) 309–317.
- [224] E.N. Rodríguez-Arias, A.E. Gainza, A.J. Hernández, P.S. Lobos, F. Ruetter, *J. Mol. Catal. A Chem.* 102 (1995) 163–174.
- [225] J. Barbour, K.C. Campbell, *J. Chem. Soc., Chem. Commun.* (1982) 1371–1372.
- [226] G.B. McGarvey, S. Kasztelan, *J. Catal.* 148 (1994) 149–156.
- [227] J.A. Rodriguez, S.Y. Li, J. Hrbek, H.H. Huang, G.-Q. Xu, *J. Phys. Chem.* 100 (1996) 14476–14484.
- [228] J. Rodriguez, S. Li, H. Huang, G.-Q. Xu, *Surf. Sci.* 370 (1997) 85–95.
- [229] S.B. Jaffe, *Ind. Eng. Chem., Process. Des. Dev.* 13 (1974) 34–39.
- [230] M. Egorova, R. Prins, *J. Catal.* 225 (2004) 417–427.
- [231] T. Kabe, W. Qian, W. Wang, A. Ishihara, *Catal. Today.* 29 (1996) 197–202.
- [232] P.G. Moses, J.J. Mortensen, B.I. Lundqvist, J.K. Nørskov, *J. Chem. Phys.* 130 (2009) 1–7.
- [233] J. V Lauritsen, M. Nyberg, R.T. Vang, M. V Bollinger, B.S. Clausen, H. Topsøe, K.W. Jacobsen, E. Laegsgaard, J.K. Nørskov, F. Besenbacher, *Nanotechnology.* 14 (2003) 385–389.
- [234] A.K. Tuxen, H.G. Füchtbauer, B. Temel, B. Hinnemann, H. Topsøe, K.G. Knudsen, F. Besenbacher, J. V. Lauritsen, *J. Catal.* 295 (2012) 146–154.
- [235] N.K. Nag, *Appl. Catal.* 10 (1984) 53–62.
- [236] E. Schachtl, J.S. Yoo, O.Y. Gutiérrez, F. Studt, J.A. Lercher, *J. Catal.* 352 (2017) 171–181.
- [237] H. Yang, Y. Wang, H. Jiang, H. Weng, F. Liu, M. Li, *Ind. Eng. Chem. Res.* 53 (2014) 12264–12269.
- [238] A.R. Beltramone, D.E. Resasco, W.E. Alvarez, T. V. Choudhary, *Ind. Eng. Chem. Res.* 47 (2008) 7161–7166.
- [239] S.C. Korre, M.T. Klein, R.J. Quann, *Ind. Eng. Chem. Res.* 34 (1995) 101–117.
- [240] S.C. Korre, M. Neurock, M.T. Klein, R.J. Quann, *Chem. Eng. Sci.* 49 (1994) 4191–4210.
- [241] A. Ishihara, J. Lee, F. Dumeignil, M. Takashi, E.W. Qian, T. Kabe, *Energy and Fuels.* 17 (2003) 1338–1345.
- [242] T. Koltai, M. Macaud, A. Guevara, E. Schulz, M. Lemaire, R. Bacaud, M. Vrinat, *Appl. Catal. A Gen.* 231 (2002) 253–261.
- [243] W. Qian, Y. Yoda, Y. Hirai, A. Ishihara, T. Kabe, *Appl. Catal. A Gen.* 184 (1999) 81–88.
- [244] M.J. Girgis, B.C. Gates, *Ind. Eng. Chem. Res.* 33 (1994) 2301–2313.
- [245] C.M. Lee, C.N. Satterfield, *Energy & Fuels.* 7 (1993) 978–980.
- [246] J.-L. Lemberon, M. Guisnet, *Appl. Catal.* 13 (1984) 181–192.
- [247] M. Nuzzi, B. Marcandalli, *Fuel Process. Technol.* 80 (2003) 35–45.
- [248] M.J. Girgis, B.C. Gates, *Ind. Eng. Chem. Res.* 30 (1991) 2021–2058.
- [249] D. Zhang, J. Zhao, Y. Zhang, X. Lu, *Int. J. Hydrogen Energy.* 41 (2016) 11675–11681.
- [250] J. Hein, O.Y. Gutiérrez, S. Albersberger, J. Han, A. Jentys, J.A. Lercher, *ChemCatChem.* 9 (2017) 629–641.
- [251] K.C. Pratt, J. V Sanders, N. Tamp, *J. Catal.* 66 (1980) 82–92.
- [252] F. Liu, S. Xu, L. Cao, Y. Chi, T. Zhang, D. Xue, *J. Phys. Chem. C.* 111 (2007) 7396–7402.
- [253] A.E. Kuperman, T. Maesen, D. Dykstra, S. Uckung, D. Fong, (2011), U.S. Patent 8,080,492 B2.

References

- [254] T.C. Ho, R. Symon, V. Buchholz, M. Daage, (1998), US005841013A.
- [255] Y.E. Licea, S.L. Amaya, A. Echavarría, J. Bettini, J.G. Eon, L.A. Palacio, A.C. Faro, *Catal. Sci. Technol.* 4 (2014) 1227–1238.
- [256] P. Arnoldy, J.A.M. Van Den Heijkant, G.D. De Bok, J.A. Moulijn, *J. Catal.* 92 (1985) 35–55.
- [257] A.M. De Jong, H.J. Borg, L.J. Van Ijzendoorn, V.G.F.M. Soudant, V.H.J. De Beer, J.A.R. Van Veen, J.W. Niemantsverdriet, *J. Phys. Chem.* 97 (1993) 6477–6483.
- [258] J.C. Muijsers, T. Weber, R.M. van Hardeveld, H.W. Zandbergen, J.W. Niemantsverdriet, *J. Catal.* 157 (1995) 698–705.
- [259] T. Weber, J.C. Muijsers, J.H.M.C. Van Wolput, C.P.J. Verhagen, J.W. Niemantsverdriet, *J. Phys. Chem.* 100 (1996) 14144–14150.
- [260] R. Cattaneo, T. Weber, T. Shido, R. Prins, *J. Catal.* 191 (2000) 225–236.
- [261] A.J. Van der Vlies, G. Kishan, J.W. Niemantsverdriet, R. Prins, T. Weber, *J. Phys. Chem. B.* 106 (2002) 3449–3457.
- [262] A.J. Van der Vlies, R. Prins, T. Weber, *J. Phys. Chem. B.* 106 (2002) 9277–9285.
- [263] W. Qian, A. Ishihara, Y. Aoyama, T. Kabe, *Appl. Catal. A Gen.* 196 (2000) 103–110.
- [264] E.J.M. Hensen, Y. van der Meer, J.A.R. van Veen, J.W. Niemantsverdriet, *Appl. Catal. A Gen.* 322 (2007) 16–32.
- [265] Y. Van Der Meer, E.J.M. Hensen, J.A.R. Van Veen, A.M. Van Der Kraan, *J. Catal.* 228 (2004) 433–446.
- [266] J. van Gestel, J. Leeglise, J.-C. Duchet, *J. Catal.* 145 (1994) 429–436.
- [267] R. Prada Silvy, P. Grange, F. Delannay, B. Delmon, *Appl. Catal.* 46 (1989) 113.
- [268] S. Texier, G. Berhault, G. Pérot, F. Diehl, *Appl. Catal. A Gen.* 293 (2005) 105–119.
- [269] T.L.M. Maesen, A.E. Kuperman, D. O'Rear, (2010), U.S. Patent 7,838,696 B2.
- [270] A. Müller, E. Diemann, *Chem. Commun.* 28 (1971) 180.
- [271] A. Müller, E. Diemann, R. Jostes, H. Bögge, *Angew. Chem. Int. Ed. Engl.* 20 (1981) 934–955.
- [272] T.C. Ho, A.R. Young, R.R. Chianelli, A.J. Jacobson, (1986), U.S. Patent 4,591,429.
- [273] C.B. Roxlo, M. Daage, A.F. Ruppert, R.R. Chianelli, *J. Catal.* 100 (1986) 176–184.
- [274] W. Eltzner, M. Breyse, M. Lacroix, M. Vrinat, *Polyhedron.* 5 (1986) 203–210.
- [275] A. Müller, *Polyhedron.* 5 (1986) 323–340.
- [276] W. Eltzner, M. Breyse, M. Lacroix, C. Leclercq, M. Vrinat, A. Müller, E. Diemann, *Polyhedron.* 7 (1988) 2405–2409.
- [277] W.-H. Pan, M.E. Leonowicz, E.I. Stiefel, *Inorg. Chem.* 22 (1983) 672–678.
- [278] G. Alonso, M.H. Siadati, G. Berhault, A. Aguilar, S. Fuentes, R.R. Chianelli, *Appl. Catal. A Gen.* 263 (2004) 109–117.
- [279] B. Yoosuk, J.H. Kim, C. Song, C. Ngamcharussrivichai, P. Prasassarakich, *Catal. Today.* 130 (2008) 14–23.
- [280] M. Ruinat De Brimont, C. Dupont, A. Daudin, C. Geantet, P. Raybaud, *J. Catal.* 286 (2012) 153–164.
- [281] G. Krüss, *Ann. Der Chemie.* 225 (1884) 1–57.
- [282] E. Corleis, *Ann. Der Chemie.* 232 (1886) 224–270.
- [283] J.W. McDonald, G.D. Friesen, L.D. Rosenhein, W.E. Newton, *Inorganica Chim. Acta.* 72 (1983) 205–210.
- [284] E. Diemann, A. Müller, P.J. Aymonino, *Z. Anorg. Allg. Chem.* 459 (1981) 191–198.
- [285] E. Peters, *Metall. Trans. B.* 4 (1976) 505.

References

- [286] M.F. Wagenhofer, H. Shi, O.Y. Gutiérrez, A. Jentys, J.A. Lercher, *Sci. Adv.* 6 (2020) eaax5331.
- [287] B.C. Lippens, B.G. Linsen, J.H. De Boer, *J. Catal.* 3 (1964) 32–37.
- [288] L. Spieß, G. Teichert, R. Schwarzer, H. Behnken, C. Genzel, *Moderne Röntgenbeugung*, Springer Fachmedien Wiesbaden, 2019.
- [289] J. Epp, *X-Ray Diffraction (XRD) Techniques for Materials Characterization*, in: *Mater. Charact. Using Nondestruct. Eval. Methods*, Elsevier Inc., 2016: pp. 81–124.
- [290] D. Yang, R.F. Frindt, *J. Appl. Phys.* 79 (1996) 2376–2385.
- [291] J. Moser, F. Lrvy, *Thin Solid Films.* 240 (1994) 56–59.
- [292] D. Yang, R.F. Frindt, *Mol. Cryst. Liq. Cryst. Sci. Technol. Sect. A. Mol. Cryst. Liq. Cryst.* 244 (1994) 355–360.
- [293] C. Geantet, L. Sorbier, *Transmission Electron Microscopy, Microanalysis, and Hydrotreating Catalysts*, in: *Catal. by Transit. Met. Sulphides*, Editions TECHNIP, Paris, 2013: pp. 434–453.
- [294] P. Afanasiev, *Appl. Catal. A Gen.* 529 (2017) 10–19.
- [295] K.D. Vernon-Parry, *III-Vs Rev.* 13 (2000) 40–44.
- [296] C. Geantet, C. Pichon, *X-Ray Absorption – EXAFS, XANES*, in: *Catal. by Transit. Met. Sulphides*, Editions TECHNIP, Paris, 2013: pp. 453–487.
- [297] A.-A. Quoineaud, V. Labruyère, *Surface Analysis by XPS*, in: *Catal. by Transit. Met. Sulphides*, 2013: pp. 487–502.
- [298] G. Mestl, H. Knözinger, *Vibrational Spectroscopies*, in: *gerhard Ertl, H. Knözinger, F. Schütz, J. Weitkamp (Eds.), Handb. Heterog. Catal., Second Edition*, Wiley VCH Verlag GmbH&Co KGaA, Weinheim, Germany, 2008: pp. 932–971.
- [299] H.G. Karge, *Concepts and Analysis of Acidity and Basicity*, in: *G. Ertl, H. Knözinger, F. Schüth, J. weitkamp (Eds.), Handb. Heterog. Catal., Wiley VCH Verlag GmbH&Co KGaA, Weinheim, Germany, 2008: pp. 1096–1122.*
- [300] H. Knözinger, *Infrared Spectroscopy for the Characterization of Surface Acidity and Basicity*, in: *G. Ertl, H. Knözinger, F. Schüth, J. WEitkamp (Eds.), Handb. Heterog. Catal., Second Edition*, Wiley VCH Verlag GmbH&Co KGaA, Weinheim, Germany, 2008: pp. 1135–1163.
- [301] A.-A. Quoineaud, V. Labruyère, *FTIR Surface Analysis: Surface Characterisation of Active Siteson Sulphides by CO and NO Adsorption*, in: *Catal. by Transit. Met. Sulphides*, Paris, 2013: pp. 502–519.
- [302] R. Ramachandran, F.E. Massoth, *Can. J. Chem. Eng.* 60 (1982) 17–22.
- [303] C. Cáceres, J.L.G. Fierro, A. Lopez Agudo, F. Severino, J. Laine, *J. Catal.* 97 (1986) 219–227.
- [304] T.A. Bodrero, C.H. Bartholomew, *J. Catal.* 84 (1983) 145–155.
- [305] J. Valyon, W.K. Hall, *J. Catal.* 84 (1983) 216–228.
- [306] Z. Hong, J.R. Regalbuto, *J. Phys. Chem.* 99 (1995) 9452–9457.
- [307] R. Candia, O. Sørensen, J. Villadsen, N.-Y. Topsøe, B.S. Clausen, H. Topsøe, *Bull. Soc. Chim. Belg.* 93 (1984) 763–773.
- [308] D. Zuo, M. Vrinat, H. Nie, F. Maugé, Y. Shi, M. Lacroix, D. Li, *Catal. Today.* 93–95 (2004) 751–760.
- [309] J. Bachelier, M.J. Tilliette, M. Cornac, J.C. Duchet, J.C. Lavalley, D. Cornet, *Bull. Soc. Chim. Belg.* 93 (1984) 743–750.
- [310] E. Delgado, G.A. Fuentes, C. Hermann, G. Kunzmann, H. Knözinger, *Bull. Soc. Chim. Belg.* 93 (1984) 735–742.
- [311] T. Zeng, X.-D. Wen, Y.-W. Li, H. Jiao, *J. Phys. Chem. B.* 109 (2005) 13704–13710.
- [312] Z. Shuxian, K.W. Hall, E. Ertl, H. Knözinger, *J. Catal.* 100 (1986) 167–175.
- [313] Y. Okamoto, M. Kawano, T. Kawabata, T. Kubota, I. Hiromitsu, *J. Phys. Chem. B.* 109 (2005)

288–296.

- [314] Y. Okamoto, Y. Katoh, Y. Mori, T. Imanaka, S. Teranishi, *J. Catal.* 70 (1981) 445–448.
- [315] F. Caron, M. Rivallan, S. Humbert, A. Daudin, S. Bordiga, P. Raybaud, *J. Catal.* 361 (2018) 62–72.
- [316] N.Y. Topsøe, A. Tuxen, B. Hinnemann, J. V. Lauritsen, K.G. Knudsen, F. Besenbacher, H. Topsøe, *J. Catal.* 279 (2011) 337–351.
- [317] M. Baerns, A. Behr, A. Brehm, J. Gmehling, K.-O. Hinrichsen, H. Hofmann, R. Palkovits, U. Onken, A. Renken, *Teil II Chemische Reaktionstechnik*, in: *Tech. Chemie*, 2013.
- [318] A. Jess, P. Wasserscheid, *Chemical Reaction Engineering*, in: A. Jess, P. Wasserscheid (Eds.), *Chem. Technol. An Integr. Textb.*, Wiley-VCH, Weinheim, 2013: pp. 175–405.
- [319] M. Boudart, *Chem. Rev.* 95 (1995) 661–666.
- [320] N.A. Bhole, M.T. Klein, K.B. Bischoff, *Ind. Eng. Chem. Res.* 29 (1990) 313–316.
- [321] K.J. Laidler, M.K. King, *J. Phys. Chem.* 87 (1983) 2657–2664.
- [322] R.D. Cortright, J.A. Dumesic, *Adv. Catal.* 46 (2000) 161–264.
- [323] J.A. Dumesic, G.W. Huber, M. Boudart, *Rates of Catalytic Reactions*, in: G. Ertl, H. Knözinger, F. Schüth, J. Weitkamp (Eds.), *Handb. Heterog. Catal.*, Second Edition, Wiley VCH Verlag GmbH&Co KGaA, Weinheim, Germany, 2008: pp. 1445–1462.
- [324] E.J.M. Hensen, G.M.H.J. Lardinois, V.H.J. De Beer, J.A.R. Van Veen, R.A. Van Santen, *J. Catal.* 187 (1999) 95–108.
- [325] C. Thomas, L. Vivier, J.L. Lemberton, S. Kasztelan, G. Pérot, *J. Catal.* 167 (1997) 1–11.
- [326] P. d'Araujo, C. Thomas, L. Vivier, D. Duprez, G. Pérot, S. Kasztelan, *Catal. Letters.* 34 (1995) 375–378.
- [327] G.W. Foltz, C.F. Melius, *J. Catal.* 108 (1987) 409–425.
- [328] H.C. Urey, D. Rittenberg, *J. Chem. Phys.* 1 (1933) 137–143.
- [329] G. Yang, S.A. Akhade, X. Chen, Y. Liu, M.-S. Lee, V.-A. Glezakou, R. Rousseau, J.A. Lercher, *Angew. Chemie.* 131 (2019) 3565–3570.
- [330] S. Albersberger, H. Shi, M. Wagenhofer, J. Han, O.Y. Gutiérrez, J.A. Lercher, *J. Catal.* 380 (2019) 332–342.
- [331] S. Texier, G. Berhault, G. Pérot, V. Harlé, F. Diehl, *J. Catal.* 223 (2004) 404–418.
- [332] A.I. Dugulan, E.J.M. Hensen, J.A.R. van Veen, *Catal. Today.* 130 (2008) 126–134.
- [333] L. Oliviero, L. Mariey, M.A. Lélías, S. Aiello, J. Van Gestel, F. Maugé, *Catal. Letters.* 135 (2010) 62–67.
- [334] R. Prada Silvy, P. Grange, B. Delmon, *Stud. Surf. Sci. Catal.* 53 (1989) 233–260.
- [335] L. Van Haandel, M. Bremmer, P.J. Kooyman, J.A.R. Van Veen, T. Weber, E.J.M. Hensen, *ACS Catal.* 5 (2015) 7276–7287.
- [336] J. Bocarando, R. Huirache-Acuña, W. Bensch, Z.D. Huang, V. Petranovskii, S. Fuentes, G. Alonso-Núñez, *Appl. Catal. A Gen.* 363 (2009) 45–51.
- [337] A. Olivas, D.H. Galván, G. Alonso, S. Fuentes, *Appl. Catal. A Gen.* 352 (2009) 10–16.
- [338] S. Shan, H. Liu, Y. Yue, G. Shi, X. Bao, *J. Catal.* 344 (2016) 325–333.
- [339] S. Eijsbouts, L.C.A. Van Den Oetelaar, R.R. Van Puijenbroek, *J. Catal.* 229 (2005) 352–364.
- [340] R.R. Chianelli, *Catal. Rev.* 26 (1984) 361–393.
- [341] M. Karroua, H. Matralis, P. Grange, B. Delmon, *Bull. Soc. Chim. Beig.* 104 (1995) 11–18.
- [342] M. Karroua, A. Centeno, H.K. Matralis, P. Grange, B. Delmon, *Appl. Catal.* 51 (1989) L21–L26.
- [343] M. Karroua, H. Matralis, P. Grange, B. Delmon, *J. Catal.* 139 (1993) 371–374.

References

- [344] B. Delmon, *Appl. Catal. A Gen.* 113 (1994) 121–124.
- [345] P. Ratnasamy, S. Sivasanker, *Catal. Rev. Sci. Eng.* 22 (1980) 401–429.
- [346] W. Luo, H. Shi, M. Wagenhofer, O. Gutiérrez, J. Lercher, *J. Phys. Chem. Lett.* 10 (2019) 5617–5622.
- [347] I. Bezverkhy, M. Danot, P. Afanasiev, *Inorg. Chem.* 42 (2003) 1764–1768.
- [348] E.J.M. Hensen, P.J. Kooyman, Y. Van der Meer, A.M. Van der Kraan, V.H.J. De Beer, J.A.R. Van Veen, R.A. Van Santen, P.J. Kooyman, Y. Van der Meer, A.M. Van der Kraan, *J. Catal.* 199 (2001) 224–235.
- [349] C.G. Frye, *J. Chem. Eng. Data.* 7 (1962) 592–595.
- [350] S.G. de León, P. Grange, B. Delmon, *Stud. Surf. Sci. Catal.* (1993) 345–348.
- [351] J. Ojeda, N. Escalona, P. Baeza, M. Escudéy, F.J. Gil-Llambías, *Chem. Commun.* 3 (2003) 1608–1609.
- [352] N. Escalona, R. García, G. Lagos, C. Navarrete, P. Baeza, F.J. Gil-Llambías, *Catal. Commun.* 7 (2006) 1053–1056.
- [353] N. Koizumi, S. Jung, Y. Hamabe, H. Suzuki, M. Yamada, *Catal. Letters.* 135 (2010) 175–181.
- [354] S.D. Kelly, N. Yang, G.E. Mickelson, N. Greenlay, E. Karapetrova, W. Sinkler, S.R. Bare, *J. Catal.* 263 (2009) 16–33.
- [355] H.R. Reinhoudt, A.D. Van Langeveld, P.J. Kooyman, R.M. Stockmann, R. Prins, H.W. Zandbergen, J.A. Moulijn, *J. Catal.* 179 (1998) 443–450.
- [356] B. Scheffer, P.J. Mangnus, J.A. Moulijn, *J. Catal.* 12 (1990) 18–30.
- [357] L. Medici, R. Prins, *J. Catal.* 163 (1996) 38–49.
- [358] G. Kishan, L. Coulier, V.H.J. De Beer, J.A.R. Van Veen, J.W. Niemantsverdriet, *Chem. Commun.* (2000) 1103–1104.
- [359] G. Kishan, L. Coulier, V.H.J. De Beer, J.A.R. Van Veen, J.W. Niemantsverdriet, *J. Catal.* 196 (2000) 180–189.
- [360] L. Coulier, V.H.J. De Beer, J.A.R. Van Veen, J.W. Niemantsverdriet, *J. Catal.* 197 (2001) 26–33.
- [361] L. Coulier, G. Kishan, J.A.R. Van Veen, J.W. Niemantsverdriet, *J. Phys. Chem. B.* 106 (2002) 5897–5906.
- [362] C. Yin, Y. Wang, S. Xue, H. Liu, H. Li, C. Liu, *Fuel.* 175 (2016) 13–19.
- [363] Y. Zhu, Q.M. Ramasse, M. Brorson, P.G. Moses, L.P. Hansen, H. Topsøe, C.F. Kisielowski, S. Helveg, *Catal. Today.* 261 (2016) 75–81.
- [364] J. Kibsgaard, A. Tuxen, K.G. Knudsen, M. Brorson, H. Topsøe, E. Lægsgaard, J. V. Lauritsen, F. Besenbacher, *J. Catal.* 272 (2010) 195–203.
- [365] E.J.M. Hensen, V.H.J. De Beer, J.A.R. Van Veen, R.A. Van Santen, *Catal. Letters.* 84 (2002) 59–67.
- [366] Y. Huang, R.J. Nielsen, W.A. Goddard, *J. Am. Chem. Soc.* 140 (2018) 16773–16782.
- [367] H. Li, C. Tsai, A.L. Koh, L. Cai, A.W. Contryman, A.H. Fragapane, J. Zhao, H.S. Han, H.C. Manoharan, F. Abild-Pedersen, J.K. Nørskov, X. Zheng, *Nat. Mater.* 15 (2016) 48–53.
- [368] L. Zavala-Sanchez, I. Khalil, L. Oliviero, J.F. Paul, F. Maugé, *ChemCatChem.* 12 (2020) 2066–2076.
- [369] J. Chen, L. Oliviero, X. Portier, F. Maugé, *RSC Adv.* 5 (2015) 81038–81044.
- [370] J. Chen, F. Maugé, J. El Fallah, L. Oliviero, *J. Catal.* 320 (2014) 170–179.
- [371] N.Y. Topsøe, *Catal. Today.* 113 (2006) 58–64.
- [372] A. Travert, C. Dujardin, F. Maugé, S. Cristol, J.F. Paul, E. Payen, D. Bougeard, *Catal. Today.* 70 (2001) 255–269.

- [373] N.Y. Topsøe, H. Topsøe, *J. Catal.* 139 (1993) 631–640.
- [374] F. Maugé, J.C. Lavalley, *J. Catal.* 137 (1992) 69–76.
- [375] N.Y. Topsøe, H. Topsøe, *J. Catal.* 75 (1982) 354–374.
- [376] N.Y. Topsøe, H. Topsøe, F.E. Massoth, *J. Catal.* 119 (1989) 252–255.
- [377] J. Chen, E. Dominguez Garcia, L. Oliviero, F. Maugé, *J. Catal.* 332 (2015) 77–82.
- [378] A.A. Tsyganenko, F. Can, A. Traver, F. Maugé, *Appl. Catal. A Gen.* 268 (2004) 189–197.
- [379] F. Maugé, J. Lamotte, N.S. Nesterenko, O. Manoilova, A.A. Tsyganenko, *Catal. Today.* 70 (2001) 271–284.
- [380] F. Vogelgsang, Y. Ji, H. Shi, J.A. Lercher, *J. Catal.* 391 (2020) 212–223.
- [381] M. Lacroix, C. Dumonteil, M. Breysse, S. Kasztelan, *J. Catal.* 185 (1999) 219–222.
- [382] P. Gajardo, A. Mathieux, P. Grange, B. Delmon, *Appl. Catal.* 3 (1982) 347–376.
- [383] G.A. Mills, E.R. Boedeker, A.G. Oblad, *J. Am. Chem. Soc.* 72 (1950) 1554–1560.
- [384] J.G. Santiesteban, J.C. Vartuli, S. Han, R.D. Bastian, C.D. Chang, *J. Catal.* 168 (1997) 431–441.
- [385] A.J. Jones, R.T. Carr, S.I. Zones, E. Iglesia, *J. Catal.* 312 (2014) 58–68.
- [386] R. Gounder, A.J. Jones, R.T. Carr, E. Iglesia, *J. Catal.* 286 (2012) 214–223.
- [387] J. Macht, M.J. Janik, M. Neurock, E. Iglesia, *Angew. Chemie.* 119 (2007) 8010–8014.
- [388] J. Macht, C.D. Baertsch, M. May-Lozano, S.L. Soled, Y. Wang, E. Iglesia, *J. Catal.* 227 (2004) 479–491.
- [389] H. Liu, E. Iglesia, *J. Catal.* 223 (2004) 161–169.
- [390] H. Liu, N. Bayat, E. Iglesia, *Angew. Chemie.* 115 (2003) 5226–5229.
- [391] F.E. Massoth, J. Miciukiewicz, *J. Catal.* 101 (1986) 505–514.
- [392] V. La Vopa, C.N. Satterfield, *J. Catal.* 110 (1988) 375–387.
- [393] M. Nagai, T. Sato, A. Aiba, *J. Catal.* 97 (1986) 52–58.
- [394] A.R. Beltramone, S. Crossley, D.E. Resasco, W.E. Alvarez, T. V. Choudhary, *Catal. Letters.* 123 (2008) 181–185.
- [395] T.C. Ho, D. Nguyen, *J. Catal.* 222 (2004) 450–460.
- [396] T.C. Ho, *J. Catal.* 219 (2003) 442–451.
- [397] N. Salazar, S.B. Schmidt, J. V. Lauritsen, *J. Catal.* 370 (2019) 232–240.
- [398] S. Humbert, G. Izzet, P. Raybaud, *J. Catal.* 333 (2016) 78–93.
- [399] J. Maternová, *Appl. Catal.* (1983) 61–66.
- [400] J. Maternová, *Appl. Catal.* 3 (1982) 3–11.
- [401] V. Stuchlý, H. Zahradníková, L. Beránek, *Appl. Catal.* 35 (1987) 23–34.
- [402] V. Stuchlý, L. Beránek, *Appl. Catal.* 35 (1987) 35.
- [403] J. Miciukiewicz, W. Zmierczak, F.E. Massoth, *Bull. Soc. Chim. Belg.* 96 (1987) 915–923.
- [404] W. Qian, g Zhang, Y. Okoshi, A. Ishihara, T. Kabe, *J. Chem. Soc. Faraday Trans.* 93 (1997) 1821–1826.
- [405] D. Wang, W. Qian, A. Ishihara, T. Kabe, *J. Catal.* 209 (2002) 266–270.
- [406] B. Temel, A.K. Tuxen, J. Kibsgaard, N.Y. Topsøe, B. Hinnemann, K.G. Knudsen, H. Topsøe, J. V. Lauritsen, F. Besenbacher, *J. Catal.* 271 (2010) 280–289.
- [407] N. Salazar, S. Rangarajan, J. Rodríguez-Fernández, M. Mavrikakis, J. V. Lauritsen, *Nat. Commun.* 11 (2020) 1–9.
- [408] E. Dominguez Garcia, J. Chen, E. Oliviero, L. Oliviero, F. Maugé, *Appl. Catal. B Environ.* 260

- (2020) 117975-undefined.
- [409] O.Y. Gutiérrez, S. Singh, E. Schachtl, J. Kim, E. Kondratieva, J. Hein, J.A. Lercher, *ACS Catal.* 4 (2014) 1487–1499.
- [410] P.A. Nikulshin, D.I. Ishutenko, A.A. Mozhaev, K.I. Maslakov, A.A. Pimerzin, *J. Catal.* 312 (2014) 152–169.
- [411] C. Dujardin, M.A. Lélías, J. van Gestel, A. Travert, J.C. Duchet, F. Maugé, *Appl. Catal. A Gen.* 322 (2007) 46–57.
- [412] H. Topsøe, B. Hinnemann, J.K. Nørskov, J. V. Lauritsen, F. Besenbacher, P.L. Hansen, G. Hytoft, R.G. Egeberg, K.G. Knudsen, *Catal. Today.* 107–108 (2005) 12–22.
- [413] M. Breysse, P. Afanasiev, C. Geantet, M. Vrinat, *Catal. Today.* 86 (2003) 5–16.
- [414] C.E. Hédoire, C. Louis, A. Davidson, M. Breysse, F. Maugé, M. Vrinat, *J. Catal.* 220 (2003) 433–441.
- [415] Y. Okamoto, K. Ochiai, M. Kawano, K. Kobayashi, T. Kubota, *Appl. Catal. A Gen.* 226 (2002) 115–127.
- [416] J. Chen, E. Dominguez Garcia, E. Oliviero, L. Oliviero, F. Maugé, *J. Catal.* 339 (2016) 153–162.
- [417] M.A. Lélías, P.J. Kooyman, L. Mariey, L. Oliviero, A. Travert, J. van Gestel, J.A.R. van Veen, F. Maugé, *J. Catal.* 267 (2009) 14–23.
- [418] M. Daage, R.R. Chianelli, A.F. Ruppert, *Stud. Surf. Sci. Catal.* 75 (1993) 571–584.
- [419] R.R. Chianelli, A.F. Ruppert, M. José-Yacamán, A. Vázquez-Zavala, *Catal. Today.* 23 (1995) 269–281.
- [420] M.P. De La Rosa, S. Texier, G. Berhault, A. Camacho, M.J. Yácaman, A. Mehta, S. Fuentes, J.A. Montoya, F. Murrieta, R.R. Chianelli, *J. Catal.* 225 (2004) 288–299.
- [421] G.A. Gonzalez, M. Alvarado, M.A. Ramos, G. Berhault, R.R. Chianelli, *Comput. Mater. Sci.* 123 (2016) 93–105.

Appendices

A1. Supporting information chapter 4

3.1 Effect of leaching

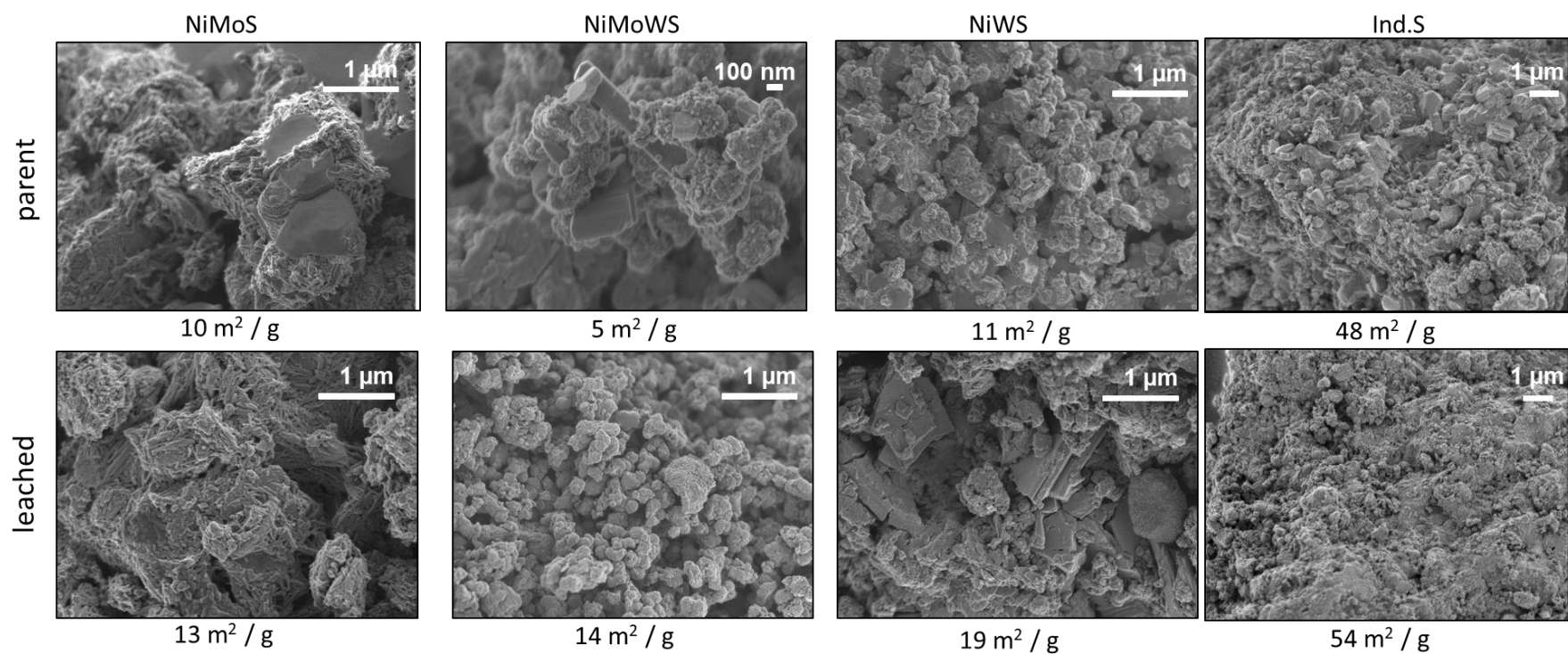


Figure S 6-1. SEM images of parent and leached TMS catalysts. Top row parent formulations with NiS_x particles present as crystalline phases. Bottom row shows the corresponding leached formulations with mainly broken, acid-treated surfaces. Below the images the BET surface areas are given.

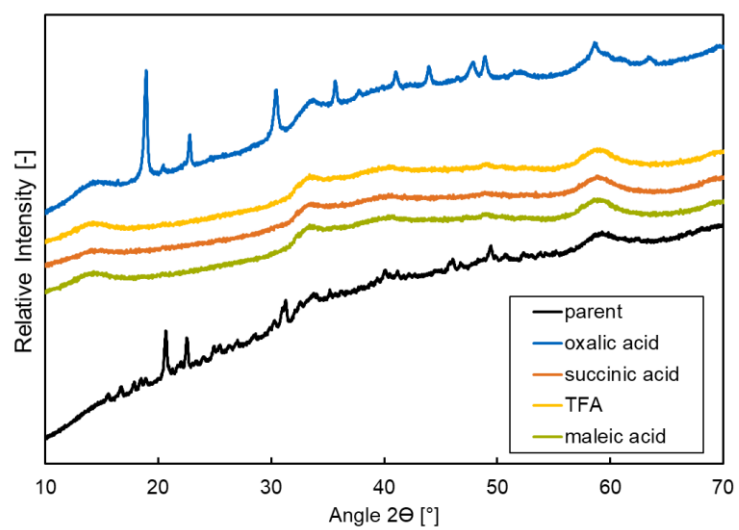


Figure S 6-2. XRD patterns of $\text{Ni}_{0.5}\text{MoS}_2$ leached with different organo acids. While the parent and oxalic acid leached formulation exhibited sharp NiS_x reflections, removal of large NiS_x was successful.

3.2 Estimation of surface SH-groups

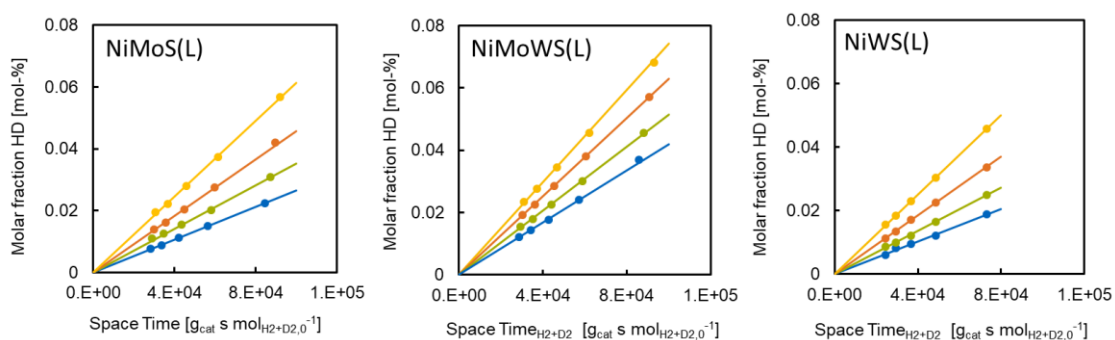
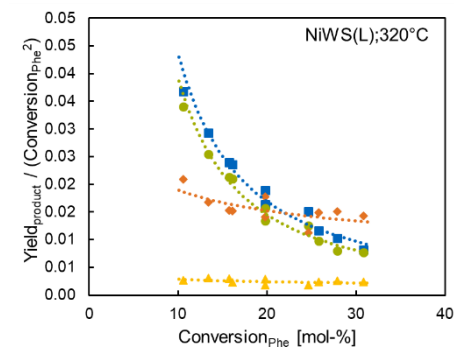
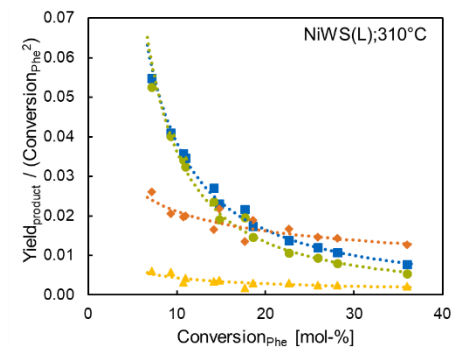
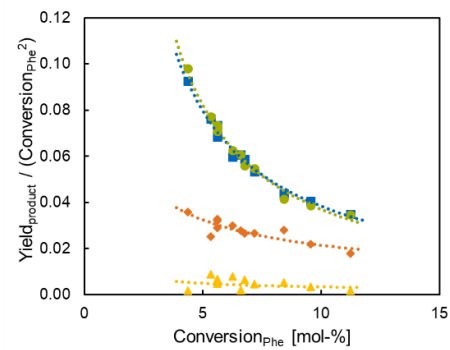
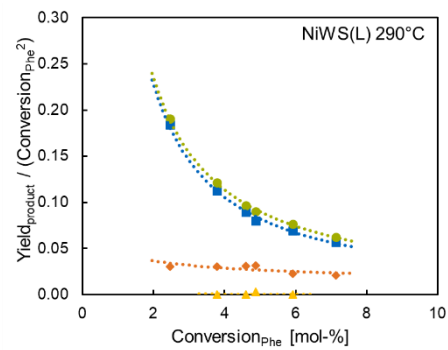
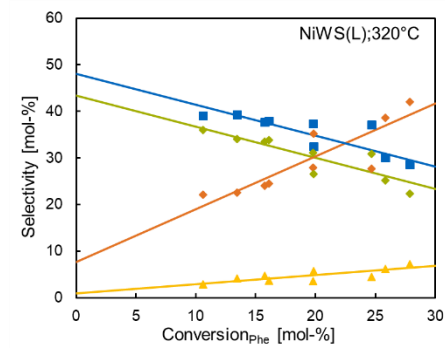
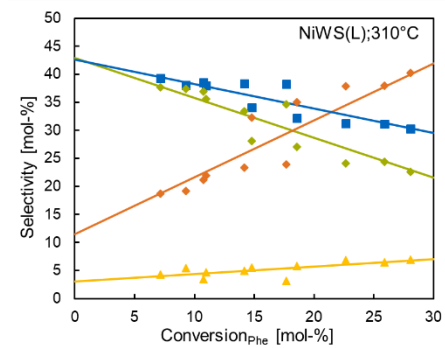
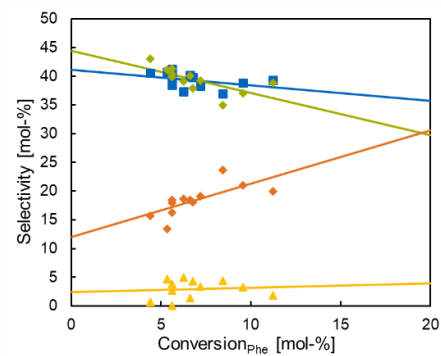
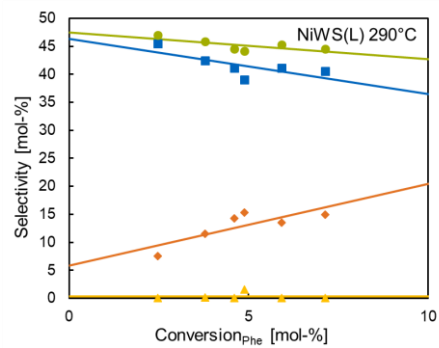


Figure S 6-3. HD-formation rates for NiMoS(L), NiMoWS(L) and NiWS(L) at the temperatures of 70°C (blue), 80°C (green), 90°C (orange) and 100°C (yellow). The molar fraction of HD was by a factor of 10 different (~0.9) to the equilibrated concentration measured on Pt-Al₂O₃ used for quantification.

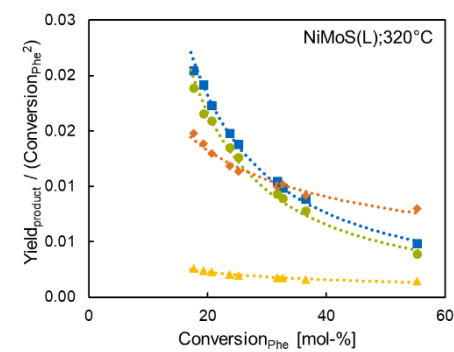
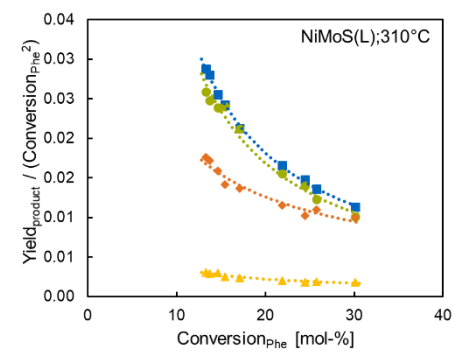
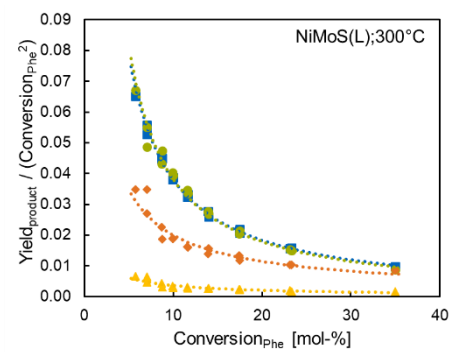
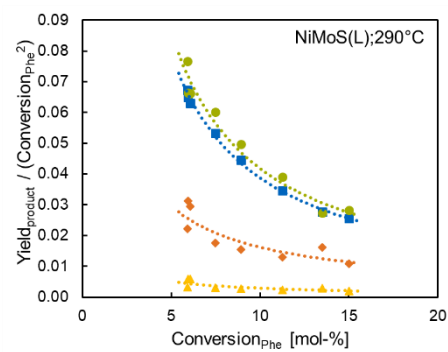
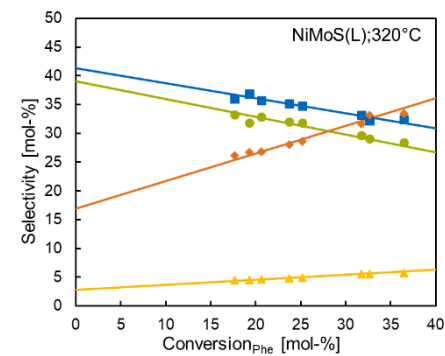
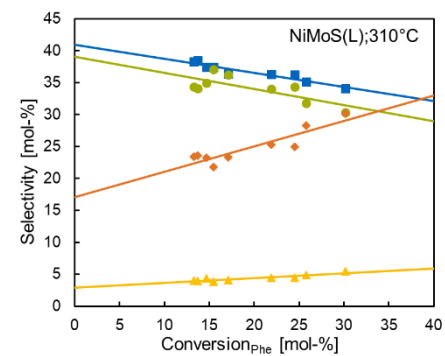
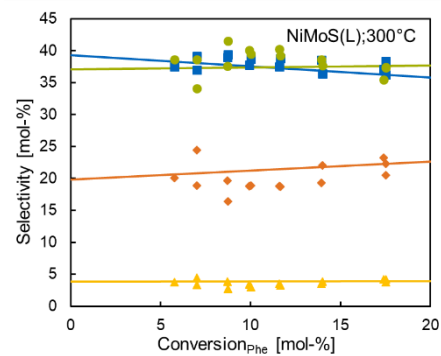
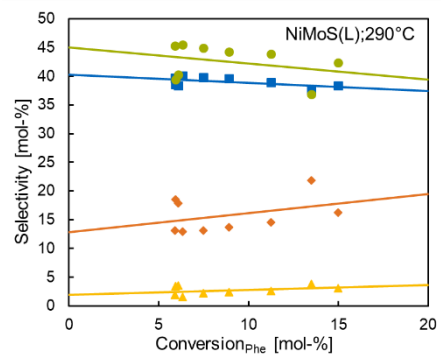
Table S 6-1. HD-formation rates and extrapolation factor from 100 to 300°C for the three leached bulk TMS.

	HD-formation rate [mmol _{HD} g _{cat} ⁻¹ h ⁻¹]				r _{300°C} / r _{100°C} [-]
	70°C	80°C	90°C	100°C	
NiMoS(L)	0.92	1.22	1.66	2.25	27.7
NiWS(L)	0.96	1.27	1.65	2.21	35.58
NiMoWS(L)	1.51	1.85	2.26	2.67	9.94

Appendices



Appendices



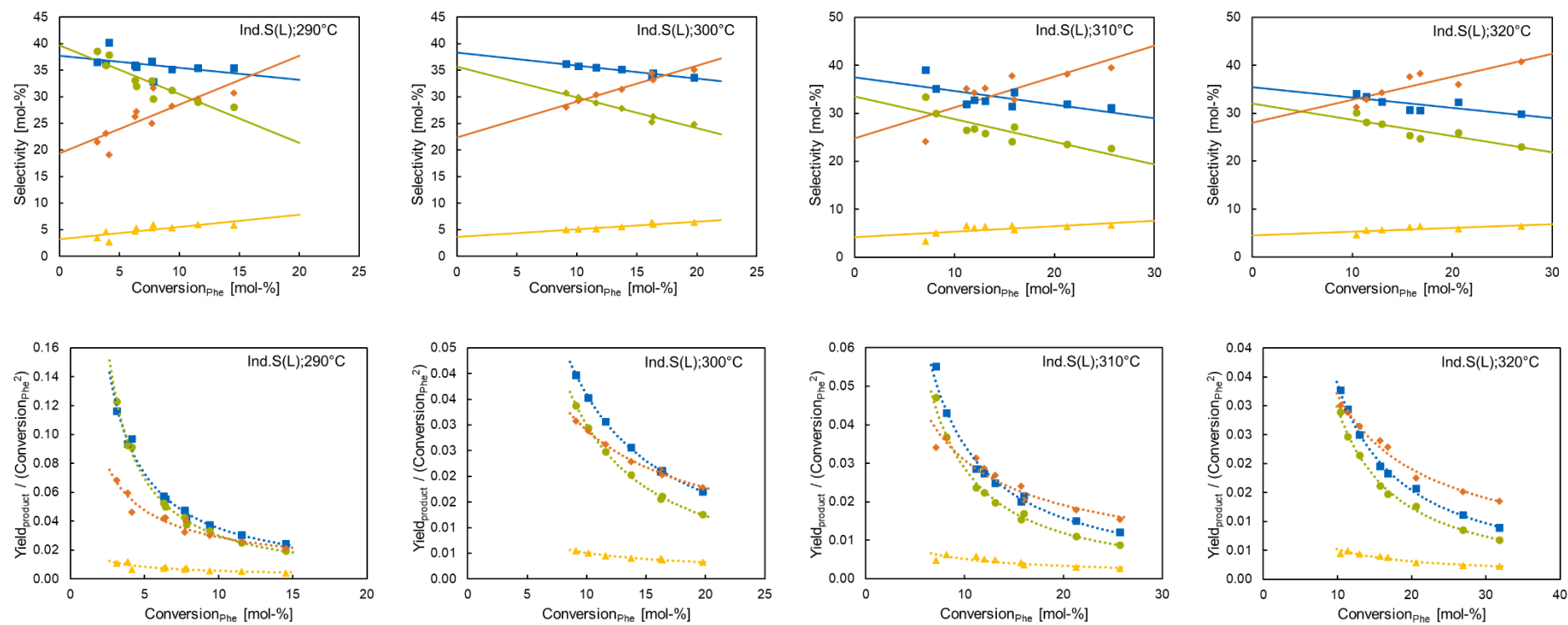
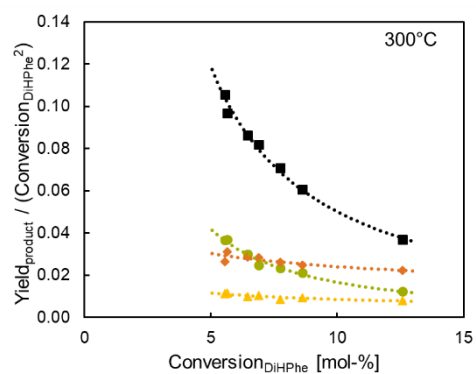
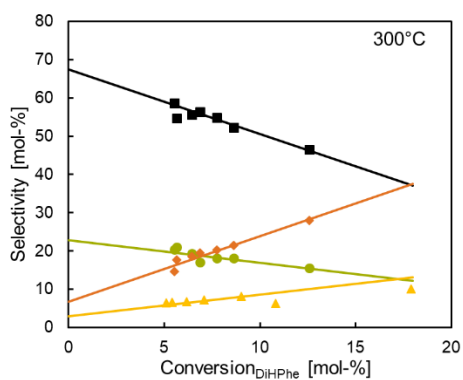
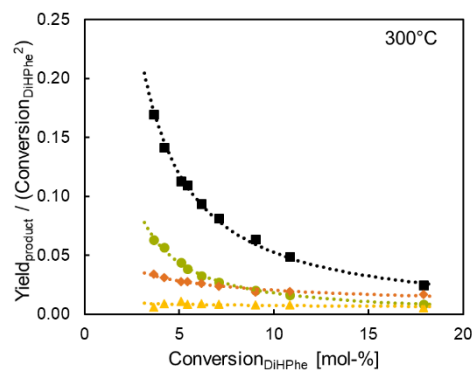
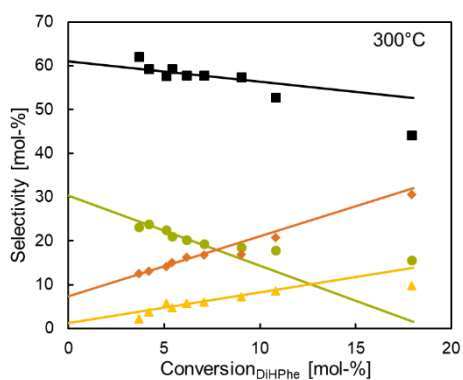
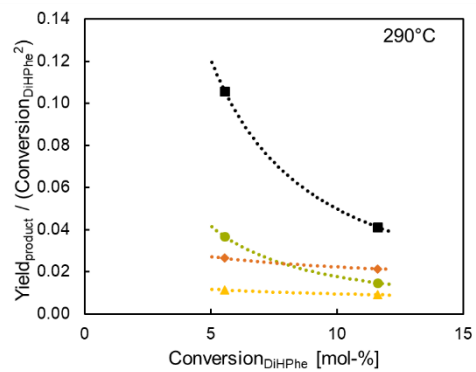
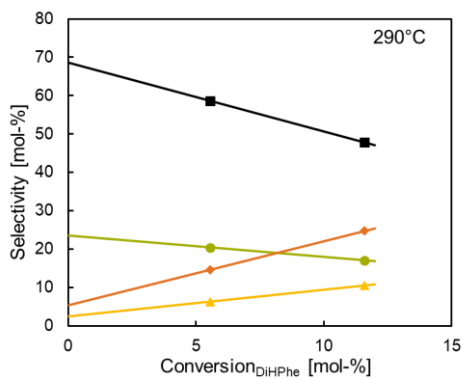


Figure S 6-4. First and second rank delplot for hydrogenation of phenanthrene on leached NiWS, NiMoS and industrial trimetallic catalyst for the temperatures 290, 300, 310 and 320°C. Blue squares: dihydrophenanthrene; green circles: tetrahydrophenanthrene; orange diamonds: symmetric octahydrophenanthrene; yellow triangles: asymmetric octahydrophenanthrene.

Industrial catalyst leached



NiWS leached



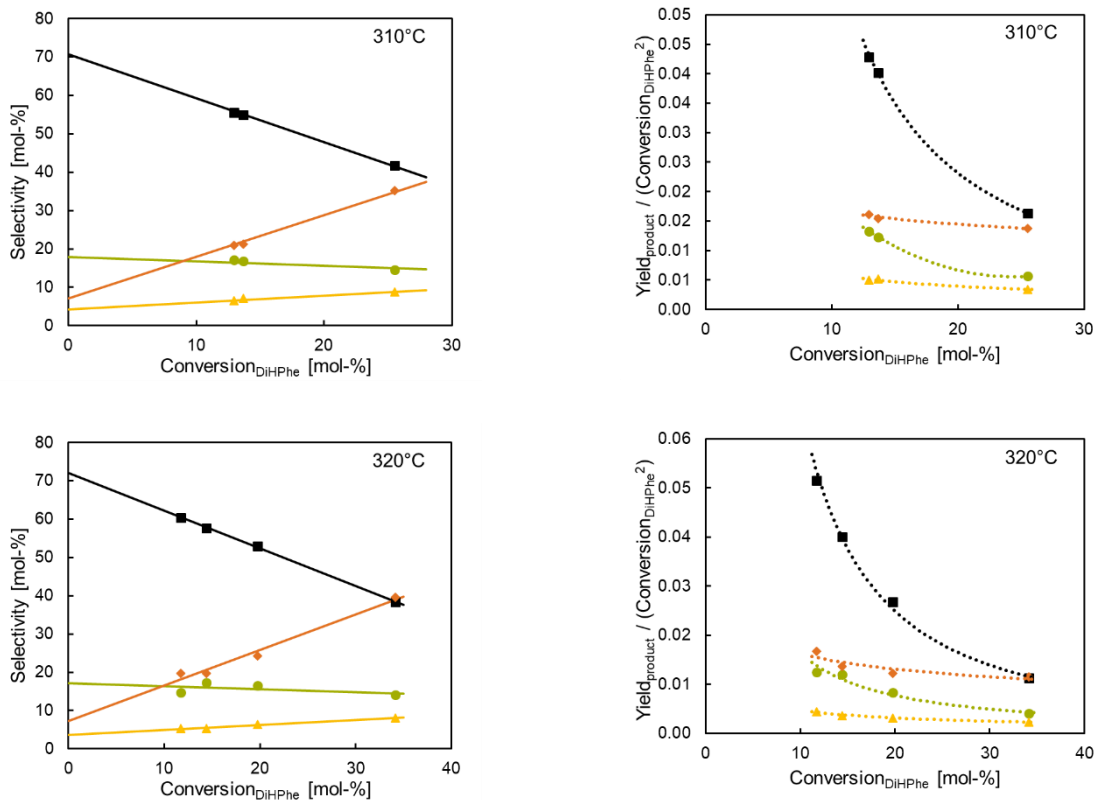


Figure S 6-5. First and second rank delplot for hydrogenation of dihydrophenanthrene on industrial trimetallic catalyst leached (first row) and NiWS leached for the temperature range 290-320°C. Black squares: phenanthrene; green circles: tetrahydrophenanthrene; orange diamonds: symmetric octahydrophenanthrene; yellow triangles: asymmetric octahydrophenanthrene.

3.3 Phenanthrene hydrogenation on bulk NiMoWS2

Table S 6-2. Initial selectivities of four hydrogenation products of phenanthrene on NiMoS(L) at varying partial pressures of H₂ and phenanthrene. The temperature range was 290/300/310/320°C.

NiMoS(L) PP _{H2} / PP _{Phe} [bar]	Initial selectivity [mol-%]				Sym / asym hydrogenation
	DiHPhe	TetHPhe	Sym-OHPhe	Asym-OHPhe	
30.48	42/43/42/44	45/47/45/48	11/11/11/8	1/0/1/1	0.9/0.9/0.9/0.9
33.86	39/40/38/38	39/40/38/38	19/15/16/15	4/3/3/2	1.0/1.1/1.1/1.2
37.28	42/42/42/41	42/39/37/36	15/17/19/19	2/3/3/4	1.0/1.1/1.1/1.1
40.65 / 0.15	40/39/41/41	45/37/39/39	13/20/17/17	2/4/3/3	0.9/1.1/1.1/1.1
0.09	39/40/42/44	43/41/42/36	15/16/14/17	3/3/2/3	0.9/1.0/1.0/1.2
0.12	43/40/40/41	45/40/39/37	10/17/19/18	2/3/3/3	1.0/1.0/1.0/1.1
0.18			n.a.		

Table S 6-3. Initial selectivities of four hydrogenation products of phenanthrene on NiWS(L) at varying partial pressures of H₂ and phenanthrene. The temperature range was 290/300/310/320°C.

NiWS(L) PP _{H2} / PP _{Phe} [bar]	Initial selectivity [mol-%]				Sym / asym hydrogenation
	DiHPhe	TetHPhe	Sym-OHPhe	Asym-OHPhe	
30.48	40/45/42/42	46/44/42/39	6/4/12/16	8/7/3/3	0.9/1.0/1.0/1.1
33.86	41/41/47/42	47/43/42/39	10/14/14/17	2/2/1/3	0.9/1.0/1.1/1.1
37.28	46/42/40/44	49/45/37/41	5/13/20/13	0/0/3/2	0.9/0.9/1.1/1.1
40.65 / 0.15	46/45/40/41	48/51/42/42	6/1/14/15	0/4/3/2	1.0/0.9/1.0/1.0
0.09	40/51/43/45	51/48/47/37	8&0/13/19	1/1/0/0	0.8/1.1/0.9/1.2
0.12	45/42/43/41	48/44/44/42	9/11/17/17	0/2/0/1	0.9/1.0/1.0/1.0
0.18	39/47/42/42	51/44/40/42	10/15/15/18	1/0/3/0	0.8/1.1/1.1/1.0

Appendices

Table S 6-4. Initial selectivities of four hydrogenation products of phenanthrene on Ind.S(L) at varying partial pressures of H₂ and phenanthrene. The temperature range was 290/300/310/320°C.

Ind.S(L) pp _{H₂} / pp _{Phe} [bar]	Initial selectivity [mol-%]				Sym / asym hydrogenation
	DiHPhe	TetHPhe	Sym-OHPhe	Asym-OHPhe	
30.48	45/36/41/42	43/38/39/39	9/22/18/17	3/4/2/2	1.0/1.0/1.0/1.1
33.86	42/39/42/44	44/40/39/39	15/20/15/16	0/1/4/1	1.0/1.0/1.1/1.1
37.28	40/44/39/41	42/39/38/36	17/17/20/20	1/0/3/3	1.0/1.1/1.0/1.1
40.65 / 0.15	38/38/38/36	40/36/34/32	19/22/25/28	3/4/4/5	0.9/1.1/1.1/1.1
0.09	42/40/40/40	40/37/35/35	18/20/21/22	0/3/3/3	1.0/1.1/1.1/1.1
0.12	45/38/41/42	42/38/35/36	15/21/21/19	0/3/3/2	1.1/1.0/1.2/1.2
0.18	40/39/41/41	44/39/38/37	15/20/19/17	1/3/2/4	0.9/1.0/1.1/1.1

Table S 6-5. Activation energies (symmetric / asymmetric hydrogenation pathway) measured for different partial pressures of H₂ and Phe. In bold the standard reaction feed of 1 wt.% Phe and 100% H₂ in gas stream is highlighted.

pp(H ₂) [bar]	40.65				37.28	33.86	30.48
	0.18	0.12	0.09	0.15	0.15		
NiMoS(L)	n.a.	106 / 115	98 / 111	106 / 115	110 / 123	109 / 121	105 / 120
NiWS(L)	125 / 118	112 / 117	120 / 118	107 / 104	113 / 118	114 / 120	108 / 127
Ind.S(L)	95 / 103	93 / 105	85 / 98	84 / 97	98 / 104	100 / 104	93 / 106

Appendices

Table S 6-6. Overall activation energies [kJ mol⁻¹] for the NiMoS, NiWS and sulfided industrial catalyst for change in H₂ or phenanthrene concentration in the feed.

pp(H ₂) [bar]	40.65				37.28	33.86	30.48
pp(Phe) [bar]	0.18	0.12	0.09	0.15	0.15		
NiMoS	n.a.	112	106	111	118	116	114
NiWS	121	115	118	116	116	118	118
Ind.S	99	100	93	94	102	103	100

Table S 6-7. Overall reaction orders in H₂ or phenanthrene for the NiMoS, NiWS and sulfided industrial catalyst for change in temperature between 290 and 320°C.

Temperature [°C]	Reaction order phenanthrene				Reaction order hydrogen			
	290	300	310	320	290	300	310	320
NiMoS	0.44	0.63	0.61	0.58	0.87	1.08	1.00	0.84
NiWS	0.83	0.80	0.84	0.84	0.91	0.77	0.83	0.78
Ind.S	0.91	0.92	0.92	0.98	1.20	1.01	1.04	0.96

Appendices

Table S 6-8. Initial selectivities for trimetallic catalysts of 'dropping' and 'one-pot' precursor synthesis method and different sulfidation protocols obtained by delplot analysis.

Catalyst	Precursor synthesis	H ₂ /S ratio during sulfidation [mol mol ⁻¹]	Initial selectivity [mol-%]				Symmetric / asymmetric hydrogenation
			DiHPhe	TetHPhe	Sym-OHPhe	Asym-OHPhe	
NiMoWS	dropping	10	40	48	11	1	0.7
		25	45	45	9	1	0.9
NiMoWS	one-pot	10	52	36	9	3	1.2
		25	40	31	25	4	0.8
Ind. NiMoWS	n.a.	10	40	38	19	3	0.8
		25	33	31	30	6	0.6
Ind. NiMoWS		25*	39	39	21	1	0.7
NiMoS	dropping	10	40	45	13	2	0.7
NiWS	dropping	10	41	45	12	2	0.8
NiMoWS	dropping	10	44	45	10	1	0.8

A2. Supporting information chapter 5

Table S 6-9. Carbon, hydrogen and nitrogen contents (in mmol/g) and the molar ratio of C/metal (Mo or Ni+Mo) in the parent and HCl-treated Ni_aMoS₂ samples.

Catalysts	C [mmol g _{cat} ⁻¹]	C/metal [mol mol ⁻¹]	H [mmol g _{cat} ⁻¹]	N [mmol g _{cat} ⁻¹]
Ni _{0.1} MoS ₂	1.8 (0.3)	0.29 (0.05)	10.7 (19.9)	1.1 (<0.1)
Ni _{0.2} MoS ₂	0.3 (0.4)	0.04 (0.06)	19.4 (6.5)	<0.1 (<0.1)
Ni _{0.4} MoS ₂	2.0 (0.3)	0.29 (0.04)	10.8 (20.0)	1.6 (<0.1)
Ni _{0.5} MoS ₂	2.3 (0.3)	0.31 (0.04)	9.0 (2.4)	1.1 (<0.1)
Ni _{0.6} MoS ₂	0.3 (0.5)	0.04 (0.07)	12.0 (5.4)	< 0.1 (<0.1)
Ni _{0.7} MoS ₂	0.4 (0.7)	0.04 (0.09)	4.9 (4.5)	<0.1 (<0.1)
MoS ₂	4.7	0.89	14.6	1.6

Table S 6-10. Initial selectivities to the hydrogenation products of phenanthrene on Ni_aMoS₂ and pure MoS₂ catalysts. Number in parentheses correspond to the leached formulations.

Catalysts	Initial selectivities (%) ^[a]				Pathway ratio
	DiHPhe	TetHPhe	sym-OHPhe	asym-OHPhe	
Ni _{0.1} MoS ₂	47 (74)	48 (23)	3 (2)	1 (1)	0.9 (3.0)
Ni _{0.2} MoS ₂	39 (42)	52 (49)	8 (9)	1 (0)	0.7 (0.7)
Ni _{0.4} MoS ₂	43 (38)	51 (50)	5 (11)	1 (2)	0.8 (0.7)
Ni _{0.5} MoS ₂	42 (36)	48 (55)	9 (8)	1 (1)	0.7 (0.6)
Ni _{0.6} MoS ₂	39 (37)	52 (55)	9 (7)	0 (1)	0.6 (0.6)
Ni _{0.7} MoS ₂	41 (38)	57 (56)	2 (6)	0 (0)	0.7 (0.6)
MoS ₂	86 (88)	14 (12)	0 (0)	0 (0)	6.1 (7.3)

^[a] Determined by extrapolation of product selectivities measured at phenanthrene conversions of 10–20% to zero contact time at 300°C and 60 bar total pressure.

Table S 6-11. Nitric oxide (NO) uptake of parent and leached (values in the parentheses) Ni_aMoS₂ formulations measured by volumetric pulsing of 10% NO in He (6.9 μmol_{NO} per pulse).

Catalysts	NO uptake [μmol g _{cat} ⁻¹]
Ni _{0,1} MoS ₂	101 (60)
Ni _{0,2} MoS ₂	135 (95)
Ni _{0,4} MoS ₂	132 (110)
Ni _{0,5} MoS ₂	73 (143)
Ni _{0,6} MoS ₂	131 (121)
Ni _{0,7} MoS ₂	157 (91)
MoS ₂	90
Ni _x S _y	35

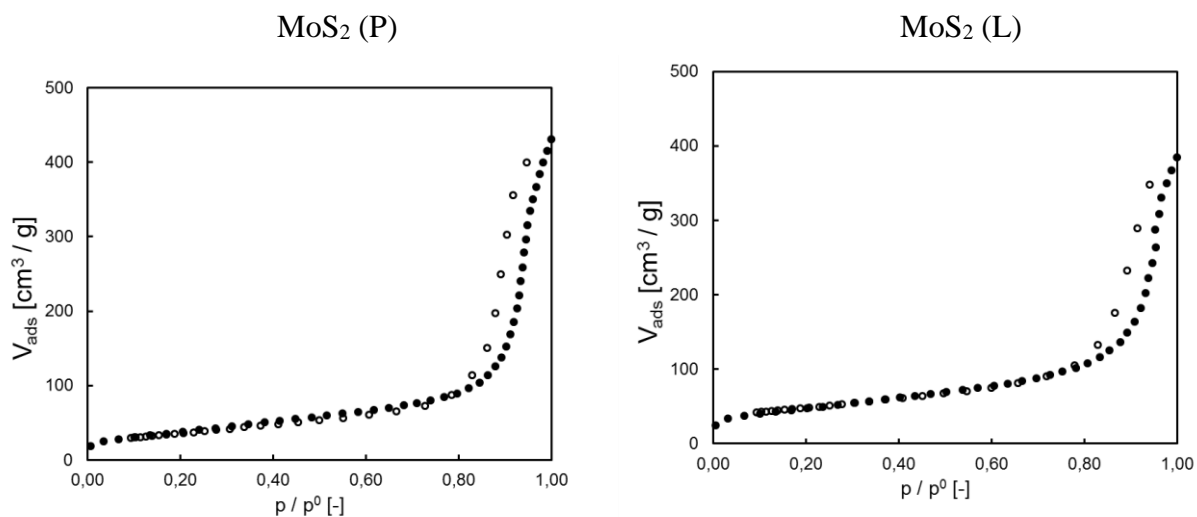


Figure S 6-6. N₂ sorption isotherms of parent and HCl-treated MoS₂ and Ni_aMoS₂ (continued on the next page)

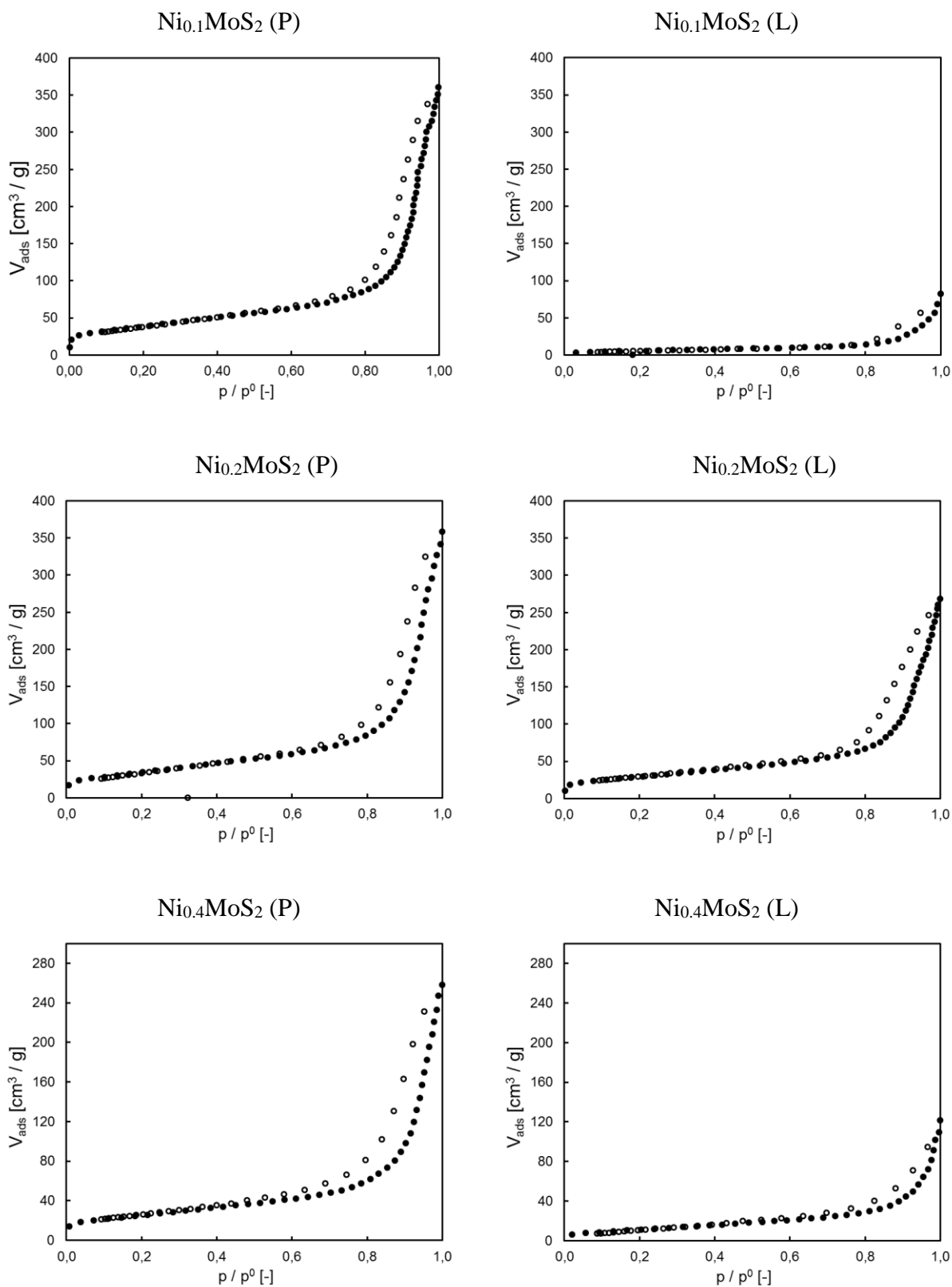


Figure S 6-6. (continued)

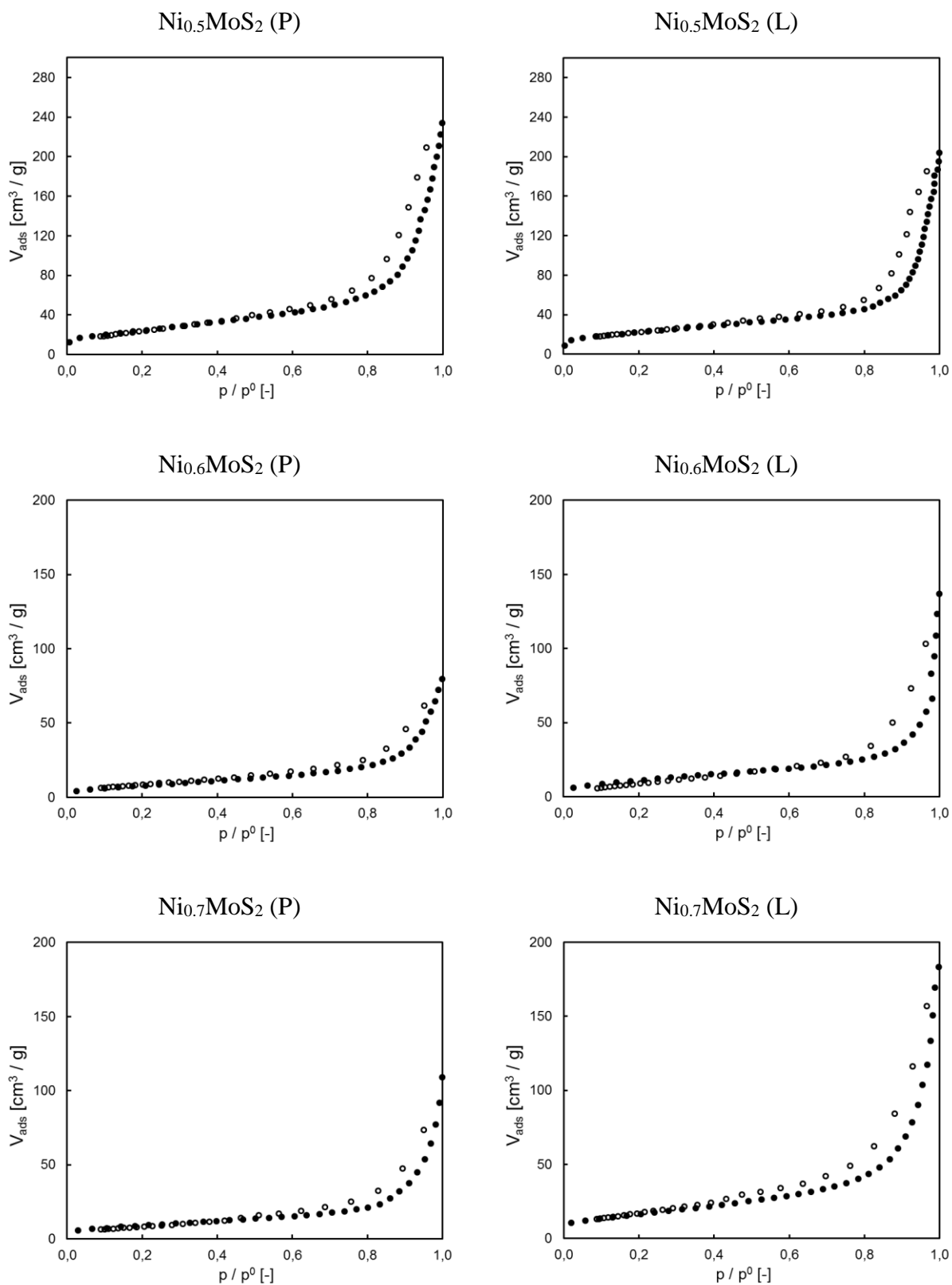


Figure S 6-6. (continued)

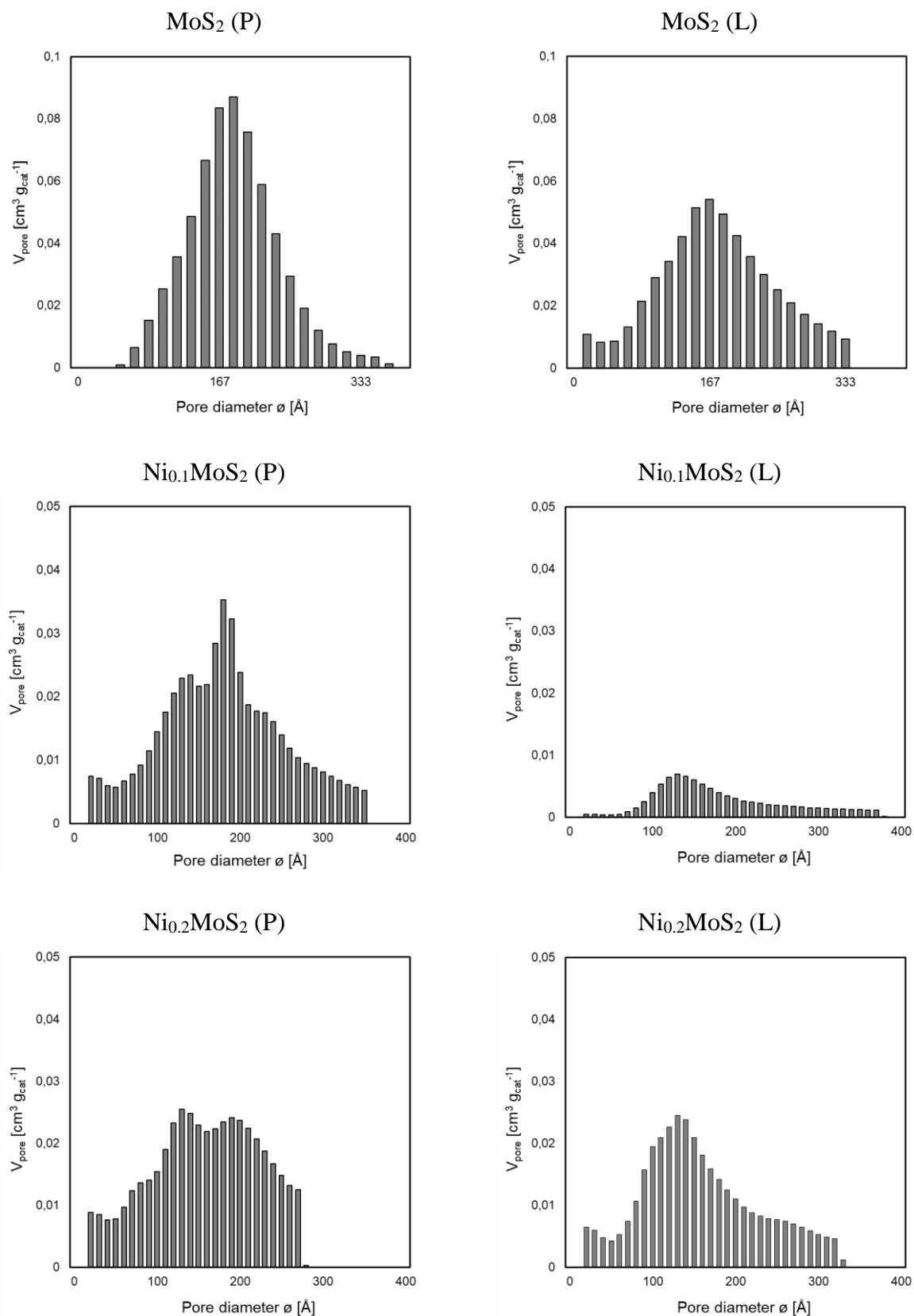


Figure S 6-7. Pore size distribution histograms of parent and HCl-treated MoS₂ and Ni_aMoS₂.

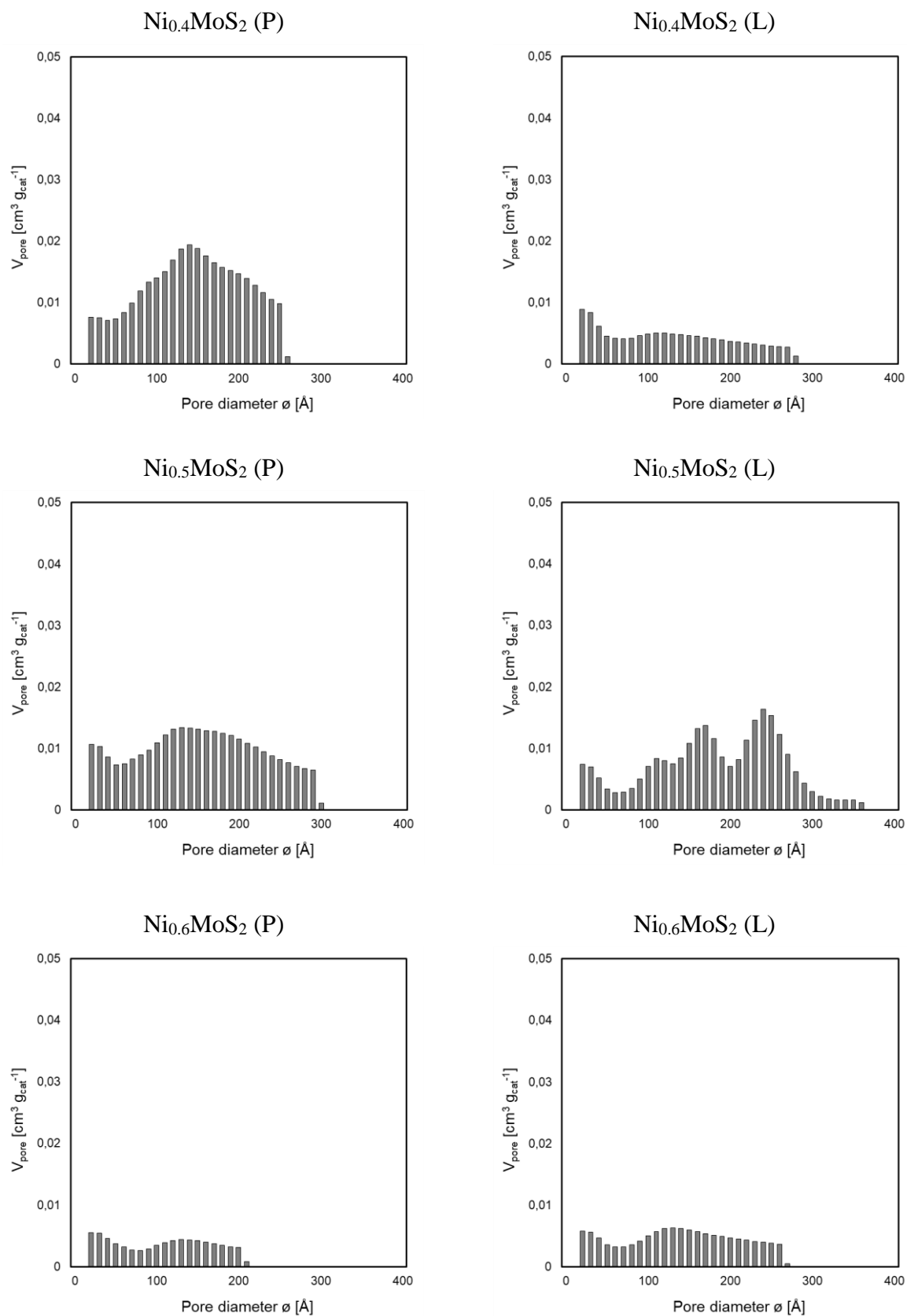


Figure S 6-7. (continued).

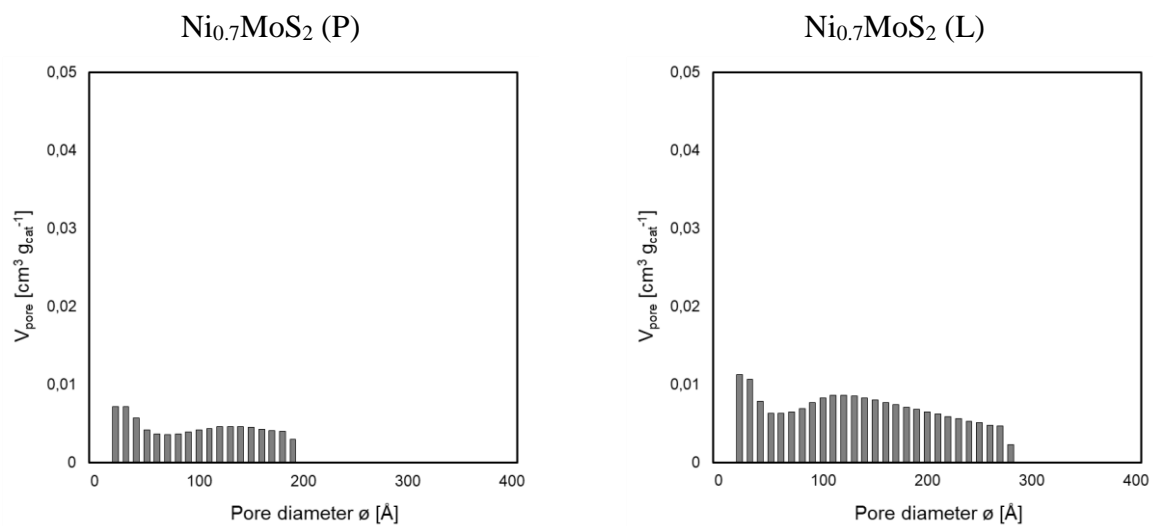


Figure S 6-7. (continued).

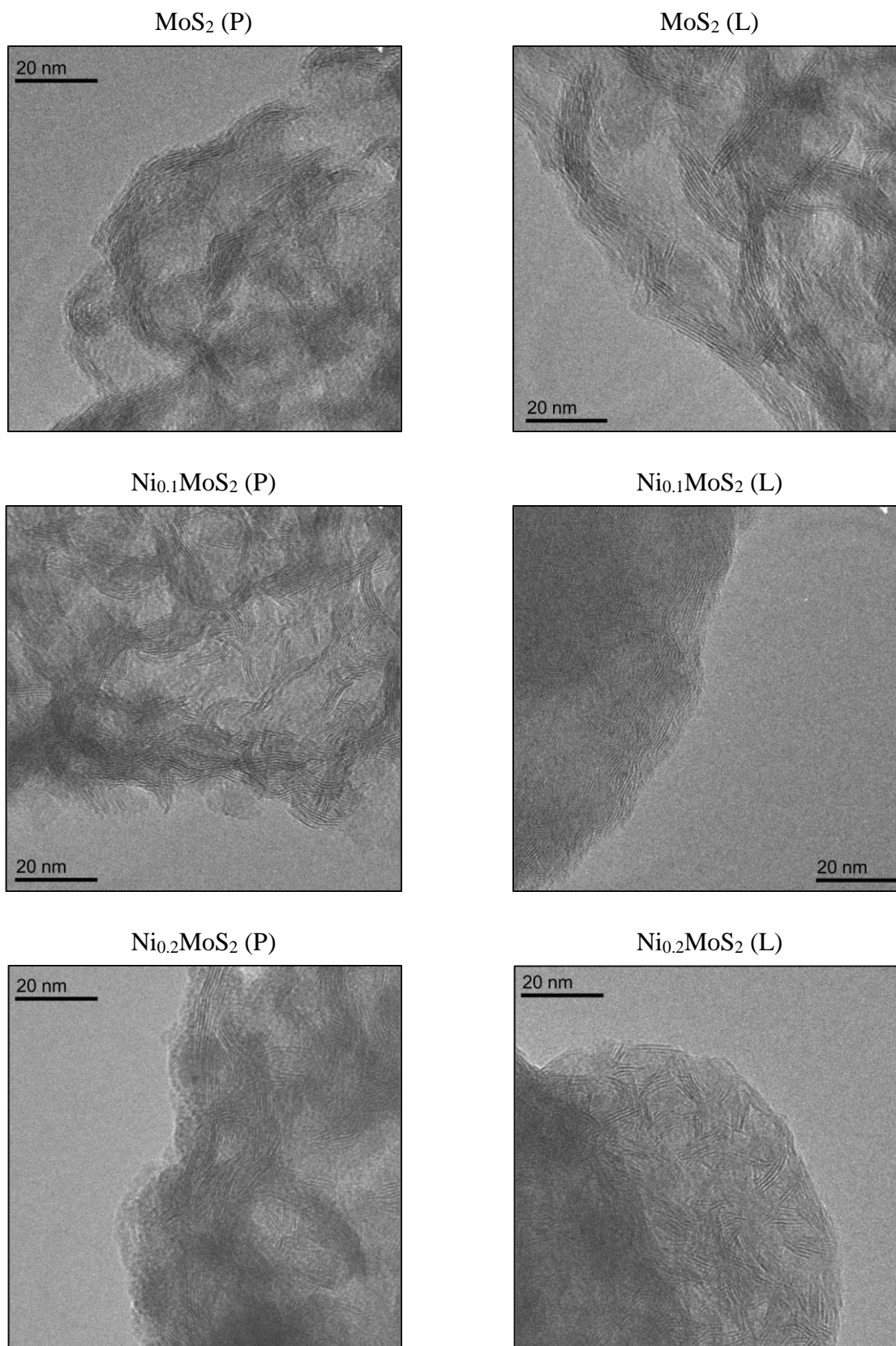
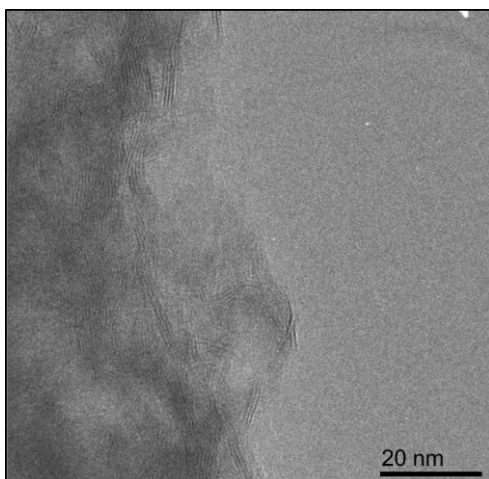
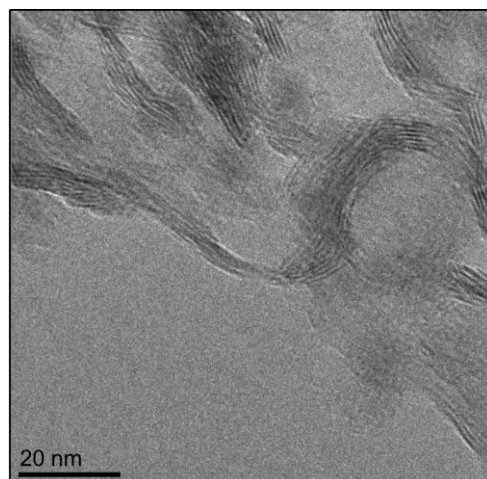


Figure S 6-8. TEM pictures of parent and HCl-treated MoS_2 and Ni_aMoS_2 .

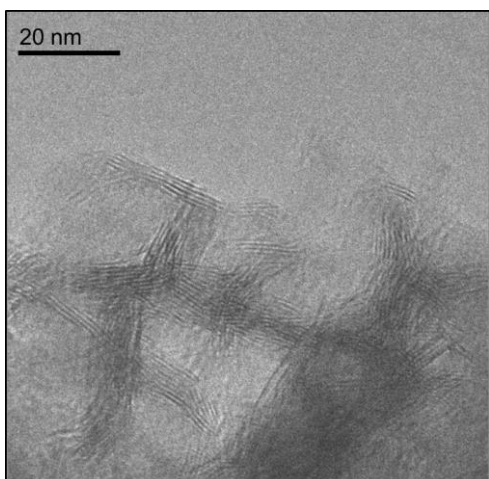
$\text{Ni}_{0.4}\text{MoS}_2$ (P)



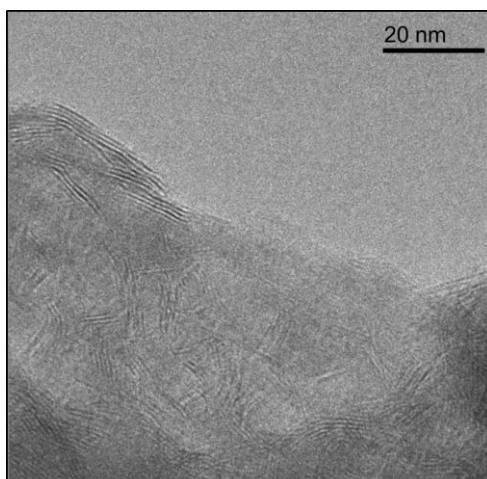
$\text{Ni}_{0.4}\text{MoS}_2$ (L)



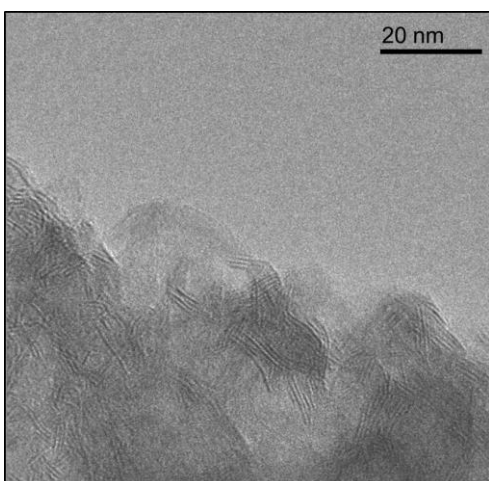
$\text{Ni}_{0.5}\text{MoS}_2$ (P)



$\text{Ni}_{0.5}\text{MoS}_2$ (L)



$\text{Ni}_{0.6}\text{MoS}_2$ (P)



$\text{Ni}_{0.6}\text{MoS}_2$ (L)

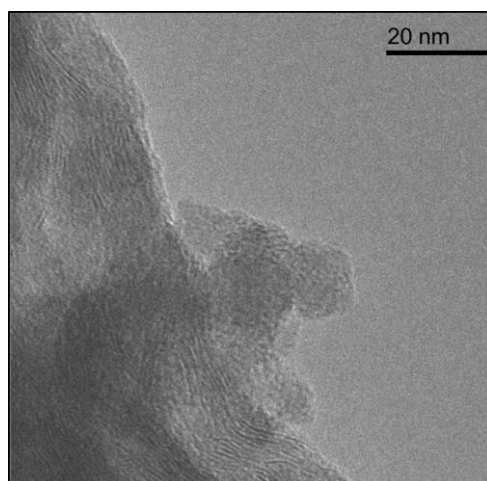


Figure S 6-8. (continued)

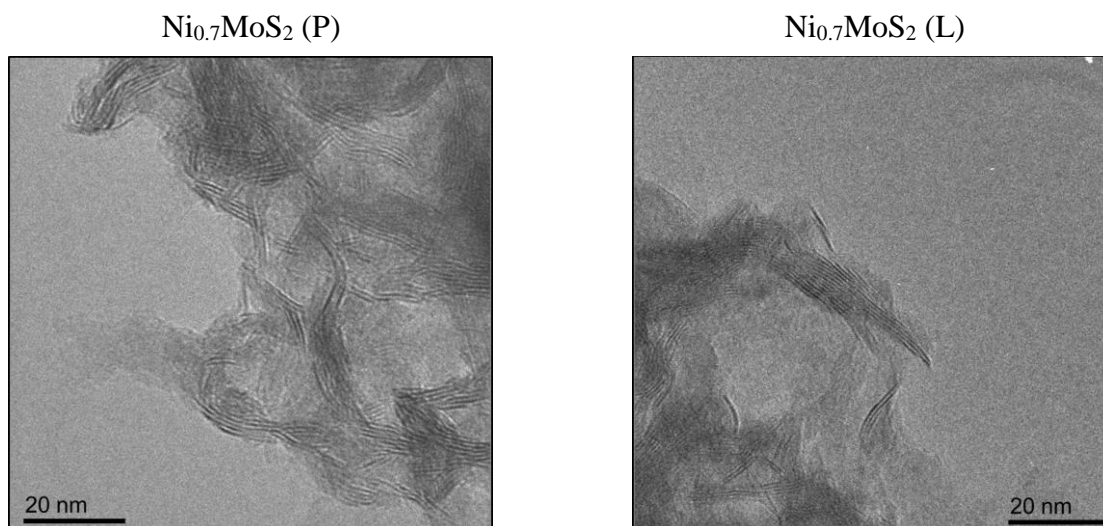


Figure S 6-8. (continued)

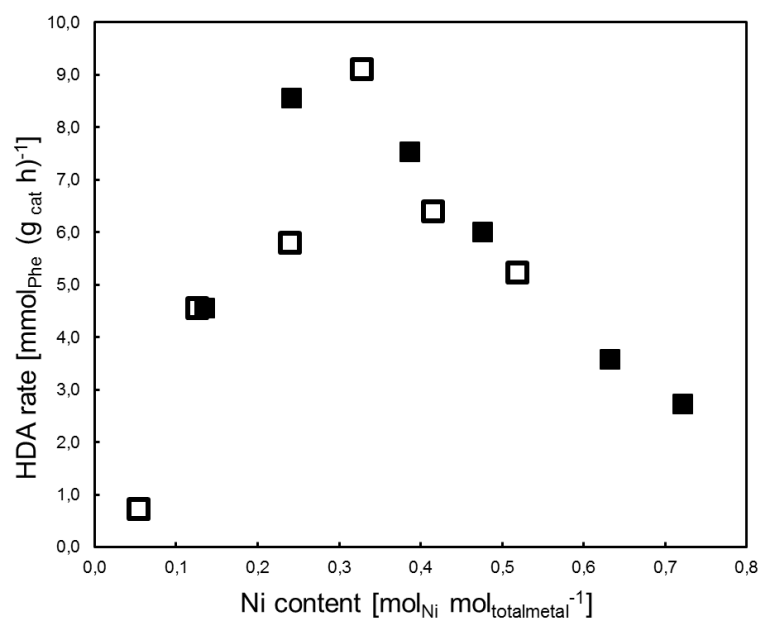


Figure S 6-9. Mass-specific phenanthrene conversion (HDA) rates shown as a function of Ni content. Full squares represent the parent samples, open squares the leached formulations.

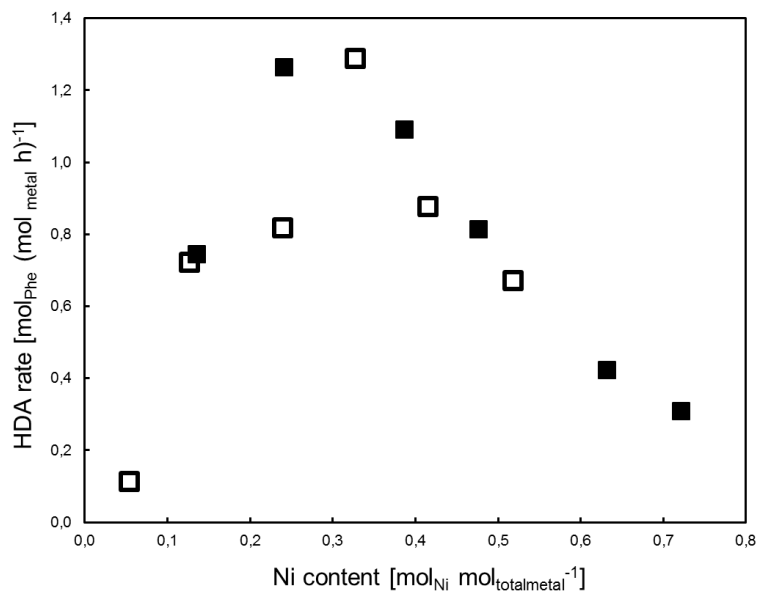


Figure S 6-10. Phenanthrene conversion (HDA) rates on a total metal (mole of total metal) basis over Ni_aMoS₂ shown as a function of Ni content. Full squares represent the parent samples, open squares the leached formulations.

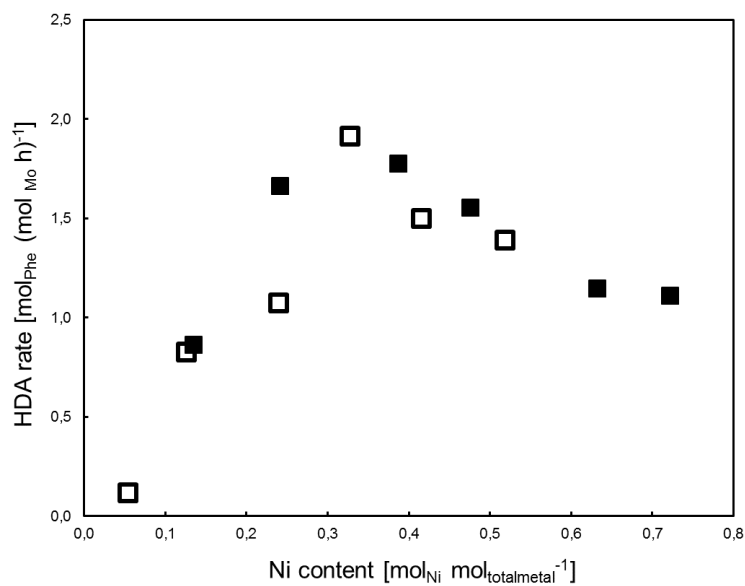


Figure S 6-11. Phenanthrene conversion (HDA) rates on the Mo content (mole of Mo) basis over Ni_aMoS₂ shown as a function of Ni content. Full squares represent the parent samples, open squares the leached formulations.

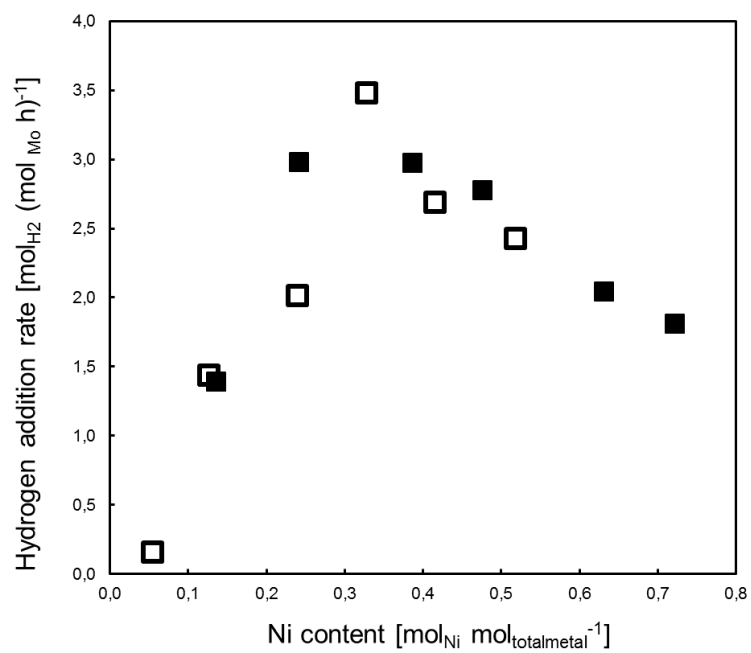


Figure S 6-12. Hydrogen addition rates on the Mo content (mole of Mo) basis over Ni_aMoS₂ shown as a function of Ni content. Full squares represent the parent samples, open squares the leached formulations.

A3. Supporting information chapter 6

1. Additional experimental details and results of characterization

The contents of H, C, N and S were quantified by oxidative combustion using an automated element analyzer instrument (Vario EL CHN Analyzer, ELEMENTAR). The gases CO₂, H₂O, N₂ and SO₂ were detected by gas chromatography. The concentrations of Ni and Mo were photometrically measured after digestion of the solids.

Physisorption of N₂ at -196°C was performed on an automated nitrogen adsorption analyzer Sorptomatic 1990 Series (Thermo Finnigan), where BET surface areas and total pore volumes (Gurvich method) of ~250 mg of sample were determined. The samples were outgassed in vacuum at 250 °C for 2 h prior to adsorption.

Powder X-ray diffraction (XRD) patterns were recorded on an Empyrean system from PANalytical equipped with a Cu X-ray tube (Cu-K_α radiation, 0.154 nm), a nickel K_β-filter, and solid-state detector (PIXcel1D) operated at 45 kV and 40 mA with step size of 0.017° and scan time of 115 s per step. The peaks were identified using the Highscore software.

These results are shown in Table S 6-12 and Table S 6-13 and Figure S 6-13.

For some catalysts, nitric oxide (NO) chemisorption was performed at ambient temperature and pressure on a continuous flow reactor connected to a mass spectrometer (Pfeiffer Vacuum QME 200). The catalyst was packed into a quartz tube and re-sulfided in a flow of H₂S (10 vol % in H₂, 100 mL min⁻¹ g⁻¹) by heating to 400°C (10°C min⁻¹) and holding at this temperature for 1 h. Subsequently, the reactor was cooled to 250°C at which the H₂S/H₂ flow was stopped, and then was cooled to 35°C in a constant flow of 8 mL min⁻¹ N₂ (i.e., 100 mL min⁻¹ g⁻¹). For the pulsing experiments, a loop with a defined volume (1.69 mL) was filled with 10 vol. % NO in helium, which was pulsed (6.9 μmol of NO per pulse) through an automated valve into the reactor. This was repeated 24 times in 30 min intervals and the breakthrough of NO was detected with a mass spectrometer (monitoring the signal at m/z = 30). Total NO uptakes were calculated by subtracting each residual peak area (i.e., NO not adsorbed) from the averaged peak area after saturation with NO and adding up the differences.

Appendices

Table S 6-12. Elemental analysis results for the studied catalysts (sulfided).

Catalysts	Ni [mmol g _{cat} ⁻¹]	Mo/W [mmol g _{cat} ⁻¹]	S [mmol g _{cat} ⁻¹]	S/metal [mol/mol]	Atomic Ni fraction [mol _{Ni} mol _{metal} ⁻¹]
MoS ₂	0	5.3	12.4	2.3	0
Ni _{0.2} MoS ₂	1.6	5.1	12.1	1.8	0.24
WS ₂	0	3.9	8.6	2.2	0
Ni _{0.2} WS ₂	1.1	3.4	8.3	1.8	0.24
Ni _{0.6} WS ₂	4.1	2.32	8.2	1.3	0.64
NiMoWS ₂	4.3	0.5/2.0	8.7	1.3	0.63

Table S 6-13. Textural properties of the studied catalysts (sulfided).

Catalysts	BET surface area [m ² g _{cat} ⁻¹]	Pore volume (Gurvich) [cm ³ g _{cat} ⁻¹]
MoS ₂	140	0.538
Ni _{0.2} MoS ₂	129	0.384
WS ₂	35	0.038
Ni _{0.2} WS ₂	109	0.070
Ni _{0.6} WS ₂	67	0.040
NiMoWS ₂	48	0.045

Appendices

Table S 6-14. Areal titrant uptake of tetrahydroquinoline (THQ) and 2,6-di-tert-butyl-4-methylpyridine (DitBMP).

Catalysts	q_{THQ} [$\mu\text{mol m}^{-2}$]	q_{DitBMP} [$\mu\text{mol m}^{-2}$]
MoS ₂	0.36	0.20
Ni _{0.2} MoS ₂	0.57	0.27
WS ₂	0.80	0.43
Ni _{0.2} WS ₂	0.35	0.17
Ni _{0.6} WS ₂	0.79	Not measured
NiMoWS ₂	1.37	0.58

Table S 6-15. NO uptake measured for representative catalysts. The data for Mo-based catalysts were reported in our previous work (J. Catal. 391 (2020) 212–223).

Catalysts	NO uptake [$\mu\text{mol g}_{\text{cat}}^{-1}$]
MoS ₂	90
Ni _{0.2} MoS ₂	135
WS ₂	68
Ni _{0.2} WS ₂	122

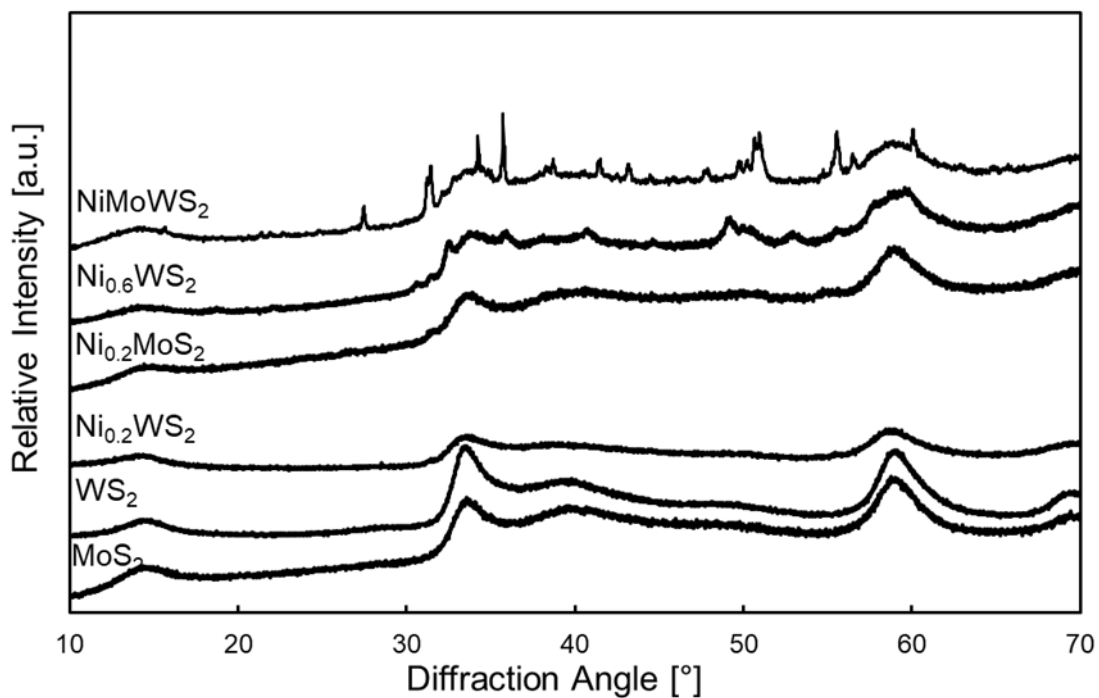


Figure S 6-13. XRD pattern of the studied TMS catalysts. Formulations with Ni content below 50 mol% do not show crystalline NiS_x diffraction peaks.

2. Additional results of titration experiments

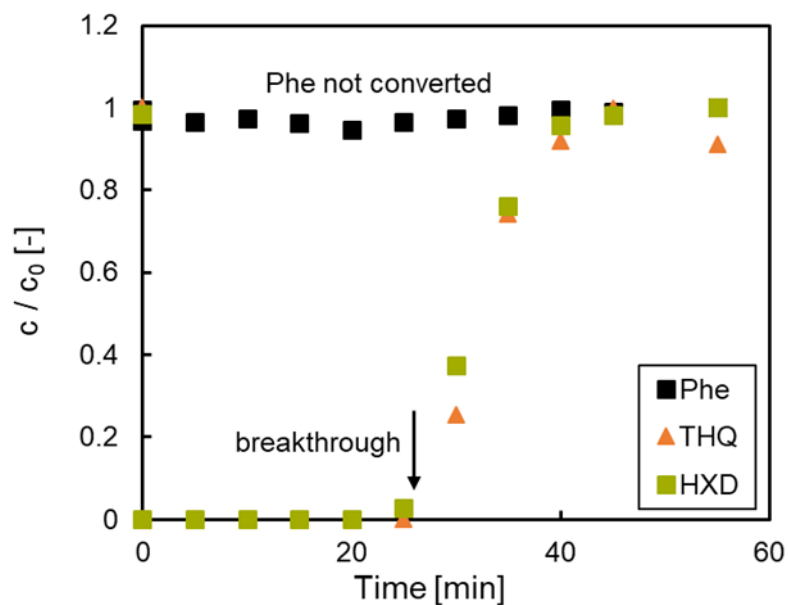


Figure S 6-14. Breakthrough behavior of the tracer (HXD) and the titrant (THQ) in a blank reactor.

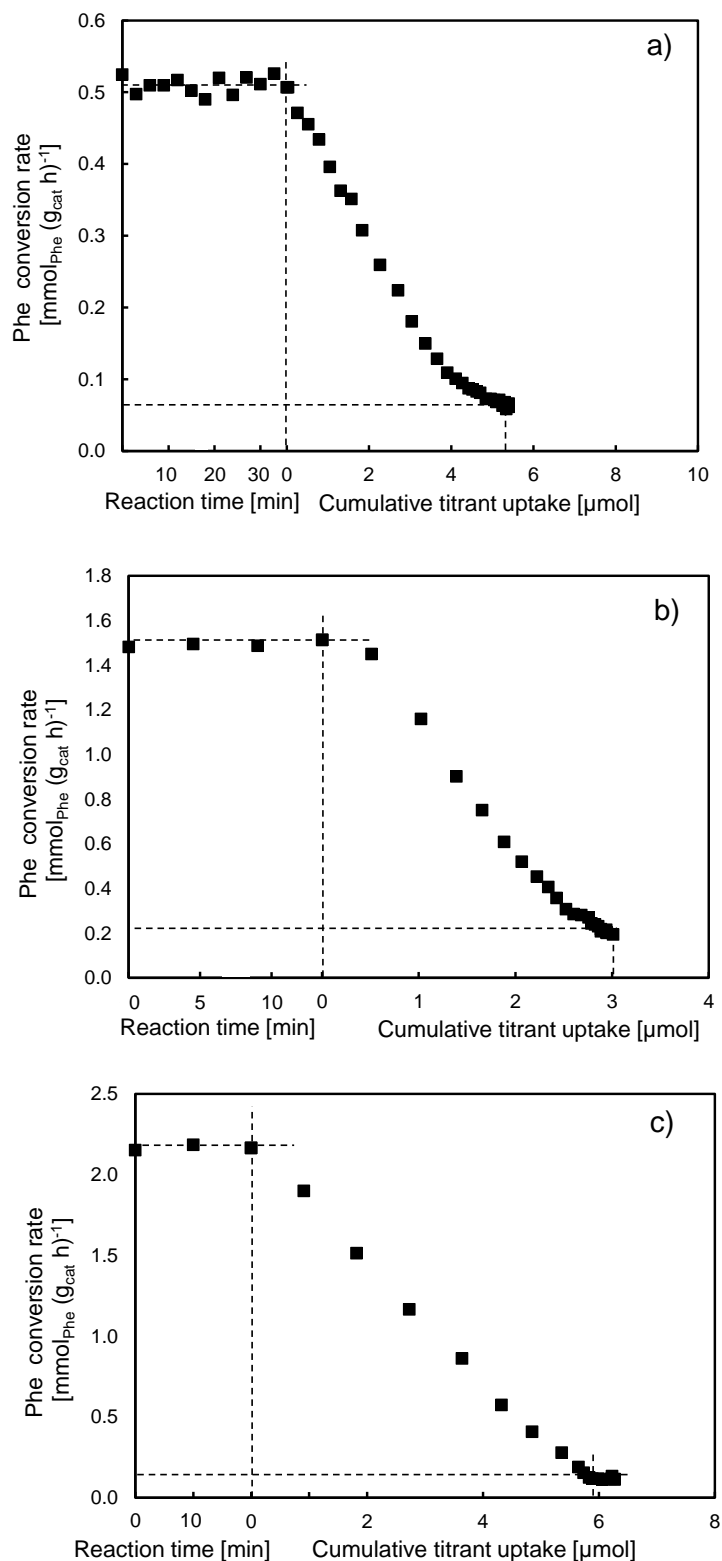


Figure S 6-15. Typical titration curves as a function of cumulative THQ uptake on (a) $\text{Ni}_{0.6}\text{WS}_2$ (240°C), (b) $\text{Ni}_{0.2}\text{WS}_2$ (270°C) and (c) industrial NiMoWS_2 catalyst (250°C). The titration started after reaching a stable activity. The more gradual decrease toward the end of titration may reflect the increasing diffusional hindrance as titration progresses. The estimated TOFs are not significantly affected by using the linear regime or the overall titration segment.

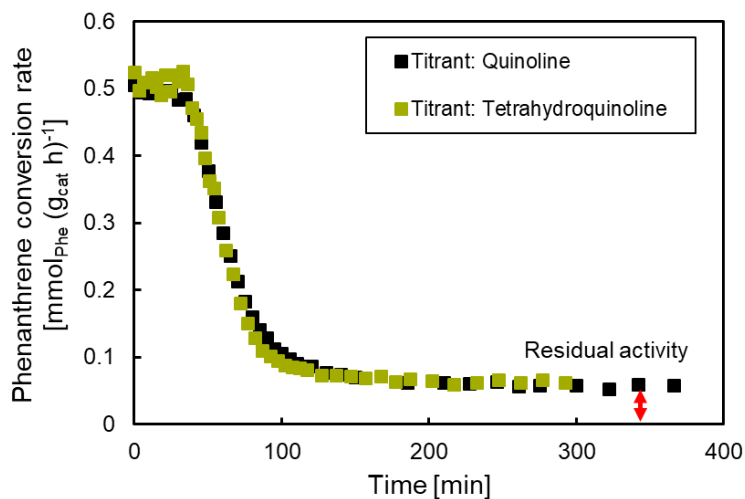


Figure S 6-16. Titration experiments with Q and THQ as the starting titrant during Phe hydrogenation on a $\text{Ni}_{0.6}\text{WS}_2$ catalyst.

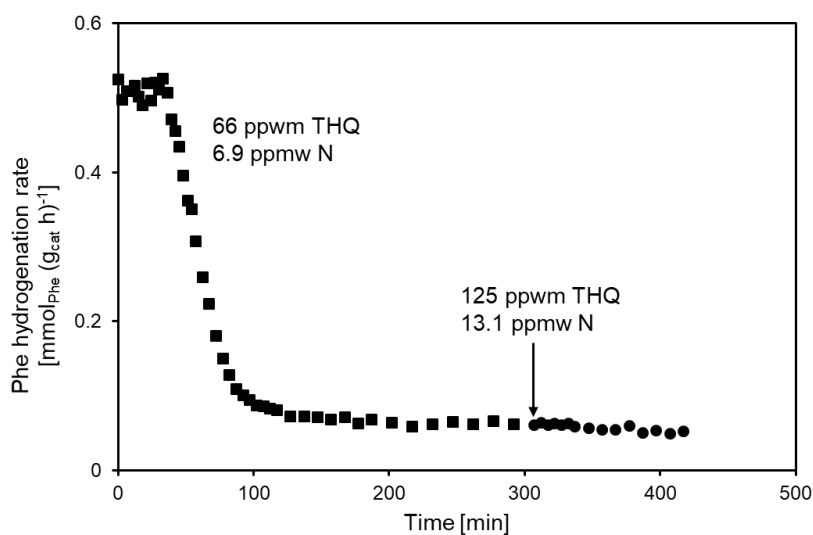


Figure S 6-17. Titration experiments on $\text{Ni}_{0.6}\text{WS}_2$ at 240°C showing that the residual activity was not affected by the change in THQ concentration (filled squares and filled circles). After titration with 66 ppwm THQ (6.9 ppwm N), the titrant concentration was increased to 125 ppwm THQ (13.1 ppwm N).

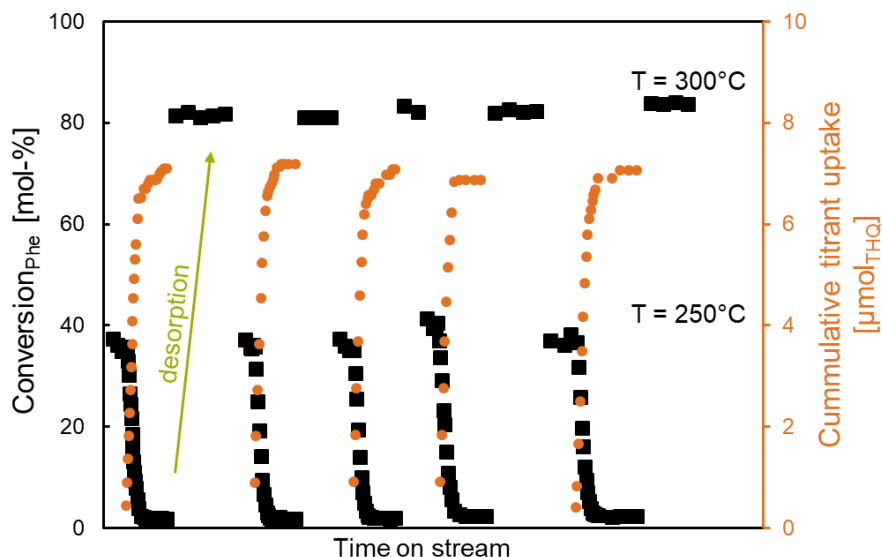


Figure S 6-18. Five repetitive cycles for titration with THQ on the industrial formulation (0.096 mg) at 250°C, $ST = 170\text{-}180 \text{ (g}_{\text{cat}} \text{ h)} \text{ mol}_{\text{Phe}}^{-1}$. The initial conversion of Phe was about 40% at 250 °C at a steady state before titration and at 2% after titration. In between each cycle, desorption of the titrant was achieved by increasing the temperature to 300°C where a conversion level of 80% was reached at the steady state.

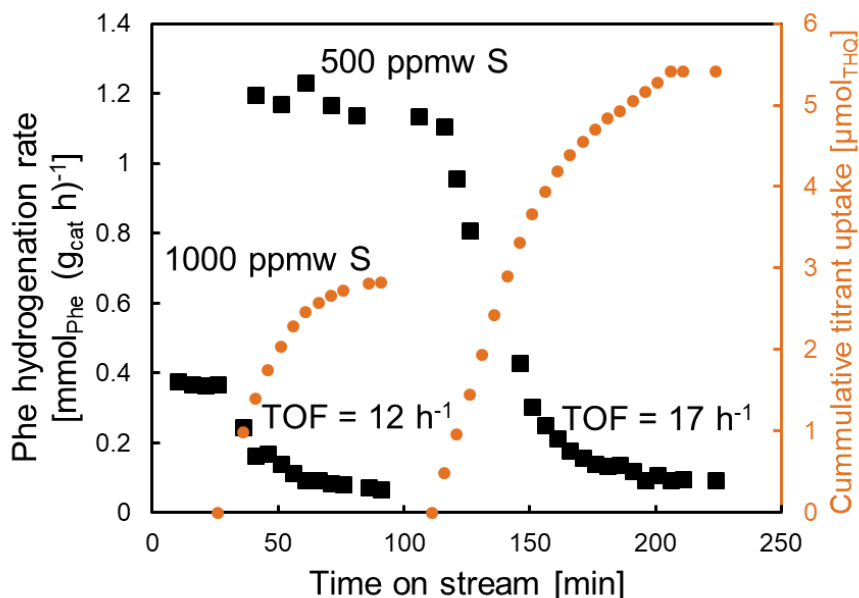


Figure S 6-19. Effect of S content on the titration profile on the WS_2 catalyst. The residual activity became much smaller at a halved S content than at the typical 1000 ppmw S content. The catalyst mass in these experiments was 0.1 g. The results show that both the catalytic activity and the titrant uptake increased drastically after the S content was reduced. The TOFs (averaged over all the titrated sites) estimated are nearly identical for the two cases. The modest difference (17 vs. 12 h^{-1}) is within experimental uncertainties, but it could be caused by the generation of some less-active sites in the 500 ppmw S case

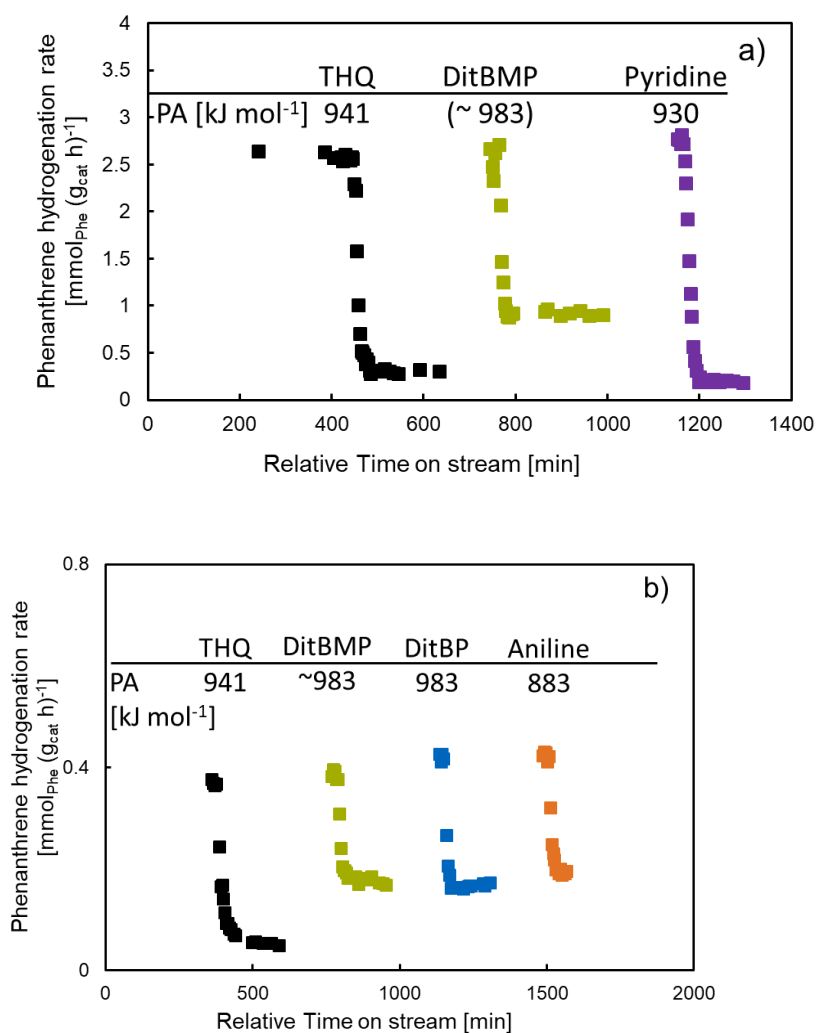


Figure S 6-20. Titration experiments using different titrants for $\text{Ni}_{0.2}\text{MoS}_2$ (upper panel) and unpromoted WS_2 (lower panel). DitBP and DitBMP showed almost identical titration behavior, indicating that the methyl group does not place additional constraints in the binding. Aniline is not sterically hindered as DitBMP and DitBP. However, the titration using aniline led to a higher level of residual activity due to its much weaker basicity

A4. Copyright

Figure Reprint permission

1-1 Request by email

“Di 12.05.2020, 16:49

Dear Mr. Vogelgsang,

Yes, you have permission to use this image with your thesis only. Should you wish to publish this online or in a book, there will be a Use Fee. We support academia and its research efforts. If you produce a version of your thesis in English, may we have a copy for our research files? Are you including Joshua Merrill and the Downer Oil Works in Corry, Pennsylvania?

The additional information about the photograph includes that John Mather was the photographer and the image was taken in July, 1866 - roughly four years after the well ceased production. Also, could you please add: Pennsylvania Historical & Museum Commission to the credit line. Please let me know if you need further information.

Sincerely,

Susan J. Beates, Curator

Drake Well Museum, Pennsylvania Historical & Museum Commission, Titusville, Pennsylvania

Beates, Susan sbeates@pa.gov”

1-2 & 3 Open source

1-4 Adopted and redrawn from references ^[16,18] ^[28] Reprint permission conveyed through Copyright Clearance Center, Inc. License order number: 5221951454133

1-5 Left plot and plot in plot adopted from Albemarle Catalyst Courier, free for download^[63,64]

1-6 Self-made based on information found in^[32,66]

2-1 a) Volcano plot adopted from^[38] Reprint permission conveyed through Copyright Clearance Center, Inc. License order number: 5221970074818; b) and b’) Plots adopted from^[84] Reprint permission conveyed through Copyright Clearance Center, Inc. License order number: 5221970220480

2-2 a) self-drawn; b) ball model of a slab adopted from^[96] Reprint permission conveyed through Copyright Clearance Center, Inc. License order number: 5221970715546; c) Redrawn rim-edge model adopted from^[97] Reprint permission conveyed through Copyright Clearance Center, Inc. License order number: 5221970843767; d) Slab morphology as function of μ_s adopted from^[98] Reprint permission conveyed through Copyright Clearance Center, Inc. License order number: 5221971043163

- 2-3 a) Intercalation model bottom adopted from^[117] Reprint permission conveyed through Copyright Clearance Center, Inc. License order number: 5221980544826. a) top intercalation model & b) contact synergy model & c) symmetrical synergy adopted from^[71] Reprint permission conveyed through Copyright Clearance Center, Inc. License order number: 5221980415188
- 2-4 a) Top: square pyramidal site for Ni promotion adopted from^[133] Reprint permission conveyed through Copyright Clearance Center, Inc. License order number: 5221981321666 a) bottom adopted from^[149] Reprint permission conveyed through Copyright Clearance Center, Inc. License order number: 5221981505688 b), c) & d) Atom resolved STM of slab adopted from^[124] Reprint permission conveyed through Copyright Clearance Center, Inc. License order number: 5221990261647
- 2-5 a) Morphology of NiMoS adopted from^[149] Reprint permission conveyed through Copyright Clearance Center, Inc. License order number: 5221991225404; b) γ -Al₂O₃ supported NiMoS adopted from^[124] Reprint permission conveyed through Copyright Clearance Center, Inc. License order number: 5221991091336; c) Formation of carbosulfide phase adopted from^[122] Reprint permission conveyed through Copyright Clearance Center, Inc. License order number: 5221990908630
- 2-6 Depiction of CUS sites a) adopted from^[102] Reprint permission conveyed through Copyright Clearance Center, Inc. License order number: 5222000330519; b) adopted from^[192] free use for dissertation; c) adopted from^[193] Reprint permission conveyed through Copyright Clearance Center, Inc. License order number 1174035-1
- 2-7 a) Equilibrium constants for HYD of Phe, b) and c) relation between HYD activity and electron density adopted from^[70] free use for dissertation; d) ionization potential vs. HYD rate adopted from^[235] Reprint permission conveyed through Copyright Clearance Center, Inc. License order number: 5222001445245
- 3-3 Eh-pH diagrams adopted from^[285] Request by email

FW: Permission reprint for PhD thesis 🖨️ 📧 Vollansicht schließen

Von: [Matt Baker](#) 25.04.2022 um 21:50 Uf

Dear Ferdinand,

Thank you for your message. Permission is granted to reproduce parts or all of this figure in your thesis. The figure caption should have a citation for the original source, along with the wording "Used with permission of The Minerals, Metals & Materials Society and ASM International." Let me know if I can be of further assistance.

Best regards,
Matt Baker

Matt Baker | Department Head, Content
The Minerals, Metals & Materials Society
370 Corporate Drive Suite 750, Pittsburgh, PA 15217
Direct: 1-724-814-3176 | Fax: 1-724-776-3770 | Toll Free: 1-800-759-4867 (Ext. 280)
mbaker@tms.org | <http://www.tms.org>

From: Ferdinand Vogelsgang <Ferdinand.Vogelsgang@gmx.de>
Sent: Sunday, April 24, 2022 12:25 PM
To: Membership <memberships@tms.org>
Subject: Permission reprint for PhD thesis

Dear Sir or Madam,

I am writing to ask for permission of reuse of two plots published in METALLURGICAL TRANSACTIONS B. The content of interest is "Fig. 6--Eh-pH diagram for the Ni-Fe-S system at 25°C. Standard conditions." and "Fig. 13--Eh-pH diagram for the Mo-S-H₂O system under completely reversible conditions. Standard conditions; acid section only. After Majima" in the publication "The 1976 Extractive Metallurgy Lecture The Metallurgical Society of AIME Direct Leaching of Sulfides: Chemistry and Applications" from Ernest Peters, METALLURGICAL TRANSACTIONS B, VOLUME 7B, DECEMBER 1976-505.

My inquiry was already send to RightsLink and Springer permission section. They suggested to directly contact you and ask for permissions, since it was neither granted to Springer or available via RightsLink.

Can you give me clearance to use the two diagram in my PhD thesis only?

Thank you in advance and best wishes,

Ferdinand Vogelsgang

Chapter 5 & Chapter 6: Permission of reprint within the right of authors granted by Elsevier. See also <https://www.elsevier.com/about/policies/copyright#Author-rights> (accessed 04.01.2022)

Publications and conference contributions

Conferences

- DGMK-Conference „Catalysis – Novel Aspects in Petrochemistry and Refining“,
Berlin, 2016
‘Hydrogenation of Polyaromatic Compounds over Unsupported Ni-Mo, Ni-W, and Ni-Mo-W Sulfide Catalysts’
- 50. Jahrestreffen Deutscher Katalytiker,
Weimar, 2017
‘Hydrogenation and hydrodesulfurization over unsupported Ni-Mo-W sulfide catalysts’
- 13th European Congress on Catalysis (EUROPACAT 2017),
Florenz, 2017
‘Roles of tungsten and molybdenum in hydrotreatment reactions over unsupported Ni-Mo-W sulfide catalysts’
- Molecular Aspects of Catalysis by Sulfides (MACS^{VIII}),
Cabourg, Normandy, France, 2019
‘Roles of tungsten and molybdenum in hydrotreatment reactions over unsupported Ni-Mo-W sulfide catalysts’

Publications

- Ferdinand Vogelgsang, Hui Shi, Johannes A. Lercher, *Journal of Catalysis* 403 (2021) 98-110.
‘Toward quantification of active sites and site-specific activity for polyaromatics hydrogenation on transition metal sulfides’
- Ferdinand Vogelgsang, Yinjie Ji, Hui Shi, Johannes A. Lercher, *Journal of Catalysis* 391 (2020) 212-223.
‘On the multifaceted roles of NiS_x in hydrodearomatization reactions catalyzed by unsupported Ni-promoted MoS₂’
- Yuran Wang, Ferdinand Vogelgsang, Prof. Yuriy Román-Leshkov, *ChemCatChem* 7, (2015), 916 – 920.
‘Acid-catalyzed Oxidation of Levulinate Derivatives to Succinates under Mild Conditions’